



MISSOURI
S&T

CENTER FOR TRANSPORTATION INFRASTRUCTURE AND SAFETY



Innovative Concrete Bridging Systems for Pedestrian Bridges: Implementation and Monitoring

by

John J. Myers, Ph.D., P.E.

Kurt E. Bloch



NUTC
R250

**A National University Transportation Center
at Missouri University of Science and Technology**

Disclaimer

The contents of this report reflect the views of the author(s), who are responsible for the facts and the accuracy of information presented herein. This document is disseminated under the sponsorship of the Department of Transportation, University Transportation Centers Program and the Center for Transportation Infrastructure and Safety NUTC program at the Missouri University of Science and Technology, in the interest of information exchange. The U.S. Government and Center for Transportation Infrastructure and Safety assumes no liability for the contents or use thereof.

Technical Report Documentation Page

1. Report No. NUTC R250	2. Government Accession No.	3. Recipient's Catalog No.	
4. Title and Subtitle Innovative Concrete Bridging System for Pedestrian Bridges: Implementation and Monitoring		5. Report Date Date: August 2013	
		6. Performing Organization Code	
7. Author/s John J. Myers, Ph.D., P.E., Kurt E. Bloch		8. Performing Organization Report No. Project # 00024651	
9. Performing Organization Name and Address Center for Transportation Infrastructure and Safety/NUTC program Missouri University of Science and Technology 220 Engineering Research Lab Rolla, MO 65409		10. Work Unit No. (TRAIS)	
		11. Contract or Grant No. DTRT06-G-0014	
12. Sponsoring Organization Name and Address U.S. Department of Transportation Research and Innovative Technology Administration 1200 New Jersey Avenue, SE Washington, DC 20590		13. Type of Report and Period Covered Final	
		14. Sponsoring Agency Code	
15. Supplementary Notes			
16. Abstract Two precast, prestressed pedestrian bridges were designed for rapid construction in Rolla, MO, utilizing high-strength concrete (HSC) and high-strength self-consolidating concrete (HS-SCC) with a target 28 day compressive strength of 68.9 MPa (10,000 psi) and release compressive strength of 24.1 MPa (3,500 psi). In addition, a glass fiber reinforced polymer (GFRP) bar reinforced deck panel system was utilized in one of the two deck panels on each bridge. Material properties were tested for compression, elastic modulus, modulus of rupture, splitting tensile strength, creep, and shrinkage following ASTM standards. Instrumentation systems within the spandrel beams and precast deck panels were implemented to monitor early and later-age temperature and strain variations between the concrete mixtures and reinforcing types. In addition, the sensors were utilized to calculate the prestress losses for HSC and HS-SCC in the spandrel beams. A live load test was completed one year after spandrel beam fabrication to investigate the differences in deflection of HSC, HS-SCC, and reinforcement types. All material and mechanical results were compared between HSC and HS-SCC. Furthermore, the results were compared to standard empirical models presented by AASHTO, ACI, and PCI.			
17. Key Words words	18. Distribution Statement No restrictions. This document is available to the public through the National Technical Information Service, Springfield, Virginia 22161.		
19. Security Classification (of this report) unclassified	20. Security Classification (of this page) unclassified	21. No. Of Pages 273	22. Price

ABSTRACT

Two precast, prestressed pedestrian bridges were designed for rapid construction in Rolla, MO, utilizing high-strength concrete (HSC) and high-strength self-consolidating concrete (HS-SCC) with a target 28 day compressive strength of 68.9 MPa (10,000 psi) and release compressive strength of 24.1 MPa (3,500 psi). In addition, a glass fiber reinforced polymer (GFRP) bar reinforced deck panel system was utilized in one of the two deck panels on each bridge.

Material properties were tested for compression, elastic modulus, modulus of rupture, splitting tensile strength, creep, and shrinkage following ASTM standards. Instrumentation systems within the spandrel beams and precast deck panels were implemented to monitor early and later-age temperature and strain variations between the concrete mixtures and reinforcing types. In addition, the sensors were utilized to calculate the prestress losses for HSC and HS-SCC in the spandrel beams. A live load test was completed one year after spandrel beam fabrication to investigate the differences in deflection of HSC, HS-SCC, and reinforcement types. All material and mechanical results were compared between HSC and HS-SCC. Furthermore, the results were compared to standard empirical models presented by AASHTO, ACI, and PCI.

TABLE OF CONTENTS

	Page
ABSTRACT.....	ii
LIST OF ILLUSTRATIONS.....	ix
LIST OF TABLES.....	xiv
NOMENCLATURE.....	xvi
SECTION	
1. INTRODUCTION.....	1
1.1. BACKGROUND.....	1
1.2. OBJECTIVES.....	2
1.3. SCOPE.....	3
1.4. ORGANIZATION OF REPORT.....	3
2. LITERATURE REVIEW.....	4
2.1. HIGH-STRENGTH CONCRETE.....	4
2.1.1. Definition of HSC.....	4
2.1.2. Material Properties of HSC.....	4
2.1.2.1 Strength.....	5
2.1.2.2 Modulus of elasticity.....	7
2.1.2.3 Creep and shrinkage.....	9
2.1.3. Prestress Loss.....	10
2.1.3.1 Myers and Yang (2005).....	11
2.1.3.2 Tadros et. al. (2003).....	13
2.1.3.3 Cousins (2005).....	13
2.2. HIGH-STRENGTH SELF-CONSOLIDATING CONCRETE.....	14
2.2.1. Definition of HS-SCC.....	14
2.2.2. Material Properties of HS-SCC.....	14
2.2.2.1 Strength.....	15
2.2.2.2 Modulus of elasticity.....	15
2.2.2.3 Creep and shrinkage.....	16
2.2.3. Prestress Loss.....	17

2.2.3.1 Kukay et. al. (2007)	17
2.2.3.2 Naito et. al. (2006)	17
2.2.3.3 Brewe (2009)	17
2.2.4. Recent Projects	18
2.2.4.1 Ritto Bridge, Japan.....	18
2.2.4.2 The Sodra Lanken Project, Sweden.....	18
2.2.4.3 Higashi-Oozu Viaduct, Japan	18
2.3. CONCRETE TEMPERATURES	18
2.4. CONCRETE BRIDGE LOAD TESTS.....	20
2.4.1. Myers and Yang (2005).....	21
2.4.2. Dwairi et. al. (2010)	21
2.5. PRECAST CONCRETE CONSTRUCTION.....	22
2.6. GLASS FIBER REINFORCED POLYMER.	22
2.6.1. Definition of GFRP	22
2.6.2. Material Properties of GFRP	23
2.6.3. GFRP in Bridge Decks.....	23
3. RESEARCH PROGRAM	24
3.1. PROGRAM TEAM	24
3.2. DESIGN DETAILS OF BRIDGES.....	24
3.2.1. HSC and HS-SCC Prestressed/Precast L Spandrel Beam.....	26
3.2.2. HSC and HS-SCC Precast Deck Panels.....	27
3.3. MIXTURE PROPORTIONING	28
4. FABRICATION AND CONSTRUCTION.....	30
4.1. INTRODUCTION	30
4.2. FABRICATION OF PRECAST SPANDREL BEAMS.....	31
4.3. FABRICATION OF PRECAST DECK PANELS.....	33
4.4. BRIDGE ERECTION.....	35
5. MATERIAL TESTING PROGRAM.....	40
5.1. INTRODUCTION	40
5.1.1. Member Cast	40
5.1.2. Curing Conditions	41

5.1.3. Overview of Testing Program	42
5.2. COMPRESSIVE STRENGTH	42
5.3. MODULUS OF ELASTICITY.....	43
5.4. MODULUS OF RUPTURE	44
5.5. SPLITTING TENSILE STRENGTH	46
5.6. CREEP AND SHRINKAGE	47
5.7. COEFFICIENT OF THERMAL EXPANSION.....	51
5.8. TENSILE STRENGTH OF GFRP	52
6. INSTRUMENTATION PLANS AND PROCEDURES	53
6.1. INTRODUCTION	53
6.2. MEASUREMENT TYPES.....	53
6.2.1. Concrete Strains	54
6.2.2. Concrete Temperatures.....	54
6.2.3. Beam Camber/Deflection.....	55
6.3. GAUGES AND MEASUREMENT SYSTEMS	55
6.3.1. Vibrating Wire Strain Gauges with Embedded Thermistors.....	55
6.3.2. Demountable Mechanical Strain Gauge.....	56
6.3.3. Tensioned-Wire Deflection Measuring System	57
6.3.4. Precise Surveying System	59
6.4. DATA ACQUISITION	60
6.4.1. Data Acquisition System	60
6.4.2. Programming and Data Collection	62
6.5. INSTRUMENTATION PLAN.....	63
6.5.1. Instrumentation Gauges and Equipment	63
6.5.2. Location of Instrumentation	64
6.5.3. Gauge Numbering and Identification	67
6.6. PREPARATION AND FIELD INSTALLATION.....	68
6.6.1. Vibrating Wire Strain Gauge Preparation	68
6.6.2. Field Installation.....	68
6.6.2.1 Prestressed precast beams	68
6.6.2.2 Precast deck panels	70

6.6.2.3 Instrumentation during shipping and erection	73
6.7. PROBLEMS ENCOUNTERED	74
7. MATERIAL TEST RESULTS AND DISCUSSION	76
7.1. INTRODUCTION	76
7.2. COMPRESSIVE STRENGTH	76
7.3. MODULUS OF ELASTICITY.....	78
7.4. MODULUS OF RUPTURE	81
7.5. SPLITTING TENSILE STRENGTH	83
7.6. CREEP	86
7.7. SHRINKAGE	92
7.8. COEFFICIENT OF THERMAL EXPANSION.....	96
7.9. TENSILE STRENGTH AND MODULUS OF ELASTICITY OF GFRP.....	97
7.10. SUMMARY	97
8. TEMPERATURE MEASUREMENTS	99
8.1. INTRODUCTION	99
8.1.1. General	99
8.1.2. Ambient Temperature Data	99
8.2. HYDRATION TEMPERATURES	99
8.2.1. Background	99
8.2.2. Measurements.....	100
8.2.3. Discussion	107
8.3. MEAN BRIDGE TEMPERATURES.....	108
8.3.1. Background	108
8.3.2. Measurements.....	108
8.3.3. Discussion	117
8.4. THERMAL GRADIENTS.....	119
8.4.1. Background	119
8.4.2. Measurements.....	119
8.4.3. Discussion	130
8.5. SUMMARY AND CONCLUSIONS	133
9. CONCRETE STRAIN MEASUREMENTS.....	135

9.1. INTRODUCTION	135
9.2. INTERPRETATION OF GAUGE READINGS	135
9.3. CONCRETE STRAINS BEFORE RELEASE.....	136
9.3.1. Background	136
9.3.2. Measurements and Discussion	136
9.4. CONCRETE STRAINS AFTER RELEASE OF PRESTRESS.....	141
9.4.1. Background	141
9.4.2. Measurements and Discussion	141
9.5. CONCRETE STRAINS IN BEAMS DURING STORAGE.....	145
9.5.1. Background	145
9.5.2. Measurements and Discussion	145
9.6. CONCRETE STRAINS IN DECK PANELS DURING FABRICATION ...	148
9.6.1. Background	148
9.6.2. Measurements and Discussion	148
9.7. CONCRETE STRAINS DUE TO TRANSPORTATION AND ERECTION	153
9.7.1. Background	153
9.7.2. Measurements and Discussion	155
9.8. SUMMARY AND CONCLUSIONS	160
10. PRESTRESS LOSS MEASUREMENTS	161
10.1. INTRODUCTION	161
10.1.1. General	161
10.1.2. Measurement of Prestress Losses Using Internal VWSGs	162
10.2. ELASTIC SHORTENING AT RELEASE.....	163
10.2.1. Background	163
10.2.2. Measurements and Discussion	163
10.3. TOTAL LOSSES	165
10.3.1. Background	165
10.3.2. Measurements and Discussion	165
10.4. SUMMARY AND CONCLUSIONS	169
11. LIVE LOAD TESTING PROGRAM	171

11.1. INTRODUCTION	171
11.2. LOAD TEST PROGRAM	171
11.2.1. Load Cases	171
11.2.2. Bridge Deflections.....	174
11.3. LIVE LOAD TEST RESULTS	179
11.3.1. Downloading the Deflection Data.....	179
11.3.2. Converting Raw Deflection Data	180
11.3.3. Theoretical Deflection Data	183
11.3.4. Deflection Results	183
11.4. SUMMARY AND CONCLUSIONS	191
12. SUMMARY, CONCLUSIONS, AND RECOMMENDATIONS	193
12.1. SUMMARY AND CONCLUSIONS OF FINDINGS	193
12.2. RECOMMENDATIONS FOR FUTURE RESEARCH.....	196
APPENICIES	
A. STEEL AND GFRP DECK PANEL REINFORCEMENT DESIGN	198
B. PROGRAM FOR DAS CR1000	203
C. GFRP TEST RESULTS	207
D. EXAMPLE STRESS AND STRAIN CALCULATIONS	209
E. PRESTRESS LOSS SAMPLE CALCULATIONS—AASHTO LRFD 2007 (REFINED)	220
F. PRESTRESS LOSS SAMPLE CALCULATIONS—PCI DESIGN HANDBOOK (2004)	231
G. LOAD TEST TEMPERATURE EFFECTS.....	238
H. ROLLA HSC PEDESTRIAN BRDIGE DEFLECTION PROFILES.....	243
I. ROLLA HS-SCC PEDESTRIAN BRDIGE DEFLECTION PROFILES.....	250
J. ROLLA PEDESTRIAN BRIDGE FABRICATION PLANS	257
BIBLIOGRAPHY.....	269

LIST OF ILLUSTRATIONS

Figure	Page
2.1. Stress Strain Relationships for Varying Concrete Strengths.	6
2.2. Concrete Strength to Cement Content to Aggregate Size (Myers, 1998).	7
2.3. Modulus of Elasticity vs. Compressive Strength for Varying Aggregates.	8
2.4. Stress vs. Time for Bridge Girder (Tadros et. al., 2003).	11
2.5. AASHTO LRFD 2007 Specification Design Thermal Gradients.	20
3.1. Bridge Locations.	25
3.2. Cross Section of HSC & HS-SCC Bridges.	26
3.3. Cross Section of HSC & HS-SCC Bridge Spandrel Beam.	27
4.1. Steel in Beam.	31
4.2. Concrete Placement for Beams.	32
4.3. Scribed Crosses Used to Prevent Cold-Joint in HS-SCC Beam.	32
4.4. Beam Storage Prior to Transfer.	33
4.5. Formwork, Steel, & GFRP for the Deck Panels.	34
4.6. Concrete Placement for Deck Panels.	34
4.7. Concrete Deck Panel Storage Prior to Transfer.	35
4.8. Abutment Placement for HSC Bridge Location.	36
4.9. Trucks Arriving with HSC & HS-SCC Beams from Marshall, MO.	36
4.10. HSC Beam Erection.	37
4.11. HSC Beam Welded to Abutment.	37
4.12. Slabs Placed on Top of Neoprene Pads on Top of HSC Beams.	38
4.13. HS-SCC Beam Erection.	38
4.14. HS-SCC Deck Panel Erection.	39
4.15. Cracking on Slab at Crane Lifting Location.	39
5.1. QC/QA Specimens Placement at Precast Plant.	40
5.2. Comparison of Marshall, MO (Sedalia, MO) & Rolla, MO Temperatures.	41
5.3. Storage of QC/QA Specimens at Missouri S&T in Rolla, MO.	41
5.4. Modulus of Elasticity Test.	43
5.5. Modulus of Rupture.	45

5.6. Splitting Tensile Strength.	46
5.7. Creep & Shrinkage Specimens & DEMEC Point Arrangements.	48
5.8. Schematic of Creep Loading Frame for 40% Target Load.	50
5.9. Creep Loading Frame & Specimens.	51
5.10. Coefficient of Thermal Expansion (CTE) Test at Missouri S&T.	52
6.1. Vibrating Wire Strain Gauge.	56
6.2. DEMEC Strain Gauge & Discs.	57
6.3. Tensioned-Wire System for Deflection.	59
6.4. Precision Surveying System.	60
6.5. Data Acquisition System.	61
6.6. DAS Components & Gauges for Each Bridge.	62
6.7. Data Acquisition System being Programmed at Precast Plant.	63
6.8. Plan Illustrating HSC Instrumentation “Cluster” Locations (Plan View).	64
6.9. Plan Illustrating HS-SCC Instrumentation “Cluster” Locations (Plan View).	65
6.10. Location of Sensors along Cross Section of Beams.	65
6.11. Location of Sensors along Cross Section of Deck Panels.	66
6.12. Location of DEMEC Points.	66
6.13. VWSGs in Beams at Fabrication in Marshall, MO.	69
6.14. DEMEC Reading.	70
6.15. Beam Storage at Marshall, MO.	70
6.16. Schematic of VWSGs Attached to Deck Panel Reinforcement.	71
6.17. VWSG Embedded in Panels.	72
6.18. Method Used to Free VWSG Wires.	72
6.19. Precast Deck Panel Storage at Marshall, MO.	73
6.20. DAS during Bridge Erection.	74
6.21. Final DAS System Attached to Bridges.	74
7.1. HSC Average Compressive Strength.	77
7.2. HS-SCC Average Compressive Strength.	77
7.3. Average Modulus of Elasticity for HSC & HS-SCC.	78
7.4. Modulus of Elasticity vs. Compressive Strength for HSC.	80
7.5. Modulus of Elasticity vs. Compressive Strength for HS-SCC.	80

7.6. Average Modulus of Rupture for HSC & HS-SCC.....	81
7.7. Modulus of Rupture vs. Compressive Strength for HSC.....	82
7.8. Modulus of Rupture vs. Compressive Strength for HS-SCC.	82
7.9. Average Splitting Tensile Strength of HSC & HS-SCC.....	84
7.10. Splitting Tensile Strength vs. Compressive Strength of HSC.	85
7.11. Splitting Tensile Strength vs. Compressive Strength of HS-SCC.	85
7.12. Creep Results for HSC & HS-SCC.....	89
7.13. Shrinkage Results for HSC & HS-SCC Precast Deck Panels.....	95
8.1. Hydration Temperature of HSC Spandrel Beam at Support.....	101
8.2. Hydration Temperature of HSC Spandrel Beam at Mid-Span.	101
8.3. Hydration Temperature of HS-SCC Spandrel Beam at Support.	102
8.4. Hydration Temperature of HS-SCC Spandrel Beam at Mid-Span.	102
8.5. Hydration Temperature of HSC Deck Panel Reinforced with Mild Steel.....	104
8.6. Hydration Temperature of HSC Deck Panel Reinforced with GFRP.....	105
8.7. Hydration Temperature of HS-SCC Deck Panel Reinforced with Mild Steel.....	105
8.8. Hydration Temperature of HS-SCC Deck Panel Reinforced with GFRP.	106
8.9. Shade Covering Bridge Deck.....	109
8.10. Maximum Daily Temperature of HSC Bridge.....	110
8.11. Maximum Daily Temperature of HS-SCC Bridge.	110
8.12. Minimum Daily Temperature of HSC Bridge.	111
8.13. Minimum Daily Temperature of HS-SCC Bridge.....	111
8.14. Average Maximum Monthly Temperature of HSC Bridge.	112
8.15. Average Maximum Monthly Temperature of HS-SCC Bridge.....	112
8.16. Average Minimum Monthly Temperature of HSC Bridge.....	113
8.17. Average Minimum Monthly Temperature of HS-SCC Bridge.....	113
8.18. Maximum Daily Thermal Gradients for HSC & HS-SCC Beams.	120
8.19. Maximum Daily Thermal Gradients for HSC & HS-SCC Deck Panels.	121
8.20. Time of Maximum Positive & Negative Gradients for Beams.....	122
8.21. Time of Maximum Positive & Negative Gradients for HS-SCC Panels.....	123
8.22. Average Maximum Monthly Gradients of Bridge Beam.	124
8.23. Average Maximum Monthly Gradients of Bridge Deck Panels.....	125

8.24. Thermal Gradients in HSC Spandrel Beams.	128
8.25. Thermal Gradients in HS-SCC Spandrel Beams.	129
8.26. Thermal Gradients in HSC Precast Deck Panels.	129
8.27. Thermal Gradients in HS-SCC Precast Deck Panels.	130
8.28. Design Positive Gradients vs. HSC Maximum Positive Gradients.	131
8.29. Design Positive Gradients vs. HS-SCC Maximum Positive Gradients.	131
8.30. Design Negative Gradients vs. HSC Maximum Negative Gradients.	132
8.31. Design Negative Gradients vs. HS-SCC Maximum Negative Gradients.	132
9.1. Strains & Temperatures at Support of HSC Beam during Fabrication.	137
9.2. Strains & Temperatures at Mid-Span of HSC Beam during Fabrication.	138
9.3. Strains & Temperatures at Support of HS-SCC Beam during Fabrication.	139
9.4. Strains & Temperatures at Mid-Span of HS-SCC Beam during Fabrication.	140
9.5. Strain Comparison at Mid-Span of HSC Spandrel Beam at Release.	142
9.6. Strain Comparison at Mid-Span of HS-SCC Spandrel Beam at Release.	143
9.7. Comparison of Stresses at Release for Top Fiber Mid-Span.	144
9.8. Comparison of Stresses at Release for Bottom Fiber Mid-Span.	144
9.9. Strain at Mid-Span of HSC Spandrel Beam at 7 Days.	146
9.10. Strain at Mid-Span of HSC Spandrel Beam at 14 Days.	146
9.11. Strain of HS-SCC Spandrel Beam at 7 Days.	147
9.12. Strain of HS-SCC Spandrel Beam at 14 Days.	147
9.13. Strain in HSC Deck Panel Reinforced with Mild Steel.	149
9.14. Strain in HSC Deck Panel Reinforced with GFRP.	150
9.15. Strain in HS-SCC Deck Panel Reinforced with Mild Steel.	151
9.16. Strain in HS-SCC Deck Panel Reinforced with GFRP.	152
9.17. Bridge Spandrel Beam Transport.	154
9.18. Bridge Spandrel Beams Set at Bridge Site.	155
9.19. Support Strain Changes during Transportation of HSC Spandrel Beam.	156
9.20. Mid-Span Strain Changes during Transportation of HSC Spandrel Beam.	156
9.21. HSC Mid-Span Spandrel Beam Strain Profile during Erection.	157
9.22. HS-SCC Mid-Span Spandrel Beam Strain Profile during Erection.	158
9.23. Strain Profile after Deck Placement for HSC Beam.	159

9.24. Strain Profile after Deck Placement of HS-SCC Beam.....	159
10.1. Measured & Predicted Elastic Shortening Losses.....	164
10.2. Measured & Predicted Total Prestress Losses for HSC Spandrel Beam.....	167
10.3. Measured & Predicted Total Prestress Losses for HS-SCC Spandrel Beam.....	168
11.1. Fork Lift Dimensions for Live Load Test.....	172
11.2. Example Fork Lift Load Path Markings.....	174
11.3. Toyota 7FGU25 Fork Lift on HSC & HS-SCC Bridges.....	174
11.4. Total Station Test Setup.....	175
11.5. Target Prisms on HSC Bridge.....	177
11.6. Target Prisms on HS-SCC Bridge.....	177
11.7. Target Prisms.....	178
11.8. HSC Beam Temperature during Load Testing.....	181
11.9. HS-SCC Beam Temperature during Load Testing.....	181
11.10. HSC Beam Adjustments due to Temperature to Baseline Reading.....	182
11.11. HS-SCC Beam Adjustments due to Temperature to Baseline Reading.....	182
11.12. HSC Spandrel Beam Deflection – Load Case B.....	184
11.13. HS-SCC Spandrel Beam Deflection – Load Case B.....	184
11.14. HSC Mild Steel Reinforced Deck Panel Deflection – Load Case D.....	185
11.15. HS-SCC Mild Steel Reinforced Deck Panel Deflection – Load Case D.....	185
11.16. HSC GFRP Reinforced Deck Panel Deflection – Load Case F.....	186
11.17. HS-SCC GFRP Reinforced Deck Panel Deflection – Load Case F.....	186
11.18. Comparison of Total Station Setups.....	188
11.19. HSC Deck Panel with Steel vs. GFRP Deflection – Load Case A & C.....	189
11.20. HSC Deck Panel with Steel vs. GFRP Deflection – Load Case D & F.....	189
11.21. HS-SCC Deck Panel with Steel vs. GFRP Deflection – Load Case A & C.....	190
11.22. HS-SCC Deck Panel with Steel vs. GFRP Deflection – Load Case D & F.....	190

LIST OF TABLES

Table	Page
3.1. HSC & HS-SCC Mixture Proportioning.....	29
4.1. Timeline of Bridge Construction.	30
5.1. Summary of Material Testing Program.	42
5.2. Specimens for Compressive Strength & Modulus of Elasticity	44
5.3. Specimens for Modulus of Rupture.	45
5.4. Specimens for Splitting Tensile Test.	47
5.5. Creep & Shrinkage Specimens.	48
6.1. Measurement Types.	54
6.2. List of Instrumentation System & Gauges.	63
6.3. Gauge Identification Designations.	67
7.1. Creep Test Summary.....	86
7.2. HSC Measured Creep Coefficients.....	87
7.3. HS-SCC Measured Creep Coefficients.....	87
7.4. HSC Measured Specific Creep	88
7.5. HS-SCC Measured Specific Creep	88
7.6. Measured & Predicted Creep at 180 days.....	92
7.7. HSC Shrinkage Strain.	94
7.8. HS-SCC Shrinkage Strain.....	95
7.9. Measured Coefficient of Thermal Expansion.	97
8.1. Summary of Measured Hydration Temperatures for Precast Spandrel Beams.	103
8.2. Summary of Measured Hydration Temperatures for Precast Deck Panel.	107
8.3. Weighted Values Implemented to Determine Average Beam Temperatures.	109
8.4. Maximum Temperature Values Recorded for HSC Bridge.....	114
8.5. Maximum Temperature Values Recorded for HS-SCC Bridge.	115
8.6. Minimum Temperature Values Recorded for HSC Bridge.	116
8.7. Minimum Temperature Values Recorded for HS-SCC Bridge.	117
8.8. Comparison between HSC & HS-SCC Bridge Temperatures.....	118
8.9. Maximum & Minimum Thermal Gradients.....	127

9.1. Concrete Expansion Factors.	136
10.1. Measured vs. Predicted Elastic Shortening Losses.	163
10.2. Measured & Predicted Total Prestress Losses for Spandrel Beams.	166
10.3. Total Prestress Losses for HSC & HS-SCC Spandrel Beams.	169
11.1. Load Case Locations & Times.	173
11.2. Target Prism Locations.	176
11.3. HSC & HS-SCC Comparison of Calculated to Measured Deflections.	191

NOMENCLATURE

Symbol	Description
A	Cement type correction factor
A_c	Area of concrete cross-section, mm ² (in ²)
A_f	Area of FRP reinforcement, mm ² (in ²)
A_s	Area of mild steel reinforcement, mm ² (in ²)
A_{ps}	Area of prestressing strand reinforcement, mm ² (in ²)
C_c	Creep coefficient
C_{ct}	Creep coefficient at time t
C_{cu}	Ultimate creep coefficient
C_E	Environmental reduction factor for various fiber type and exposure conditions
D_L	Dead load
e	Eccentricity, mm (in.)
E_c	Modulus of elasticity of concrete, Pa (psi)
E_{ci}	Modulus of elasticity of concrete at release, Pa (psi)
E_f	Modulus of elasticity of FRP, Pa (psi)
E_{ps}	Modulus of elasticity of prestressing strand, Pa (psi)
E_s	Modulus of elasticity of mild steel, Pa (psi)
f'_c	Compressive strength of concrete, Pa (psi)
f'_{ci}	Compressive strength of concrete at release, Pa (psi)
f_{cgs}	Stress at the center of gravity of the prestressing strand, Pa (psi)
f_{cl}	Stress corresponding to 0.00005 $\mu\epsilon$ utilized for determining modulus of elasticity, Pa (psi)
f_{ct}	Splitting tensile strength, Pa (psi)
f_f	Tensile stress in FRP, Pa (psi)
f_{fu}	design tensile strength of FRP, Pa (psi)
f_{fu}^*	Guaranteed tensile strength of FRP, Pa (psi)
f'_{pi}	Initial stress in prestressing strand, Pa (psi)
f_{pu}	Nominal ultimate strength of prestressing strand, Pa (psi)

f_{py}	Yield stress of prestressing strand, Pa (psi)
f_r	Flexural tensile strength, Pa (psi)
f_s	Stress in mild steel, Pa (psi)
f_y	Yield stress of mild steel, Pa (psi)
H, RH, λ	Relative humidity, %
I_c	Moment of inertia of concrete cross-section, mm ⁴ (in ⁴)
k_1	Modification factor for coarse aggregate type
k_2	Modification factor for type of supplementary cementitious material
k_s	Volume to surface area ratio of specimen factor
k_{hc}	Humidity for creep factor
k_f	Concrete compressive strength factor
k_{td}	Time-development factor
LL	Live load
M	Moment, N-m (lbs-ft)
M_n	Nominal moment capacity, N-m (lbs-ft)
M_u	Factored moment, N-m (lbs-ft)
P	Prestressing force, N (lbs)
P_o	Prestressing force at release, N (lbs)
$R_{read,i}$	DEMEC gauge reading
$R_{read,o}$	Initial DEMEC gauge reading
$R_{refer,i}$	Reference bar DEMEC gauge reading
$R_{refer,o}$	Initial reference bar DEMEC gauge reading
s	Slump, mm (in.)
t_i	Creep loading age, days
t	Concrete maturity, days
t_{la}	Loading age correction factor
T_0	Initial temperature reading
T_1	Temperature reading
T_i	Measured internal temperature during load test, °C (°F)
T_{D1}	Measured internal temperature during initial dead load test, °C (°F)
T_{D2}	Measured internal temperature during final dead load test, °C (°F)

V_u	Factored shear force at section, N (lbs)
V_c	Nominal shear strength provided by concrete with steel flexural reinforcement, N (lbs)
V/S	Volume to surface area ratio, mm (in.)
w_c, γ_c	Concrete density, kg/m ³ (lbs/ft ³)
w_u	Factored uniform load, N/m (lbs/ft)
y_b, y_t	Distance from the centroid of concrete to the top and bottom fibers, respectively, mm (in.)
α	Air content, %
α_c	Linear expansion factor for EM-5 VWSG wire, $\mu\epsilon/^\circ\text{C}$ ($\mu\epsilon/^\circ\text{F}$)
$\alpha_{concrete}$	Coefficient of thermal expansion of the concrete, $\mu\epsilon/^\circ\text{C}$ ($\mu\epsilon/^\circ\text{F}$)
β_1	Factor which relates equivalent rectangular compressive stress block to the neutral axis depth
γ_{cc}	Cement content correction factor
γ_{cr}	Creep correction factor
γ_{la}	Loading age correction factor
γ_s	Slump correction factor
$\gamma_{V/S}$	Volume to surface area ratio correction factor
γ_α	Air content correction factor
γ_ψ	Fine aggregate percentage correction factor
$\delta_{p,A}$	Deflection in the deck panel at location "A", mm (in.)
$\delta_{p,i}$	Deflection in the deck panel at the location of the load, mm (in.)
$\delta_{b,i}$	Deflection in the beam at the location of the load, mm (in.)
δ_{Load}	Deflection induced by the live load, mm (in.)
δ_i	Total measured deflection, mm (in.)
δ_1	Measured deflection during initial dead load test, mm (in.)
δ_2	Measured deflection during final dead load test, mm (in.)
Δf_{TOTAL}	Total prestress loss within the concrete, Pa (psi)
Δf_{ES}	Prestress loss due to elastic shortening, Pa (psi)
Δf_{RE}	Prestress loss due to relaxation of the strand, Pa (psi)
Δf_{CR}	Prestress loss due to creep, Pa (psi)
Δf_{SH}	Prestress loss due to shrinkage, Pa (psi)

ΔT	Change in temperature, °C (°F)
$\Delta \varepsilon_{TEMP}$	Change in strain due to temperature, $\mu\varepsilon$
ε	Total measured strain, $\mu\varepsilon$
ε_{cgs}	Strain at the center gravity of the prestressing strains, $\mu\varepsilon$
ε_{cl}	Strain corresponding to 40% of the ultimate stress for determining the modulus of elasticity, Pa (psi)
ε_{cu}	Strain at the ultimate stress of concrete, $\mu\varepsilon$
ε_r	Real strain, $\mu\varepsilon$
ε_{sh}	Shrinkage strain, $\mu\varepsilon$
$\eta\beta$	Concrete expansion factor, $\mu\varepsilon/^\circ\text{C}$ ($\mu\varepsilon/^\circ\text{F}$)
ρ_f	FRP reinforcement ratio
v_u	Ultimate creep
$\psi(t, t_i)$	Creep coefficient

1. INTRODUCTION

1.1. BACKGROUND

Throughout the course of history, advancements in the materials used by civil engineers in the design and construction of bridges, buildings, and roads have made improvements to the infrastructure of the nation. Current advancements to bridge construction have lowered costs, reduced construction time, and increased the service life of the structures.

One such advancement has been the use of high-strength concrete (HSC) in prestressed bridges. By using HSC, large sustainable bridge structures were built with relatively compact sections. With the improved service life of bridges and reduced concrete in construction, the use of HSC allows for economic savings.

Recently, high-strength self-consolidating concrete (HS-SCC) has been developed as a viable alternative to HSC. With the added benefit of being highly flowable and not requiring vibration during fabrication, HS-SCC can be very beneficial in situations where there is congested steel or a need for rapid construction. Combined with precast, prefabricated bridge sections, construction time can be greatly reduced. By reducing the erection time of a bridge, any impedance to the infrastructure can be minimized.

The key to HS-SCC's ability to not require vibration lies in the gradation of the concrete aggregates and the admixtures applied to the mixture. By using higher doses of high range water reducers (HRWR) and fine aggregate (FA) amounts and proportions, a higher viscosity can be achieved in the concrete mixture. In addition, the HRWR lowers the water to cementitious materials ratio (w/cm) increasing the strength of the concrete. The strength and durability of the concrete is augmented further by the use of pozzolans such as fly ash and micro silica within the mixture.

With the correct mixture proportion, HS-SCC can produce strength results close to that of HSC. However, before HS-SCC can be used as a viable alternative to HSC, performance related issues require close inspection. For example, the behavior of prestress loss, shear, creep, shrinkage, thermal gradients, mechanical property development, time dependent behavior, and serviceability under varying loads between

HSC and HS-SCC remain an issue for investigation due to the inherent differences in the mixture proportions.

Another advancement that has been applied to increasing the sustainability of bridge structures is substituting mild steel rebar with glass fiber reinforced polymer (GFRP) bars in deck panels. GFRP bars have the positive attribute of being non-corrosive within the concrete where steel reinforcement would normally result in corrosion and cause cracking and spalling of the concrete.

However, GFRP bars do have a few limiting attributes. The first attribute is that the stress-strain behavior of GFRP bars are linear-elastic until failure. This produces a lack of ductility that is typically present in most bridge designs. Secondly, the modulus of elasticity of GFRP bars are typically around 41.4 GPa (6,000 ksi) as opposed to 200 GPa (29,000 ksi) for steel. The lowered modulus of elasticity of the GFRP bars can decrease the stiffness of cracked sections and decrease the shear strength of bridge sections that are reinforced with GFRP bars. ACI 440.1R (2003) calls for the addition of steel reinforcement to slabs if adequate shear strength is not obtained with GFRP reinforcement alone.

By combining the attributes of HSC and GFRP, improved sustainability in slab sections is possible. By using HSC, which typically will not crack at service loads due to its high strength, any shrinkage cracks that might have resulted will not be as high of a concern because the GFRP will not corrode due to moisture in the concrete.

1.2. OBJECTIVES

The objectives of this report is to understand and compare the differences between the thermal gradients, prestress losses, beam curvatures, and time dependent behavior of HSC and HS-SCC beams. In addition, the effect of having mild steel and glass fiber reinforced polymer (GFRP) within concrete structures is monitored for differences in concrete temperature, concrete strain, and deflection in each deck panel. The goal is to see if a combination of HS-SCC and GFRP can produce durable structures that can be built rapidly.

1.3. SCOPE

In this investigation, two precast, prestressed pedestrian bridges were erected along Lions Club Drive in Rolla, MO, consisting of HSC and HS-SCC. Each beam was monitored to determine the differences between thermal gradients, prestress losses, beam curvatures, development lengths, and time dependent behavior. In addition, mild steel and GFRP were used within the deck panels to correlate the effects of reinforcement type to concrete temperature, concrete strain, and deflection within the bridge deck. These goals were achieved by using embedded vibrating wire strain gauges (VWSG) with built-in thermistors, surface mechanical strain gauges (DEMEC), tensioned-wire deflection measuring system, and precise surveying to determine the differences in HSC and HS-SCC for early-age and later-age monitoring. In addition, material test specimens were prepared and tested using standard ASTM testing procedures to determine and compare the compression, elastic modulus, modulus of rupture, split cylinder, creep, and shrinkage of both materials.

1.4. ORGANIZATION OF REPORT

The report is organized into an introduction to HSC and HS-SCC with a statement of the scope of the project. In Section 2, an investigation of previous projects that exhibited similarities in the scope of the research is discussed. Section 3 gives specific details on the design of the precast, prestressed pedestrian bridges. In Section 4, details on the beam and deck panel fabrication, site storage, and bridge erection are displayed. Section 5 displays the mechanical and material testing program. Section 6 provides details on the various instruments that were used throughout the project. Section 7, Section 8, Section 9, and Section 10 give the results for material and mechanical properties, temperature, strain, and prestress losses of both the HSC and HS-SCC bridges. Section 11 discusses the results of a static live load test. Finally, the summary, conclusions, and recommendations are given for the results of the comparison of HSC to HS-SCC in Section 12.

2. LITERATURE REVIEW

2.1. HIGH-STRENGTH CONCRETE

2.1.1. Definition of HSC. The definition of high-strength concrete (HSC) has varied throughout the years. In 1950, HSC was defined as any concrete that had a compressive strength of 34 MPa (5,000 psi) (ACI 363R, 2010). With continued advancements in the composition and materials in concrete, compressive strengths above 138 MPa (20,000 psi) have been used in the field. Recently, the American Concrete Institute (ACI) has defined HSC as any concrete that has a compressive strength greater than or equal to 55 MPa (8,000 psi) (ACI 363R, 2010).

HSC has been widely used throughout the world due to its enhanced properties. Higher strength in concrete allows for large sustainable structures to be built with relatively compact sections. Many of the world's tallest buildings would not be feasible without using HSC in the column and wall elements. Taipei 101, located in Taipei, Taiwan, was mentioned in the most recent ACI 363R "Report on High-Strength Concrete" as an example of how HSC was used to create one of the world's tallest structures. In addition, HSC is useful in creating longer span bridges that require fewer beams than required in conventional concrete. Furthermore, HSC is used on beam and slabs to produce structures with higher durability (ACI 363R, 2010).

2.1.2. Material Properties of HSC. In addition to increased strength, HSC has many other improved characteristics when compared to conventional concrete. Examples include: increased modulus of elasticity (E_c), reduced creep (CR), increased resistance to abrasion (AB), and reduced permeability increasing the durability of structural members when compared to conventional concrete. The improved characteristics of the concrete are due to the composition of the concrete matrix. Typically, higher coarse aggregate content with smaller nominal maximum size aggregate and decreased water to cementitious materials ratio (w/cm) helps create a strong dense matrix. Additionally, mineral and chemical admixtures are utilized to decrease the water content and facilitate later-age strength gain of the material to produce a concrete with optimum strength (Young et. al., 2002). These facets also help improve

shrinkage and creep within the mixture. However, the extent of reduction of creep and shrinkage is continuously under investigation.

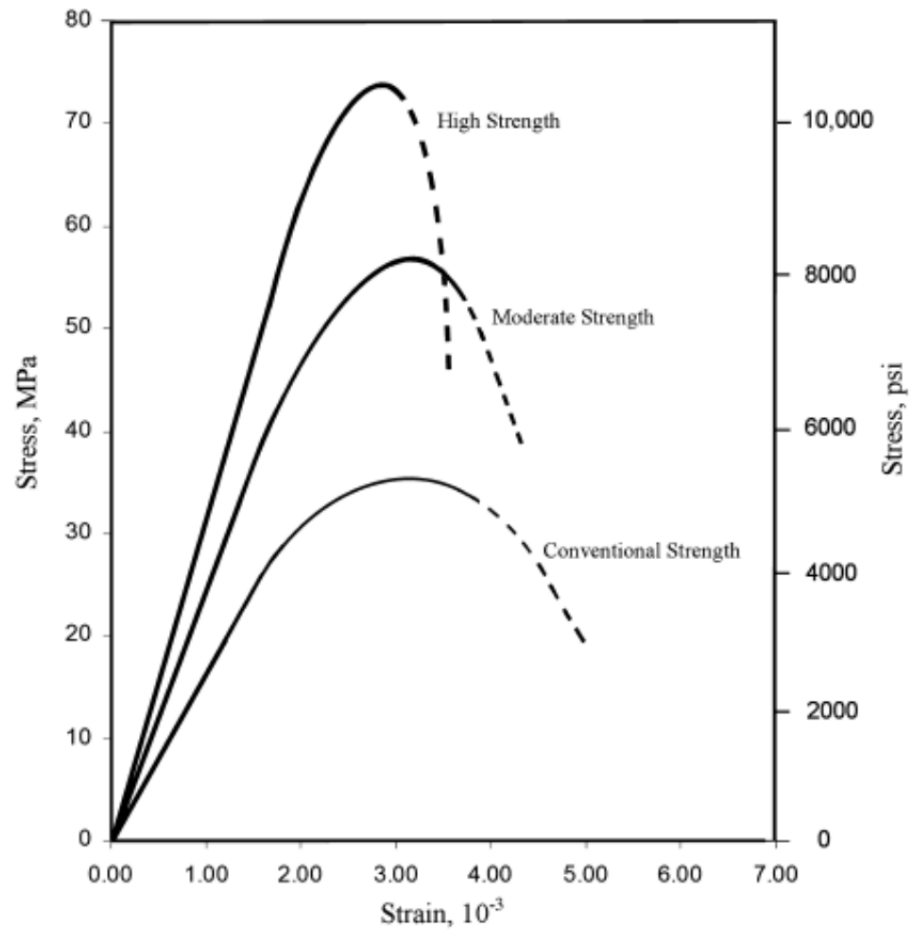
Another area under investigation is the shear strength of HSC. Currently, ACI 318 (2008) limits the compressive strength of HSC to 69 MPa (10,000 psi) in the design equations for shear. The current American Association of State Highway Transportation Officials Load Resistance Factor Design (AASHTO LRFD) – Bridge Design Specification limits the concrete compressive strength to 69 MPa (10,000 psi) in design equations unless specified within the articles or when physical tests are implemented to obtain a relationship between the specific properties, such as shear, and concrete compressive strength (AASHTO, 2007). Current belief to limiting the concrete shear strength is due to the uncertainty caused by the increased amount of paste and smaller size aggregate. These two components can potentially decrease the aggregate interlock that is required to have adequate shear resistance (ACI 318, 2008).

With modifications in the material components found within HSC, new models have been proposed by ACI 363R (2010) to take into account the differing characteristics of the HSC mixture compared to conventional concrete. Specific equations for concrete strength, stiffness, shrinkage, and creep are provided in greater detail in Section 7.

2.1.2.1 Strength. The compressive strength, split tension, and flexural strength of HSC are important in the design of structures. Compression and split tension are tested in 150 x 300 mm (6 x 12-in.) cylinders for normal strength concrete (NSC). However, with HSC, 100 x 200 mm (4x 8-in.) cylinders are often utilized in compression and split tension tests due to limitations in testing machine capacity. The flexural tensile strength, or modulus of rupture, is tested with 150 x 150 x 500 or 600 mm (6 x 6 x 21 or 24-in.) beams. As concrete strength increases, strength curves become steeper and more linear and are less ductile than NSC. A comparison of compressive stress and compressive strain for varying concrete strengths is presented in Michael A. Caldarone's *High-Strength Concrete: A Practical Guide*, as displayed in Figure 2.1 (Caldarone, 2009).

Strength of concrete material is dependent upon the constituent materials, such as aggregate amount, aggregate type, cement type, and how the materials interact at the interface zone. To produce greater strength in HSC, smaller angular aggregate is used

and added to a higher percentage of paste. The angular aggregate allows for more surface area to come into contact with the paste and increases the bond at the interface zone. However, the smaller the aggregate, the more paste has to be added to insure similar strength levels. If too much paste is added to the mixture, the overall strength can be reduced. This is illustrated in Figure 2.2 for a mixture with a constant slump (Myers, 1998).



(Caldarone, 2009)

Figure 2.1. Stress Strain Relationships for Varying Concrete Strengths.

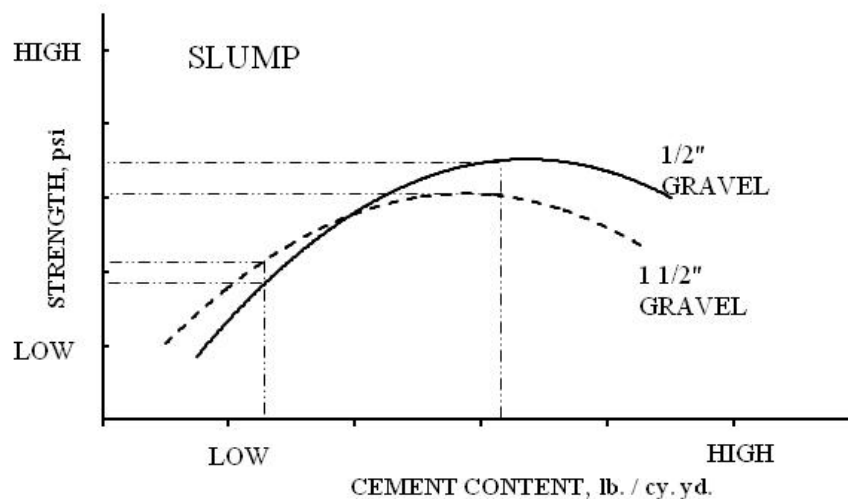


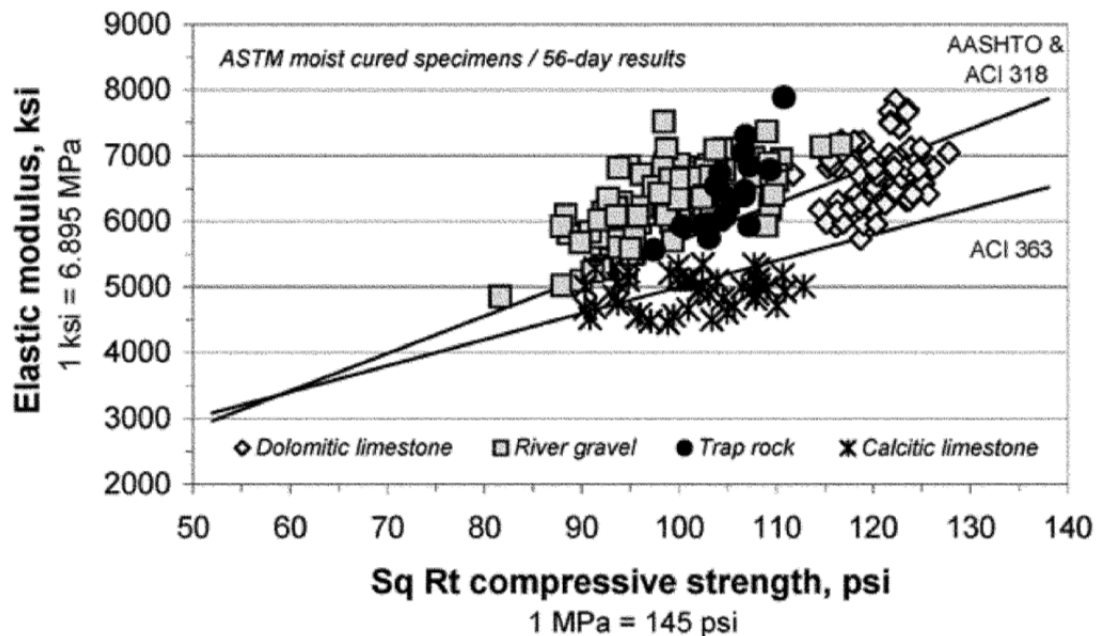
Figure 2.2. Concrete Strength to Cement Content to Aggregate Size (Myers, 1998).

Strength of the material is also dependent upon curing conditions and temperature. Cylinders cured with techniques such as match cured or member cured tended to produce strengths less than those moist cured (Myers and Yang, 2005). As concrete hydration temperatures increase, the strength within the mixture decreases. Myers and Carrasquillo (2000) determined that as concrete hydration temperatures exceed 77°C (170°F) microcracking within the material results in lower compressive strength.

2.1.2.2 Modulus of elasticity. The modulus of elasticity is an important facet of understanding the mechanical properties of concrete. Knowing the stiffness of the concrete is essential to determine the serviceability and structural performance of concrete structures. Due to the correlation between concrete compressive strength and concrete stiffness, many of the factors that influence the compressive strength of concrete will influence the stiffness of the material. The factors that influence the stiffness include the cement and the stiffness, quality, and percentage of coarse aggregates. However, the modulus of elasticity is largely controlled by the properties of the coarse aggregate. The stiffness of the concrete can be improved by increasing the amount of the coarse aggregate, utilizing stiffer coarse aggregates that are still compatible with in the cement matrix, or using aggregates which are more angular or crushed. If care is not taken to

ensure that the stiffness of the aggregate and paste is not compatible, microcracking can occur due to the presence of stress concentrations (Myers, 1999).

Generally a relationship can be found that correlates the modulus of elasticity with the compressive strength of concrete. Research has found that standard equations such as those in ACI 318 (2008) for NSC can overestimate the modulus of elasticity of concretes with higher strength (ACI 363R, 2010). Figure 2.3, presented in ACI 363R (2010) illustrates the modulus of elasticity of HSC with dolomitic limestone, river gravel trap rock, and calcitic limestone produced by Myers (1999). The models shown within the graph are presented in equations 2 and 4 in Section 7. It should be noted that in some cases, the ACI 363R (2010) equation, equation 4 in Section 7, sometimes greatly underestimates the stiffness of HSC. For example, in NCHRP Report 628, Tadros et. al. (2003) reported that ACI 318 (1998) and AASHTO Specification (1998) correlated better with the results from specimens tested than the ACI 363 (1992) which tended to remain a lower bound expression.



(ACI 363R-10 Adapted from Myers, 1999)

Figure 2.3. Modulus of Elasticity vs. Compressive Strength for Varying Aggregates.

2.1.2.3 Creep and shrinkage. In order to have a better understanding of the performance of normal or high-strength concrete, the creep and shrinkage of the material should be known. Creep is an increase in strain over a period of time due to the presence of sustained stress. Total shrinkage is a decrease in the volume of cement and is composed of drying shrinkage, autogenous shrinkage, and carbonation (ACI 209R, 1997). Shrinkage that is typically monitored is drying shrinkage. Drying shrinkage is a decrease in the volume of cement due to moisture loss in concrete.

Properties that influence creep include the amount and type of aggregate and w/cm. Aggregate properties such as stiffness, size, and shape can influence the amount of creep and shrinkage by improving the aggregate interlock within the material which increases the resistance to creep. If aggregate absorption is high and the aggregate is not fully saturated in the mixture, the aggregate has the potential to remove water from the paste and increase the creep. As the w/cm is decreased, the amount of free water is reduced creating a denser mixture. The denser mixture is more resistant to creep (Cousins, 2005).

Shrinkage is controlled largely by the w/cm ratio, the volume to surface ratio of the specimen, and the ambient curing conditions. As higher percentages of water are within the concrete, shrinkage will increase as higher percentages of free water dissipates from the concrete matrix. Specimens that are larger in size and shape have less shrinkage because more of the water is entrapped within the interior of the specimens. As specimens become smaller in size and shape, a higher percentage of the water is at the surface and can be diffused quite easily causing higher shrinkage. As relative humidity increases, the amount of shrinkage will decrease. Cousins (2005) determined using ACI 209 (1992) and the AASHTO LRFD Specification (1998) that the shrinkage can decrease 67% when the relative humidity is increased from 40% to 80% (Cousins, 2005).

Current research has shown that drying shrinkage of HSC can be more or less than that of conventional concrete. However, the shrinkage rate of HSC has been found to be less than that of normal strength concrete. In normal strength concrete, shrinkage occurs largely due to drying shrinkage caused from internal water diffusing from the concrete resulting in volume change. Due to differences in chemical components between HSC and conventional concrete, chemical and autogenous shrinkage has been

found to affect the shrinkage of HSC. Chemical shrinkage is any decrease in volume due to the hydration of the cement. Chemical shrinkage creates voids within the paste and typically does not dramatically change the overall volume. Autogenous shrinkage is a chemical shrinkage that occurs during the initial set of the concrete that affects the overall volume change of the concrete. It is difficult to monitor autogenous shrinkage. However, it has been found to affect HSC greater than normal concrete (ACI 363R, 2010).

HSC has enhanced characteristics that are typically overestimated when compared to creep and shrinkage models for normal strength concrete (NSC). Modified equations have been presented to create more accurate predictions of the creep and shrinkage of HSC. These equations are presented in greater detail in Section 7.

2.1.3. Prestress Loss. Determining the prestress losses of HSC beams are important to determine the stresses and deflections during service conditions of HSC structures. Many empirical models have been presented to estimate prestress loss. They are presented in greater detail in Section 10 and Appendix E for AASHTO LRFD Refined Method (2007) and Appendix F for PCI Design Handbook (2004). Prestress loss occurs when the stress in the prestressing strands reduces due to shortening of the concrete around the strands, relaxation of the tendon stresses, and external loads and elements that diminish the initial prestressing force applied to the concrete (PCI, 2004). Figure 2.4 illustrates the prestress losses over a girder's life cycle as presented in NCHRP Report 496. In the report, the components of prestress losses are as follows (Tadros et. al., 2003):

1. Losses due to anchorage seating, initial relaxation between tensioning and transfer, changes in temperature of the strand and embedded strand
2. Losses at transfer due to prestress force and the self-weight of the beam
3. Losses due to creep, shrinkage, and relaxation of the strands before deck placement
4. Gain due to deck weight
5. Long-term losses from creep, shrinkage, relaxation of the strands, and deck shrinkage

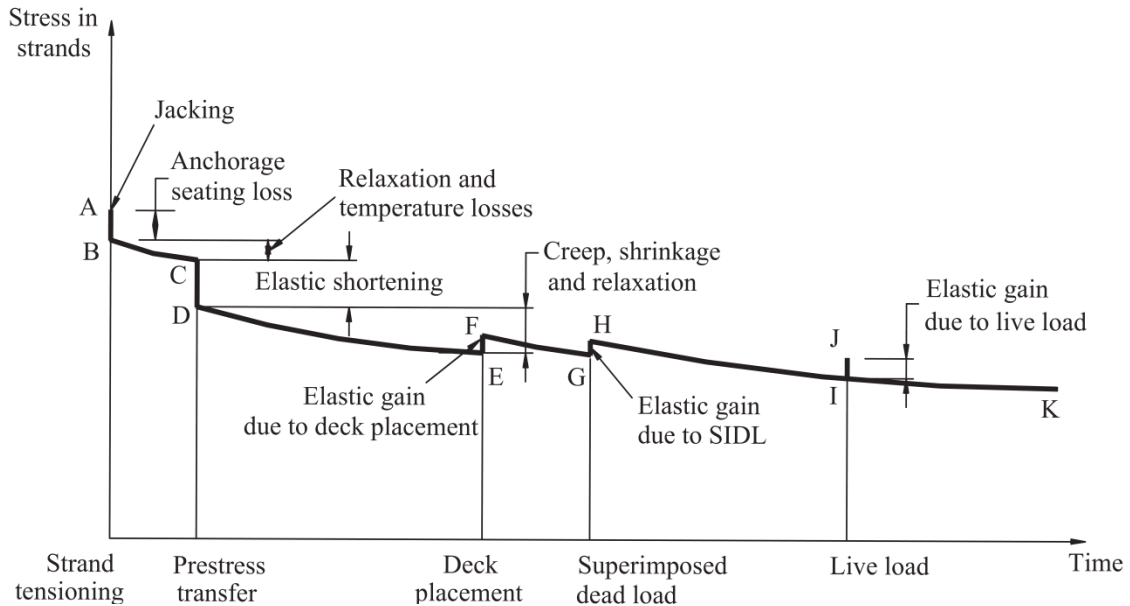


Figure 2.4. Stress vs. Time for Bridge Girder (Tadros et. al., 2003).

Factors that influence the amount of prestress loss within a beam are compressive strength, modulus of elasticity, creep, shrinkage, and strand relaxation. With the improved characteristics of HSC, prestress losses with HSC are lower than compared to NSC. However, in order to accurately predict the prestress losses of HSC, accurate models must be established for the material properties of HSC.

2.1.3.1 Myers and Yang (2005). The first fully high-performance concrete (HPC) bridge in Missouri, Bridge A6130, located in Pemiscot County near Hayti, MO, had a 56 day design strength of 70 MPa (10,152 psi). The prestressing strands had a diameter of 15.2 mm (0.6-in.). Both of the girders and cast-in-place (CIP) deck were composed of HPC material.

VWSGs, resistance strain gauges, and thermistors were utilized throughout the cross section of the girders to monitor the prestress losses throughout the bridges life cycle. In addition, the jacking stress and instantaneous losses were monitored via a load cell attached to the prestressing strands before tensioning. A Datalogger CR23X provided by Campbell Scientific, Inc. was used to receive the data from the sensors. The strains determined from the sensors were converted into prestress loss by multiplying the strain at the center gravity of the prestressing steel by the modulus of elasticity of the

prestressing strand. Any losses determined by the sensors had to be corrected for relaxation losses and pre-release losses from early-age shrinkage, relaxation, and thermal effects.

Measured elastic shortening losses were compared to theoretical elastic shortening losses utilizing transformed section properties with measured modulus of elasticity, gross section properties with measured modulus of elasticity, and gross section properties with approximate modulus of elasticity. Total prestress losses were compared to theoretical prestress losses proposed by AASHTO Standard (1996), AASHTO LRFD (2002), PCI Design Handbook (1999), and Gross (1999). In addition, a time-step method was implemented using measured parameters. Gross utilized similar equations to that of the PCI Design Handbook. However, the equation also takes into account pre-release losses involving strand relaxation and thermal effects during concrete hydration.

The measured losses between jacking and placement ranged between 1.58 to 18.75 MPa (0.23 to 2.72 ksi) with an average of 0.60% of the jacking stress. The measured losses were lower than the calculated losses of 4.62 to 11.58 MPa (0.67 to 1.68 ksi) with an average of 0.14% of the jacking stress.

Overall, the elastic shortening losses were determined to be higher than those predicted by any exact method. It was reasoned that the increase in losses was due to restraint applied by the formwork against shortening. In addition, any differences between the predicted losses based on known modulus to those with approximate modulus tended to be less than 2%.

The 1,396 MPa (202.5 ksi) nominal jacking stress had measured total losses that averaged 289.2 MPa (41.9 ksi) or 20.7% nominal jacking stress. 53.7% of the total loss was contributed by elastic shortening. The PCI Handbook method, time-step method, and method recommend by Gross (1999) were close to the measured losses by about 4 to 12%. However, the predicted losses determined by the AASHTO Standard Specification were 45 to 55% higher than measured. In addition, the AASHTO LRFD Specification's theoretical losses were 50 to 60% higher than measured. It was noted that due to the higher elastic shortening losses caused by the restraint from the placement bed, the actual prestress losses may have been lower than predicted for all methods. It was

recommended that the PCI Handbook and method recommended by Gross (1999) were good estimators for design prestress losses (Myers and Yang, 2005).

2.1.3.2 Tadros et. al. (2003). Seven full-scale bridge girders in Nebraska, New Hampshire, Texas, and Washington were instrumented with VWSGs embedded in the girders and monitored with a data-acquisition system to determine the prestress loss of the HPC girders. The total prestress losses averaged 265 MPa (38.5 ksi) with a 19.0% initial elastic loss of the 1,396 MPa (202.5 ksi) jacking stress. Results were compared to the AASHTO LRFD (1998) refined and lump sum methods, both of which tended to over-predicted the total losses. In addition, the results were utilized to determine a modified prestress loss expressions that were recommended for AASHTO LRFD Specification and later added to the AASHTO LRFD 2007 Specification (AASHTO, 2007). This modified expression is presented in greater detail in Appendix E (Tadros et. al., 2003).

2.1.3.3 Cousins (2005). Prestress losses were investigated in nine HPC girders with compressive strengths ranging from 55 to 69 MPa (8,000 to 10,000 psi) on two bridges in Virginia. Pinner's Point Bridge, located on Virginia Route 164, utilized prestressed AASHTO Type V and Type VI Modified girders, reinforced with thirty-seven or forty, 13 mm (0.5-in.) diameter, grade 270, low-relaxation prestressing tendons with nine or twelve strands harped on 2.7 m (9 ft) from the mid-span spanning 26 m (85 ft). Dismal Swamp Bridge, located on U.S. 17 in Chesapeake, Virginia, utilized prestressed PCBT-45 (bulb-T) girders with twenty-six, 13 mm (0.5-in.) diameter, grade 270, low-relaxation prestressing tendons with six strands harped spanning 19 m (62 ft). VWSGs were utilized throughout at the centroid of the prestressing force to determine prestress loss. A Campbell Scientific CR10X Datalogger was used to measure the strains and temperatures in the girders.

Measured prestress loss from the girders was correlated to the PCI Bridge Design Manual (1999), AASHTO Standard Specification (1996), AASHTO LRFD Specification (1998), and NCHRP 496 Methods (2003). The AASHTO Standard of 1996 and LRFD of 1998 were determined to over-estimate the measured total losses by 18% to 98%. The PCI Building Design method was determined to be the most reliable estimator of total losses by estimating within 10% of the measured losses in the HPC girders. The NCHRP

496 Refined and Approximate methods were found to be within 18% of the HPC total measured losses (Cousins, 2005).

2.2. HIGH-STRENGTH SELF-CONSOLIDATING CONCRETE

2.2.1. Definition of HS-SCC. Self-consolidating concrete (SCC) was developed in Japan in the 1980's as a concrete that would ensure consolidation in situations where durability and service life were of key interest. Over time, SCC has been used to expedite construction time and reduce construction costs. The precast industry has grown in production of SCC since 2000. Since 2000, 135,000 m³ (177,000 yd³) of SCC is estimated to have been placed. By 2002, the amount was found to have been increased to 1.8 million m³ (2.3 million yd³). (ACI 237R, 2007).

SCC has been used in conventional concrete structures and applications due to its increased workability. Due to the material constituents within the concrete, vibration is not required. This allows for a decrease in required labor and an increase in productivity. In addition, the concrete is useful in architectural applications, pumping, and congested steel applications (Trent, 2007). Self-consolidating concrete utilizes HRWR and, in some cases, viscosity-modifying admixtures (VMA) to create a concrete that will behave fluidly and without segregation (ACI 237R, 2007).

Recently, high-strength self-consolidating concrete (HS-SCC) has been developed and utilized in structural applications. HS-SCC has all of the benefits of SCC with the added addition of increased strength. High-strength structures can be built rapidly in the field or at precasting yards with less required labor. With higher loads being resisted by the concrete, more prestressing steel can be added in prestressed applications. The HS-SCC can accommodate the increased congestion of steel by its improved flowability.

2.2.2. Material Properties of HS-SCC. HS-SCC has the benefit of increased strength and fluidity. However, even though there are added improvements with SCC and HS-SCC. There are still a few design concerns with the material. Some of the concerns have been managed, while others are still undergoing investigation. One of the issues that have been dealt with is a means of creating a standard test for quality control and assurance. Standard slump testing is not applicable with SCC. However, slump flow

tests using inverted slump cone (ASTM C 1611, 2005) have been used to determine the workability of SCC.

Issues that still are under investigation include prestress loss, shear, creep, shrinkage, thermal gradients, mechanical property development, time dependent behavior, and serviceability under varying loads.

2.2.2.1 Strength. The inclusion of admixtures such as air entrainment, smaller percentage of coarse aggregate, and higher w/cm in HS-SCC can cause compressive strengths to be typically less than HSC. In a test conducted by Khayat and Mitchell for the NCHRP Report 628 (2009), 3 different nominal maximum sized of 19 mm (0.75-in.), 12.5 mm (0.50-in.), and 12.5 mm (0.375-in.) with two w/cm ratios of 0.33 and 0.38 and three binder types of Type I/II cement, Type III cement with 30% slag replacement, and Type III cement with 20% Class C fly ash replacement were tested for material properties. It was determined that smaller crushed aggregate tended to have a higher compressive strength than gravel. In addition, concretes that contained higher w/cm had better passing ability, filling capacity, and fluidity retention. However, smaller w/cm was found to have greater static stability, compressive strength, flexural strength, and stiffness. The passing ability and filling capacity of SCC increases with the addition of air entrainment. However, with air entrainment, the compressive strength and static stability will decrease (Khayat and Mitchell, 2009).

2.2.2.2 Modulus of elasticity. Due to the addition of air entrainment and lower percentages of coarse aggregate, the modulus of elasticity of SCC and HS-SCC can be lower than that of HSC. Furthermore, stiffness can be decreased even more if the w/cm is increased to further improve workability. Khayat and Mitchell (2009) discovered that, at the release of prestress, the coefficients on the square root of the compressive strength used for the modulus of elasticity tended to be 4 to 11% lower for SCC than HSC at ultimate strengths around 55 MPa (8,000 psi).

Brewe (2009) found that the modulus of elasticity of HS-SCC with a 28 day compressive strength of 62 MPa (9,000 psi) was 31,940 MPa (4635 ksi) which was lower than predicted by AASHTO LRFD Specification (2007) for the mixture investigated. This was expected due to the lower fraction of coarse aggregate. However, further

contribution to the low stiffness was thought to have been attributed to softer limestone aggregate utilized (Brewer, 2009).

In a study conducted by Naito et. al. (2006), high-early strength concrete (HESC) was compared to SCC with design compressive strength of 47 MPa (6,800 psi) within 24 hours and 55 MPa (8,000 psi) at 28 days. The modulus of elasticity was found to be lower for SCC than HESC during cylinder testing. However contradicting results for the modulus of elasticity were determined with infield testing of camber and elastic shortening that indicated the stiffness of SCC to be higher than HESC (Naito et. al., 2006).

2.2.2.3 Creep and shrinkage. Creep and shrinkage of SCC and HS-SCC is expected to be somewhat higher than that of HSC due to typical SCC mixtures containing smaller percentages of coarse aggregate, smaller coarse aggregate size, and higher binder content than conventional concrete (Khayat and Mitchell, 2009). Due to the slightly smaller maximum size aggregate within the mixture and somewhat higher percentages of fine aggregate within SCC and HS-SCC mixtures, w/cm ratios can be slightly higher than that of HSC mixtures because of an increase in water demand imposed by the aggregate constituents (ACI 211.4R, 2008). The higher w/cm can further influence the creep and shrinkage behavior of HS-SCC.

Testing completed by Khayat and Mitchell (2009) determined that drying shrinkage and creep increased with higher binder content in SCC with strengths of around 55 MPa (8,000 psi). However, it was discovered that drying shrinkage tends to increase with an increase in w/cm, whereas autogenous shrinkage decreases with an increase in w/cm. Concrete that contained higher binder content and lower w/cm had a high autogenous shrinkage which varied between 100 and 350 $\mu\epsilon$ depending upon the composition of the mixture (Khayat and Mitchell, 2009).

Naito et. al. (2006) conducted a test utilizing 150 mm diameter by 300 mm (6-in. diameter by 12-in.) cylinders to monitor the shrinkage of SCC to that of HESC. Both the HESC and SCC values were over predicted by ACI 209 (1997) by 18% for SCC and 39% for HESC. On average, the SCC had 39% higher shrinkage strain than HESC. The creep for HESC was determined to be 6% higher than predicted by ACI 209, and the creep for

SCC was 40% higher than predicted by ACI 209. Therefore, the ACI 209 was found to over predict shrinkage and under predict creep (Naito et. al., 2006).

2.2.3. Prestress Loss. Due to lower stiffness values and higher creep and shrinkage values, HS-SCC has the potential for larger prestress losses when compared with HSC. The following presents research for SCC and HS-SCC prestress losses.

2.2.3.1 Kukay et. al. (2007). A two span continuous bridge was fabricated with precast, prestressed SCC girders with the length of each span being 27.2 m (89.3 ft). The compressive strength was 69.5 MPa (10.1 ksi) at release and 72.2 MPa (11.1 ksi) at 28 days. The girders fabricated were the first HS-SCC girders constructed in the state of Utah.

Each of the girders was instrumented with embedded vibrating wire strain gauges (VWSGs) with integral thermistors in four of the twelve girders at the centroid of the prestressing strands and centroid of the composite girder. Data were read every 15 minutes during curing, every minute during destressing, and every half-hour thereafter. Data were monitored for placing, curing, de-stressing, and deck placement. The measured strain and prestress losses were compared with NCHRP 496 (Tadros et. al., 2003).

After a year of monitoring, the average prestress loss was 160 MPa (23 ksi) and had a total loss of 11.5% of nominal jacking stress. When compared to NCHRP 496, when the actual compressive strengths were used in the empirical relationship, only 21% of the values were within 10% of the field values. In addition, the values were typically un-conservative (Kukay et. al., 2007).

2.2.3.2 Naito et. al. (2006). Four 10 m (35 ft) long bulb-tee girders were fabricated, two of conventional HESC and two of SCC. Embedded VWSGs were used throughout the beams to monitor strains to calculate the loss of prestressing. The prestressing force losses at 28 days were less for the SCC girders than the HESC girders. Additionally, the SCC had 16% higher effective prestress and HESC had 13% higher effective prestress than estimated by PCI (1999) (Naito et. al., 2006).

2.2.3.3 Brewe (2009). Six prestressed HS-SCC girders, with a reduced scale, were monitored for prestress losses with DEMEC strain gauges. The measured prestress losses were compared to methods described by AASHTO LRFD Fourth Edition (2007),

PCI Design Handbook (2004), and AASHTO LRFD Third Edition (2004). The 2007 AASHTO LRFD refined method tended to underestimate the beams by an average of 18%. The prestress loss calculated with the PCI Method over predicted the prestress loss exhibited by the beams by an average of 21%. The measured prestress loss was overestimated by 10% for the third edition of the AASTHO LRFD (Brewer, 2009).

2.2.4. Recent Projects. Currently, SCC and HS-SCC are utilized throughout Japan and Europe because of their positive attributes. However, HS-SCC has not been fully implemented in the United States due to the issues listed previously. Examples of structures that utilized SCC are as follows:

2.2.4.1 Ritto Bridge, Japan. The Ritto Bridge on the New Meishin Expressway in Japan required a 50 MPa (7,250 psi) compressive strength on the 65 m (213 ft) high pier. Due to a congested steel arrangement required for earthquake resistance, a HS-SCC was utilized for the bridge (Ouchi et. al., 2003).

2.2.4.2 The Sodra Lanken Project, Sweden. The Sodra Lanken Project in Sweden required wall sections, arch sections, and rock lining for the tunnels in the project. SCC was required because of the inability to use vibration on these structural locations (Ouchi et. al., 2003).

2.2.4.3 Higashi-Oozu Viaduct, Japan. The Highashi-Oozu Viaduct in Japan utilized T-girders that were made with a HS-SCC with a compressive strength of 50 MPa (7,250 psi). HS-SCC was utilized due to two reasons. One reason was because conventional concrete was not creating a proper girder surface due to the dimensions of the forms. In addition, neighbors complained from the noise from vibrating the concrete. With the use of HS-SCC, vibration was eliminated. (Ouchi et. al., 2003).

2.3. CONCRETE TEMPERATURES

Concrete hydration temperatures, bridge temperatures, and thermal gradients that occur throughout a bridges life cycle are concern because of cracking that can result from excessive stresses induce by thermal effects (Myers and Yang, 2005). In comparison to NSC, HSC and HS-SCC can have higher concrete hydration temperatures which typically need to be monitored more closely than HSC because of microcracking that can occur when temperatures exceed 77°C (170°F) (Myers and Carrasquillo, 2000).

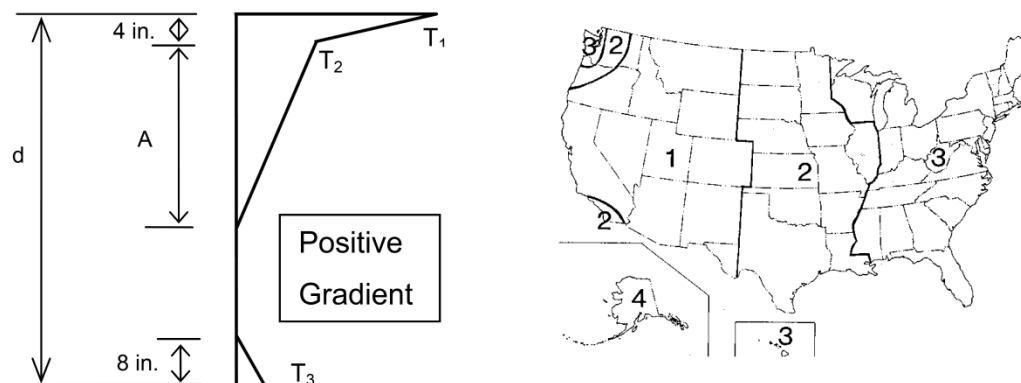
Myers and Yang (2005) determined that HPC girders fitted with VWSGs with built-in thermistors and thermocouples in MoDOT Type 2 girders produced a maximum concrete hydration temperature of 57°C (46°F). The equivalent temperature rise ranged from 5.1 to 5.9°C per 100 kg/m³ (5.7°F per 100 lb/yd³) of cement or 4.6°C per 100 kg/m³ (4.8°F per 100 lb/yd³) of cementitious material. ACI 363R (2010) suggests that the equivalent maximum temperature values of 10 to 14°C per 100 kg/m³ (11 to 15°F per 100 lb/yd³).

Mean bridge temperatures on bridges can influence the axial deformation of concrete due to temperature effects that occur due to the change in temperature. Bridge A6130 in Pemiscot County near Hayti, MO, achieved maximum average bridge temperatures around 43°C (109°F) and minimum average bridge temperatures on any day around 15°C (59°F). The mean bridge temperatures are dependent upon the location and climatic conditions at the bridge site.

AASHTO LRFD (2007) provides standard thermal gradients used for design. Figure 2.5 illustrates the thermal gradients specified by AASHTO LRFD Specification (2007).

Temperature data is often coupled in VWSGs. By determining the temperature values, thermal strains can be determined and temperature effects for concrete can be removed from strain values (Myers and Yang, 2005).

In some cases, the thermal gradients presented by AASHTO LRFD (2007), can underestimate the positive gradient of HSC. However, negative gradients have been found to be similar. Myers and Yang (2005) determined that the AASHTO LRFD model tended to underestimate measured positive gradients of the HSC bridge by 6.1 °C (11°F) at the bottom of the bottom of the beam, but only tended to produce values less than 2.2°C (4°F) than measured negative gradients.



Positive Gradient

Zone	T ₁ (°F)	T ₂ (°F)
1	54	14
2	46	12
3	41	11
4	38	9

Negative Gradient:

Determined by multiplying positive gradient values by -0.5

$$1\text{-in.} = 25.4 \text{ mm} \quad ^\circ\text{F} = ^\circ\text{C} * 1.8 + 32$$

Notes:

Dimension "A" shall be taken as:	
12-in.	For concrete superstructures 16-in. or more in depth
(d-4)-in.	For concrete superstructures less than 16-in. in depth

Temperature T₃ is taken as 0.0°F unless a site specific study is completed to determine an appropriate value, but shall not exceed 5.0°F

Figure 2.5. AASHTO LRFD 2007 Specification Design Thermal Gradients.

2.4. CONCRETE BRIDGE LOAD TESTS

To obtain a better understanding of HSC and HS-SCC bridges during serviceability states, live load testing has been recommended to monitor changes in deflection and strain as the HSC structural members undergo time dependent factors modifying the material and mechanical properties of the structure. Two types of live load testing programs are often utilized in monitoring deflections. One test involves the use of precise survey equipment, laser-based, and is accurate to 0.13 mm (0.005-in.) when the total station is at a distance of 61 m (200 ft) from the targets. This method was utilized in a project involving monitoring bridges strengthened with fiber reinforced polymer (FRP) by Holdener (2008). Another method for monitoring deflections during a live load test

involves the use of linear variable differential transformers (LVDTs). With this method, accuracy of 0.03 mm (0.001-in.) can be achieved (Myers and Yang, 2005). However, the presence of excess water and high clearance heights can limit the use of LVDTs.

In addition to deflection, sensors within a bridge member can be utilized to measure the changes in strain during load testing. Either the measured strains can be compared to theoretical strains or the applied measured moment can be compared to theoretical applied moment. The measured moment is determined by applying a trend line to the strain profile to measure the slope. The slope of the trend line is converted into curvature by taking the inverse of the slope and multiplying it by negative one. Multiplying the curvature by the modulus of elasticity and moment of inertia of the member loaded provides an estimate of the moment applied.

2.4.1. Myers and Yang (2005). Two MoDOT dump trucks weighing 218.8 kN (49,220 lbs) and 201.6 kN (47,380 lbs) were applied to bridge A6130 in Pemiscot County near Hayti, MO, during a live load testing program. Measured strain values were measured with internal VWSGs. Deflection was measured with LVDTs. The curvature of the cross section was determined for each load case and converted into applied moment. The measured moments were compared to moments calculated with finite element software (FEM) for continuous beams and fixed beams. Results showed that the bridge's behavior was closest to the fixed model. In addition, the live load distribution coefficients were found to be similar to those calculated from AASHTO LRFD Specification (2002) (Myers and Yang, 2005).

2.4.2. Dwairi et. al. (2010). A HPC bridge in Raleigh, North Carolina, consisting of AASHTO Type III prestressed concrete I-girders with 17.5 m (57.4 ft) spans was load tested with a Type 3S2 AASHTO designation truck to monitor deflection and strain. Deflection was monitored with LVDTs and internally embedded VWSGs measured strain. The bridge was loaded twice, once with the truck fully loaded and once with half the load at ten different loading locations along the bridge. When comparing the strain induced by the truck loaded with half the weight to that of a fully loaded, the values were approximately half. This indicated that the bridges were loaded elastically.

Measured strains were compared to strain calculations assuming continuous beams and AASHTO (2007) load distribution factors. The calculated strains tended to be higher than those measured (Dwairi et. al, 2010).

2.5. PRECAST CONCRETE CONSTRUCTION

The use of precast concrete in the construction of concrete bridges has allowed for rapid construction of bridges allowing for minimal lane closure and increased work zone safety. Prefabricated elements can be closely monitored at precasting plants for improved quality control. Although prefabricated systems can have a slightly higher initial material cost, especially when coupled with new materials such as FRP, the life-cycle cost can make prefabricated construction economically feasible because of the expedited erection time and possibility of improved durability. For example, 1,300 m² (14,000 ft²) of concrete deck panels was replaced in Fairfax County, VA, over Route 50 utilizing prefabricated deck panels to replace the deteriorating panels. The old deck panels were removed and new deck panels installed with a crane. After only 3 hours, the bridge was reopened to traffic after a rapid-setting overlay was applied to the bridge (Shahawy, 2003). In addition, fully prefabricated bridges were constructed in Baldorioty de Castro Avenue Overpass in San Juan, Puerto Rico. The bridges were erected in an average of 29 hours. The process involved utilizing cast-in-place (CIP) footings with driven piles being post-tensioned to precast box girders. Once the box girders were post-tensioned to the footings, the precast pier cap was post-tensioned to the precast box girders. After two piers were in place, box beams with span lengths of 30 m (100 ft) were attached to the substructure (Shahawy, 2003).

2.6. GLASS FIBER REINFORCED POLYMER.

2.6.1. Definition of GFRP. New construction materials have been researched and implemented to increase the life of structures. One such material is that of glass fiber reinforced polymer (GFRP). GFRP bars consist of a glass composite material that has been fashioned into a reinforcing bar. The bar consists of longitudinal fibers that are bound together by a rigid polymer resin material (ACI 440.1R, 2003).

2.6.2. Material Properties of GFRP. GFRP is useful because of its corrosion resistance. In addition, the strong material is fairly lightweight and provides a high-strength-to-weight ratio. The strength of FRP and GFRP bars is controlled by the type of fiber and the fiber-volume fraction. The fiber-volume fraction is the ratio of the volume of the fiber content to the total volume of the bar divided by a specific unit of length (Kocaoz and Nanni, 2004).

Concerns with the use of GFRP are due to the materials only having high tensile strength in the direction of the fibers. This in turn affects the shear strength and bond performance of the GFRP bars when in concrete. Compressive strength of GFRP bars has also been found to be 55% of the tensile strength. Unlike mild steel, the tensile strength of GFRP remains elastic until failure and does not exhibit yielding. This lack in ductility of the material has to be accounted for in the design process (ACI 440.1R, 2003).

GFRP is not recommended for cases with the need for fire resistance. The GFRP can soften and lose strength and stiffness when the temperatures within the concrete become higher than the glass-transition temperature which is typically 65 to 120°C (150 to 250°F) (ACI 440.1R, 2003).

2.6.3. GFRP in Bridge Decks. A test completed by Phillips, Harlan, Roberts-Wollman, and Cousins (2005) was completed in Virginia to investigate the durability of GFRP bars in bridge decks. Route 668 Bridge over Gills Creek in Franklin County, VA, was reinforced with GFRP bars on the top mat and steel bars on the bottom. Resistance strain gauges and VWSGs, and thermocouples were placed throughout the decks close to the interior bridge girders and monitored by a CR23X Datalogger. Live load testing was run on June 23, 2003, and June 17, 2004, using a dump truck with a front axle weight of 60.1 kN (13.5 kips) and rear axle weight of 161 kN (36.3 kips). Results showed that the stresses within the GFRP bars were compressive and particularly small with the largest being -0.90 MPa (-130 psi). The interior girder at the abutment experienced the highest tensile stress of 0.52 MPa (75 psi) which was lower than the 95.8 MPa (13.9 ksi) provided by ACI 440.1R (2003). Any differences in stresses determined in the 2003 and 2004 load tests were minor. The 2004 test had a slightly higher compressive strain. However, no cracking was found using visual inspection (Phillips et.al, 2005).

3. RESEARCH PROGRAM

3.1. PROGRAM TEAM

Dr. John J. Myers at the Missouri University of Science and Technology (Missouri S&T) served as the principal investigator. Kurt Bloch served as the lead graduate research assistant. Other Missouri S&T graduate students including Wei Zheng, Charles Werner, Dan Kienitz, and Courtney Greene assisted in the preparation of instrumentation and material tests. In addition, Krista Porterfield, Amanda Heady, Sarah Stach, and Hope Mooberry, civil and architectural undergraduates at Missouri S&T, assisted in many of the material and bridge tests. Technical help was provided by Brian Swift, Gary Abbott, Jason Cox, and Steve Gabel in the setup of the instrumentation systems. Coreslabs Structures, Inc. in Marshall, Missouri, and Hughes Brothers of Seward, NE, supported this research project with their facilities and materials. The project was sponsored by the City of Rolla, and the National University Transportation Center (NUTC). The Center for Infrastructure Engineering Studies (CIES) and the Department of Civil, Architectural, and Environmental Engineering (CArEE) at Missouri S&T provided technician and staff support as noted.

3.2. DESIGN DETAILS OF BRIDGES

Two precast, prestressed, pedestrian single span bridges were erected in Phelps County in Rolla, MO, along Lions Club Drive consisting of HSC and HS-SCC. The design of the bridges was done jointly by Coreslabs Structures, Inc. and Missouri S&T. The HSC bridge is located near Highway O and spans a length of 14.6 m (48 ft) and has a width of 3.0 m (10 ft). The HS-SCC single span bridge is located near Rolla Street and spans a length of 10.7 m (34 ft) and has a width of 3.0 m (10 ft). The locations of each bridge can be seen in the map presented in Figure 3.1.



Figure 3.1. Bridge Locations.

Each bridge implemented prestressed “L” spandrel beams to function as the structural support of the bridge and the handrails for the pedestrians. Both bridges have two precast deck panels to form the bridge deck. One precast deck panel was reinforced with mild steel and the other was reinforced with GFRP. Both the precast deck panels and the beams were fabricated by Coreslabs Structures, Inc. in Marshall, MO, during the months of July and August 2009. Construction of the bridge abutments began August 2009, and the bridges were erected on September 30, 2009. The pedestrian trail was open to foot traffic during the spring of 2010. A cross section of the bridge is illustrated in Figure 3.2. Design drawings for the spandrel beams and deck panels provided by Coreslabs, Inc. of Marshall, MO are presented in Appendix J.

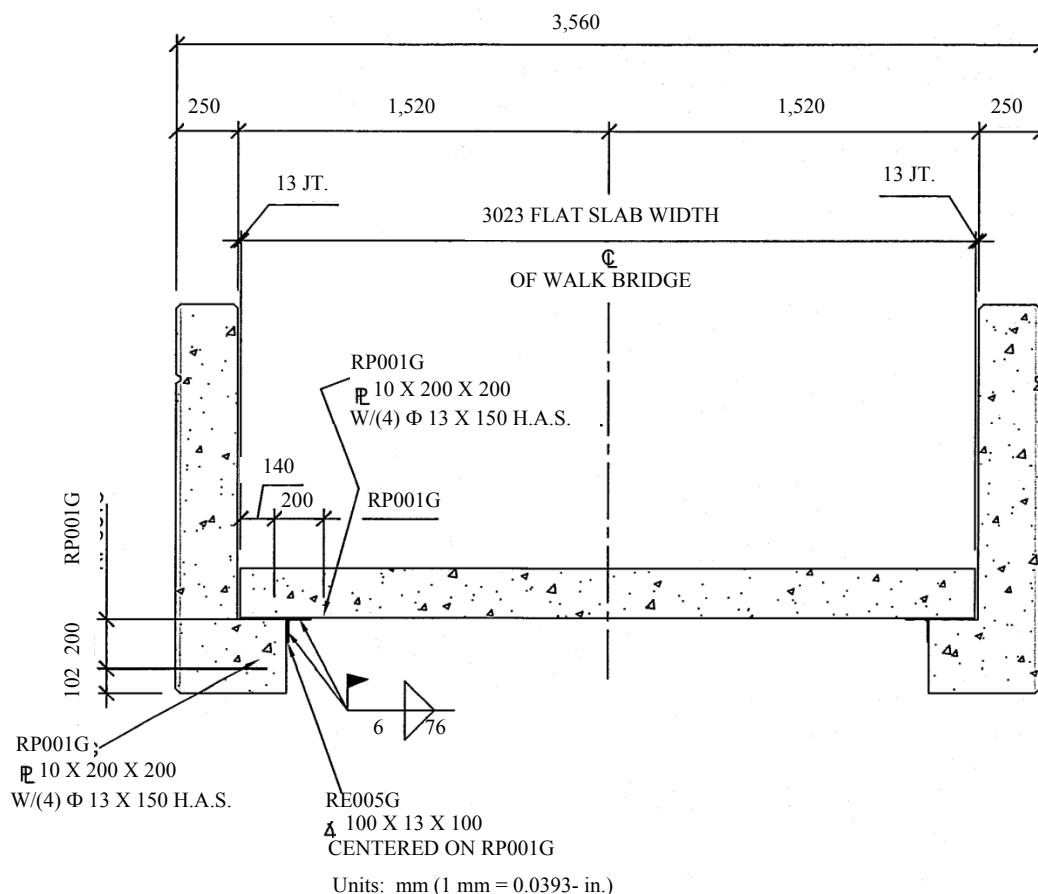


Figure 3.2. Cross Section of HSC & HS-SCC Bridges.

3.2.1. HSC and HS-SCC Prestressed/Precast L Spandrel Beam. The HSC and HS-SCC beams were prestressed “L” spandrel beams that were 14.6 m (48 ft) long and 10.7 m (34 ft) long respectively. Each bridge had a target compressive strength of 68.9 MPa (10,000 psi) and a release strength of 24.1 MPa (3,500 psi).

Within each beam are twelve 13 mm (0.5 in) diameter, seven wire, low relaxation, Grade 270 (1,860 MPa) prestressing strands used to reinforce the single span concrete bridges. The dimension of the beams and the strand layout and initial prestressing force on each strand is illustrated in Figure 3.3. The “L” beam is laying down in the figure because the beams were cast and pretensioned in this manner. None of the twelve strands were draped.

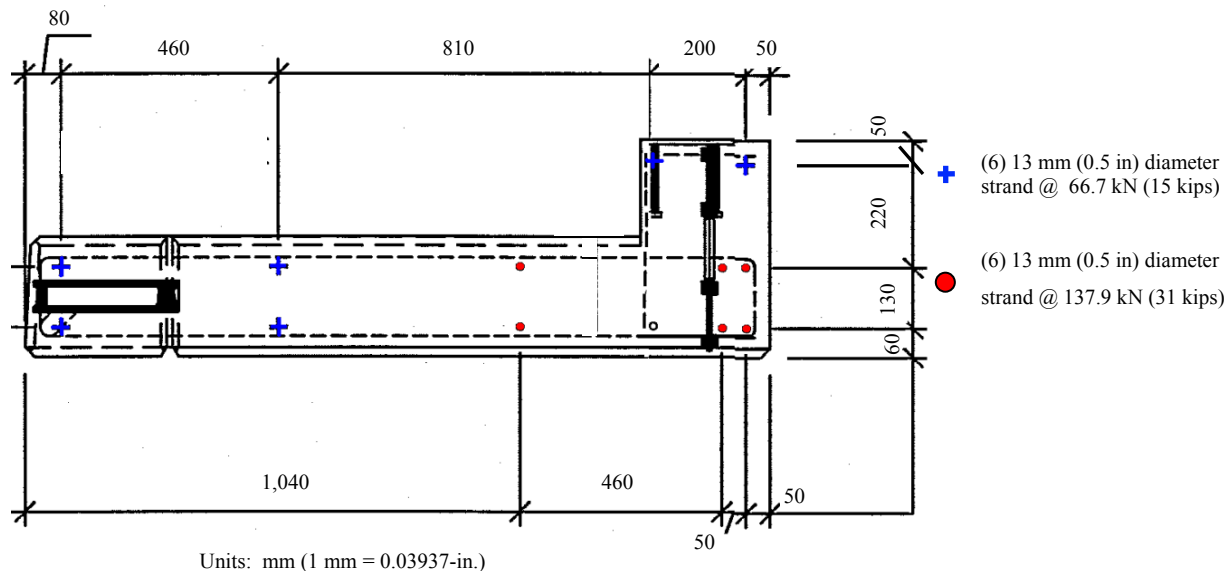


Figure 3.3. Cross Section of HSC & HS-SCC Bridge Spandrel Beam.

3.2.2. HSC and HS-SCC Precast Deck Panels. The precast decks of each bridge utilized the same mixture proportion as the beams. Two different types of reinforcements were added to each bridge to monitor the differences in thermal gradients and time dependent behavior between mild steel and glass fiber reinforced polymer (GFRP) bars in both HSC and HS-SCC deck panels. Each deck panel was 200 mm (8-in.) thick and 3,000 mm (119-in.) wide. The HSC deck was 7,300 mm (288-in.) long, and the HS-SCC deck was 5,200 mm (204-in.) long. The mild steel was spaced at 230 mm (9-in.) on center 40 mm (1.75-in.) from the bottom of the deck panels reinforced only with steel. However, the GFRP reinforced deck panels had the GFRP spaced at 150 mm (6-in.) on center at 40 mm (1.75-in.) from the bottom with mild steel replacing GFRP every 450 mm (18-in.) on center. The mild steel was added to the deck panels to meet the shear strength requirements. Concrete reinforced solely with GFRP bars has a depth to the neutral axis after the concrete has cracked that is smaller than the depth to the neutral axis when reinforced only with mild steel. This occurs because of differences in the axial stiffness provided by the stiffness of the reinforcing bars. With the decreased

depth to the neutral axis, the compression region is reduced and crack widths are increased. Therefore, the contribution of shear resistance provided by the coarse aggregate tends to be reduced in members reinforced solely with GFRP bars when compared to mild steel due to differences in the modulus of elasticity of the reinforcing bars (ACI 440.1R, 2003).

The mild steel used within the deck panels were 13 mm (0.5-in.) Grade 60 (413 MPa) rebar. The Size 6 GFRP bars were provided and manufactured by Hughes Brothers of Seward, NE, and were a new GFRP Aslan 102 product. Currently the Aslan 100 GFRP has a diameter of 20 mm (0.75-in.), bar area of 285 mm² (0.442 in²), tensile strength of 620 MPa (90 ksi), and elastic modulus of 40.8 GPa (5.92 Msi). The new Aslan 102 GFRP should have the same cross sectional properties. However, the modulus of elasticity is predicted to be around 48 GPa (7 Msi), and the tensile strength should be higher than average. Testing was completed by Hughes Brothers, Inc. in Seward, NE on the GFRP to determine the exact properties. The results are presented in Section 7. Spread sheets using ACI 440.1R (2003) to design the GFRP reinforcement in the precast deck panels are featured in Appendix A.

3.3. MIXTURE PROPORTIONING

The mixture proportioning designed by Coreslabs Structures, Inc. for both the HSC and HS-SCC bridge beams and deck panels are displayed in Table 3.1. Both the beams and deck panels used the same mixture proportions. Differences in the measured mechanical and material properties between the mixtures and casting dates occurred due to the slight variation in the moisture conditions of the constituent materials at batching and water usage. It should be noted that the HSC did not have air entrainment specified because of the disconnected capillary structure system resulting from the low w/cm ratio. With this disconnected capillary system, HSC is unlikely to be exposed to the necessary 91.7% saturation level for freeze-thaw (F-T) damage to occur (Myers, 1998). While one would expect that HS-SCC would perform similarly, experimental data regarding the F-T resistance of HS-SCC is limited at this time; therefore air entrainment additive was specified.

Table 3.1. HSC & HS-SCC Mixture Proportioning.

Type	Material	Weight
HSC		
Cementitious Material	Ashgrove Gray Type III	444 kg/m ³ (750 lbs/yd ³)
	Microsilica	34 kg/m ³ (58 lbs/yd ³)
Coarse Aggregate	13 mm (1/2") Canyon Gray Granite	1,006 kg/m ³ (1,695 lbs/yd ³)
Fine Aggregate	Kaw River Sand	733 kg/m ³ (1,235 lbs/yd ³)
Admixtures	3.55 L (0.94 gal) HRWR	1.07 kg/m ³ (4 lbs/yd ³)
	0.95 L (0.25 gal) Retarder	
Water		69 kg/m ³ (259 lbs/yd ³)
w/cm		0.326
HS-SCC		
Cementitious Material	Ashgrove Gray Type III	392 kg/m ³ (660 lbs/yd ³)
	Thomas Hill Type C Fly Ash	71 kg/m ³ (120 lbs/yd ³)
Coarse Aggregate	Grade E Cedar Valley Limestone	608 kg/m ³ (1,025 lbs/yd ³)
Fine Aggregate	Kaw River Sand	801 kg/m ³ (1,350 lbs/yd ³)
	9.5 mm (3/8") Cedar Valley Limestone Chips	277 kg/m ³ (467 lbs/yd ³)
Admixtures	1.02 L (0.27 gal) Air Entrainment	5.34 kg/m ³ (9 lbs/yd ³)
	3.03 L (0.8 gal) HRWR	
Water		151 kg/m ³ (254 lbs/yd ³)
w/cm		0.338

4. FABRICATION AND CONSTRUCTION

4.1. INTRODUCTION

In this section, the fabrication and erection of the precast beams and deck panels are discussed. In addition, any construction related issues are presented. Table 4.1 lists the dates and times of the bridge construction.

Table 4.1. Timeline of Bridge Construction.

Activity	Start Time and Date	Notes
Beam Placement 1	2:00 p.m. 7/27/2009	Placed: HB1, SB1
Beam Release	6:00 a.m. 7/28/2009	Released: HB1, SB1
Beam Sandblast	8:00 a.m. 7/28/2009	Sandblasted: HB1, SB1
Beam Placement 2	11:00 a.m. 7/30/2009	Placed: HB2*, SB2*
Beam Release	9:00 a.m. 7/31/2009	Release: HB2*, SB2*
Beam Sandblast	10:00 a.m. 8/3/2009	Sandblast: HB2*, SB2*
Deck Panel Placement	10:30 a.m. 8/21/2009	Placed: HS1*, HS2*, SS1*, SS2*
HSC Beam Erection	9:45 a.m. 9/30/2009	Erect: HB1, HB2*
HSC Deck Panel Erection	11:35 a.m. 9/30/2009	Erect: HS1*, HS2*
HS-SCC Beam Erection	3:15 p.m. 9/30/2009	Erect: SB1, SB2*
HS-SCC Deck Panel Erection	4:25 p.m. 9/30/2009	Erect: SS1*, SS2*
* Beams and deck panels which are instrumented HB (High-Strength Concrete Beam) SB (High-Strength Self-Consolidating Beam) HS (High-Strength Concrete Deck Panel) SS (High-Strength Self-Consolidating Deck Panel)		

4.2. FABRICATION OF PRECAST SPANDREL BEAMS

An instrumentation plan for the bridging system was presented to the City of Rolla, MO and Coreslabs Structures, Inc. on February 2, 2009. The document clarified when and how the researchers would need access to the bridge to instrument the beams and fabricate material samples.

The fabrication of the beams began July 27, 2009, through July 31, 2009, at the Coreslabs Structures, Inc. precasting plant in Marshall, MO. The beams were cast inside their concrete fabrication building. The mild steel and prestressed strands were placed into the steel forms. The location of the steel prior to concrete placement is shown in Figure 4.1. The concrete was brought in by two trucks and cast into the beam forms using a concrete bucket. Another truck was brought in to cast the haunch of the beams. The placement of concrete can be seen in Figure 4.2. In the second beam placement on July 30, 2009, the HS-SCC beam's haunch did not have a batch ready at the exact time needed. Figure 4.3 displays the crosses scribed into the concrete to prevent a cold joint. To date, there has not been a problem with this concrete joint. The HSC beams were vibrated with a vibrating precasting bed. The HS-SCC beams did not require vibration.



Figure 4.1. Steel in Beam.



a.) Web Placement with Concrete Truck

b.) Haunch Placement with Concrete Bucket

Figure 4.2. Concrete Placement for Beams.

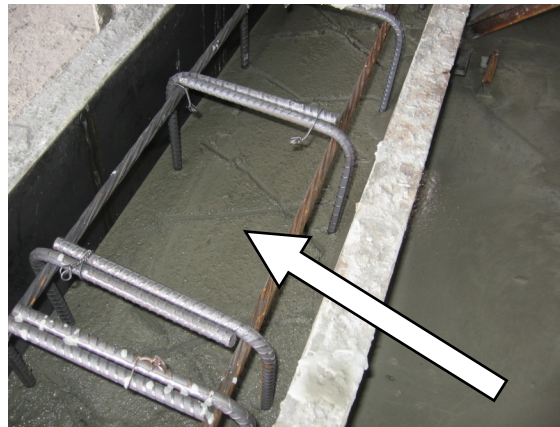


Figure 4.3. Scribed Crosses Used to Prevent Cold-Joint in HS-SCC Beam.

Fifteen to sixteen hours after the first set of beams had been cast and twenty-four hours after the second set of beams had been cast, the strands were released and the steel forms removed. The beams were picked up with a crane and placed on a truck trailer bed. The beams were stored outside and later sandblasted. They can be seen on Figure 4.4. The beams remained outside at Coreslabs Structures, Inc. until the transfer of the

beams for erection. While at the precasting plant, instrumentation systems monitored the temperature and strains within the second set of beams.



Figure 4.4. Beam Storage Prior to Transfer.

4.3. FABRICATION OF PRECAST DECK PANELS

The fabrication of the deck panels began August 20, 2009, through August 24, 2009, at the precasting plant in Marshall, MO. The slabs were fabricated within their fabrication building on the same precasting beds as the spandrel beams. The mild steel and GFRP bars were placed within the steel forms the day before the deck panels were placed. A photograph of the mild steel and GFRP placed prior to fabrication is presented in Figure 4.5. Two concrete trucks were required to cast the HSC and the HS-SCC within the deck panels. The placement can be seen in Figure 4.6. After the concrete was cast, a broom finish was applied to the top of the precast deck panels. On August 24, 2009, the forms were stripped and the deck panels were placed onto the back of a semi-truck trailer via a crane. The deck panels were stored on the trailer until the transfer of the deck panels to the jobsite for the bridge erection. This is shown in Figure 4.7.



Figure 4.5. Formwork, Steel, & GFRP for the Deck Panels.



Figure 4.6. Concrete Placement for Deck Panels.



Figure 4.7. Concrete Deck Panel Storage Prior to Transfer.

4.4. BRIDGE ERECTION

Before the beams and deck panels were shipped to Rolla, MO, the abutments were constructed at the jobsite. The abutments were constructed in several placing operations during the month of August 2009. Concrete placement for one of the abutments is shown in Figure 4.8. The day before the beams and the deck panels were transported to Rolla, MO, the sensors were connected to the two respective data acquisition systems to monitor strain variations within the members during transfer of the members to the jobsite. On the morning of September 29, 2009, the beams and deck panels were shipped to Rolla, MO, and erected along Lions Club Drive. The erection sequence is shown in Figures 4.9 to 4.14. The following processes occurred during the construction of the bridges: the “Missouri Monster”, a large Grove Crane (GMK 5210) with a 1,870 kN (210 ton) capacity and boom of 64 m (210 ft), was set up at the jobsite to lift the structural members; the HSC beams were placed and welded to embed plates in the abutments; the HSC deck panels were placed on neoprene pads resting on the precast beams, the crane was moved and placed at the second jobsite; the HS-SCC beams were placed and welded to the embed plates in the abutments; and the HS-SCC slabs were placed upon neoprene pads resting on the precast beams. The following day, the deck

panels were welded to the beam embed plates. Some minor map cracking with a thickness of about 0.25 mm (0.01-in.) on 1 (or 2) deck panels was noticed at the lifting point(s). Representative cracks are displayed in Figure 4.15. These cracks were injected with a high-strength epoxy. In addition, the lifting inserts on the precast beams and deck panels were filled with a high-strength epoxy to prevent lift hook corrosion and improve durability.



Figure 4.8. Abutment Placement for HSC Bridge Location.



Figure 4.9. Trucks Arriving with HSC & HS-SCC Beams from Marshall, MO.



a.) Crane Lifting Instrumented HSC Beam



b.) Maneuvering of HSC to Proper Location on Abutment



c.) Non-Instrumented HSC Beam Set on Embed Plates

Figure 4.10. HSC Beam Erection.



Figure 4.11. HSC Beam Welded to Abutment.



Figure 4.12. Slabs Placed on Top of Neoprene Pads on Top of HSC Beams.



a.) Crane Lifting Instrumented HS-SCC Beam



b.) Maneuvering of Instrumented HS-SCC to Proper Location on Abutment



c.) Non-Instrumented HS-SCC Beam Set on Embed Plates

Figure 4.13. HS-SCC Beam Erection.



Figure 4.14. HS-SCC Deck Panel Erection.

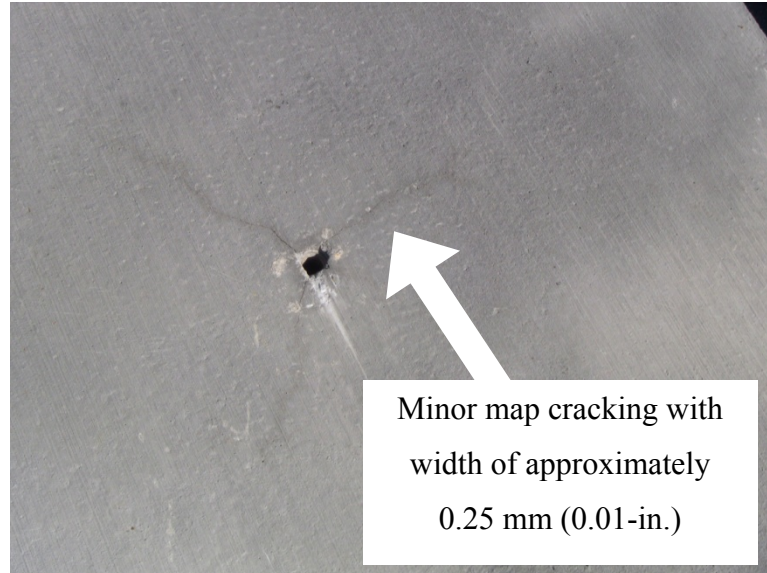


Figure 4.15. Cracking on Slab at Crane Lifting Location.

5. MATERIAL TESTING PROGRAM

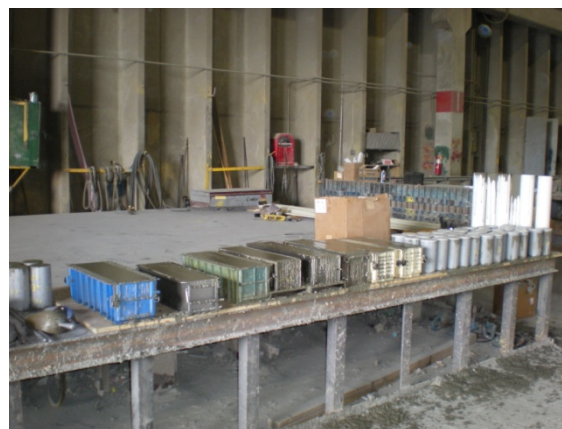
5.1. INTRODUCTION

In order to have a comparison of HSC and HS-SCC, material and mechanical test results were required. This section details the mechanical and material testing program of both mixture proportions including: compressive strength, modulus of elasticity, modulus of rupture, splitting tensile strength, creep, and shrinkage. In addition, to have a greater understanding of the GFRP reinforcement, the tensile strength and modulus of elasticity tests were completed on the GFRP bars. Hughes Brothers in Seward, NE completed these GFRP material tests for the project team.

5.1.1. Member Cast. The precast spandrel beams and deck panels were fabricated at Coreslabs Structures, Inc., located in Marshall, MO. Both the beams and deck panels were fabricated in the same bed at varying dates. The dates are specified in Table 4.1 previously. The concrete quality control/quality assurance (QC/QA) specimens were cast next to the beams and deck panels to have them experience similar temperature and atmospheric conditions. The specimens are shown in Figure 5.1.



a.) Precast Spandrel Beam QC/QA Specimens



b.) Precast Deck Panel QC/QA Specimens

Figure 5.1. QC/QA Specimens Placement at Precast Plant.

5.1.2. Curing Conditions. For the first 24 hours, the specimens were field cured. With this method of curing, the specimens were fabricated close to their corresponding beams or deck panels. After 24 hours, the QC/QA specimens were taken to Rolla, MO, and stored in an outside storage area on campus which had similar environmental ambient conditions as the members in Marshall, MO. Environmental conditions monitored from National Climatic Data Center (NCDC) data for Marshall, MO and Rolla, MO are shown in Figure 5.2. Only the creep and shrinkage specimens were placed within an enclosed temperature controlled environment due to creep fixture frame setups. Figure 5.3 displays the location of the material specimens during storage.

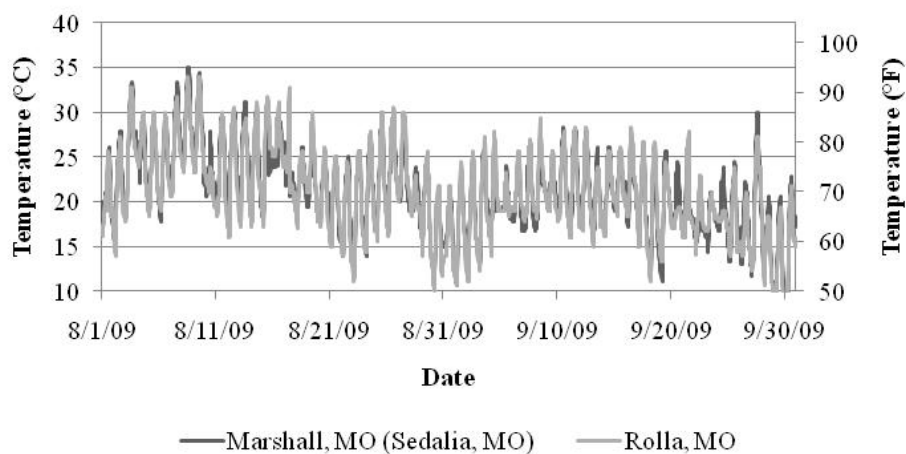


Figure 5.2. Comparison of Marshall, MO (Sedalia, MO) & Rolla, MO Temperatures.



a.) Summer Storage



b.) Winter Storage

Figure 5.3. Storage of QC/QA Specimens at Missouri S&T in Rolla, MO.

5.1.3. Overview of Testing Program. Table 5.1 lists the material testing program for the precast beams and precast deck panels.

Table 5.1. Summary of Material Testing Program.

Tests	Test Method	Specimens	Dates of Test
Compressive Strength	ASTM C39-05	100 mm dia. x 200 mm long cylinder (4-in. dia. x 8-in. long cylinder)	Release, 4 days, 7 days, 14 days, bridge erection, 28 days, 1 year, 2 years
Modulus of Elasticity	ASTM C469-02		
Splitting Tensile Strength	ASTM C496-04		
Modulus of Rupture	ASTM C78-08	150 mm x 150 mm x 500 mm/600 mm (6-in. x 6-in. x 21-in. 6-in. x 6-in. x 24-in.)	Release, 7 days, 28 days, 1 year
Creep	ASTM C512-02	100 mm dia. x 600 mm long cylinder (4-in. dia. x 24-in. long cylinder)	After bridge erection
Shrinkage	ASTM C157-08		After beam and deck panel placement

5.2. COMPRESSIVE STRENGTH

The compressive strength tests performed followed ASTM C39 (2005) “Standard Test Method for Compressive Strength of Cylindrical Concrete Specimens” using 100 mm (4-in.) diameter by 200 mm (8-in.) long cylinders. The compressive strength at release of prestressing for the beams was tested at Coreslabs Structures, Inc. All subsequent compressive strength testing was completed at Butler-Carlton Civil Engineering Hall in the Construction Materials Load Frame Laboratory at the Missouri University of Science and Technology in Rolla, MO. The testing apparatus used at Missouri S&T was a 5,340 kN (1,200 kips) Forney compression machine. The specimens were loaded at 240 ± 100 kPa per second (35 ± 15 psi per second) which

corresponds to 1.9 ± 0.8 kN per second (440 ± 188 lbs per second) loading. Neoprene pads in steel end caps were used in testing instead of sulfur mortar caps due to the higher stiffness required to test the high compressive strengths of the concrete.

5.3. MODULUS OF ELASTICITY

In order to determine serviceability and performance of precast, prestressed concrete structures, the modulus of elasticity (MOE) is required. The MOE was determined by using ASTM C469 (2002) “Standard Test Method for Static Modulus of Elasticity and Poisson’s Ratio of Concrete in Compression” using 100 mm (4-in.) diameter by 200 mm (8-in.) long cylinders. The specimens placed within a testing apparatus used at Butler-Carlton Civil Engineering Materials Load Frame Laboratory at Missouri S&T in Rolla, MO. Missouri S&T was a 5,340 kN (1,200 kips) Forney compression machine. The specimens were loaded at 240 ± 100 kPa per second (35 ± 15 psi per second) which corresponds to 2.0 ± 0.8 kN per second (440 ± 188 lbs per second) loading which is identical to compression testing. Two MOE tests were run for each specimen and at each test age and averaged. In order to determine the MOE, the stress, f_{cl} , at a strain of 0.00005 and the strain, ϵ_{cl} , at 40% of the ultimate stress, f'_c , was required. The modulus of elasticity was calculated by $(0.4f'_c - f_{cl})/(\epsilon_{cl} - 0.00005)$. The testing apparatus is displayed in Figure 5.4. Table 5.2 summarizes the compressive strength tests and modulus of elasticity tests completed on the various mixture proportions.



Figure 5.4. Modulus of Elasticity Test.

Table 5.2. Specimens for Compressive Strength & Modulus of Elasticity

HSC Beam		HS-SCC Beam		HSC and HS-SCC Deck Panel
7/27/2009	7/30/2009	7/27/2009	7/30/2009	8/21/2009
7 days*	Release*	7 days*	Release*	Release
28 days	7 days	28 days	4 days	4 days
1 year	14 days	1 year	7 days	7 days
	28 days		14 days	28 days
	Erection		28 days	1 year
	1 year		Erection	
	2 year		1 year	
			2 year	
9 cylinders	21 cylinders	9 cylinders	21 cylinders	18 cylinders
Beams: 60 cylinders; Deck Panels: 36 cylinders; Total Specimens: 96 cylinders				
* Tests that were unable to run Modulus of Elasticity Tests				

5.4. MODULUS OF RUPTURE

The modulus of rupture tests were performed in accordance with ASTM C78 (2008) “Standard Test Method for Flexural Strength of Concrete (Using Simple Beam with Third-Point Loading)” using beams that were 150 mm (6-in.) by 150 mm (6-in.) by either 500 mm (21-in.) or 600 mm (24-in.). The specimens were tested at Butler-Carlton Civil Engineering Hall in the Construction Materials Load Frame Laboratory at the Missouri S&T in Rolla, MO, by a Tinius-Olsen testing machine. The specimens were loaded continuously at a rate of 0.86 and 1.21 MPa per minute (125 and 175 psi per minute) until failure. The testing apparatus is displayed in Figure 5.5. Table 5.3 lists the specimens that were placed and used for modulus of rupture testing.



Figure 5.5. Modulus of Rupture.

Table 5.3. Specimens for Modulus of Rupture.

HSC		HS-SCC	
Placed: 7/30/2009	Placed: 8/21/2009	Placed: 7/30/2009	Placed: 8/21/2009
7 days (2)	Release (2)	7 days (2)	Release (2)
28 days (2)	7 days (2)	28 days (2)	7 days (2)
1 year (1)	28 days (2)*	1 year (2)	28 days (2)
	1 year (2)*		1 year (2)*
5 beams	8 beams	6 beams	8 beams
HSC: 13 beams; HS-SCC: 14 beams; Total: 27 beams			
* Tests that used 150 mm (6-in.) by 150 mm (6-in.) by 600 mm (24-in.) beams			

5.5. SPLITTING TENSILE STRENGTH

The splitting tensile strength tests were performed in accordance with ASTM C496 (2004) “Splitting Tensile Strength of Cylindrical Concrete Specimens” using 100 mm (4-in.) diameter by 200 mm (8-in.) long cylinders. The tests were completed at the Butler-Carlton Civil Engineering Hall in the Construction Materials Load Frame Laboratory at Missouri S&T with a modified Forney compression machine. In order to run this test, plates were set within the machine and wooden strips were utilized to induce the stress locations required in the ASTM. The test setup is shown in Figure 5.6. The specimens were loaded at a continuous rate of 0.7 to 1.4 MPa per minute (100 to 200 psi per minute) until failure. Table 5.4 lists the specimens that were placed and tested for determining the splitting tensile strength.



a.) Forney Compression Machine Utilized for Split Tension Test



b.) Modified Split Tension Load Frame

Figure 5.6. Splitting Tensile Strength.

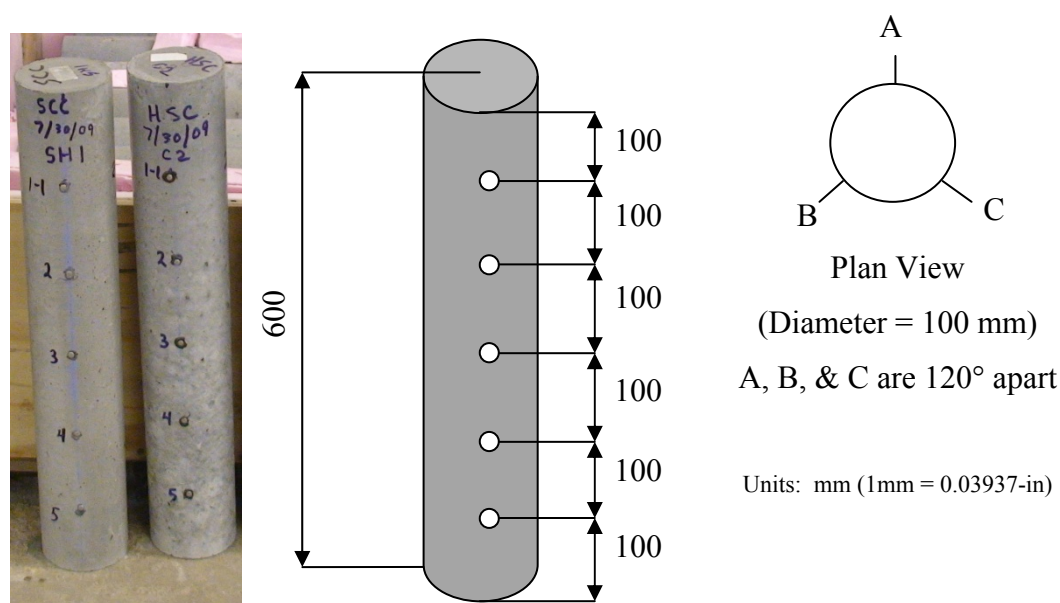
Table 5.4. Specimens for Splitting Tensile Test.

HSC			HS-SCC		
Placed: 7/27/2009	Placed: 7/30/2009	Placed: 8/21/2009	Placed: 7/27/2009	Placed: 7/30/2009	Placed: 8/21/2009
7 days (2)	4 days (2)	Release (3)	7 days (2)	4 days (2)	Release (3)
28 days (2)	7 days (2)	4 days (3)	28 days (2)	7 days (2)	4 days (3)
1 year (2)	28 days (3)	7 days (3)	1 year (2)	28 days (3)	7 days (3)
	Erection (3)	28 days (3)		Erection (3)	28 days (3)
	1 year (3)	1 year (3)		1 year (3)	1 year (3)
	2 year (3)	2 year (3)		2 year (3)	2 year (3)
HSC: 7/27/2009 (6 cylinders), 7/30/2009 (16 cylinders), 8/21/2009 (18 cylinders)					
HS-SCC: 7/27/2009 (6 cylinder), 7/30/2009 (16 cylinders), 8/21/2009 (18 cylinders)					
Total: 80 cylinders					

5.6. CREEP AND SHRINKAGE

A modified version of ASTM C512 (2002) “Standard Test Method for Creep of Concrete in Compression” was used to determine the creep of 100 mm (4-in.) diameter by 600 mm (24-in.) long cylinders loaded to 20 to 40 percent of the design strength of 68.9 MPa (10,000 psi). In addition, the same cylinders were used to determine the shrinkage of the specimens using a modified version of ASTM C157 (2008) “Standard Test Method for Length Change of Hardened Hydraulic-Cement Mortar and Concrete.” The concrete specimens are similar to the cylinders used by Myers’ research on high-performance concrete (Myers, 1998). Figure 5.7 displays the cylindrical specimens and the location of the various DEMEC points used to determine the strain of the specimens. Each specimen was placed in 100 mm (4-in.) diameter by 600 mm (24-in.) polyvinyl chloride (PVC) pipes. Within 24 hours of placement, the specimens were de-molded and DEMEC points were outfitted with five-minute quick set epoxy on the specimens and preliminary readings were taken. Nine locations on each cylinder could be read to determine the change in strain over that length. The average of all of the readings was computed to be the total strain of the specimen. Table 5.5 lists the specimens made to

determine the creep and shrinkage of HSC and HS-SCC. Additional cylindrical specimens were fabricated in case of damage during transportation or demolding.



a.) Image of Creep & Shrinkage Specimens

b.) Schematic of Creep & Shrinkage Specimens

Figure 5.7. Creep & Shrinkage Specimens & DEMEC Point Arrangements.

Table 5.5. Creep & Shrinkage Specimens.

Material:	HSC		HS-SCC	
Placed:	7/30/2009	8/21/2009	7/30/2009	8/21/2009
Shrinkage:	SH1, SH2	SH1, SH2, SH3	SH1, SH2	SH1, SH2, SH3
Creep:	C1, C2	C1, C2	C1, C2	C1, C2
HSC: 9 cylinders; HS-SCC: 9 cylinders; Total: 18 cylinders				

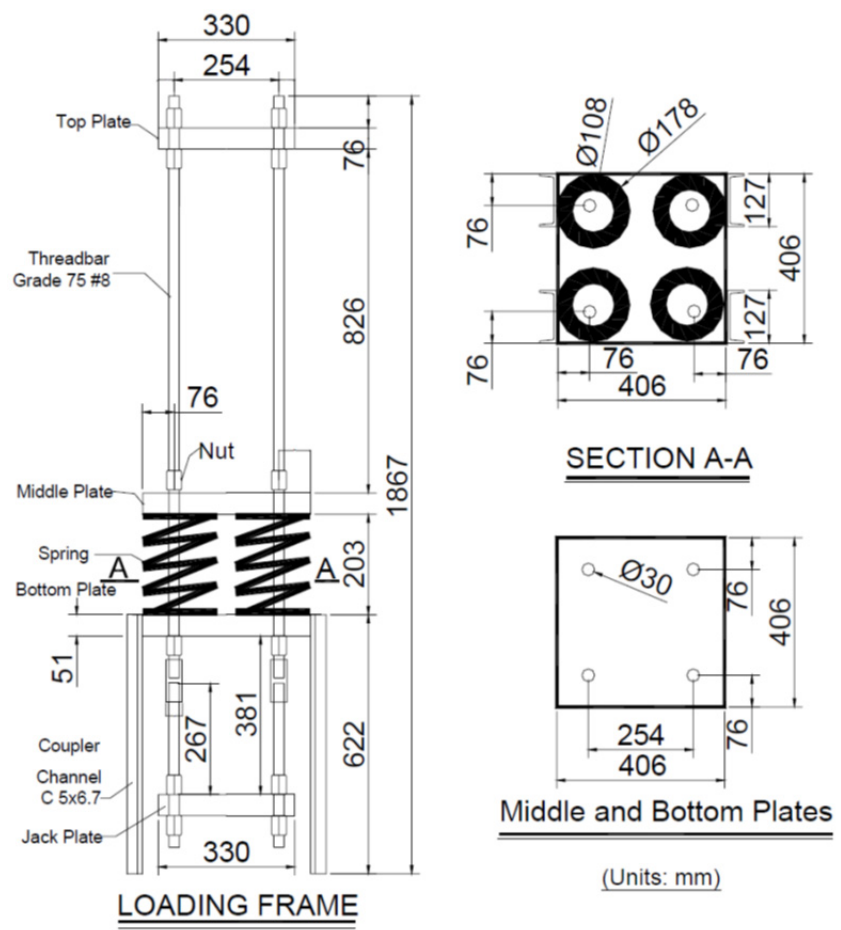
Due to limited availability of transportation for some specimens, not all specimens were able to be de-molded within twenty-four hours of fabrication. Only the deck panel creep and shrinkage cylinders were able to be de-molded at 24 hours. The

beam creep and shrinkage cylinders were de-molded 6 days after placing. Data from the deck panel specimens were used to interpolate the lost early-age shrinkage data since the mixture proportions were identical. To ensure enough data were obtained in order to interpolate the data lost, specimens were read every day for the first two weeks, every other day for the next week, every few days until December, and then every few weeks, thereafter. The specimens were stored and monitored in the Engineering Research Lab (ERL) Structural Engineering Laboratory to keep the specimens within an area that would maintain an average relative humidity of 55% and a temperature around 21.1°C (70°F). However, fluctuations in humidity and temperature did occur on days when the loading dock door was opened and closed for large scale specimen delivery and removal.

The creep specimens were loaded after the bridge erection when the bridge experienced loading applied by the deck panels and service loads. While waiting for the bridges to be erected, the specimens were sulfur capped to provide a smooth surface that would be in uniform contact with the load frame. In addition, the load frames were assembled. Two different spring types were used. For the frames that would load 20% of the target load, springs had an average radius of 158 mm (6.2-in.) and an approximate stiffness of 1.32 kN/mm (7.50 k/in). For the frames that would load 40% of the target load, the springs had an average radius of 195mm (7.7-in) and an approximate stiffness of 1.795 kN/mm (10.25 k/in).

After the bridge was erected on September 30, 2009, the creep specimens were loaded in the creep frames on October 3, 2009. In order to load the specimens, a jack and load cell were required to be positioned under the load frame on a jack plate. After the creep specimen was centered within the frame, the jack increased the load to the required stress level of either 13.8 MPa (2,000 psi) or 27.6 MPa (4,000 psi). Once the required axial load was obtained, the bolts were tightened and the jack was removed. In Figure 5.8, a representative schematic is provided for the creep load frame utilized for the 27.6 MPa (4,000 psi) stress level. This schematic was provided by Myers and Yang in their research on HPC girders and used in the creep load frame assembly since the same creep frames were implemented in their research (Myers and Yang, 2005). The creep frames were identical for the 13.8 MPa (2,000 psi) stress level. However, instead of 50 mm (2.0-in.) thick top, middle, and bottom plates, 40 mm (1.5-in.) plates were utilized. Secondly,

different spring sizes were utilized as mentioned previously. Readings were taken in the same interval as those of the shrinkage specimens. Since the stiffness of the springs are known, any additional load required due to load lost from relaxation of the springs can be added with the jack. The load was re-adjusted to match the initial load when it dropped by at least 2%. Figure 5.9 displays images of the apparatuses used to apply the required sustained load to the creep specimens.



(Myers and Yang, 2005)

Conversion: 1 mm = 0.0394-in.

Figure 5.8. Schematic of Creep Loading Frame for 40% Target Load.



a.) Creep Frames at ERL Structural Engineering Laboratory



b.) Example Creep Cylinder Loaded in Creep Frame

Figure 5.9. Creep Loading Frame & Specimens.

5.7. COEFFICIENT OF THERMAL EXPANSION

The coefficient of thermal expansion (CTE) was necessary to help determine the strains with thermal effects removed. In order to determine the CTE, the following method was utilized. A shrinkage specimen was taken from each concrete mixture. The test was completed a year after curing to ensure that shrinkage strain was not contributing to the change in length of the specimen. Initial strain and temperature readings were taken on each specimen utilizing the DEMEC gauge and a laser surface thermometer. The temperature was taken at the top, middle, and bottom of each specimen. Each specimen was placed into a freezer set at -25°C (-13°F). The freezer is shown in Figure 5.10. After 24 hours, each specimen was taken out and strain and temperature readings were immediately taken. Due to the rapid temperature change of the specimens while reading the strain readings, an average temperature was determined using the temperature immediately after the specimens were removed from the freezer and after strain readings were taken. Calculation of the CTE is provided in equation 1. In equation 1, $\alpha_{concrete}$ is the CTE of the concrete mixture, $\Delta\epsilon_{temp}$ is the change in strain measured, and ΔT is the difference in measured temperatures.

$$\alpha_{concrete} = \frac{\Delta \varepsilon_{temp}}{\Delta T} \quad (1)$$



Figure 5.10. Coefficient of Thermal Expansion (CTE) Test at Missouri S&T.

5.8. TENSILE STRENGTH OF GFRP

To determine the tensile strength of the GFRP, ASTM D 7205 (2006) “Standard Test Method for Tensile Properties of Fiber Reinforced Polymer Matrix Composite Bars” was implemented. Eight 1,200 mm (48-in.) samples were cut using a diamond blade cutoff saw and anchored into a schedule 40 pipe using an expansive grout as a potting material. A Baldwin Model 534 kN (120,000-lbs) capacity tension compression machine fitted with “V” grips was utilized to test the specimens for tensile strength and modulus of elasticity. An Epsilon Model 3543 extensometer was utilized to determine the strain of the GFRP bars. The extensometer monitored strain to 50% of the load after it was removed. The specimens were loaded at 13 mm per minute (0.5-in. per minute). Hughes Brothers Inc. in Seward, NE, completed the required testing on the materials and provided the material properties of the GFRP bars because of the specialized materials and testing apparatuses used in testing.

6. INSTRUMENTATION PLANS AND PROCEDURES

6.1. INTRODUCTION

Section 6 gives an overview of the gauges and instrumentation systems used in the research project. In addition, the data acquisition system (DAS) used, the preparation and installation of the gauges used, and any problems that occurred are discussed.

The instrumentation system created monitored the beams and deck panels during the early-age and later-ages of the HSC and HS-SCC bridges. The primary goals of the instrumentation system program were as follows:

1. Monitor immediate and long-term prestress losses;
2. Monitor deflection from transfer through service life;
3. Compare the measured deflections with predicted deflections;
4. Monitor stresses along the spans at the center of gravity of the steel due to prestressing; applied loads, and thermal effects;
5. Develop stress/strain blocks along the depth of the members at both the near-end supports and mid-span;
6. Monitor thermal gradients at similar cross-sections;
7. Evaluate distribution of loading with a live load test after the construction has been completed;
8. Monitor transfer length for prestressing strands in the actual beams used in the Structure;
9. Examine the properties of normal HSC compared to HS-SCC;
10. Compare the performance of precast deck panels with varying reinforcements.

6.2. MEASUREMENT TYPES

Throughout the research program, three measurement types were made. They include strain, temperature, and bridge camber or deflection. A list of the systems used is presented in Table 6.1.

Table 6.1. Measurement Types.

Measurement Type	Gauges and Instrumentation System	Measurement Data
Concrete Strains	Vibrating Wire Strain Gauges; Surface Mechanical Strain Gauges	Beam Curvature; Response of Live Load; Prestress Losses
Concrete Temperatures	Thermistors	Hydration Temperatures; Thermal Gradients; Varying Seasonal Temperatures; Strain and Deflection; Measurement Corrections
Beam Camber/ Deflection	Tension Wire System; Precise Surveying	Response due to Self-Weight, Prestress, Deck Panel, and Live Load; Time-Dependent Behavior (Creep)

6.2.1. Concrete Strains. Concrete strains were monitored in a bridge beam and both deck panels of each bridge. Vibrating wire strain gauges (VWSGs) were embedded within the concrete to monitor both the beams and deck panels. In addition, surface demountable mechanical (DEMEC) strain gauges were used as a secondary system to monitor strain. Furthermore, the DEMEC system was used to determine the transfer length.

The VWSGs were placed at the location of each prestressing strand to determine the strain profile within the beams during fabrication, erection, and service life. In addition, the VWSGs were placed within the deck panels to determine the strain due to load and temperature and shrinkage.

6.2.2. Concrete Temperatures. The VWSGs contained built-in thermistors to monitor the temperature profiles within the concrete beams and deck panels. This system monitored the concrete hydration temperatures and temperature gradients during varying seasons. In addition, corrections were made to the strain and deflection from the effects of temperature.

6.2.3. Beam Camber/Deflection. The early-age and later-age deflection behavior of each bridge was monitored. Two systems were used to monitor the deflection of the beams. During prestress and storage at the precasting plant, a tension wire system was used to determine the camber of the beams. After the bridges were erected a live load test using precise surveying was used to determine the deflection behavior of the bridges.

6.3. GAUGES AND MEASUREMENT SYSTEMS

The following are the gauges and instrumentation systems used to monitor the strain, temperature, and deflection or camber of the bridge beams and deck panels.

6.3.1. Vibrating Wire Strain Gauges with Embedded Thermistors. The VWSGs were used to monitor both strain and concrete within the concrete. Embedded VWSGs were selected for this project because of their durability and have been found to be reliable for several years in field conditions (Myers and Yang, 2005). In addition, VWSGs are extremely simple to install within concrete structures. The simplicity in the installation can promote more accurate results.

A VWSG uses stress vibrations to determine strain. The VWSGs used in this project were EM-5 series manufactured by Roctest, Inc. shown in Figure 6.1. This system uses two end pieces that are joined together by a protective tube. Inside the tube is a steel wire. O-rings seal the tube and the end piece together. The end pieces allow for transfer of deformation in the concrete to the wire by the two flat circular end pieces. As the tension within the wire changes, the resonant frequency is read by an electromagnet. The frequency is converted into strain by a DAS.



(Image Provided by Roctest, Inc.)

Figure 6.1. Vibrating Wire Strain Gauge.

The range of the EM-5 is 3,000 $\mu\epsilon$ with a minimum of 1 $\mu\epsilon$. The operating temperature is from -20 to 80°C (-4 to 176°F). When the gauges were ordered, 12.2 m (40 ft) of cable was provided to ensure that enough wire was provided to navigate around the reinforcement and steel formwork and connect to the DAS.

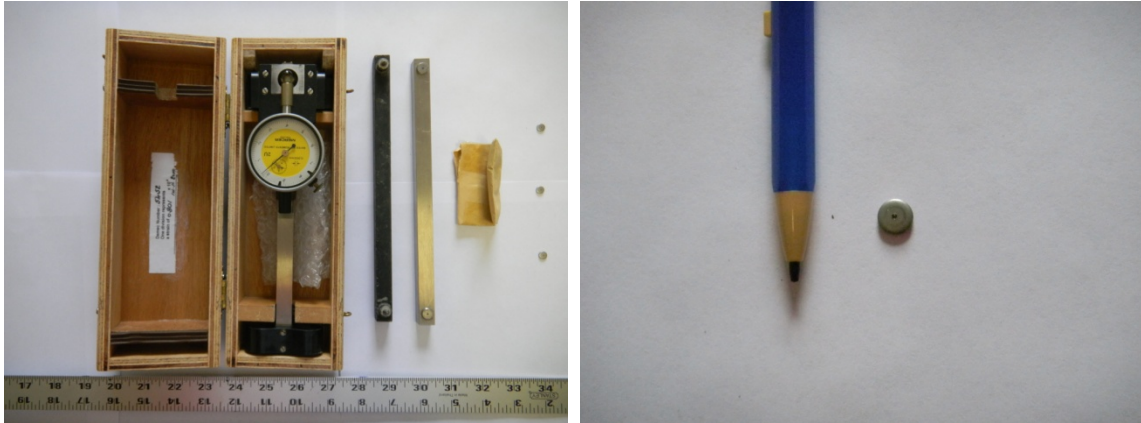
For each bridge, 16 VWSGs were used at specific points of interest. More were not used because of the cost of VWSGs and available project budget. For this project, the VWSG had a unit cost of \$140.

6.3.2. Demountable Mechanical Strain Gauge. A demountable mechanical (DEMEC) strain gauge is useful for determining the strain of concrete by using a single instrument. The system utilizes a standard dial or digital gauge that is attached and supported by a bar. The gauge, set bar, and discs are shown in Figure 6.2. Discs are mounted on each end of the bar. One end is fixed, the other can move on a pivot. The dial gauge measures the movement of the pivot.

Manufactured discs with holes are set at the predetermined locations with a setting bar. The discs are attached to locations with a five-minute quick set epoxy. After the discs set to the location, initial readings are taken. Readings are taken by setting the gauge into the stainless steel discs and writing down the dial reading. To take into account changes in temperature, a reference bar is used to take a standard reading. To determine the strain, ϵ , of the specimen, 8.01×10^{-6} is multiplied by the reading, $R_{\text{read},i}$

subtracted by the reference bar, $R_{refer,i}$, subtracted from the original reading, $R_{read,o}$, minus the original reference bar, $R_{refer,o}$. This is displayed in equation 2.

$$\varepsilon = 8.01 * 10^{-6} * [(R_{read,i} - R_{refer,i}) - (R_{read,o} - R_{refer,o})] \quad (2)$$



a.) DEMEC Gauge, Set Bar, Reference Bar, and Discs

b.) Example DEMEC Gauge Discs

Figure 6.2. DEMEC Strain Gauge & Discs.

6.3.3. Tensioned-Wire Deflection Measuring System. The tension-wire system is useful for determining camber readings particularly for longer span elements. Typically, the system utilizes a piano wire anchored into the beam and tensioned with a weight. A precise scale is outfitted to the beam. Baseline readings are made to the beam before release to determine. After the beam is released from the forms, continued readings are made to determine the changes in beam camber and deflection. This system was previously used at Missouri S&T, former University of Missouri—Rolla (Myers and Yang, 2005).

However, a modified system had to be used for this project. Two concerns did not allow for the effective use of an anchored piano wire system. The first issue was the orientation of the beams during fabrication. At fabrication, the beams were lying horizontally on the prestressing beds. When the strands would be cut, the beams would

camber in the horizontal plane instead of the vertical. A weighted wire system would not keep the beam taut. In addition, aesthetics of the bridge were a large concern as well. Drilling holes and attaching a precise ruler to the bridge where pedestrians would see the bridge would detract from the bridge's aesthetics.

A new system was created. It was assumed that the center gravity of the beam would provide an adequate baseline reading for determining camber and deflection. On each side of the beams, a line was drawn denoting the center of gravity of the concrete (CGC) of the beam section. After the beam was released, a 0.22 kN (50 lbs) fishing line was pulled across the CGC at each end until taut. A ruler with an accuracy of 2 mm (0.063-in.) was placed at the mid-span of the beam. A marker was used to denote where the CGC was located from the bottom of the beam on the ruler. A reading was taken of where the fishing line intersected the ruler. By subtracting the reading from the known CGC the camber or deflection could be determined. Figure 6.3 shows a picture of the process. Each reading was made with a new piece of fishing line.

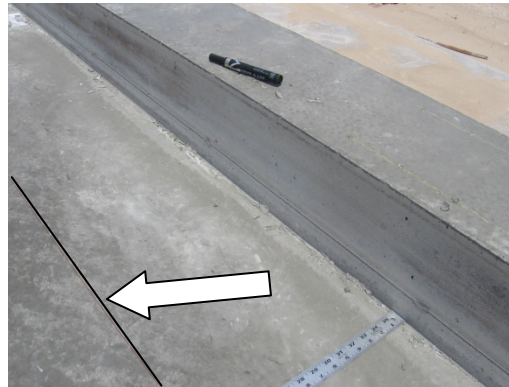
This process, however, was determined to be fairly inaccurate. The difference in measured and predicted values was as high as 3 mm (0.125-in.) per reading and approximately 300% different from theoretical. Lack of precision offered by the ruler, human error on determining the exact location of the CGC at each end, and lack of sufficient stiffness in the tension line could cause such a large discrepancy. It is recommended that a more precise method is implemented for future research.



a.) Fishing Line with Tensile Strength of 0.22 kN (50 lbs) Tensioned at CGC on Right Side of HSC Beam



b.) Fishing Line with Tensile Strength of 0.22 kN (50 lbs) Tensioned at CGC on Left Side of HSC Beam



c.) Ruler Incremented at 1.6 mm (0.063-in.) Placed at Mid-Span of HSC Beam

Figure 6.3. Tensioned-Wire System for Deflection.

6.3.4. Precise Surveying System. After the bridge erection, it was no longer feasible to use a tensioned-wire system for determining beam camber and deflection. A precise survey system was used for later-age serviceability monitoring of the bridges. This system utilized a laser based Leica TCA 2003 model total station, sets of prisms, levels, and steel plates that were attached to the underside of the bridge at predetermined locations with epoxy. The prisms are attached to the steel plates and a base line reading is made with the survey equipment. Additional readings are taken with the laser based system at different loadings and times of the day to monitor effects of temperature and

load on the bridge. The system determines the difference between the original and the new readings to monitor the total camber or deflection. Figure 6.4 displays the precise surveying system at HSC Bridge site.



Figure 6.4. Precision Surveying System.

6.4. DATA ACQUISITION

6.4.1. Data Acquisition System. The DAS was designed and built by research faculty at Missouri S&T at the Civil Engineering Department. It was designed to have ample channels for VWSGs in the project and any addition sensors required for the project. The components of the DAS were provided by Campbell Scientific, Inc. of Logan, UT.

Each bridge had one DAS box. Within each box there was a CR1000 measurement and control system, an AVW200-series 2-channel vibrating wire spectrum analyzer module, two AM16/32B relay multiplexers, and a PS100 and CH100 power supply and charging regulators with a 12 volt thermals adapter. Data were downloaded

from the DAS via a laptop with an integrated software package. Figure 6.5 shows the DAS configuration.

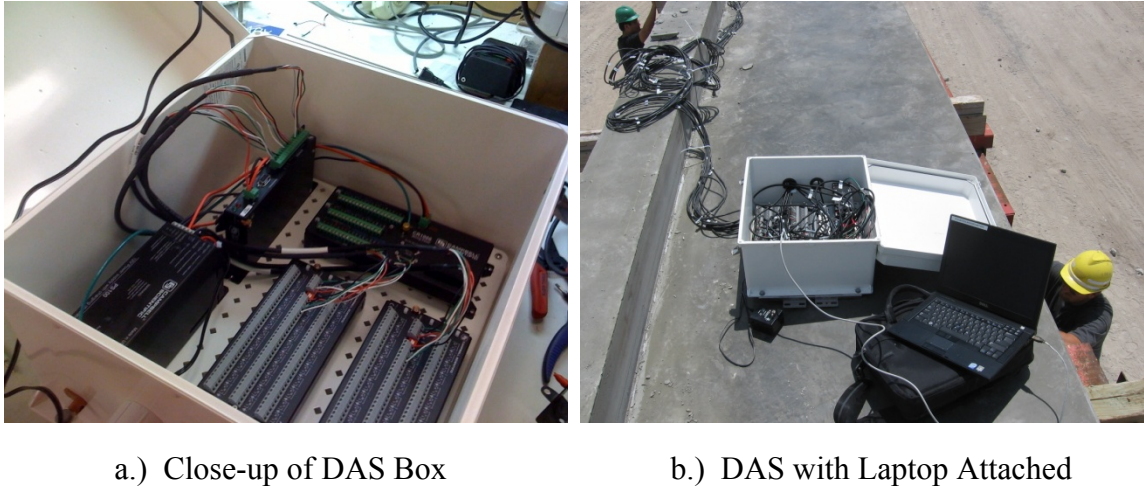


Figure 6.5. Data Acquisition System.

During placing of the beams, 10 VWSGs were connected to each DAS system. When the deck panels were ready to be placed, the DAS systems were disconnected and connected into the VWSGs for the fabrication of the deck panels. Each DAS monitored 6 VWSGs. When the structural components were ready to be transferred, the DAS was connected to the 10 sensors within the beam to monitor the effects of transportation related strains. After bridge erection, the DAS was mounted on the side of each bridge and connected to all 16 VWSGs. A solar panel was mounted as well to provide power to the system. The final configuration of each DAS is illustrated in Figure 6.6.

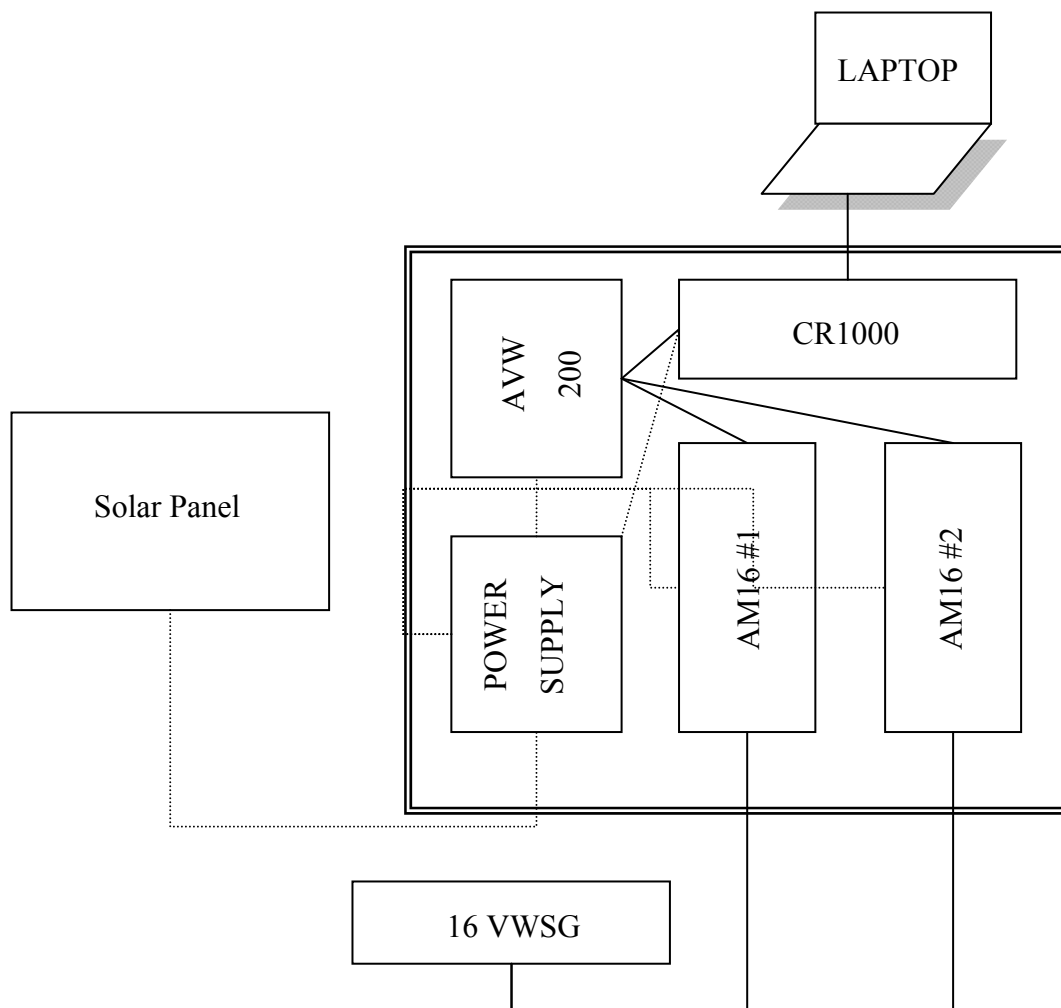


Figure 6.6. DAS Components & Gauges for Each Bridge.

6.4.2. Programming and Data Collection. A personal computer and LoggerNet software supplied with the Datalogger were used for programming the DAS for collecting and storing the data. A personal computer was used to write any new software required for the DAS to change the number of sensors and reading interval. For example, when the beams were originally fabricated the sensors were told to read at 60 second intervals. After the bridge erection, however, the interval was decreased to reading every 10 minutes. Figure 6.7 displays the DAS system being programmed at the precast plant. In addition, a sample program written for the gauges and channels is displayed in Appendix B.



Figure 6.7. Data Acquisition System being Programmed at Precast Plant.

6.5. INSTRUMENTATION PLAN

6.5.1. Instrumentation Gauges and Equipment. Table 6.2 lists and describes the instrumentation, equipment, and gauge types are used in this project. In total, 32 VWSGs were used in the beams and decks. Two DASs were used to monitor both bridges. The VWSGs provided both the strain and temperature profiles within the beams and deck panels. A tensioned-wire system was used to determine early-age camber and deflection measurements. After erection, precise surveying was used for later-age serviceability measurements.

Table 6.2. List of Instrumentation System & Gauges.

Equipment and Gauges	Quantity	Description
DAS	2	Acquires data from sensors
VWSG with built-in thermistors	32	Monitors strain and temperature
DEMEC strain gauge	1	Monitors strain
Tensioned-wire deflection system	2	Monitors early-age camber and deflection
Precise surveying system	1	Monitors later-age camber and deflection

6.5.2. Location of Instrumentation. Figure 6.8 and 6.9 illustrate the cluster locations of the sensors within the beams and deck panels. Each span is denoted with an “A” or a “B”. The “A” represents the deck panels which were reinforced with mild steel reinforcement. The span denoted “B” represents the deck panels which were reinforced with a GFRP.

Figures 6.10 and 6.11 display the location of the sensors within the beams and deck panels respectively. The VWSGs were placed within the beam at each location of prestressing steel. The VWSGs within the deck panels were placed close to the center of the deck. At this location, the sensors were tied in the middle and 40 mm (1.5-in.) from the top and bottom of the deck panel. In addition, the top and bottom sensors were oriented in the lateral direction of the bridge to measure the flexural strains. The middle sensor was oriented in the longitudinal direction of the bridge to measure the strains caused by temperature and shrinkage.

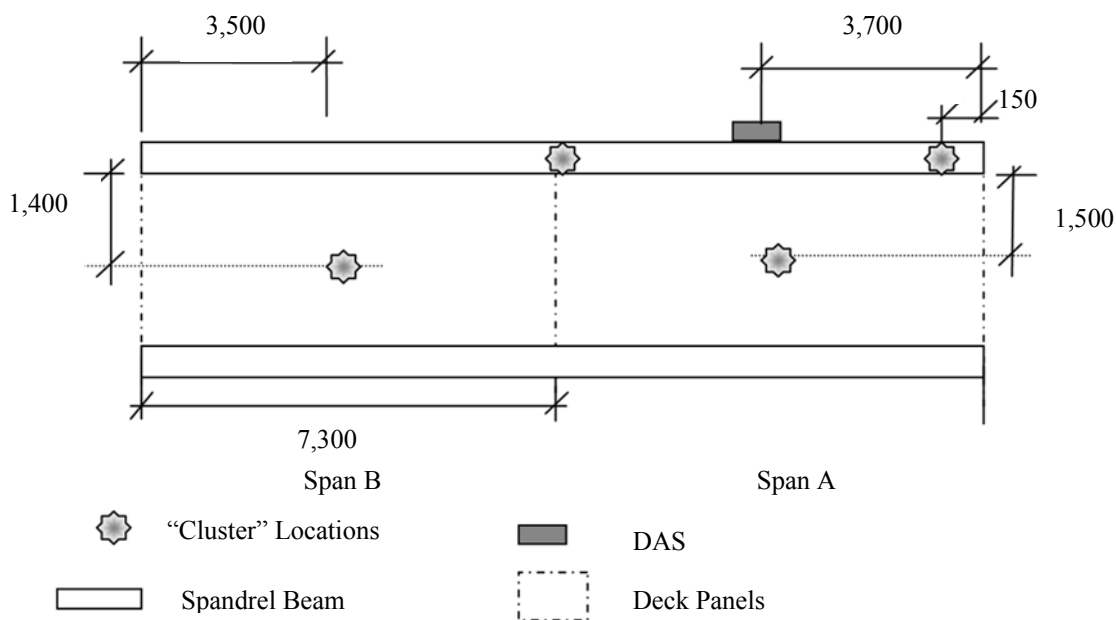
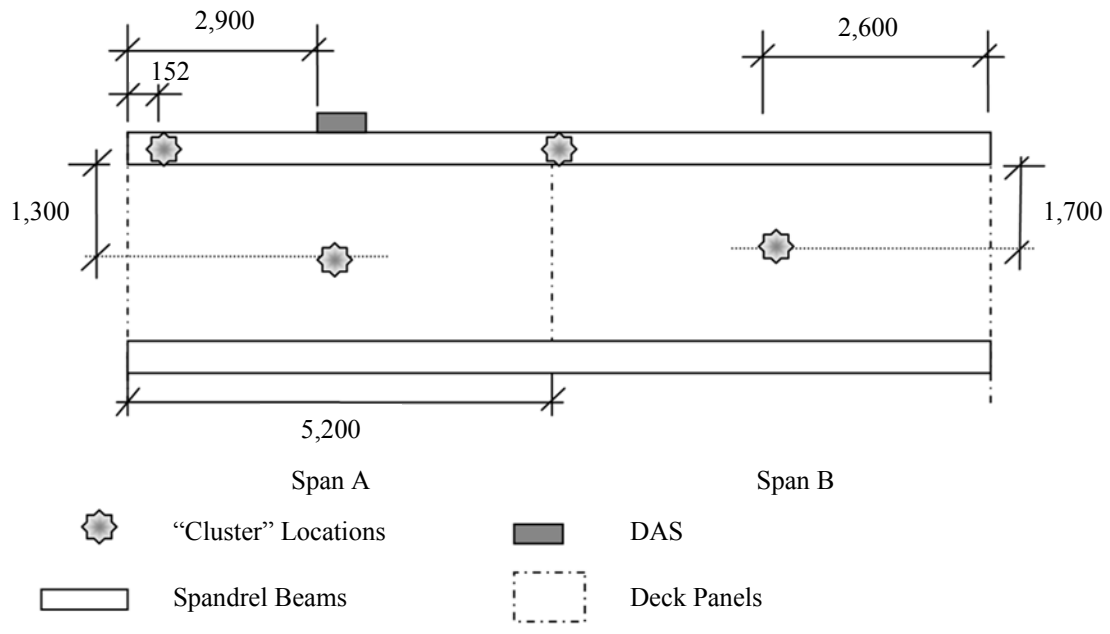
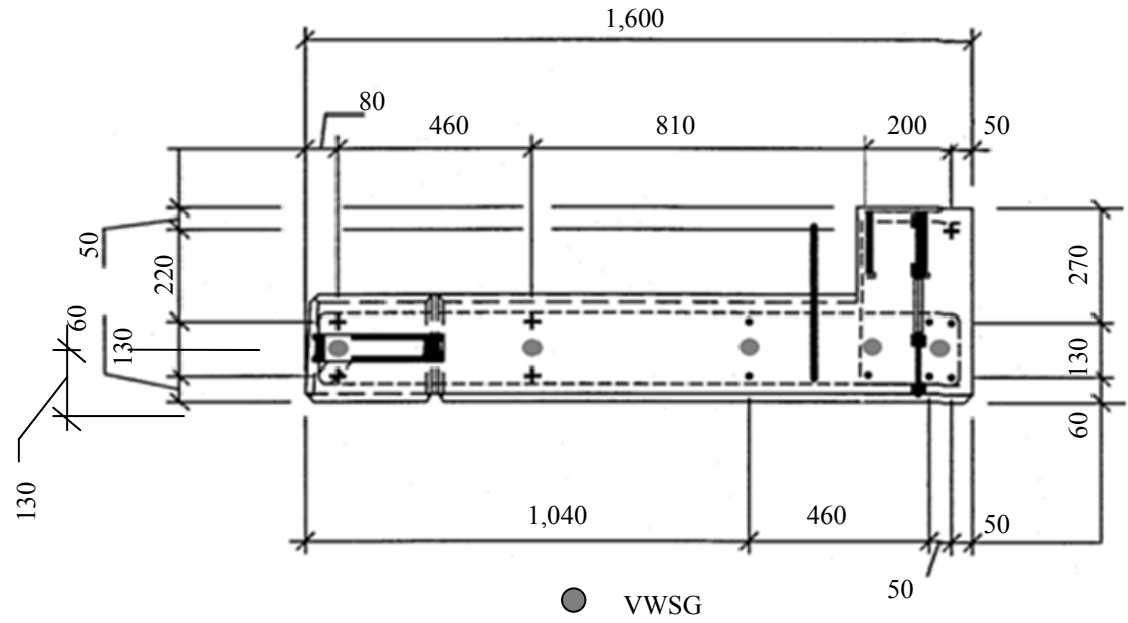


Figure 6.8. Plan Illustrating HSC Instrumentation “Cluster” Locations (Plan View).



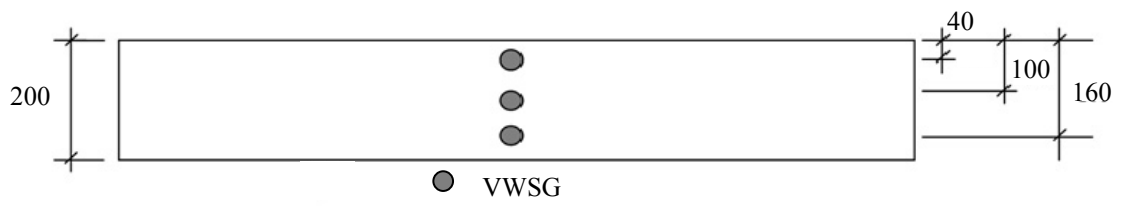
Units: mm (1 mm = 0.03937-in.)

Figure 6.9. Plan Illustrating HS-SCC Instrumentation "Cluster" Locations (Plan View).



Units: mm (1 mm = 0.03937-in.)

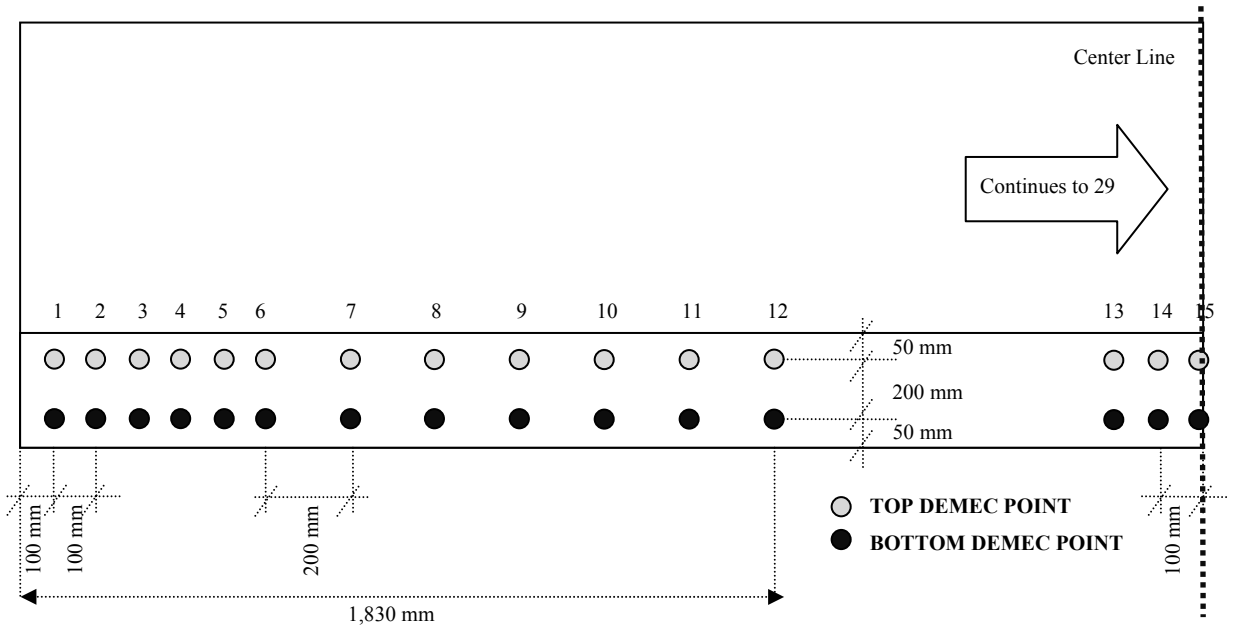
Figure 6.10. Location of Sensors along Cross Section of Beams.



Units: mm (1 mm = 0.03937-in.)

Figure 6.11. Location of Sensors along Cross Section of Deck Panels.

DEMEC strain gauges were used to determine the early-age strain and transfer length of the bridge beams. Within 20 hours of the beams being placed, the DEMEC points were mounted on the side of the beams. The location and numbering of the DEMEC points are displayed in Figure 6.12.



Units: mm (1 mm = 0.03937-in.)

Figure 6.12. Location of DEMEC Points.

The DEMEC system worked best for determining the strain in the shrinkage and creep specimens. The DEMEC points applied to the beams did not work optimally. This is due largely to the epoxy used on the beams. Due to the ambient and concrete hydration temperatures of the concrete, many DEMEC points debonded or shifted leading to no data or inaccurate data. This issue was attributed to the poor performance of the epoxy used at the precast plant.

6.5.3. Gauge Numbering and Identification. Table 6.3 summarizes the instrumentation used within the bridge beams and decks. The location of each sensor is specified as well.

Table 6.3. Gauge Identification Designations.

Gauge Identification Code		Description	Location from Top Fiber
HSC	HS-SCC		
CB-S1	SB-S1	Located near the support	80 mm (3-in.)
CB-S2	SB-S2		540 mm (21-in.)
CB-S3	SB-S3		1,040 mm (41-in.)
CB-S4	SB-S4		1,350 mm (53-in.)
CB-S5	SB-S5		1,550 mm (61-in.)
CB-M1	SB-M1	Located at the mid-span of the beam	80 mm (3-in.)
CB-M2	SB-M2		530 mm (21-in.)
CB-M3	SB-M3		1,040 mm (41-in.)
CB-M4	SB-M4		1,350 mm (53-in.)
CB-M5	SB-M5		1,550 mm (61-in.)
CS-A1	SS-A1	At mid-span of deck panel reinforced with mild steel	40 mm (1.5-in.)
CS-A2	SS-A2		100 mm (4-in.)
CS-A3	SS-A3		160 mm (6.5-in.)
CS-B1	SS-B1	At mid-span of deck panel reinforced with GFRP	40 mm (1.5-in.)
CS-B2	SS-B2		100 mm (4-in.)
CS-B3	SS-B3		160 mm (6.5-in.)

6.6. PREPARATION AND FIELD INSTALLATION

6.6.1. Vibrating Wire Strain Gauge Preparation. All of the gauges were prepared at Butler-Carlton Civil Engineering Hall Electronics Technician's Lab at Missouri S&T prior to field installation. To prepare for field installation, the internal components of each DAS was mounted into the correct box and wired together. The VWSGs were given an identification code and labeled accordingly for the location in the beam or deck panel.

6.6.2. Field Installation. The sensors were connected to the precast spandrel beams and monitored by the DAS during fabrication, transportation, erection, and service of the bridges. Whereas, the sensors were connected to the precast deck panels and monitored by the DAS during fabrication and service of the bridges.

6.6.2.1 Prestressed precast beams. The day before the beams were cast, the VWSG were installed after the prestressing strands had been tensioned. Two DASs were used to monitor the two beams. The VWSGs were installed at their corresponding locations by using zip ties on the prestressing strands above and below their locations. Figure 6.13 displays images and of the VWSGs within the beam. In addition, a representative schematic is shown for the VWSGs centered between tendons in Figure 6.13. Because the wire length was 12.2 m (40 ft), the DAS could be moved if required.

Early in the morning the following day, before the strands were detensioned, DEMEC points were outfitted on the beams to monitor early-age strain and transfer length. After the epoxy set, an initial reading was taken. Figure 6.14 shows the DEMEC points on the beams.

Twenty-four hours after placing the concrete, the precast, prestressed beams were detensioned and the steel forms were stripped. At this moment, the sensors had to be disconnected from the DAS. This had to be done to allow for the wires to move out of the forms with the beam. Immediately after the forms were removed, the sensors were reconnected to the DAS for continued monitoring. In addition, a second reading was taken of DEMEC points to determine the transfer length.

Coreslabs Structures, Inc. took care to ensure that a power supply was close to the beams to give keep the DAS plugged in while at the precasting yard. This allowed for the bridge beams to be monitored during sand blasting and storage. The DAS was

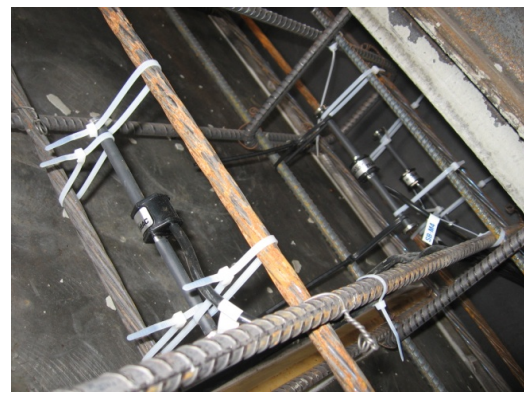
disconnected when the precast deck panels were ready to be fabricated. Site storage of the beams can be seen in Figure 6.15.



a.) VWSGs at Support



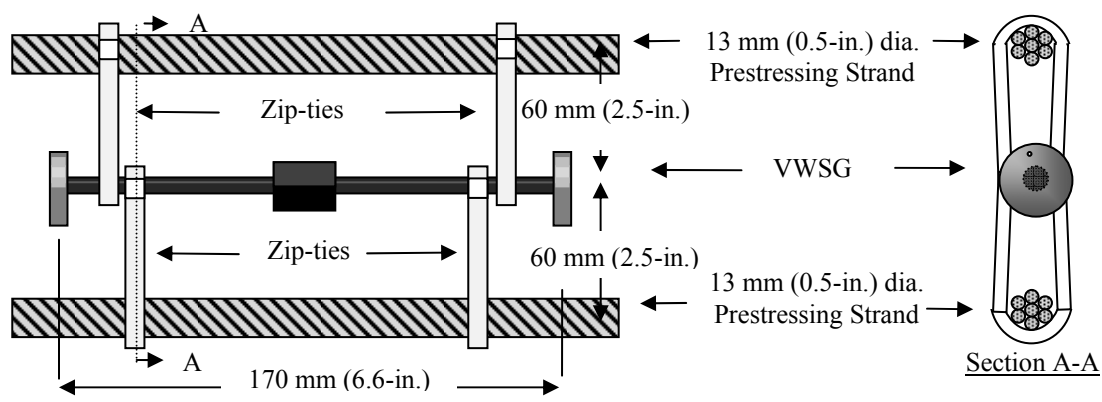
b.) VWSGs at Mid-Span



c.) VWSGs Attached to Prestress Strands



d.) VWSG Wire Conduit Exit



e.) Schematic of VWSGs Attached to Prestress Strands

Figure 6.13. VWSGs in Beams at Fabrication in Marshall, MO.



a.) DEMEC Points on Beam



b.) DEMEC Reading with Gauge

Figure 6.14. DEMEC Reading.



a.) Sand-Blasted Side of Spandrel Beam Storage



b.) Non-Sand-Blasted Side of Spandrel Beam Storage

Figure 6.15. Beam Storage at Marshall, MO.

6.6.2.2 Precast deck panels. The day before the concrete deck panels were fabricated, the beam sensors were disconnected from the DAS. The VWSGs were tied off to the top and bottom reinforcement and suspended in the middle to provide the necessary monitoring profile at the middle depth of the deck panel. A schematic is presented in Figure 6.16 to illustrate the method which the VWSGs were tied to the

reinforcement. The images of the VWSG locations are displayed in Figure 6.17. In some situations, additional steel was added to the bridge deck panels to provide a location to attach the VWSGs. A hole was cut into the side of the forms to allow for the gage wire to be connected to the DAS. In addition, the wire leading to the exit on the forms were zip tied to the reinforcement to keep the wire from protruding from the top and bottom of the deck panels. To ensure that the wire would exit from the bottom of the deck panel in an efficient fashion and avoid being pinched, a PVC pipe filled with installation and duct tape was used. Figure 6.18 shows the method used to keep the wire on the bottom of the slab.

Seventy-two hours after the deck panels had been placed, the forms were removed. Once again, the sensors had to be unhooked from the DAS to allow them to be pulled out of the forms. Immediately after the forms were removed, the DAS was re-connected to the VWSGs for continued monitoring.

Coreslabs Structures, Inc. ensured a power supply was supplied to keep the DAS charged while in storage. The storage of the beams is shown in Figure 6.19.

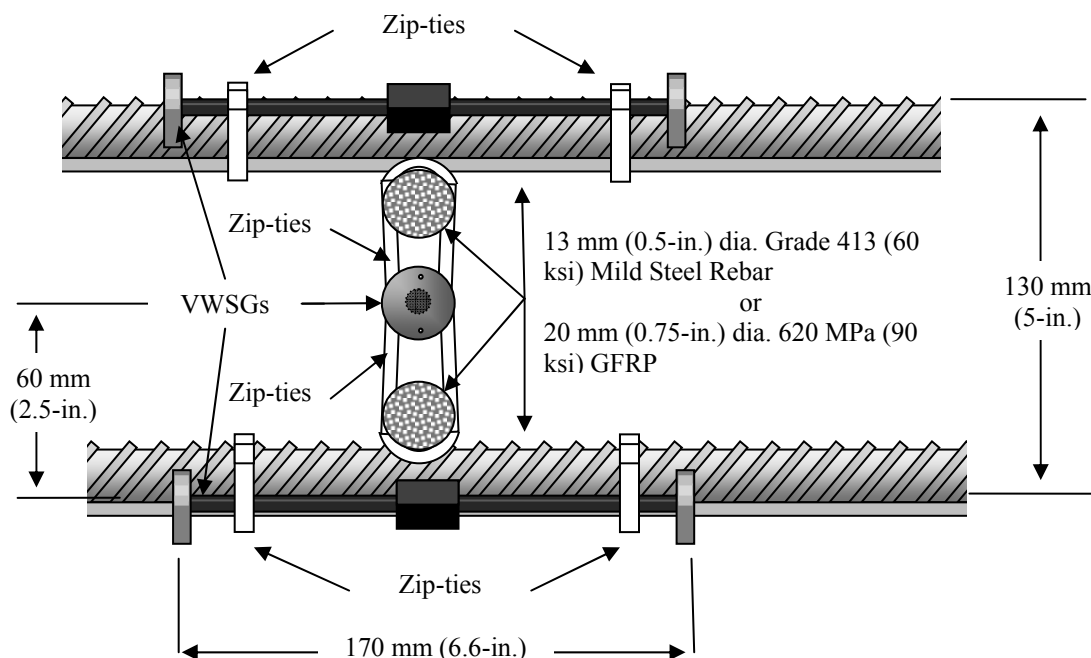
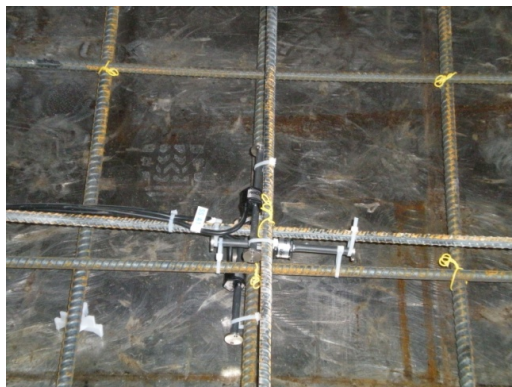


Figure 6.16. Schematic of VWSGs Attached to Deck Panel Reinforcement.



a.) HSC Mild Steel VWSG Arrangement



b.) HS-SCC Mild Steel VWSG Arrangement



a.) HSC GFRP VWSG Arrangement



b.) HS-SCC GFRP VWSG Arrangement

Figure 6.17. VWSG Embedded in Panels.



a.) Before Concrete Placement



b.) After Concrete Placement & Form Removal

Figure 6.18. Method Used to Free VWSG Wires.



Figure 6.19. Precast Deck Panel Storage at Marshall, MO.

6.6.2.3 Instrumentation during shipping and erection. A day before the structural components were transported to Rolla, MO, the DAS system was disconnected from the deck panels and connected to the spandrel beam VWSGs to monitor the beam strains during transportation and erection.

During erection, the DAS was strapped to the beams and lifted with a crane into the final erected position. This is shown in Figure 6.20. After the bridge had been erected, the spandrel beams and deck panels were connected to the DAS. However, a few days later, PVC pipes were outfitted under the bridge to provide permanent protection and cover for the wires to protect them from being damaged. In addition, the DAS was mounted to the side of the bridge with a solar panel. Images of the PVC pipes and the mounted DAS can be seen in Figure 6.21.



a.) Strapping & Securing of the DAS Box



b.) Lifting of Spandrel Beam with DAS Box Attached

Figure 6.20. DAS during Bridge Erection.



a.) Mounted DAS on Side of Bridge



b.) DAS & PVC VWSG Conduit

Figure 6.21. Final DAS System Attached to Bridges.

6.7. PROBLEMS ENCOUNTERED

The installation of the instrumentation went reasonably well. However, due to a few unforeseeable occurrences, problems arose.

The original instrumentation plan involved the use of load cells to determine the early-age prestress losses. Before the research team arrived at the precast plant, the fabricator had pre-tensioned the tendons.

As was mentioned previously, due to the fabrication of the beams, conventional tensioned-wire deflection was not possible to determine early-age camber and deflection. The theoretical CGC was utilized for baseline deflection and camber readings which did not provide the same level of accuracy as measuring deflection and camber with a measured baseline. Furthermore, the fishing line used to determine the beam deformation proved to be less accurate than the conventional tension-wire system due to lack of ruler precision, human error on determining the exact location of the CGC, and lack of stiffness in the fishing line.

During transportation and erection of the beams, several of the sensors produced nonsensical results or “noise” due to the large movement and vibration of the beams during shipment. However, after the beams were placed, the sensors functioned adequately.

It was determined that the solar panels have worked very well for the HS-SCC bridge because of its location and aptness for receiving adequate sunlight. However, it was determined that the HSC bridge did not receive adequate sunlight due to large tree cover. Anytime the voltage becomes lower than 9 volts, the DAS does not function. After learning of this issue and losing some data, a second battery was purchased. The second battery is utilized any time the charge becomes low on the HSC bridge. The voltage is monitored once a month when the data is retrieved from the DAS to a laptop. The battery charge of the bridge has not been an issue since the reading rate was lowered from once a minute to every ten minutes. Since February of 2010, no data has been lost.

7. MATERIAL TEST RESULTS AND DISCUSSION

7.1. INTRODUCTION

Material tests began after the bridge beams were fabricated on July 30, 2009 in the Construction Materials and Structural Engineering Research Laboratories in Butler-Carlton Civil Engineering Hall at Missouri S&T in Rolla, MO. The tests completed include compressive strength, modulus of elasticity, modulus of rupture, splitting tensile strength, creep, shrinkage, tensile strength of GFRP and modulus of elasticity of GFRP as summarized in Section 5. Section 7 presents and discusses the results of the tests. Error bars presented for each test result data set are for one standard deviation.

7.2. COMPRESSIVE STRENGTH

The test results for the linear average compressive strength for the HSC and HS-SCC are presented in Figure 7.1 and 7.2 respectively. On average, the compressive strength of the HSC was higher than that of HS-SCC. HSC had an average release strength of 46.6 MPa (6,760 psi) and an average 28 day strength of 84.3 MPa (12,230 psi). HS-SCC had a slightly lower average release strength of 44.8 MPa (6,500 psi) and an average 28 day strength of 69.8 MPa (10,130 psi). The compressive strength can vary for HSC and HS-SCC depending on the aggregate type and shape, w/cm ratio, and type of additives in the concrete (MacGregor, 2009). The addition of softer limestone aggregate, higher w/cm, and air entrainment is a reason for the slightly lower strength in HS-SCC. The HSC compressive strength was slightly higher due to the addition of stiffer granite aggregate, lower w/cm ratio, and lack of air entrainment.

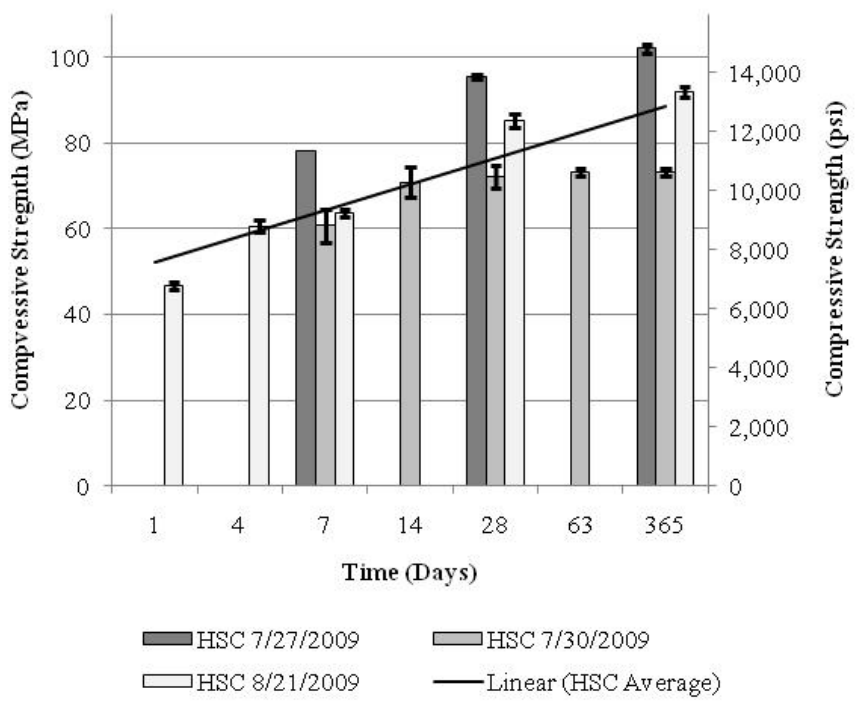


Figure 7.1. HSC Average Compressive Strength.

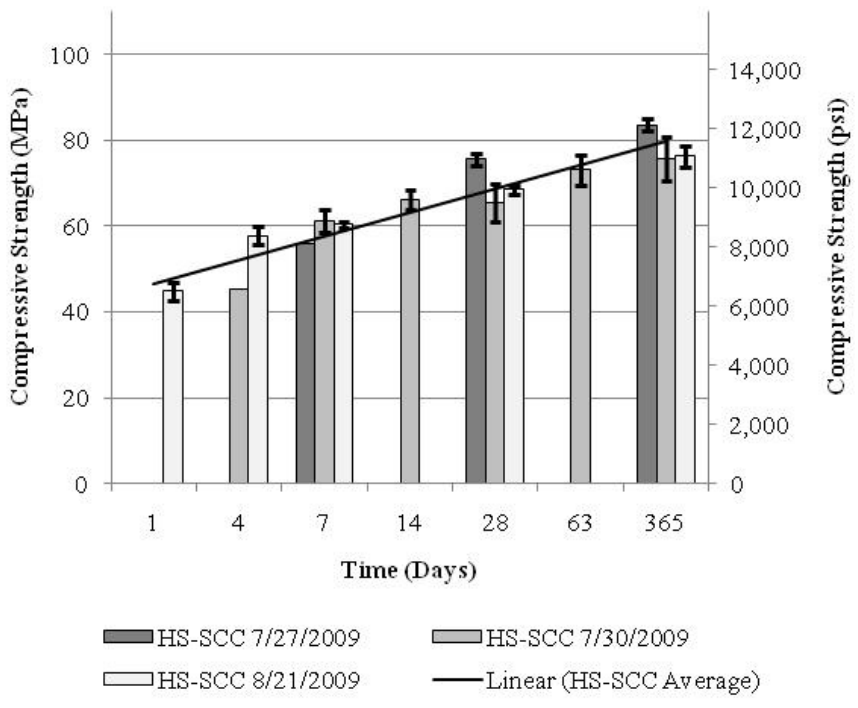


Figure 7.2. HS-SCC Average Compressive Strength.

7.3. MODULUS OF ELASTICITY

The average modulus of elasticity of the HSC and HS-SCC mixtures are presented in Figure 7.3. The average modulus of elasticity of HSC at 28 days was measured 31.3 GPa (4,540 ksi) and HS-SCC at 28 days was measured 33.6 GPa (4,870 ksi). On average the mix with the highest percentage of stiffer coarse aggregate, such as the granite coarse aggregate in the HSC mix, should have a higher modulus of elasticity of the concrete when compared to a mix with smaller percentage of softer coarse aggregate, such as the limestone in HS-SCC (MacGregor, 2009). However, if too stiff of aggregate is used within a mixture, it has been found that stress concentrations can decrease the performance of the concrete (Myers, 1999). These factors may have contributed to the lower than average modulus of elasticity results found for both the HSC and HS-SCC mixture when compared to ACI empirical relationships for high-strength and normal strength concrete.

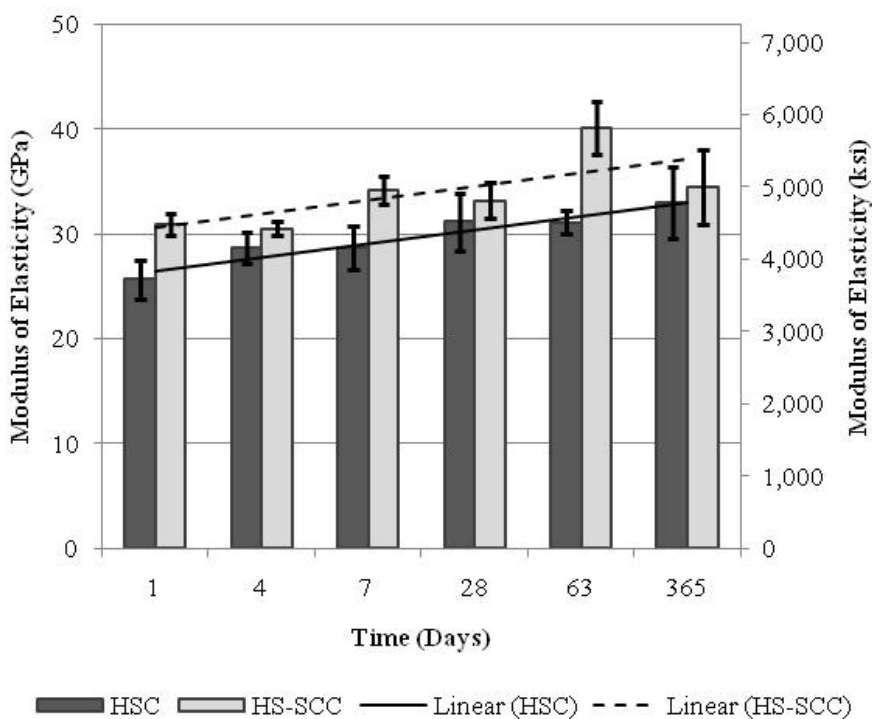


Figure 7.3. Average Modulus of Elasticity for HSC & HS-SCC.

In Figures 7.4 and 7.5, the modulus of elasticity test results for HSC and HS-SCC are compared to current empirical relationships from ACI 318 (2008) for conventional concrete and ACI 363 (Equation 6-5 in ACI 363R-10 and ACI 363-97) for HSC displayed in equations 3, 4, and 5 consecutively. Measured material properties were used within these empirical models. In equations below, E_c is modulus of elasticity (psi), f'_c is compressive strength (psi), w_c is the unit weight of the concrete (lbs/ft³), k_1 is a variable for aggregate type (1.2 for crushed limestone, calcined bauxite aggregates; 0.95 for crushed quartzite, crushed andesite, crushed basalt, crushed clay slate, and crushed cobblestone aggregates; 1.0 for other coarse aggregates), and k_2 is a variable for mineral admixtures (0.95 for silica fume, slag cement, fly ash fume; 1.10 for fly ash; 1.0 for any other type of mineral admixture). For this research project, the values for k_1 were equal to 1.0 for HSC and 1.2 for HS-SCC due to the aggregate type. In addition, the k_2 values varied between 0.95 for HSC due to the silica fume in the mixture and 1.10 for the HS-SCC because of the addition of fly ash. It is evident that the test results were found to be lower than those predicted by all of the empirical relationships. However, from the empirical relationships presented, the ACI 363R (2010) Equation 6-5, presented in equation 4, fit the HSC data the best. The HS-SCC data fit best to the ACI 363 (1997) empirical relationship presented in equation 5.

$$E_c = w_c^{1.5} 33 \sqrt{f'_c} \quad (\text{psi}) \quad (\text{ACI 318-08}) \quad (3)$$

$$E_c = 4.86 * 10^6 k_1 k_2 \left(\frac{w_c}{150} \right)^2 \left(\frac{f'_c}{8700} \right)^{1/3} \quad (\text{psi}) \quad (\text{ACI 316-10}) \quad (4)$$

$$E_c = 40,000 \sqrt{f'_c} + 10^6 \quad (\text{psi}) \quad (\text{ACI 363-97}) \quad (5)$$

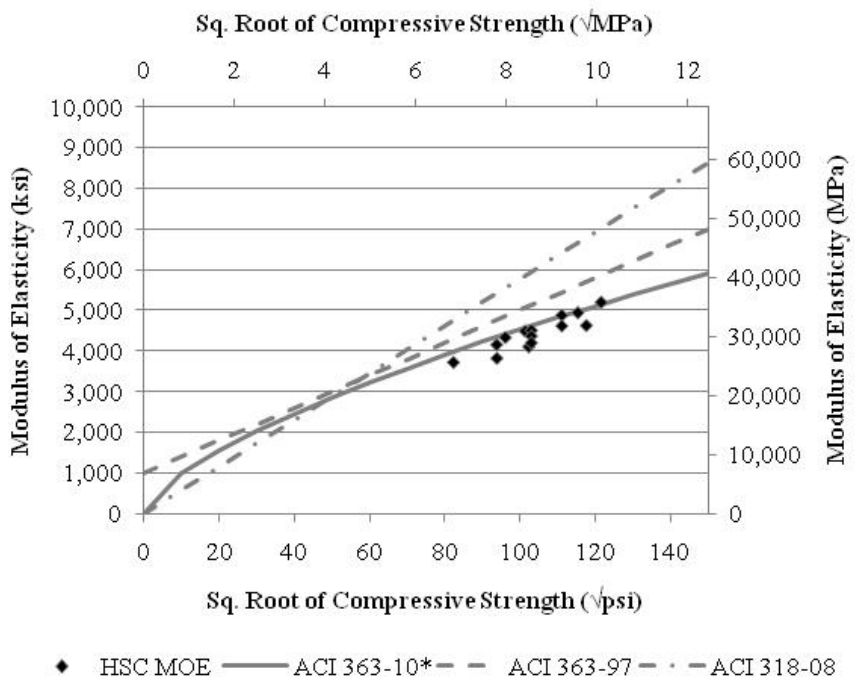


Figure 7.4. Modulus of Elasticity vs. Compressive Strength for HSC.

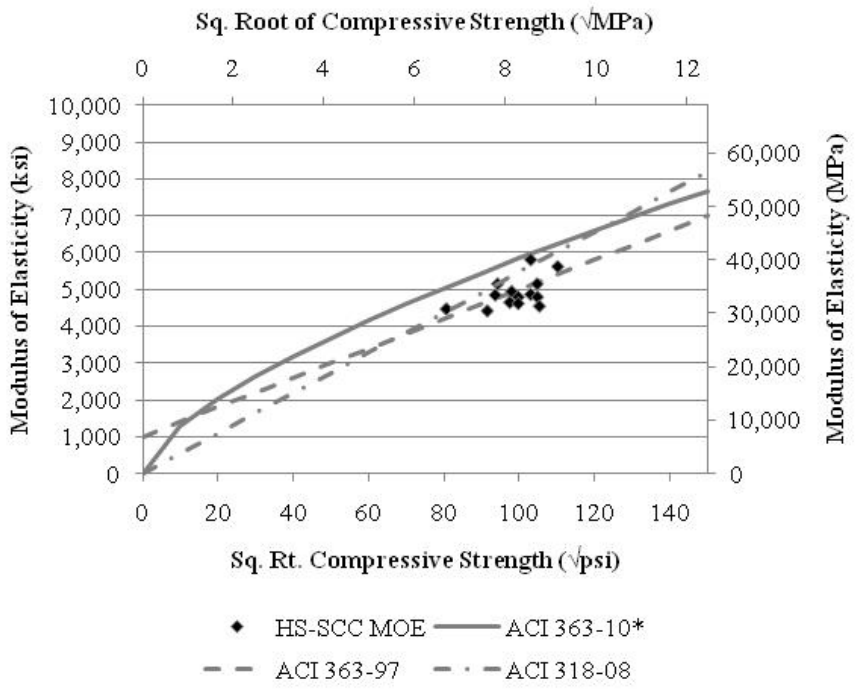


Figure 7.5. Modulus of Elasticity vs. Compressive Strength for HS-SCC.

7.4. MODULUS OF RUPTURE

Figure 7.6 presents the average modulus of rupture for both HSC and HS-SCC. In addition, Figures 7.7 and 7.8 illustrates the results obtained from the modulus of rupture tests on the HSC and HS-SCC samples. Two equations used to predict the modulus of rupture that are recommended by ACI 318 (2008) for conventional concrete and ACI 363R (2010) for HSC are presented in equation 6 and 7 consecutively. In the equations below, f_r is the flexural tensile strength (psi) and f_c' is the compressive strength (psi).

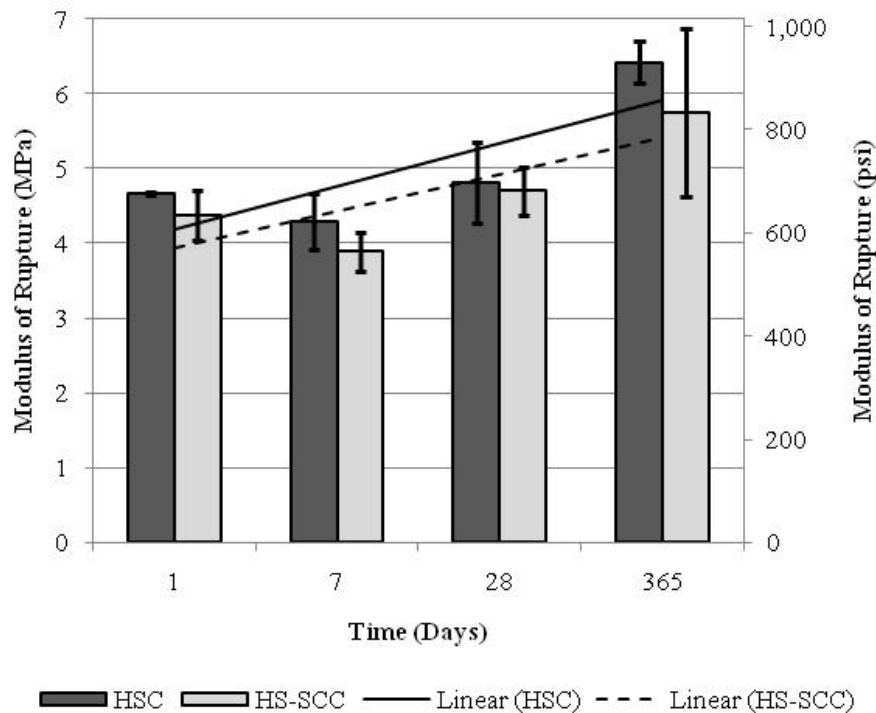


Figure 7.6. Average Modulus of Rupture for HSC & HS-SCC.

$$f_r = 7.5\sqrt{f_c'} \text{ (psi) (ACI 318-08)} \quad (6)$$

$$f_r = 11.7\sqrt{f_c'} \text{ (psi) for } 3,000 \text{ psi} < f_c' < 12,000 \text{ psi (ACI 363R-10)} \quad (7)$$

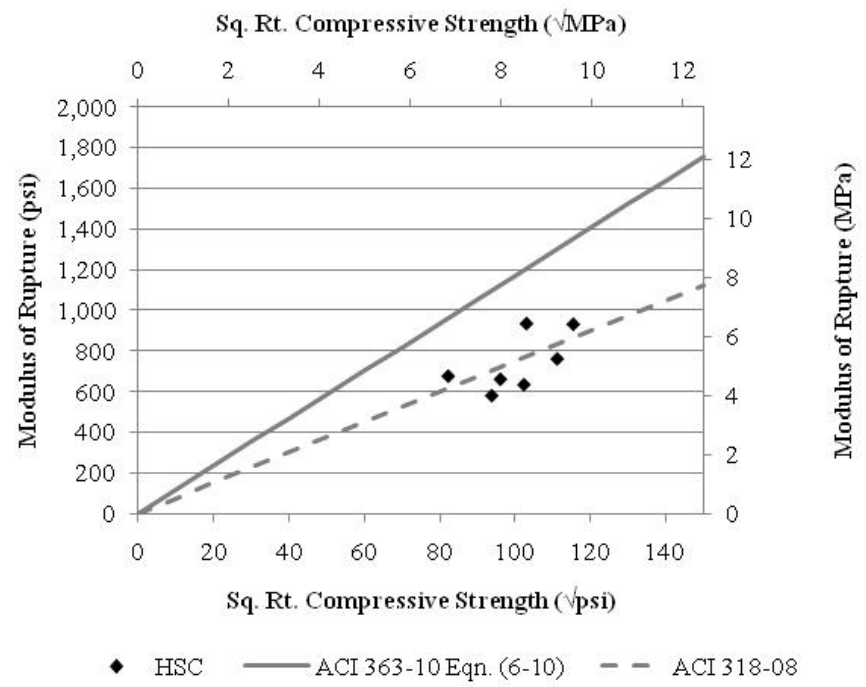


Figure 7.7. Modulus of Rupture vs. Compressive Strength for HSC.

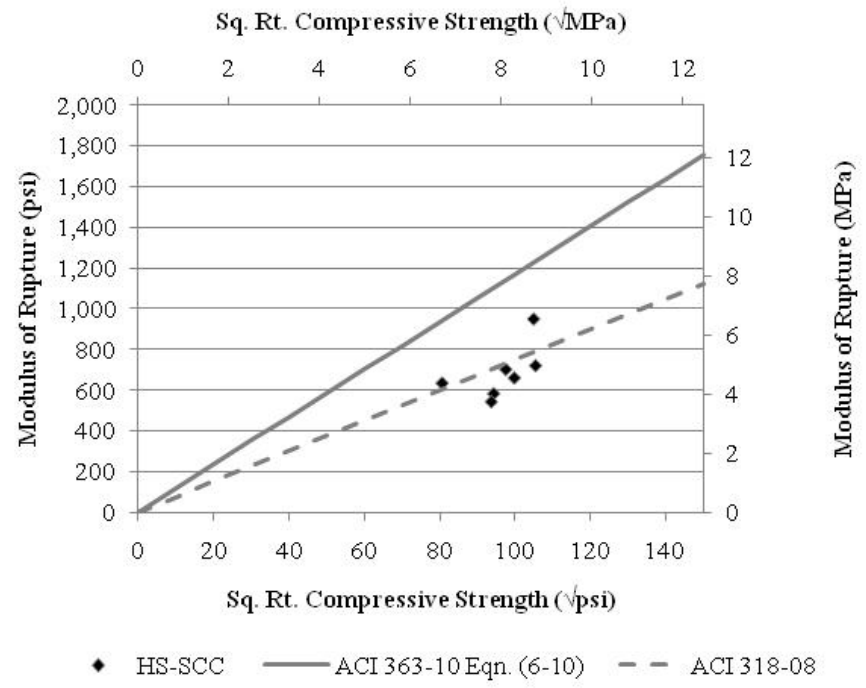


Figure 7.8. Modulus of Rupture vs. Compressive Strength for HS-SCC.

The modulus of rupture of HSC at 28 days was 4.8 MPa (700 psi) which was slightly higher than the modulus of rupture of HS-SCC at 28 days of 4.7 MPa (680 psi). However, the differences are not statistically significant. Any variability in modulus of rupture strength can be attributed to variability in coarse aggregate type and size between the HSC and HS-SCC mixes (MacGregor, 2009).

In Figures 7.7 and 7.8, the results obtained are compared to the empirical relationships. The results obtained are much lower than that predicted for HSC. However, from the data obtained, it appears that the ACI 318 (2008) expression for modulus of rupture for conventional concrete displayed in equation 6 is closest to the data. The lower modulus of rupture values can be attributed to the smaller size of coarse aggregate and type of coarse aggregate present in the mixture (ACI 363R, 2010).

7.5. SPLITTING TENSILE STRENGTH

In addition to running modulus of rupture tests, split cylinder tests were completed to determine the tensile strength of HSC and HS-SCC. The average results from testing are presented in Figure 7.9. Three equations used to predict the splitting tensile strength of concrete included two empirical models presented for HSC in ACI 363 and one for conventional concrete in ACI 318. Equation 8 and 9 are splitting tensile strength empirical models presented in ACI 363 (2010) for HSC with equation 8 composed by Myers and Carrasquillo for HSC member cured cylinders with Dolomitic Limestone coarse aggregate. Equation 10 is utilized for determining the splitting tensile strength of conventional concrete as presented in ACI 318 (2005). In the equations below, f_{ct} is the splitting tensile strength (psi) and f_c' is the compressive strength (psi). The results from these tests are illustrated in Figures 7.10 and 7.11 for HSC and HS-SCC respectively.

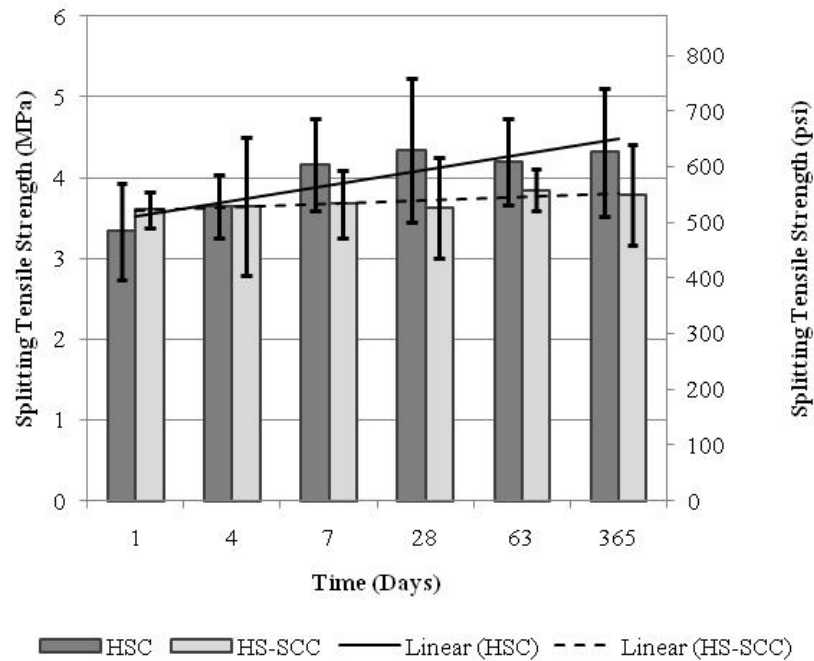


Figure 7.9. Average Splitting Tensile Strength of HSC & HS-SCC.

The split tensile strength of HSC at 28 days was 4.4 MPa (640 psi) which was slightly higher than the split tensile strength of HS-SCC at 28 days of 3.6 MPa (530 psi) at 28 days. Due to the high and overlapping standard deviation of mixtures, any differences in results between HSC and HS-SCC are not statistically significant. Any variability in splitting tensile strength can be attributed to variability in coarse aggregate type and size between the HSC and HS-SCC mixtures (MacGregor, 2009).

$$f_{ct} = 8.66\sqrt{f'_c} \text{ (psi) Member-Cured (Dolomitic Limestone) (ACI 363R-10)} \quad (8)$$

$$f_{ct} = 7.4\sqrt{f'_c} \text{ (psi) for } 3,000 \text{ psi} < f'_c < 12,000 \text{ psi (ACI 363R-10)} \quad (9)$$

$$f_{ct} = 6.7\sqrt{f'_c} \text{ (psi) (ACI 318-05)} \quad (10)$$

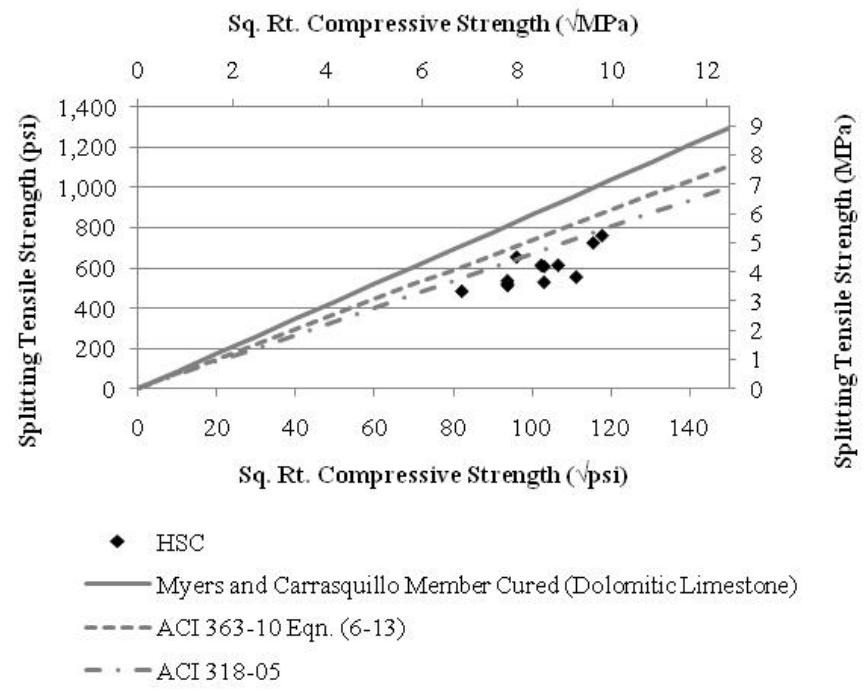


Figure 7.10. Splitting Tensile Strength vs. Compressive Strength of HSC.

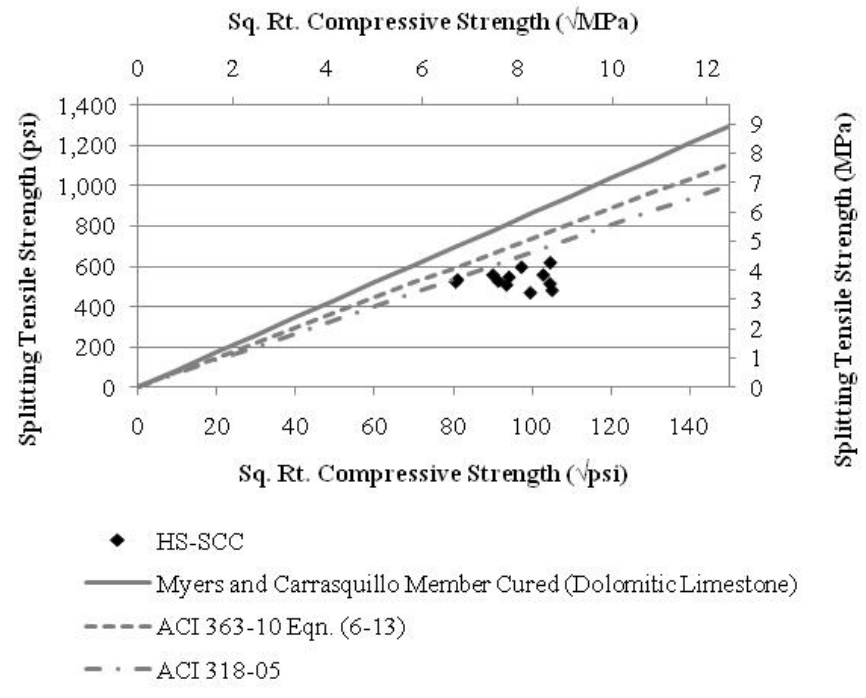


Figure 7.11. Splitting Tensile Strength vs. Compressive Strength of HS-SCC.

All of the relationships overestimated the splitting tensile strength of both HSC and HS-SCC. The empirical relationship in ACI 318 (2005), shown in equation 9, gives the closest results to the experimental data. Variables that affect the compressive strength of concrete also influence the split tension of the concrete. Variability in HSC and HS-SCC split tension strength can be dependent upon aggregate size, quantity, and type as well as w/cm and additives in the concrete. However, it has been found that as the strength of concrete increased, the splitting tensile strength tended to decrease. In a study completed by Dewar (1964), it was found that the splitting tensile strength decreased from 10% of compressive strength to approximately 5% of compressive strengths as compressive strengths increased to 84 MPa (12,100 psi) (ACI 363R, 2010).

7.6. CREEP

Creep is a continuous deformation that occurs when a constant stress is applied to a structural member. For the beam and deck panel creep specimens, the strain was measured before and after loading to determine the elastic strain. Table 7.1 provides a summary of the loads applied to the creep specimens. Tables 7.2 and 7.3 provide the creep coefficients for both HSC and HS-SCC. Tables 7.4 and 7.5 present the specific creep for both HSC and HS-SCC. In addition, Figures 7.11 illustrates the creep strain for both the HSC and HS-SCC specimens at 20 to 40% of design strength to current date.

Table 7.1. Creep Test Summary.

Material	Placement Date	ID	Design Compressive Strength	Loading Force	Stress Level
HSC HS-SCC	7/30/2009 8/21/2009	C1	68.9 MPa (10 ksi)	111.2 kN (25 kips)	27.4 MPa (4 ksi)
HSC HS-SCC	7/30/2009 8/21/2009	C2	68.9 MPa (10 ksi)	222.4 kN (50 kips)	13.7 MPa (2 ksi)

Table 7.2. HSC Measured Creep Coefficients

Specimen ID	Placement Date	Creep Coefficient			
		7 days	28 days	56 days	180 days
C1	7/30/2009	1.12	1.21	1.31	1.55
C1	8/21/2009	1.22	1.32	1.40	1.63
C2	7/30/2009	1.16	1.29	1.39	1.62
C2	8/21/2009	1.17	1.26	1.33	1.52
Average HSC		1.17	1.27	1.36	1.58
% of Creep at 180 days		73.9	80.5	86.0	100.0
1 kN = 224.8 lbs; 1 MPa = 145.04 psi					

Table 7.3. HS-SCC Measured Creep Coefficients

Specimen ID	Placement Date	Creep Coefficient			
		7 days	28 days	56 days	180 days
C1	7/30/2009	1.23	1.48	1.64	1.99
C1	8/21/2009	1.21	1.40	1.54	1.90
C2	7/30/2009	1.25	1.47	1.65	1.96
C2	8/21/2009	1.27	1.52	1.68	1.99
Average HS-SCC		1.24	1.47	1.62	1.96
% of Creep at 180 days		63.2	74.8	82.9	100.0
1 kN = 224.8 lbs; 1 MPa = 145.04 psi					

Table 7.4. HSC Measured Specific Creep

Specimen ID	Placement Date	Specific Creep ($\mu\epsilon/\text{psi}$)			
		7 days	28 days	56 days	180 days
C1	7/30/2009	0.328	0.356	0.384	0.454
C1	8/21/2009	0.270	0.291	0.308	0.358
C2	7/30/2009	0.335	0.373	0.404	0.470
C2	8/21/2009	0.286	0.310	0.327	0.372
Average HSC		0.305	0.333	0.356	0.414
1 kN = 224.8 lbs; 1 MPa = 145.04 psi					

Table 7.5. HS-SCC Measured Specific Creep

Specimen ID	Placement Date	Specific Creep ($\mu\epsilon/\text{psi}$)			
		7 days	28 days	56 days	180 days
C1	7/30/2009	0.275	0.331	0.367	0.446
C1	8/21/2009	0.357	0.413	0.456	0.562
C2	7/30/2009	0.359	0.424	0.473	0.563
C2	8/21/2009	0.361	0.433	0.476	0.565
Average HS-SCC		0.338	0.400	0.443	0.534
1 kN = 224.8 lbs; 1 MPa = 145.04 psi					

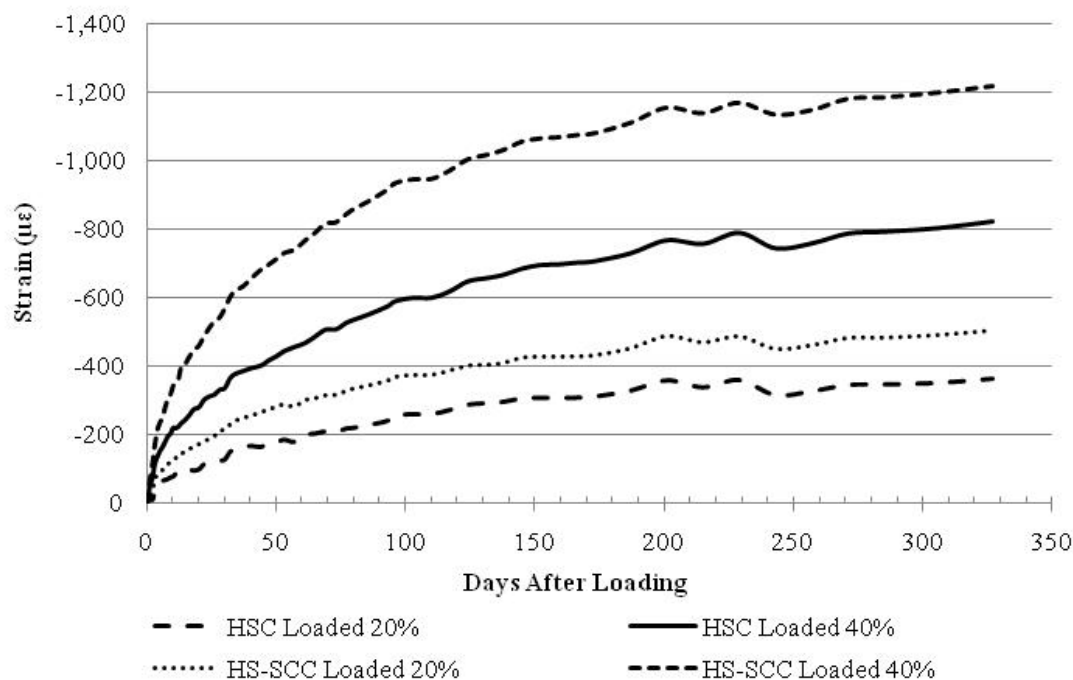


Figure 7.12. Creep Results for HSC & HS-SCC.

From the data presented in the above tables, the HS-SCC underwent a greater amount of creep than HSC. This is due to the type and amount of coarse aggregate within the respective mixtures. The HSC contained a larger percentage of the coarse aggregate of granite when compared to the percentage of the coarse aggregate of limestone in the HS-SCC mixture. Furthermore, when granite is compared to limestone it has a higher stiffness. These factors will influence the amount of creep (MacGregor, 2009).

The values of HSC and HS-SCC were compared to empirical models. The models implemented were AASHTO LRFD (2007), ACI 209 (1997), and a method recommended by NCHRP 628 for determining the creep of self-consolidating concrete.

The AASHTO LRFD (2007) model for determining creep of HSC was updated by NCHRP 426 (Tadros et. al., 2003). The empirical model is presented in equations 11 through 15. In the model, $\psi(t, t_i)$ is the creep coefficient, k_s is a factor for volume-to-surface ratio of the specimen, k_{hc} is a factor for humidity for creep, k_f is a factor for the

concrete strength, k_{td} is a factor for time development, V/S is the volume to surface ratio (in.), H is the relative humidity (%), f'_{ci} is the compressive strength at release (psi), t_i is the age (days) in which the load is applied, and t is the concrete maturity age (days).

$$\psi(t, t_i) = 1.9k_s k_{hc} k_f k_{td} t_i^{-0.118} \quad (11)$$

$$k_s = 1.45 - 0.13(V/S) \geq 1.0 \quad (12)$$

$$k_{hc} = 1.56 - 0.008H \quad (13)$$

$$k_f = \frac{5}{1+f'_{ci}} \quad (14)$$

$$k_{td} = \left(\frac{t}{61-4f'_{ci}} \right) \quad (15)$$

The ACI 209 (1997) model developed for conventional concrete creep is displayed in equations 16 through 24. In the following model, v_u is the ultimate creep and γ_{cr} is the creep correction factor. In the expression for the creep correction factor, γ_{la} is the correction factor for the age of loading, γ_λ the correction factor for ambient relative humidity, $\gamma_{V/S}$ is the correction factor for the volume to surface ratio, γ_s is the correction factor for the slump, γ_ψ is the correction factor for fine aggregate percentage, and γ_α is the correction factor for air content. Within each correction factor t_{la} is concrete age at loading (days), λ is the ambient relative humidity (%), V/S is the volume to surface ratio (in.), s is the slump (in.), ψ is the ratio of fine aggregate to total aggregate by weight (%), and α is the air content (%).

$$v_u = 2.35\gamma_c \quad (16)$$

$$\gamma_{cr} = \gamma_{la}\gamma_\lambda\gamma_{V/S}\gamma_s\gamma_\psi\gamma_\alpha \quad (17)$$

$$\gamma_{la} = 1.25(t_{la})^{-0.118} \text{ for moist cured concrete} \quad (18)$$

$$\gamma_{la} = 1.13(t_{la})^{-0.094} \text{ for steam cured concrete} \quad (19)$$

$$\gamma_\lambda = 1.27 - 0.0067\lambda \text{ for } \lambda \geq 40 \quad (20)$$

$$\gamma_{V/S} = \frac{2}{3} (1 + 1.13e^{-0.54(V/S)}) \quad (21)$$

$$\gamma_s = 0.82 + 0.067s \quad (22)$$

$$\gamma_{\psi} = 0.88 + 0.0024\psi \quad (23)$$

$$\gamma_{\alpha} = 0.46 + .09\alpha \leq 1.0 \quad (24)$$

NCHRP 628 (Khayat and Mitchell, 2009) developed a modified expression for AASHTO LRFD (2007) to determine the creep of SCC. This expression is presented in equations 25 through 29. The expression utilizes the same variables as the AASHTO LRFD expression except A is a factor for the cement type. A is 1.19 for Type I/II cement and 1.35 for Type III with 20% fly ash binder. In addition, all variables in this method are in the metric (SI) system; therefore, V/S is in mm and f'_{ci} is in MPa.

$$\psi(t, t_i) = 1.9k_s k_{hc} k_f k_{td} t_i^{-0.118} \times A \quad (25)$$

$$k_s = 1.45 - 0.13(V/S) \geq 0.0 \quad (26)$$

$$k_{hc} = 1.56 - 0.008H \quad (27)$$

$$k_f = \frac{35}{7 + f'_{ci}} \quad (28)$$

$$k_{td} = \left(\frac{t}{61 - 0.58f'_{ci} + t} \right) \quad (29)$$

The measured creep to theoretical creep values for HSC and HS-SCC are presented in Table 7.6. The HSC measured creep coefficient at 180 days was 1.58 which is lower than the predicted value of 2.10 determined by AASHTO (2007), higher than the predicted value of 1.08 using ACI Committee 209 report method (ACI 209R, 1997), and lower than the predicted 2.51 using the NCHRP 628 document (Khayat and Mitchell, 2009). The HS-SCC measured creep coefficient at 180 days was 1.96 which is lower than the predicted value of 2.14 obtained by AASHTO (2007), higher than the predicted value of 1.08 obtained by ACI Committee 209 report method (ACI 209R, 1997), and lower than the predicted value of 2.55 obtained by the NCHRP 628 modified AASHTO equation. The values obtained by the ACI equation are not as accurate as possible due to the equation requirements and the fact that ACI 209 was not based upon more modern HPC. The equation utilizes modification factors to determine the creep coefficient. These modification factors include method of curing, relative humidity, volume-surface

ratio, slump, percentage of fine aggregate, and air content. The modification factor for method of curing are limited to moist cure and steam cured. For this project, the test materials were cured within a room at room temperature and relatively low humidity. In addition, the slump data were not known. Without proper modification factors, the values obtained by the ACI equation are not as accurate as possible.

Table 7.6. Measured & Predicted Creep at 180 days

Material	HSC	HS-SCC
Measured	1.58	1.96
<i>AASHTO LRFD 2007</i>	<i>2.10</i>	<i>2.14</i>
<i>ACI 209-97</i>	<i>1.08</i>	<i>1.08</i>
<i>NCHRP 628</i>	<i>2.51</i>	<i>2.55</i>

7.7. SHRINKAGE

ACI 209R (1992) defines shrinkage as a decrease in the volume of concrete over time which includes drying shrinkage, autogenous shrinkage, and carbonation. The shrinkage monitored by the specimens was drying shrinkage. Drying shrinkage is a decrease in concrete volume due to the loss of moisture within a concrete by evaporation. The amount of shrinkage for both the HSC and HS-SCC are displayed in Tables 7.7 and 7.8 respectively. In addition, the empirical results derived from shrinkage equations recommended by AASHTO (2007), ACI 209R (1997), and NCHRP Report 628 developed by Khayat and Mitchell (2009) for modifications to the AASHTO LRFD (2004) for SCC are documented within the tables. In addition, Figure 7.13 illustrates the shrinkage curves for the HSC and HS-SCC precast deck panels.

The AASHTO LRFD (2007) developed for HSC by Tadros et. al (2003) empirical model is presented in equations 30 through 34. In the model, ϵ_{sh} is the shrinkage, k_s is a factor for volume-to-surface ratio of the specimen for shrinkage, k_{hs} is a factor for humidity for shrinkage, k_f is a factor for the concrete strength, k_{td} is a factor for time

development, V/S is the volume to surface ratio (in.), H is the relative humidity (%), f'_{ci} is the compressive strength at release (psi), and t is the concrete maturity age (days).

$$\varepsilon_{sh} = k_s k_{hs} k_f k_{td} 0.48 \times 10^{-3} \quad (30)$$

$$k_s = \left[\frac{\frac{t}{26e^{0.36(V/S)+t}}}{\frac{t}{45+t}} \right] \left[\frac{1064-94(V/S)}{923} \right], \quad V/S \leq 6.0\text{-in.} \quad (31)$$

$$k_{hs} = 2.00 - 0.014H \quad (32)$$

$$k_f = \frac{5}{1+f'_{ci}} \quad (33)$$

$$k_{td} = \left(\frac{t}{61-4f'_{ci}} \right) \quad (34)$$

The ACI 209 (1997) model developed for conventional concrete shrinkage is displayed in equations 35 through 44. In the following model, $(\varepsilon_{sh})_u$ is the ultimate shrinkage and γ_{sh} is the shrinkage correction factor. Within the concrete correction factor, γ_λ is the correction factor for ambient relative humidity, $\gamma_{V/S}$ is the correction factor for the volume to surface ratio, γ_s is the correction factor for the slump, γ_{cc} is the correction factor for cement content, γ_ψ is the correction factor for fine aggregate percentage, and γ_α is the correction factor for air content. Within each correction factor λ is the ambient relative humidity (%), V/S is the volume to surface ratio (in.), s is the slump (in.), ψ is the ratio of fine aggregate to total aggregate by weight (%), c is the cement content (lbs/ft³), and α is the air content (%).

$$(\varepsilon_{sh})_u = 780\gamma_{sh} \times 10^{-6} \quad (35)$$

$$\gamma_{sh} = \gamma_\lambda \gamma_{V/S} \gamma_s \gamma_\psi \gamma_c \gamma_\alpha \quad (36)$$

$$\gamma_\lambda = 1.40 - 0.0102\lambda \quad \text{for } 40 \leq \lambda \leq 80 \quad (37)$$

$$\gamma_\lambda = 3.00 - 0.030\lambda \quad \text{for } 80 \leq \lambda \leq 80 \quad (38)$$

$$\gamma_{V/S} = 1.2e^{-0.12V/S} \quad (39)$$

$$\gamma_s = 0.89 + 0.041s \quad (40)$$

$$\gamma_{cc} = 0.75 + 0.00036c \quad (41)$$

$$\gamma_{\psi} = 0.3 + 0.014\psi \text{ for } \psi \leq 50\% \quad (42)$$

$$\gamma_{\psi} = 0.9 + 0.002\psi \text{ for } \psi > 50\% \quad (43)$$

$$\gamma_{\alpha} = 0.95 + 0.008\alpha \leq 1.0 \quad (44)$$

NCHRP 628 (Khayat and Mitchell, 2009) developed a modified expression for AASHTO LRFD (2004) model to determine the shrinkage of SCC. This expression is presented in equations 45 through 47. The expression utilizes the same variables as the AASHTO LRFD expression A is a factor for the cement type. A is 0.918 for Type I/II cement and 1.065 for Type III with 20% fly ash binder. In addition, all variables in this method are in the metric (SI) system; therefore, V/S is in mm.

$$\varepsilon_{sh} = k_s k_{hs} \left(\frac{t}{55+t} \right) 0.56 \times 10^{-3} \times A \text{ (steam cured)} \quad (45)$$

$$k_s = \left[\frac{\frac{t}{26e^{0.0142(V/S)+t}}}{\frac{t}{45+t}} \right] \left[\frac{1064 - 3.7(V/S)}{923} \right], \quad V/S \leq 6.0\text{-in.} \quad (46)$$

$$k_{hs} = 2.00 - 0.014H \quad (47)$$

Table 7.7. HSC Shrinkage Strain.

Material	Placement Date	Shrinkage Strain ($\mu\epsilon$)			
		7 days	28 days	56 days	180 days
HSC	7/30/2009	75	410	492	655
HSC	8/21/2009	172	380	475	608
Average HSC		123	395	483	631
<i>AASHTO 2007</i>		96	240	319	411
<i>ACI 209R-97</i>		144	384	532	723
<i>NCHRP Report 628</i>		121	343	496	717

Table 7.8. HS-SCC Shrinkage Strain.

Material	Placement Date	Shrinkage Strain ($\mu\epsilon$)			
		7 days	28 days	56 days	180 days
HS-SCC	7/30/2009	120	372	446	590
HS-SCC	8/21/2009	173	377	450	556
Average HS-SCC		146	375	448	573
<i>AASHTO 2007</i>		97	244	327	424
<i>ACI 209R-97</i>		142	379	525	715
<i>NCHRP Report 628</i>		121	343	496	717

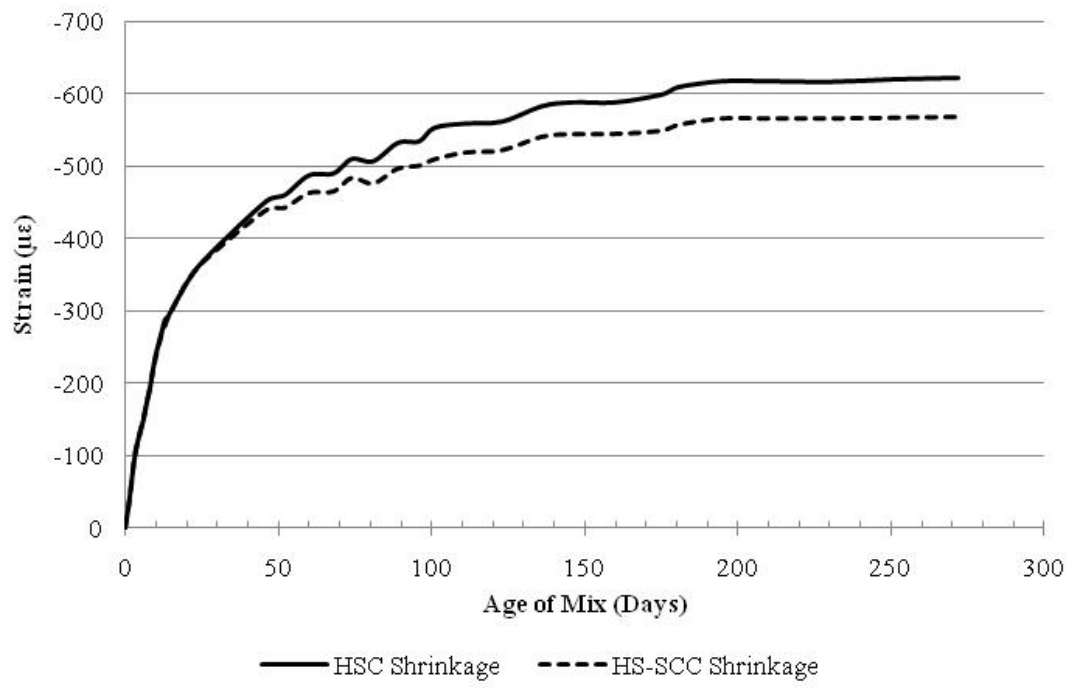


Figure 7.13. Shrinkage Results for HSC & HS-SCC Precast Deck Panels.

The total amount of shrinkage for the HSC was greater than that of the HS-SCC. Typically, higher w/cm concretes produce greater amounts of shrinkage. In addition, the material with the highest creep should have the highest shrinkage rate. Since the HS-SCC mixture had a higher w/cm ratio and larger amount of creep due to the presence of softer coarse aggregate, one would expect the HS-SCC to have a higher amount of shrinkage. However, this was not the case with this research project. In a previous study it was reported that a concrete that contains limestone can have less shrinkage when compared to a stiffer aggregate, such as gravel, due to a possible chemical reaction between the paste and the limestone creating a stronger bond at the interface zone (All-Attar, 2008). In this research project, the HSC mixture had stiffer granite aggregate and the HS-SCC contained limestone aggregate. It is possible that the type of aggregate within the mixture could play a more substantial role on shrinkage due to the w/cm ratio being relatively close between the mixture proportions.

As shown in Tables 7.7 and 7.8, both the HSC and HS-SCC values were compared to empirical equations. On average, the HSC and HS-SCC had more shrinkage than predicted by the AASHTO (2007) model. In addition, the empirical models presented by ACI 209 (1997) and NCHRP 628 (Khayat and Mitchell, 2009) modified AASHTO equation overestimated the amount of shrinkage.

7.8. COEFFICIENT OF THERMAL EXPANSION

The coefficient of thermal expansion (CTE) is important to determine the amount of strain within a structure that occurs from change in temperature. In some cases, a rapid change in temperature can lead to cracking within the concrete. The CTE is largely a function of the type and amount of aggregate within the concrete.

Two specimens for each mixture were tested for the coefficient of thermal expansion. The average results for the HSC mixture were $5.7 \mu\epsilon/^\circ\text{C}$ ($10.3 \mu\epsilon/^\circ\text{F}$). The HS-SCC average CTE results were $5.0 \mu\epsilon/^\circ\text{C}$ ($8.9 \mu\epsilon/^\circ\text{F}$). The HSC had a slightly higher CTE. This can be attributed to the higher percentage of coarse aggregate within the HSC mixture. The measured CTE for each mixture and placement date is presented in Table 7.9.

Table 7.9. Measured Coefficient of Thermal Expansion.

Mixture	Placement Date	Coefficient of Thermal Expansion	
		$\mu\epsilon/^\circ\text{C}$	$\mu\epsilon/^\circ\text{F}$
HSC	7/30/2009	5.69	10.2
HSC	8/21/2009	5.70	10.3
HS-SCC	7/30/2009	4.42	8.0
HS-SCC	8/21/2009	5.49	9.9

7.9. TENSILE STRENGTH AND MODULUS OF ELASTICITY OF GFRP

The tensile strength and modulus of elasticity of the GFRP bars were determined to compare with the design values. The design values utilized for design were for Aslan 100 GFRP which has a diameter of 19 mm (0.75-in.), bar area of 285 mm² (0.442 in²), tensile strength of 620 MPa (90 ksi), and elastic modulus of 40.8 GPa (5.92 Msi). However, a new GFRP formulation provided by the manufacturer was utilized in the bridge spandrels. Testing by the manufacturer provided the tensile strength of the GFRP to be around 793 MPa (115,000 psi) and stiffness to be close to 47.7 GPa (6,910 ksi). The data sheet from the testing is presented in the Appendix C.

7.10. SUMMARY

Material tests were completed on HSC and HS-SCC and were compared with various code empirical relationships. In addition, the tensile strength and modulus of elasticity of GFRP bars were completed.

It was determined that the compressive strength of HSC was higher than that of HS-SCC. The modulus of elasticity of both the HSC and HS-SCC produced values lower than predicted by the empirical relationships. However, ACI 363R (2010) Equation 6-5 gave the best fit for the HSC data. In addition, the HS-SCC data fit best with ACI 363R (2010) equation for modulus of elasticity.

Equations given by ACI 363R for HSC tended to overestimate the modulus of rupture of the specimens. Both the HSC and HS-SCC results were closer to the ACI 318 (2008) equation for modulus of rupture for normal strength concrete.

The splitting tensile strength was overestimated for the HSC and HS-SCC specimens by both ACI 363R (2010) and ACI 318 (2005) methods. The ACI 318 (2005) for conventional concrete produced the closest results to the experimental data.

The HS-SCC experienced a significantly higher degree of creep than the HSC specimens which is particularly noteworthy. The HSC experienced a slightly higher degree of shrinkage than the HS-SCC specimens. The measured values of creep and shrinkage did not correspond well with the empirical relationships specified by AASHTO LRFD (2007), ACI 209R (1997), and method recommend by the NCHRP 628 (Khayat and Mitchell, 2009) for determining creep and shrinkage of self-consolidating concrete. However, the AASHTO LRFD (2007) was a reasonable approximation of the HS-SCC measured creep coefficient.

8. TEMPERATURE MEASUREMENTS

8.1. INTRODUCTION

8.1.1. General. The knowledge on how temperature impacts a concrete structure can have a vital impact on its design. If care is not taken in the temperature profile within a structure, additional deflections, strains, and stresses may result within the structure. The stresses will not typically induce a failure in strength but can be noteworthy particularly if the structures boundary elements are restrained. However, thermal cracking can modify the serviceability of a structure and induce corrosion in the reinforcement of the structure.

To monitor the temperature within both the HSC and HS-SCC, VWSGs with thermistors were utilized at locations of interest at the mid-span and support of the girders and the center of the deck panels. Data were collected from early-age concrete hydration through storage, erection, and service. In addition, data were compared to the ambient temperatures.

8.1.2. Ambient Temperature Data. Ambient temperature data were monitored by National Climatic Data Center (NCDC) at locations closest to the bridge fabrication site and erection site (Ref NCDC). When the bridge was fabricated in Marshall, MO, the closest NCDC weather station was in Sedalia Memorial Airport (03994/DMO) in Sedalia, MO, which is approximately 48 km (30 mi) from the fabrication site. In Rolla, MO, temperature data were provided from a monitoring station in Rolla/Vichy National Airport (13997/VH) which is approximately 21 km (13 mi) from the bridge site. During transportation the Jefferson City, MO, NCDC weather station at Jefferson City Memorial Airport (03963/JEF) and Columbia, MO, NCDC weather station at Columbia Regional Airport (03945/COU) were reviewed.

8.2. HYDRATION TEMPERATURES

8.2.1. Background. The temperature within concrete during concrete hydration follows a number of phases. At the very beginning of mixing, a spike in temperature occurs which can last for the first few minutes. A dormant period occurs after the initial heat of mixing. During this phase, the concrete remains plastic. After a few hours, an

initial set occurs and the temperature within the mixtures begins to rise as the cementitious material reacts with the water in the mixtures. After final set is reached, small amounts of heat are generated allowing the concrete to lose the excess heat and equalize with the surrounding ambient temperatures (Myers and Yang, 2005).

Due to the high amount of cementitious material in high-strength concrete and high-strength self-consolidating concrete, there is a higher amount of heat generated during concrete hydration. In addition, factors such as w/cm, member size, and environmental conditions can affect the heat of hydration of the concrete member. According to ACI Committee 363 (ACI 363R, 2010), the temperature rise of high-strength concretes can range from approximately 10 to 14°C per 100 kg/m³ (11 to 15°F per 100 lbs/yd³) of cement.

It has also been reported that if concrete hydration temperatures exceed 77°C (170°F), a negative effect could occur to the concrete properties. Adversely effected properties include, reduced compressive strength, reduced modulus of elasticity, and increased permeability due to extensive and wider microcracking (Myers and Carrasquillo, 2000).

8.2.2. Measurements. As described in Section 6, the concrete hydration temperatures of the HSC and HS-SCC were monitored with VWSGs with built-in thermistors at the support and mid-span of a representative beam and the mid-span of each deck panel. The hydration curves for the support and mid-span of each beam are represented in Figures 8.1 through 8.4. In addition, Table 8.1 presents the hydration temperature data for the HSC and HS-SCC spandrel beams. The ambient temperature provided is from the NCDC weather station (03994/DMO) in Sedalia, MO (Ref NCDC).

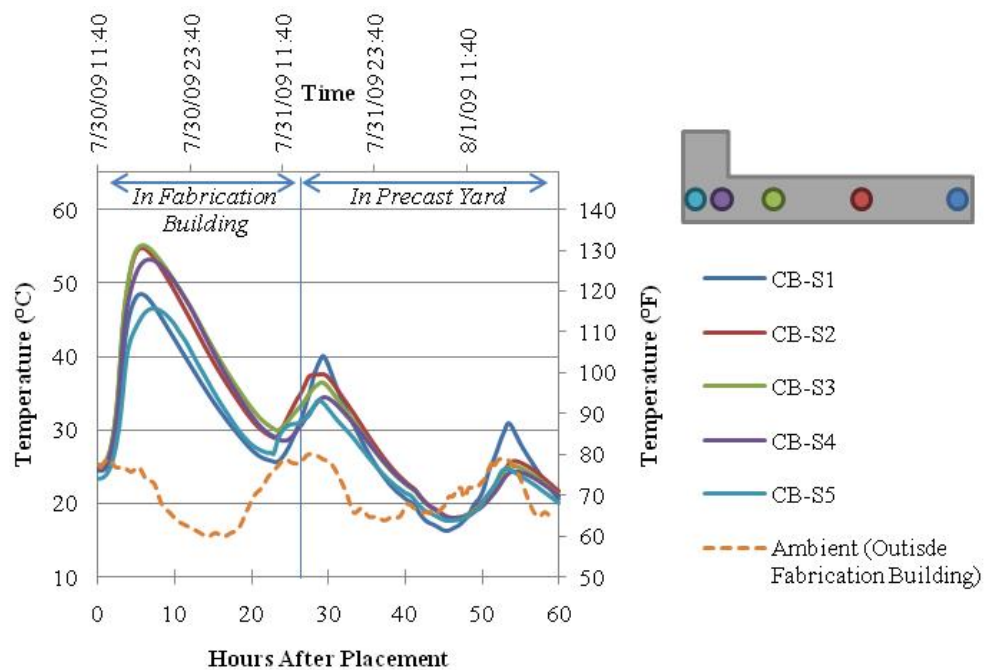


Figure 8.1. Hydration Temperature of HSC Spandrel Beam at Support.

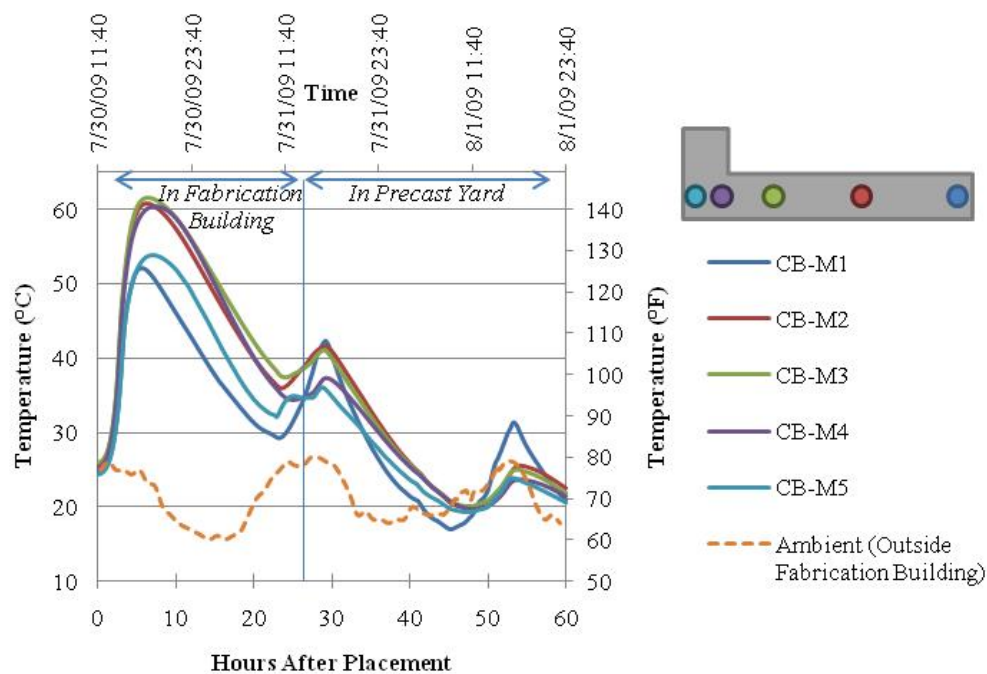


Figure 8.2. Hydration Temperature of HSC Spandrel Beam at Mid-Span.

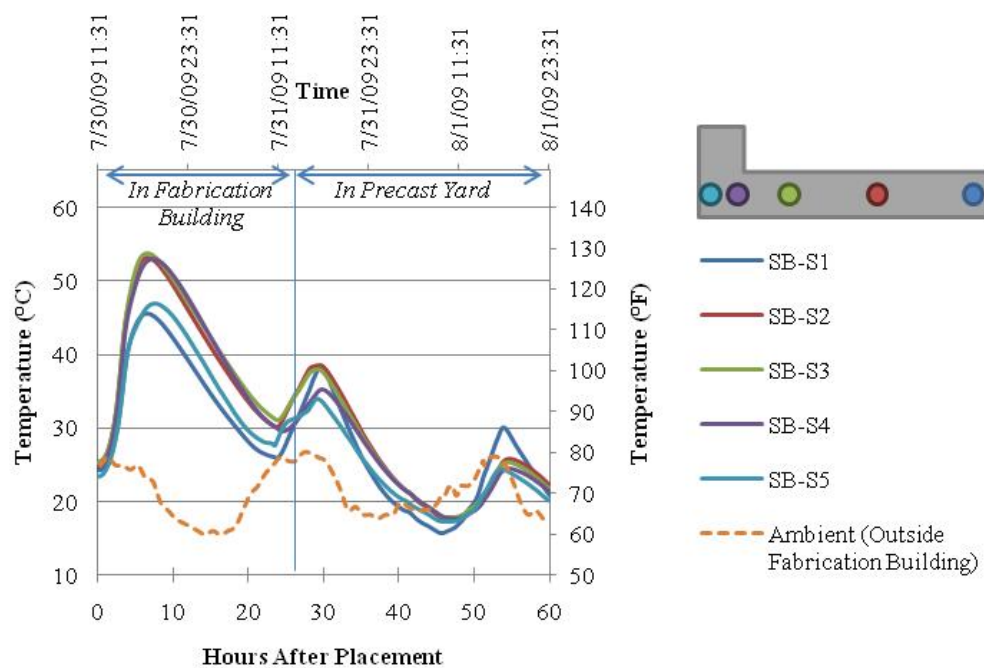


Figure 8.3. Hydration Temperature of HS-SCC Spandrel Beam at Support.

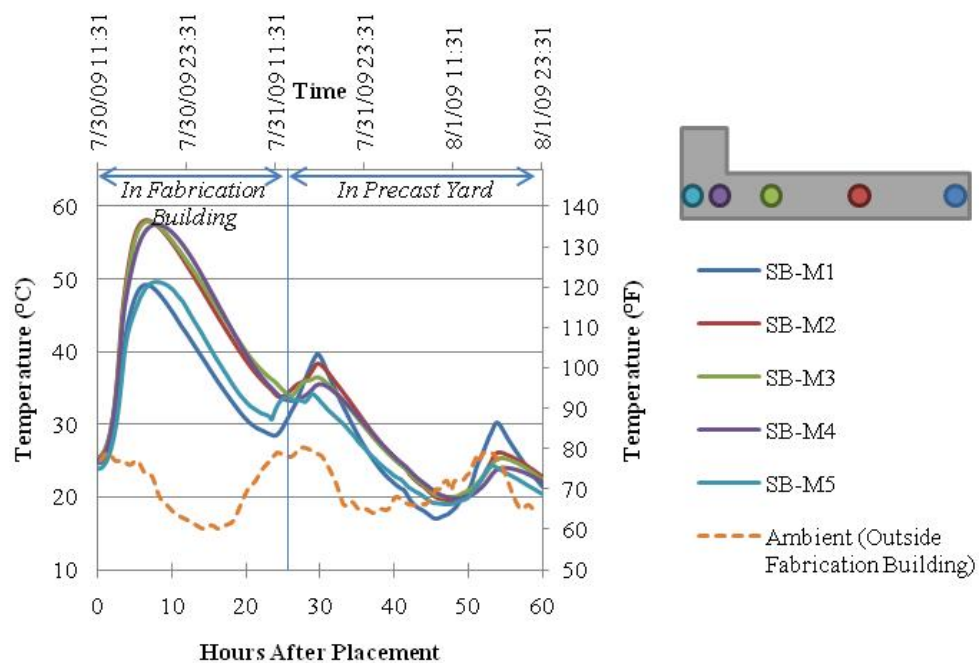


Figure 8.4. Hydration Temperature of HS-SCC Spandrel Beam at Mid-Span.

Table 8.1. Summary of Measured Hydration Temperatures for Precast Spandrel Beams.

Spandrel Beam	HSC	HSC	HS-SCC	HS-SCC
Location	Support	Mid-Span	Support	Mid-Span
Placement Date	7/30/2009	7/30/2009	7/30/2009	7/30/2009
Placement Time	11:40	11:40	11:40	11:40
Avg. Placement Temp.	25°C	25°C	25°C	25°C
Avg. Temp at End of Dormant Phase	25°C	26°C	26°C	26°C
Peak Hydration Temp.	55°C	62°C	54°C	58°C
Location of Peak Hydration Temp.	CB-S3	CB-M3	SB-S3	SB-M2
Max. Temp. Rise after Dormant	30°C	36°C	28°C	32°C
Maximum Gradient	11°C	13°C	9°C	12°C
Maximum Gradient Location	CB-S3 to CB-S5	CB-M1 to CB-M3	SB-S1 to SB-S4	SB-M1 to SB-M4
Temperature: °F = (1.8 * (°C)) + 32				

The average placement temperature for both the HSC and HS-SCC spandrel beams was 25°C (77°F). The peak hydration temperature for the HSC beam occurred at 560 mm (22-in.) from the bottom fiber at the mid-span of the member and was 62°C (143°F). In addition, the peak hydration temperature of the HS-SCC beam occurred at 560 mm (22-in.) from the bottom fiber that the mid-span of the girder and was 58°C (136°F). The peak hydration temperature for the top and bottom fiber of both the HSC and HS-SCC spandrel beams were approximately 10°C (18°F) cooler than at the centroid of the L-girder. During hydration, this section of the beam was closest to the forms and allowed for higher heat loss than at the centroid of the member. In addition, the maximum temperature rise of 36°C (65°F) for the HSC spandrel beam was slightly higher than the HS-SCC beam's maximum rise of 32°C (58°F).

In addition to the hydration curves for the HSC and HS-SCC spandrel beams, the hydration temperatures were monitored for the HSC and HS-SCC precast deck panels. The hydration curves for each deck panel are represented in Figures 8.3 through 8.8 reinforced with either mild steel or GFRP. Table 8.2 provides the hydration temperature data for the HSC and HS-SCC precast deck panels.

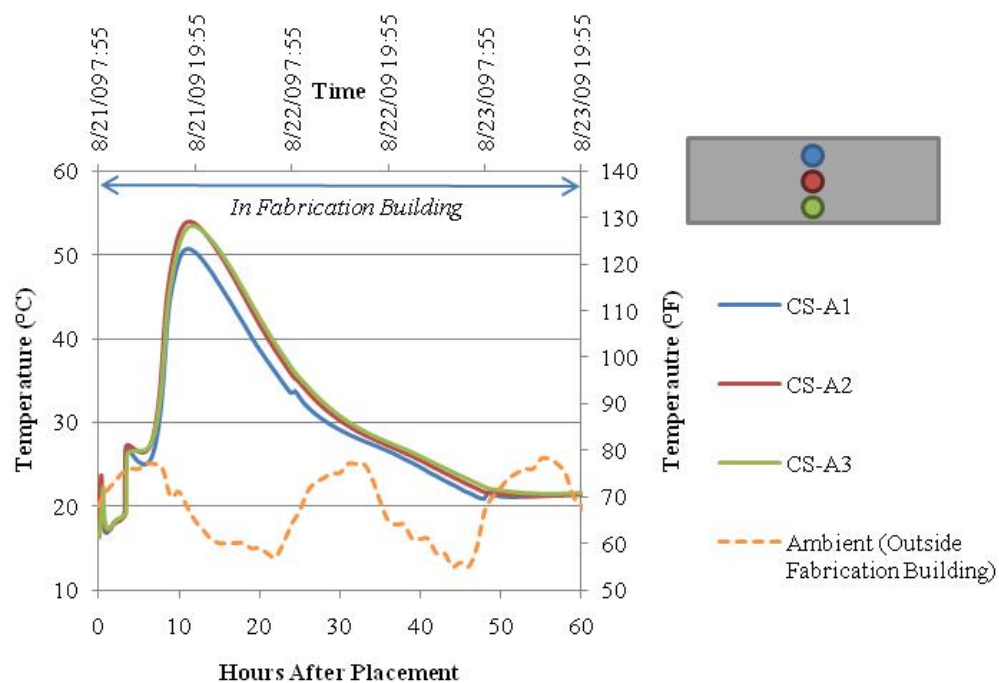


Figure 8.5. Hydration Temperature of HSC Deck Panel Reinforced with Mild Steel.

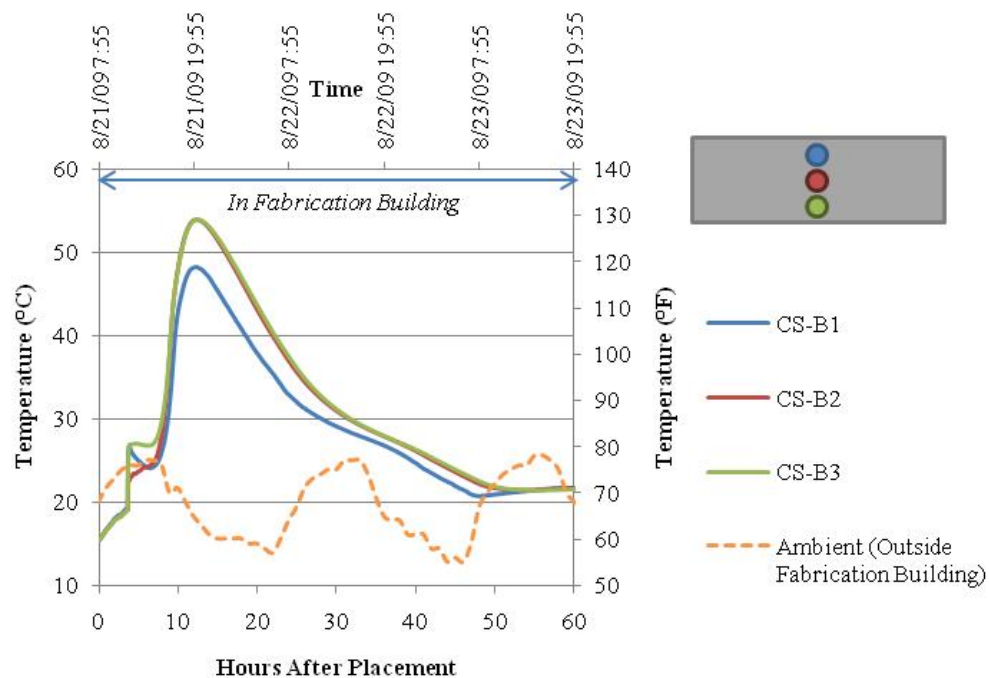


Figure 8.6. Hydration Temperature of HSC Deck Panel Reinforced with GFRP.

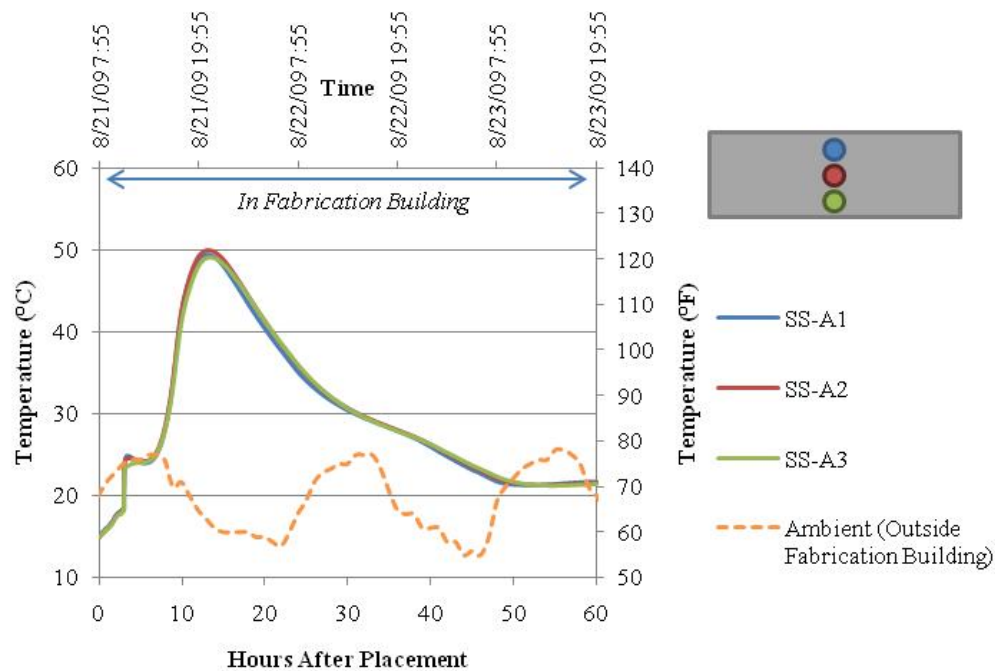


Figure 8.7. Hydration Temperature of HS-SCC Deck Panel Reinforced with Mild Steel.

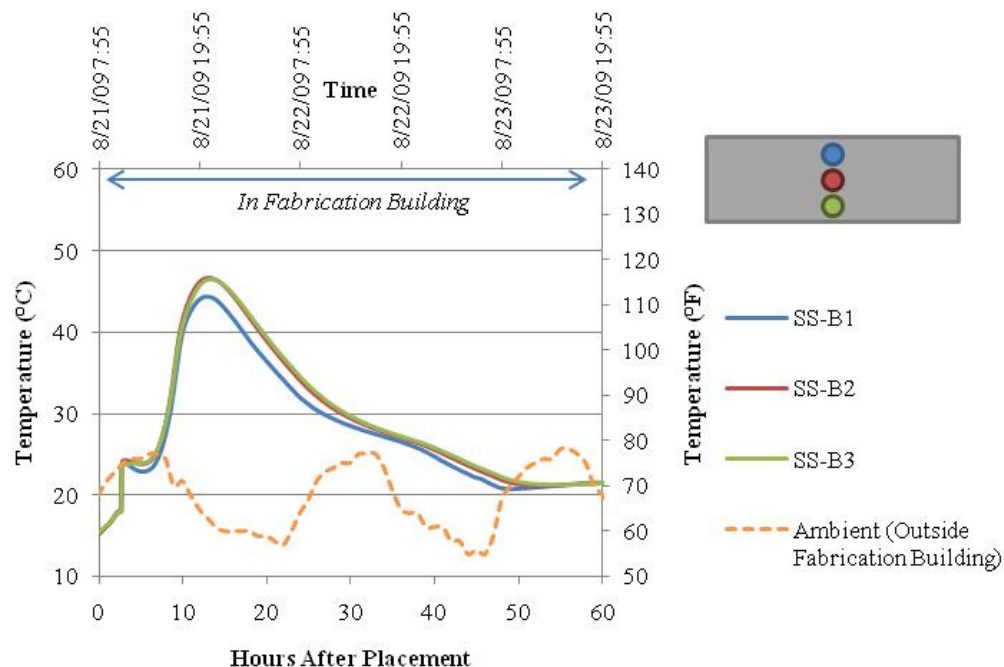


Figure 8.8. Hydration Temperature of HS-SCC Deck Panel Reinforced with GFRP.

The average placement temperature for the HSC precast deck panels was 19°C (66°F) and HS-SCC precast deck panels was 18°C (64°F). The peak hydration temperature of 54°C (129°F) for the HSC precast deck panel occurred at the centroid of the precast deck panel. In addition, the maximum hydration temperature occurred at the centroid of the HS-SCC precast deck panel and was 50°C (122°F). The HSC deck panels had a slightly higher maximum temperature rise of 27°C (49°F) when compared to the maximum temperature rise of 26°C (47°F) in the HS-SCC deck panels. Due to the shallow cross section, 200 mm (8-in.) thick, the temperature variation was minimal. The top fiber tended to be 5°C (9°F) cooler than the centroid of the deck panel because of greater heat loss or temperature dissipation at the surface.

Table 8.2. Summary of Measured Hydration Temperatures for Precast Deck Panel.

Deck Panel	HSC	HSC	HS-SCC	HS-SCC
Reinforcement	Mild Steel	GFRP	Mild Steel	GFRP
Placement Date	8/21/2009	8/21/2009	8/21/2009	8/21/2009
Placement Time	11:00	11:00	10:30	10:30
Avg. Placement Temp.	19°C	19°C	18°C	18°C
Avg. Temp at End of Dormant Phase	27°C	27°C	24°C	24°C
Peak Hydration Temp.	54°C	54°C	50°C	47°C
Location of Peak Hydration Temp.	CS-A2	CS-B2	SS-A2	SS-B2
Max. Temp. Rise after Dormant	27°C	27°C	26°C	23°C
Maximum Gradient	5°C	8°C	1°C	3°C
Maximum Gradient Location	CS-A1 to CS-A2	CS-B1 to CS-B3	SS-A2 to SS-A3	SS-B1 to SS-B3
Temperature: °F = (1.8 * (°C)) + 32				

8.2.3. Discussion. The maximum temperature rise of 36°C (65°F) for the HSC spandrel beams occurred at the mid-span of the member with an equivalent maximum temperature rise of 8.1°C per 100 kg/m³ (8.6°F per 100 lb/yd³) of cement or 7.5°C per 100 kg/m³ (8.0°F per 100 lb/yd³) of cementitious material. However, the HS-SCC had a maximum temperature rise of 32°C (58°F) at the mid-span with an equivalent maximum temperature rise of 8.2°C per 100 kg/m³ (8.7°F per 100 lb/yd³) of cement or 6.9°C per 100 kg/m³ (7.4°F per 100 lb/yd³) of cementitious material.

The precast deck panels had the highest temperature rise occur on the deck panels reinforced with mild steel. The HSC deck panels maximum temperature rise was 27°C (49°F) with an equivalent maximum temperature rise of 6.1°C per 100 kg/m³ (6.5°F per 100 lb/yd³) of cement and 5.6°C per 100 kg/m³ (6.0°F per 100 lb/yd³) of cementitious material. Whereas, the HS-SCC deck panels had a maximum temperature rise of 26°C (47°F) with an equivalent maximum temperature rise of 6.7°C per 100 kg/m³ (7.1°F per

100 lb/yd³) of cement or 5.6°C per 100 kg/m³ (6.0°F per 100 lb/yd³) of cementitious material. On average, the maximum equivalent temperature rise was lower for the deck panels than the spandrel beams because of the member size and depth when compared to the spandrel beam cross section. The spandrel beams also had a higher volume to surface area (V/S) than the deck panels. Both the HSC and HS-SCC Spandrel beams V/S ratios were 110 mm (4.4-in.) and deck panel was 90 mm (3.6-in.). The higher V/S ratio will have higher concrete hydration temperatures. The temperature rise was higher for the HSC when compared to the HS-SCC members because of the type of supplementary cementitious materials added to the HS-SCC mixture. Unlike the HSC mixture, the HS-SCC mixture contained fly ash which helped reduce the rise in temperature (Myers and Carrasquillo, 2000).

8.3. MEAN BRIDGE TEMPERATURES

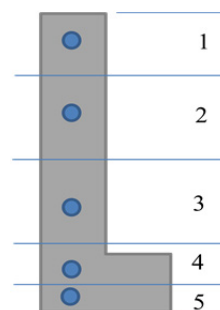
8.3.1. Background. Throughout the course of a bridge's life, the bridge will expand and contract due to the seasonal temperature cycle. A study was conducted to determine the mean bridge temperatures of HSC and HS-SCC to obtain a better understanding of the similarities and differences between the materials. In addition, the mean temperature in the deck panels was determined to see if there were differences in mean temperature in deck panels reinforced with mild steel or GFRP.

8.3.2. Measurements. The mean bridge temperatures were measured with thermistors within the VWSGs embedded in the concrete before beam and deck panel fabrication. Temperatures were recorded every 10 minutes during later-ages. On some occasions, there are a few days in October and November 2009 that contain missing data due to a power shortage caused by inadequate power provided by the battery.

An average cross-sectional temperature reading was determined for each precast beam. The average temperature was determined by assigning a given weight to each sensor. The weighted value was determined by calculating the area of concrete surrounding each sensor and dividing it by the total cross sectional area. The weights for each sensor are provided in Table 8.3. The average deck temperature was calculated to be the average of all three sensors within the deck panel.

Table 8.3. Weighted Values Implemented to Determine Average Beam Temperatures.

Sensor Section	Weight
Sensor 1	0.165
Sensor 2	0.262
Sensor 3	0.220
Sensor 4	0.204
Sensor 5	0.149



Spandrel Beam Cross-Section

Images of the typical afternoon conditions are shown in Figure 8.9. The daily maximum and minimum temperatures for HSC and HS-SCC bridges are provided in Figures 8.10 to 8.13. In addition, the average maximum and minimum temperatures for a calendar month for the HSC and HS-SCC bridges are illustrated in Figures 8.14 to 8.17. For both the HSC and HS-SCC bridges, the maximum ambient temperature remained slightly higher than the average beam and deck panel temperatures. At most, the ambient temperature was approximately 1°C (2°F) warmer than the average beam and deck panel temperature. On the other hand, the minimum average beam temperature tended to stay approximately 1°C (2°F) warmer than the minimum average ambient temperature. However, a number of trees, as shown in Figure 8.9, provided shade for the bridges.



a.) HSC Bridge



b.) HS-SCC Bridge

Figure 8.9. Shade Covering Bridge Deck.

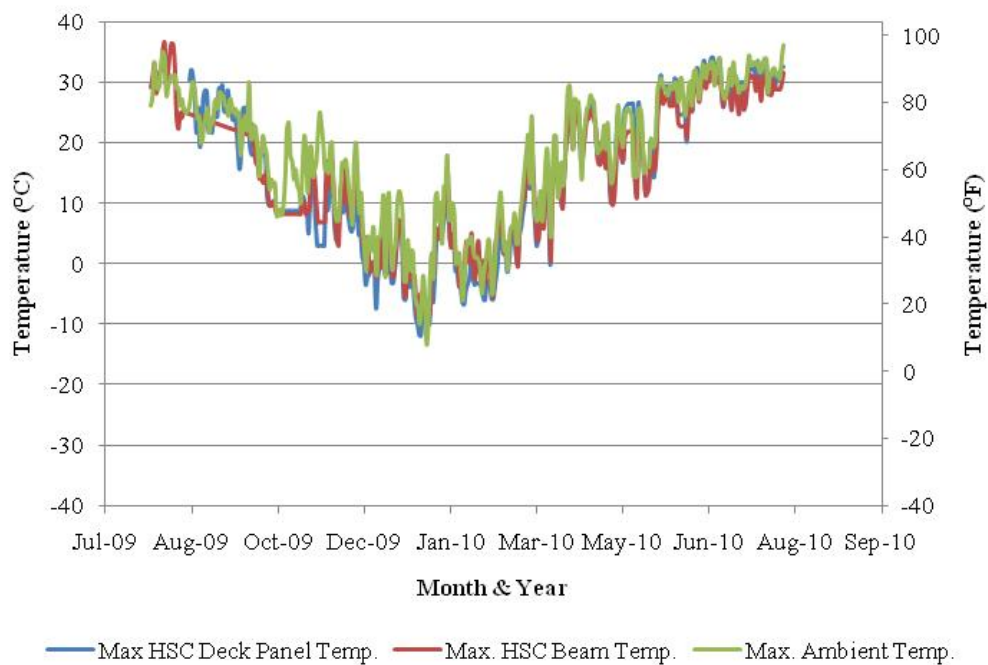


Figure 8.10. Maximum Daily Temperature of HSC Bridge.

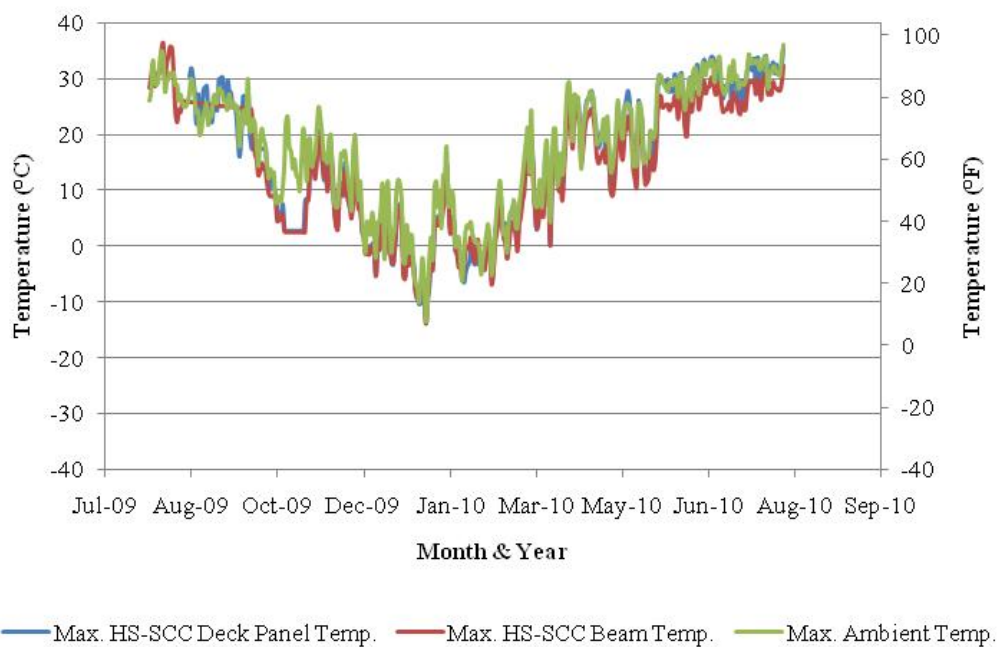


Figure 8.11. Maximum Daily Temperature of HS-SCC Bridge.

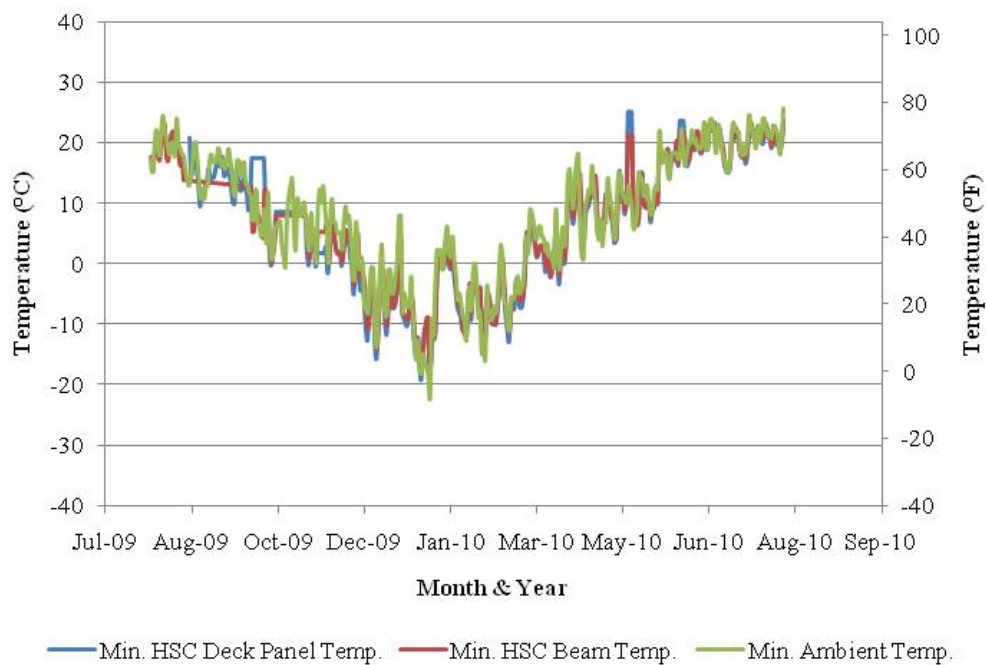


Figure 8.12. Minimum Daily Temperature of HSC Bridge.

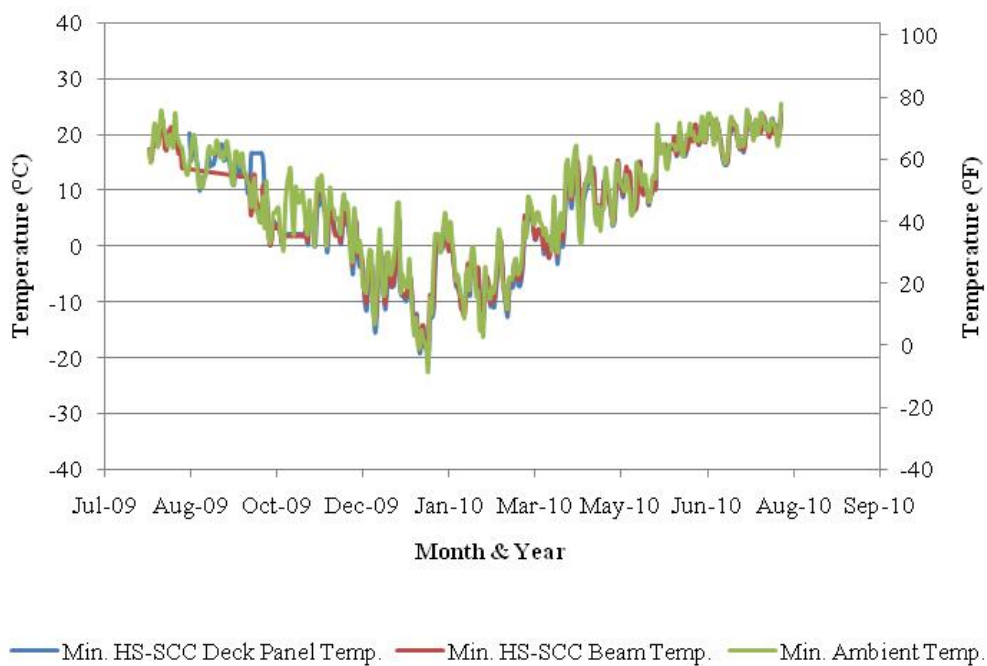


Figure 8.13. Minimum Daily Temperature of HS-SCC Bridge.

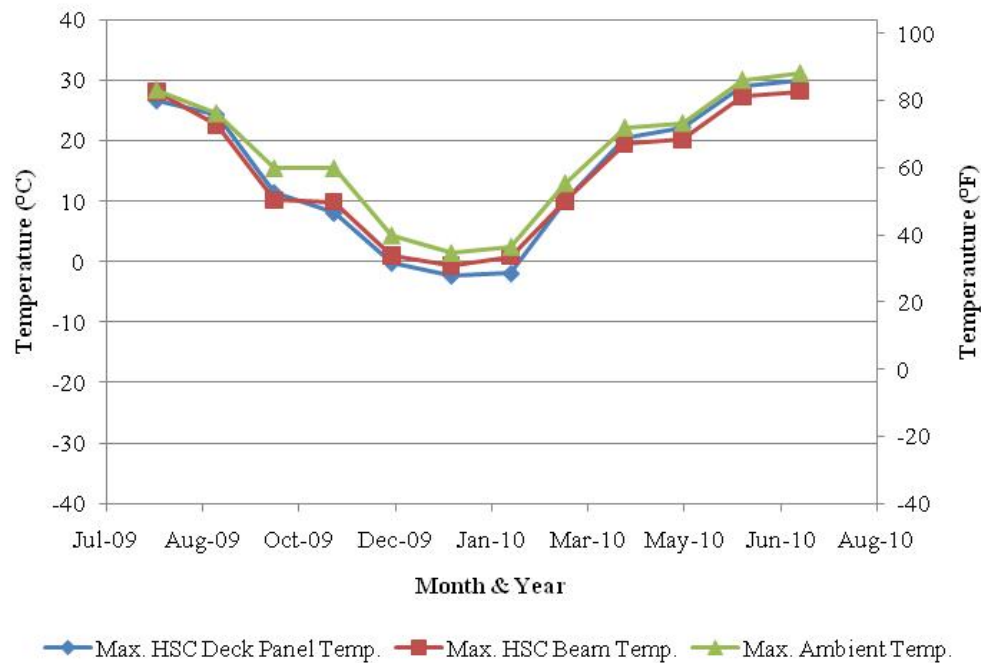


Figure 8.14. Average Maximum Monthly Temperature of HSC Bridge.

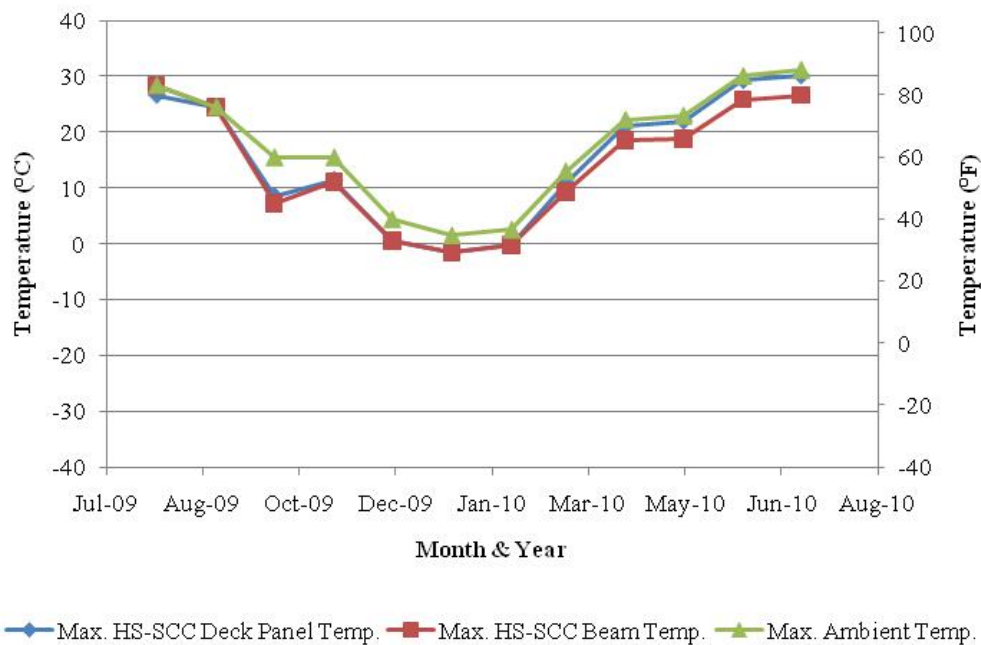


Figure 8.15. Average Maximum Monthly Temperature of HS-SCC Bridge.

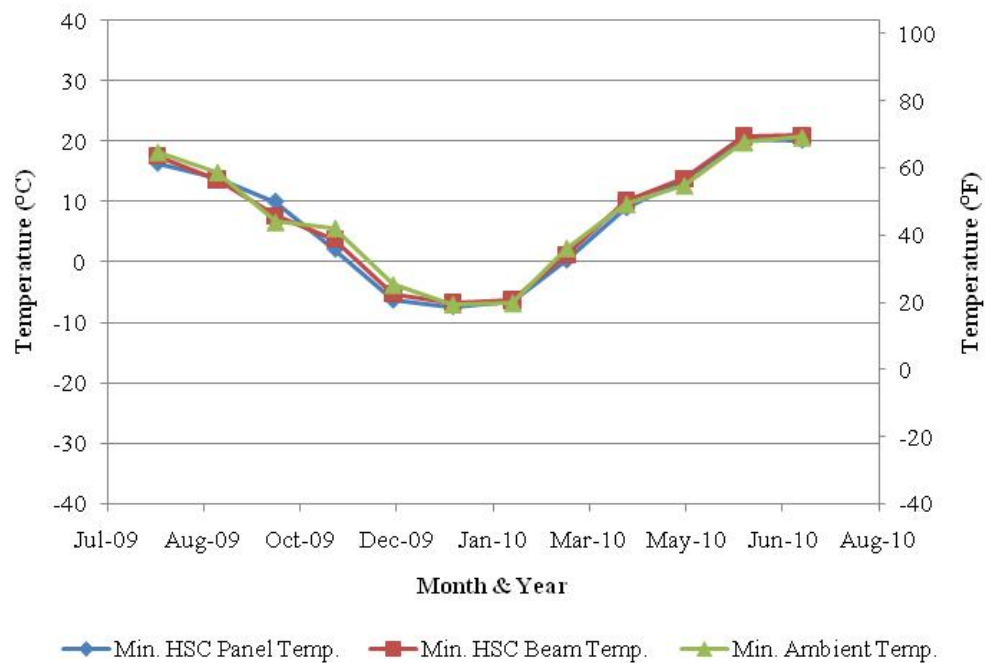


Figure 8.16. Average Minimum Monthly Temperature of HSC Bridge.

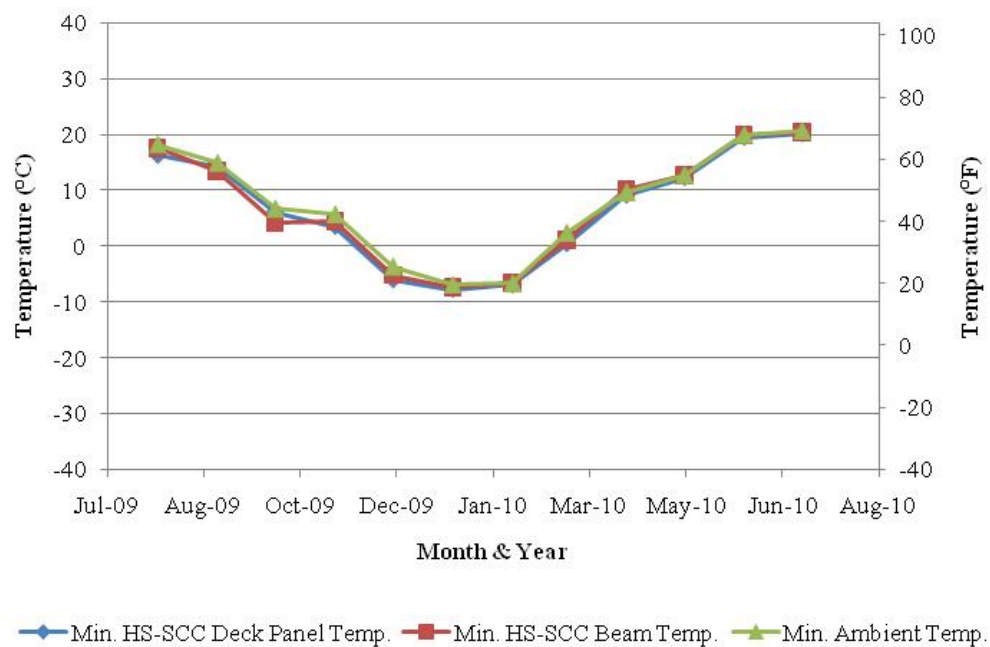


Figure 8.17. Average Minimum Monthly Temperature of HS-SCC Bridge.

Table 8.4 and 8.5 provide the maximum temperatures recorded for the HSC and HS-SCC bridges. In addition, Table 8.6 and 8.7 provide the minimum temperatures recorded for the HSC and HS-SCC bridges. As mentioned before, the maximum ambient temperatures tended to be slightly higher than the maximum HSC and HS-SCC average bridge temperatures. In addition, the minimum ambient temperatures tended to be slightly lower than the minimum HSC and HS-SCC average bridge temperatures.

Table 8.4. Maximum Temperature Values Recorded for HSC Bridge.

Member	Precast Spandrel Beam		Precast Deck Panel	
Description	Support	Mid-Span	M. Steel	GFRP
Absolute Maximum Temperature				
Avg. Temp.	36.46°C	35.2°C	34.26°C	33.84°C
Amb. Temp.	36.10°C	36.10°C	36.10°C	36.10°C
Lowest Daily Maximum Temperature				
Avg. Temp.	-8.92°C	-9.93°C	-11.93°C	-12.44°C
Amb. Temp.	-13.30°C	-13.30°C	-13.30°C	-13.30°C
Highest Average Daily Maximum Temperature per Month				
Avg. Temp.	28.30°C	28.07°C	30.03°C	29.79°C
Amb. Temp.	31.19°C	31.19°C	31.19°C	31.19°C
Lowest Average Daily Maximum Temperature per Month				
Avg. Temp.	0.11°C	-1.57°C	-2.13°C	-2.41°C
Amb. Temp.	1.45°C	1.45°C	1.45°C	1.45°C
Temperature: °F = (1.8 * (°C)) + 32				

Table 8.5. Maximum Temperature Values Recorded for HS-SCC Bridge.

Member	Precast Spandrel Beam		Precast Deck Panel	
Description	Support	Mid-Span	M. Steel	GFRP
Absolute Maximum Temperature				
Avg. Temp.	35.33°C	36.34°C	35.61°C	35.44°C
Amb. Temp.	36.10°C	36.10°C	36.10°C	36.10°C
Lowest Daily Maximum Temperature				
Avg. Temp.	-13.75°C	-14.15°C	-14.10°C	-13.83°C
Amb. Temp.	-13.30°C	-13.30°C	-13.30°C	-13.30°C
Highest Average Daily Maximum Temperature per Month				
Avg. Temp.	28.36°C	28.40°C	30.38°C	29.76°C
Amb. Temp.	31.19°C	31.19°C	31.19°C	31.19°C
Lowest Average Daily Maximum Temperature per Month				
Avg. Temp.	-1.69°C	-1.29°C	-2.25°C	-0.97°C
Amb. Temp.	1.45°C	1.45°C	1.45°C	1.45°C
Temperature: °F = (1.8 * (°C)) + 32				

Table 8.6. Minimum Temperature Values Recorded for HSC Bridge.

Member	Precast Spandrel Beam		Precast Deck Panel	
Description	Support	Mid-Span	M. Steel	GFRP
Absolute Minimum Temperature				
Avg. Temp.	-18.01°C	-17.81°C	-18.77°C	-19.19°C
Amb. Temp.	-22.20°C	-22.20°C	-22.20°C	-22.20°C
Highest Daily Minimum Temperature				
Avg. Temp.	23.92°C	25.05°C	25.46°C	25.15°C
Amb. Temp.	25.60°C	25.60°C	25.60°C	25.60°C
Lowest Average Daily Minimum Temperature per Month				
Avg. Temp.	-6.82°C	-6.58°C	-7.36°C	-7.44°C
Amb. Temp.	-6.96°C	-6.96°C	-6.96°C	-6.96°C
Highest Average Daily Minimum Temperature per Month				
Avg. Temp.	20.41°C	21.46°C	20.27°C	20.22°C
Amb. Temp.	20.66°C	20.66°C	20.66°C	20.66°C
Temperature: °F = (1.8 * (°C)) + 32				

Table 8.7. Minimum Temperature Values Recorded for HS-SCC Bridge.

Member	Precast Spandrel Beam		Precast Deck Panel	
Description	Support	Mid-Span	M. Steel	GFRP
Absolute Minimum Temperature				
Avg. Temp.	-20.33°C	-19.81°C	-19.14°C	-20.25°C
Amb. Temp.	-22.20°C	-22.20°C	-22.20°C	-22.20°C
Highest Daily Minimum Temperature				
Avg. Temp.	24.00°C	24.66°C	23.76°C	23.62°C
Amb. Temp.	25.60°C	25.60°C	25.60°C	25.60°C
Lowest Average Daily Minimum Temperature per Month				
Avg. Temp.	-7.60°C	-7.22°C	-7.83°C	-7.72°C
Amb. Temp.	-6.96°C	-6.96°C	-6.96°C	-6.96°C
Highest Average Daily Minimum Temperature per Month				
Avg. Temp.	20.08°C	20.88°C	20.23°C	20.66°C
Amb. Temp.	20.66°C	20.66°C	20.66°C	20.66°C
Temperature: °F = (1.8 * (°C)) + 32				

8.3.3. Discussion. A comparison was completed between the HSC and HS-SCC bridge temperature values for the bridge precast spandrel beams and precast deck panels. Table 8.8 provides the differences in temperature values in support to support, mid-span to mid-span, difference of support to mid-span, mild steel reinforced to mild-steel reinforced, GFRP to GFRP, difference of mild steel to GFRP between HSC and HS-SCC bridge measurements.

Table 8.8. Comparison between HSC & HS-SCC Bridge Temperatures.

Support to Support	Mid-Span to Mid-Span	Difference of Support to Mid-Span	Mild Steel to Mild Steel	GFRP to GFRP	Difference of Mild Steel to GFRP	Average Difference between Materials
Absolute Maximum Temperature						
1.12°C	-1.14°C	2.26°C	-1.36°C	-1.60°C	0.25°C	-0.08°C
Lowest Daily Maximum Temperature						
4.83°C	4.22°C	0.61°C	2.16°C	1.38°C	0.78°C	2.33°C
Absolute Minimum Temperature						
2.32°C	2.00°C	0.31°C	0.37°C	1.06°C	-0.69°C	0.90°C
Highest Daily Minimum Temperature						
-0.08°C	0.39°C	0.46°C	1.70°C	1.52°C	0.18°C	0.70°C
Total Average Difference Between HSC & HS-SCC						0.96°C
Temperature: °F = (1.8 * (°C)) + 32						
Positive values indicate that HSC had higher temperature levels.						

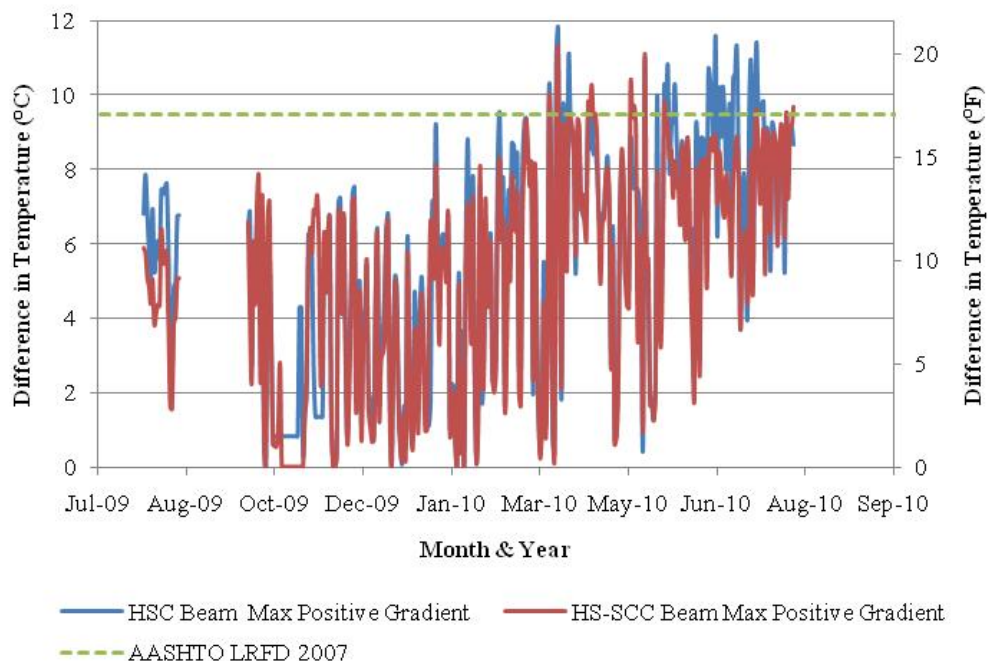
Overall, the HSC bridge was approximately 1°C (2°F) warmer than the HS-SCC bridge. The presence of a higher percentage of larger aggregate could cause this increase in temperature. In addition, the HSC bridge contains 30% more concrete than the HS-SCC bridge. This larger mass of concrete (i.e. thermal mass) can take more time for the heat to dissipate. However, the difference in location causing different shade or wind could also cause temperature variations within the bridge members. In addition, on average, bridges that contained mild steel reinforcement tended to remain approximately 0.1°C (0.2°F) warmer than reinforced with GFRP. These variations are not considered statistically significant.

8.4. THERMAL GRADIENTS

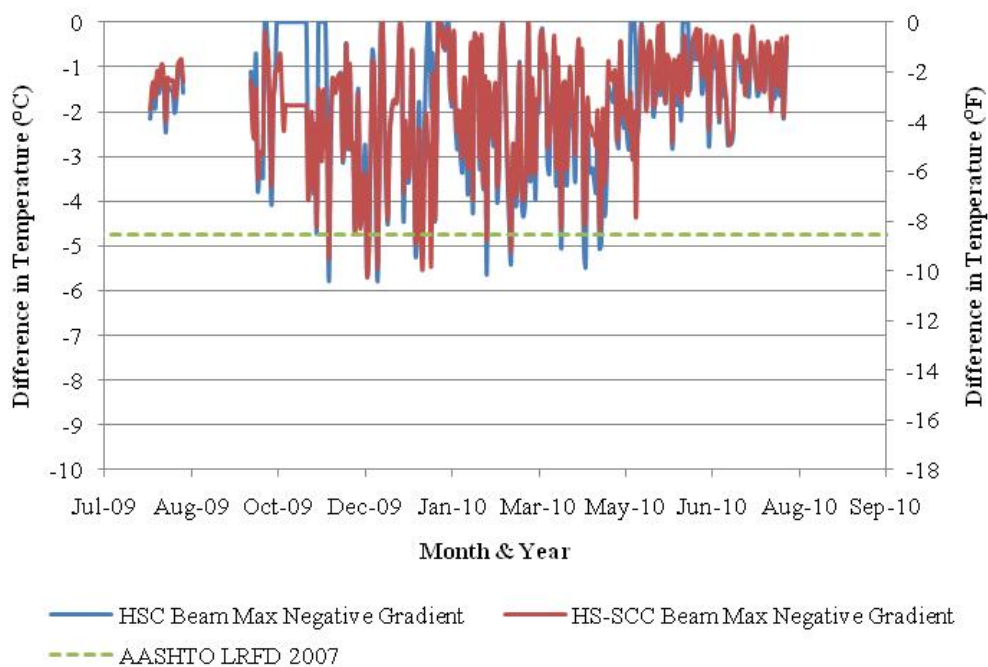
8.4.1. Background. Thermal gradients occur in concrete structures due to the daily temperature cycles. A positive thermal gradient occurs when the top of a concrete structure heats up much more rapidly than the bottom of the structure. A negative thermal gradient occurs when a structure absorbs heat throughout the day and the top dissipates heat more rapidly than the bottom during the night. Thermal gradients can lead to cracking within a concrete structure due to the stresses induced by differential strains on the top and bottom of the concrete member. Section 3.12.3 of AASHTO LRFD Bridge Design Specifications (2007) provides design values for positive and negative gradients for concrete structures provided the concrete surface, geographic location, and depths within a member.

8.4.2. Measurements. By utilizing the data provided from the thermistors within the VWSGs, temperature gradients could be measured within the beams and deck panels. The daily maximum and negative thermal gradients from July 2009 to July 2010 are illustrated in Figures 8.18 and 8.19 and the daily occurrences are presented in Figures 8.20 and 8.21. The average monthly gradients positive and negative gradients from July 2009 to July 2010 are illustrated in Figures 8.22 and 8.23 for the precast beams and deck panels. The spandrel beams' gradients are compared to the AASHTO LRFD Specification (2007) design positive and negative gradients.

There are some days in which there are no positive or negative gradients present on the gradient profiles. This is due to a variety of reasons. For example, during the months of August and September no data were recorded in the beams because of deck panel fabrication. When the deck panels were placed after the beams, it was not feasible to monitor the temperature of the beams and deck panels due to the distance between members. A positive gradient may also not be recorded during a period of time when the top fiber never becomes warmer than the bottom fiber of the structural member, such as in the winter. In addition, a negative gradient may also not be recorded during a period of time when the bottom fiber never becomes warmer than the top fiber of the structural member, such as in the summer.

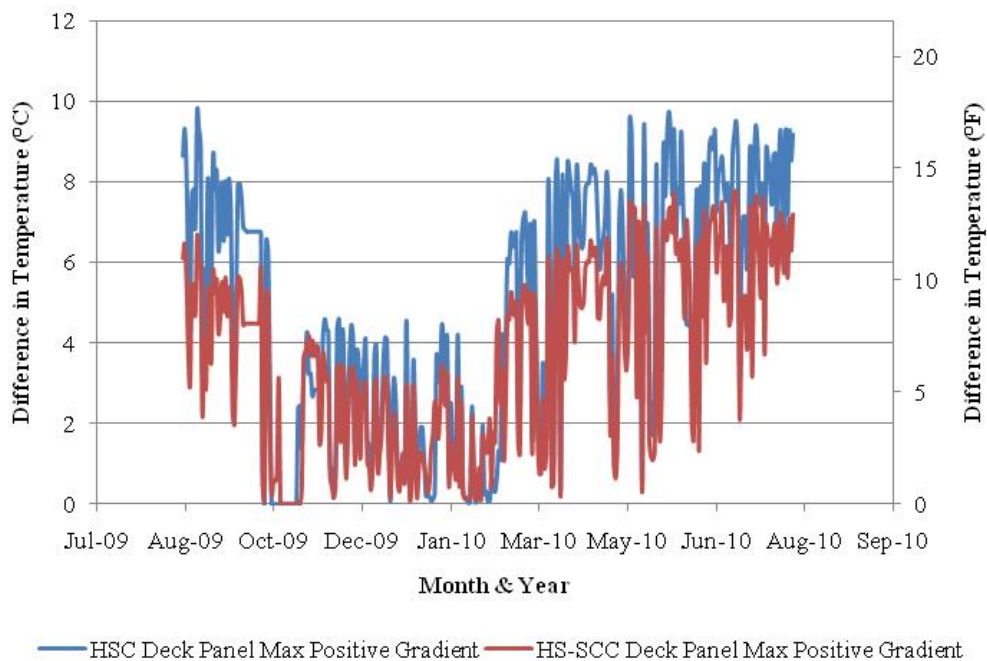


a.) Maximum Daily Positive Thermal Gradients

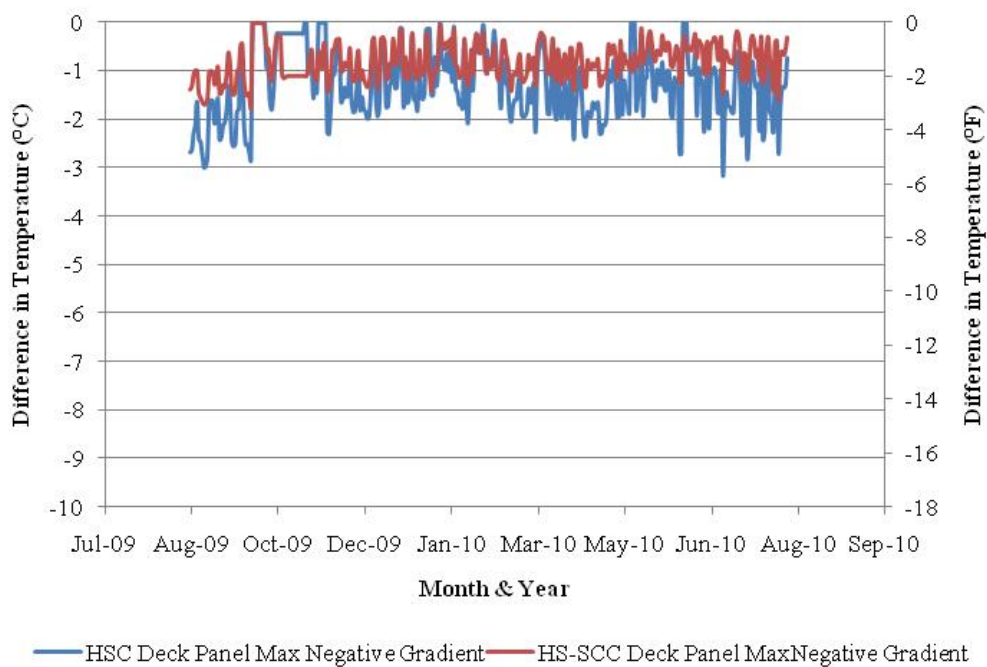


b.) Maximum Daily Negative Thermal Gradients

Figure 8.18. Maximum Daily Thermal Gradients for HSC & HS-SCC Beams.

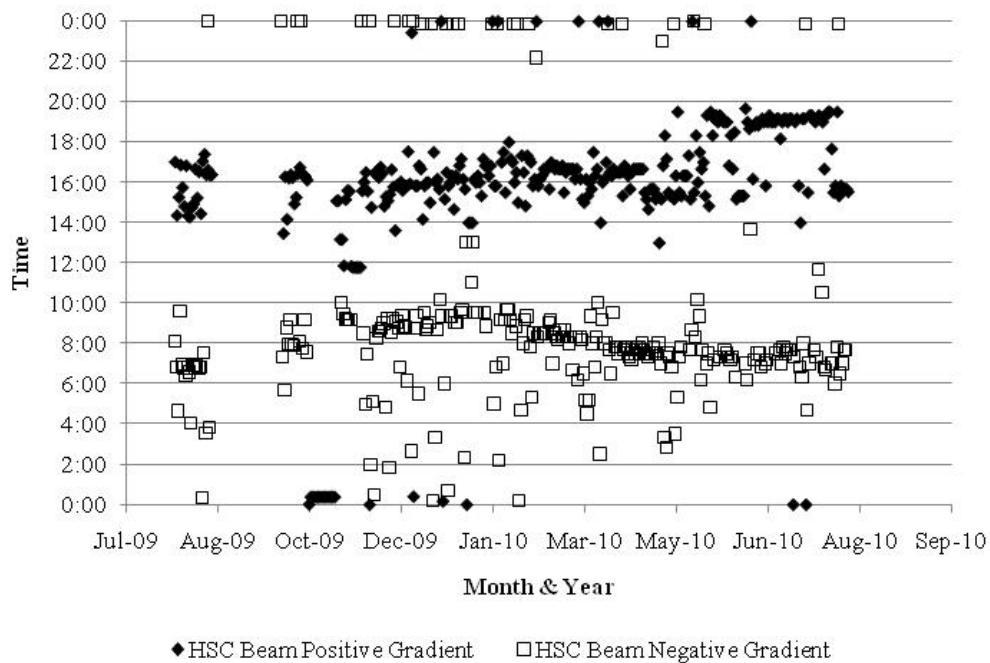


a.) Maximum Daily Positive Thermal Gradients

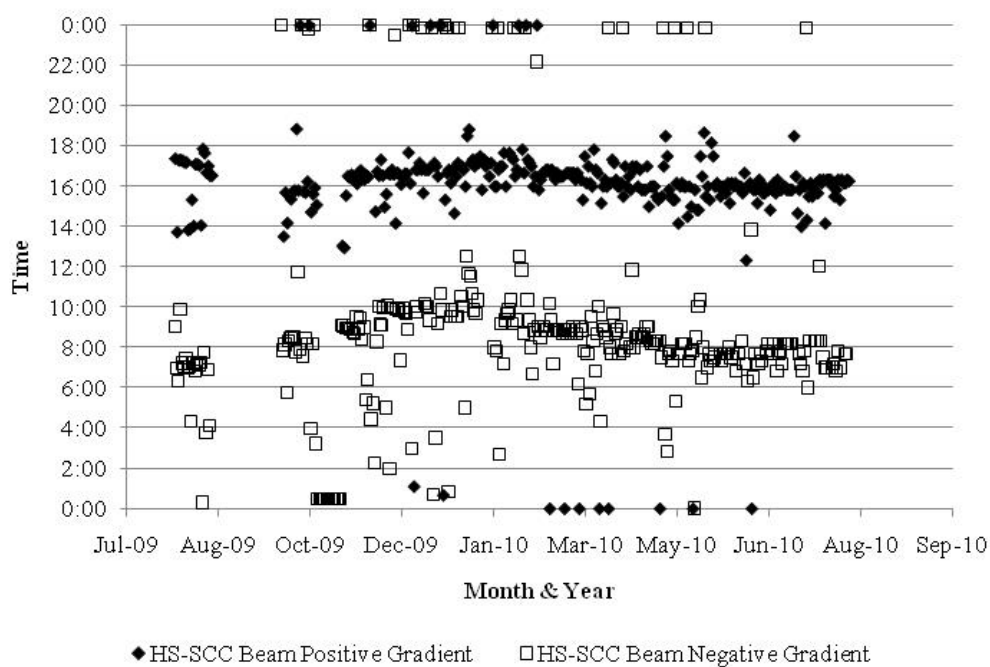


b.) Maximum Daily Negative Thermal Gradients

Figure 8.19. Maximum Daily Thermal Gradients for HSC & HS-SCC Deck Panels.

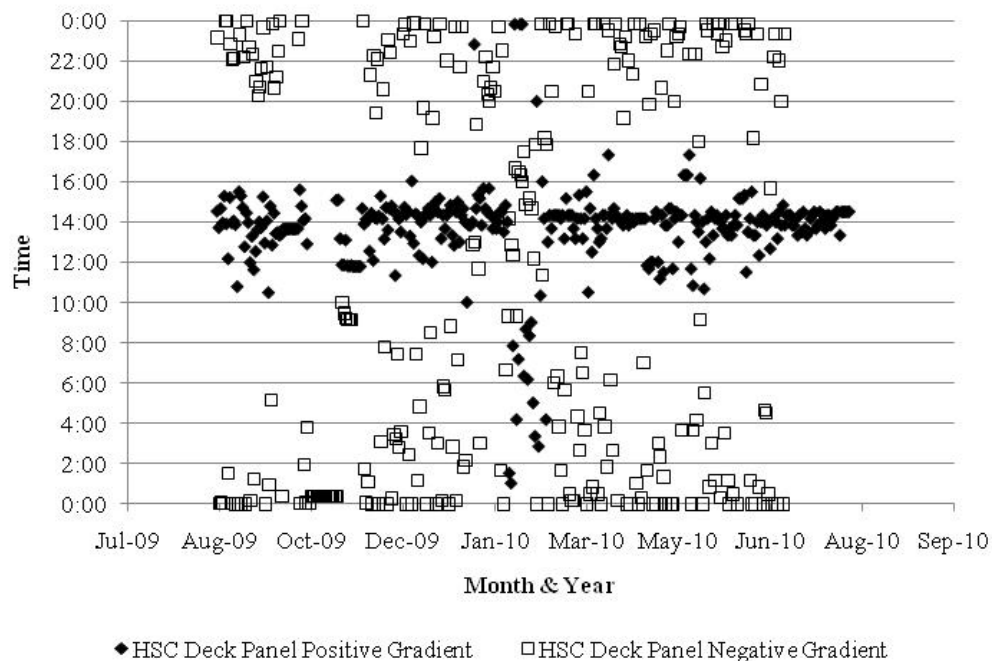


a.) HSC Beams

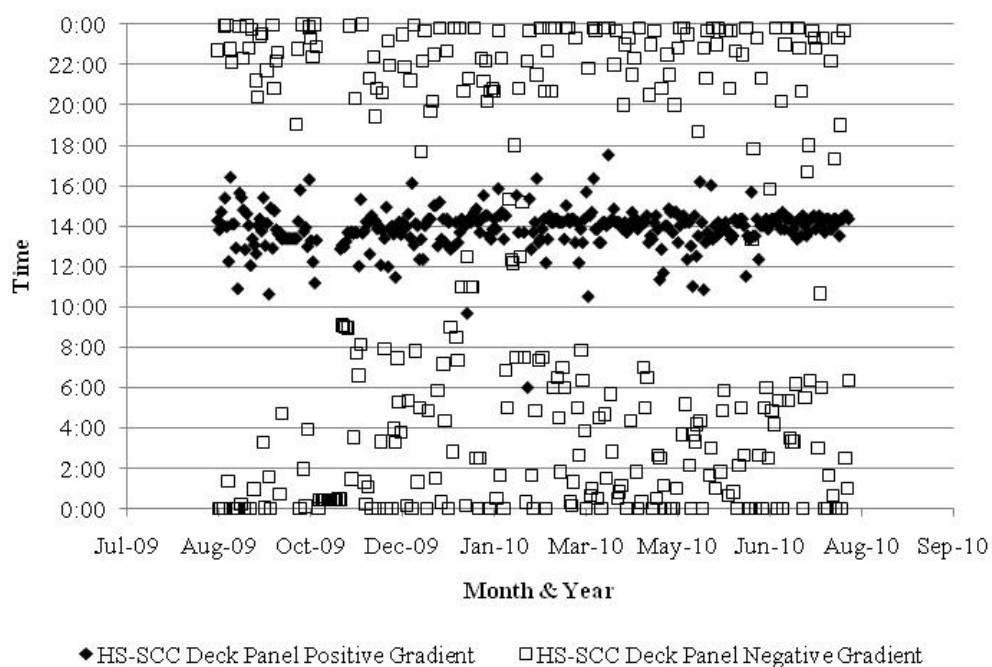


b.) HS-SCC Beams

Figure 8.20. Time of Maximum Positive & Negative Gradients for Beams.

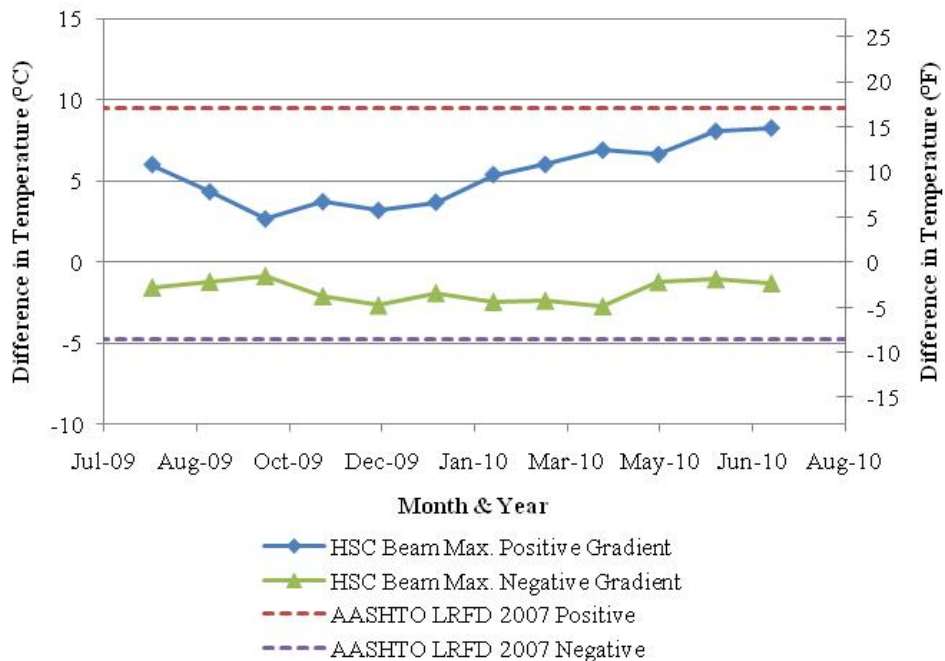


a.) HSC Deck Panels

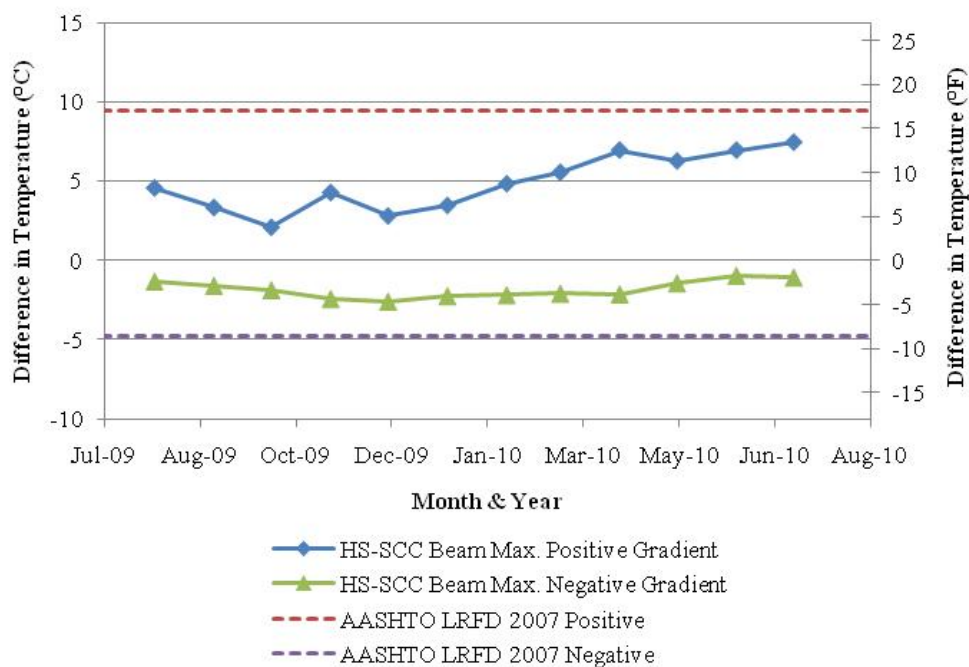


b.) HS-SCC Deck Panels

Figure 8.21. Time of Maximum Positive & Negative Gradients for HS-SCC Panels.



a.) HSC Beams

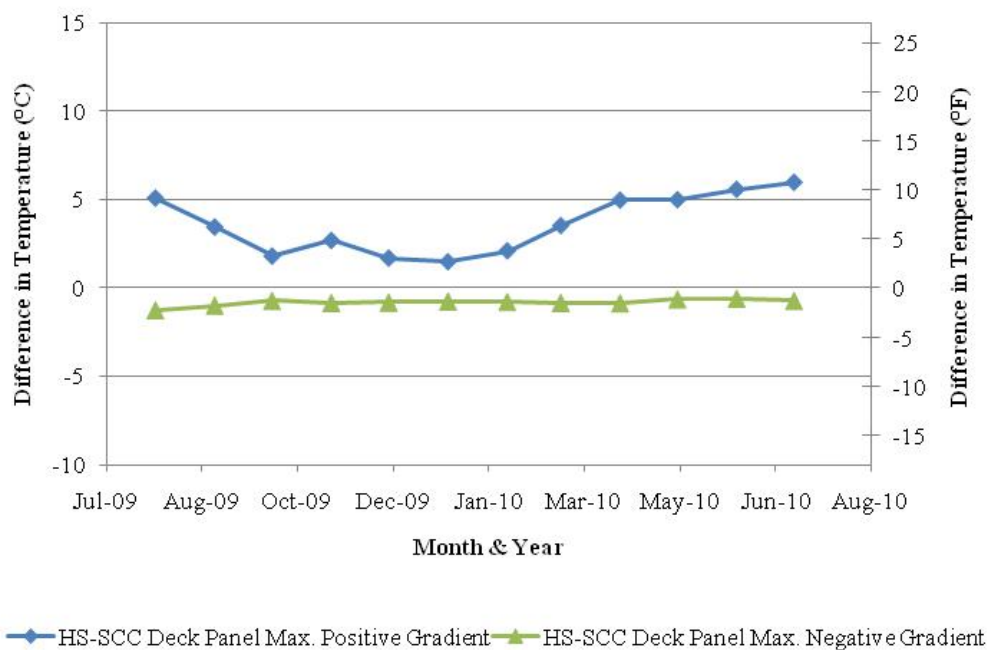


b.) HS-SCC Beams

Figure 8.22. Average Maximum Monthly Gradients of Bridge Beam.



a.) HSC Deck Panels



b.) HS-SCC Deck Panels

Figure 8.23. Average Maximum Monthly Gradients of Bridge Deck Panels.

The maximum positive and negative gradients tended to be slightly higher for the HSC bridge than the HS-SCC bridge. The HSC precast spandrel beams positive thermal gradient averaged 0.4°C (0.8°F) higher than HS-SCC precast spandrel beams. The negative gradients tended to be much closer than the positive gradients. However, the HSC precast spandrel beams averaged a thermal gradient 1°C (2°F) higher than the HS-SCC precast deck panels. In addition, the HSC precast deck panels maximum thermal gradient tended to be 0.5°C colder than the HS-SCC precast deck panels. Differences in thermal gradients can be attributed to the higher coarse aggregate content and larger mass of concrete in the HSC bridge when compared to the HS-SCC bridge. However, since temperature variation was minimal, differences in thermal gradients are more likely attributed to differences due to shade and position of the sun. Furthermore, both the HSC and HS-SCC had maximum and minimum daily gradients that were outside the design specification provided by AASHTO (2007). The monthly average stayed within the design values. It is recommended that the AASTHO specification be investigated for new guidance on gradients for main beam/girders elements that do not rest below the deck as in the case with these pedestrian bridges.

For both bridges, the maximum positive gradients tended to occur between 2:00 PM and 6:00 PM for the precast spandrel beams and 12:00 PM and 4:00 PM for the precast deck panels. This remained uniform throughout the year. However, it should be noted that the time in the data acquisition system remained at daylight savings time throughout the year. The maximum thermal gradients occurred during the summer months in which more solar radiation is present to cause the tops of the beams and deck panels to become warmer than the bottoms. However, the negative gradients tended to be more uniform throughout the year. There was an increase in the maximum negative thermal gradients in the winter; however, it is not as dramatic as the positive thermal gradients. The maximum positive and negative thermal gradient for the HSC precast deck panels and beams are presented in Table 8.9.

Table 8.9. Maximum & Minimum Thermal Gradients.

Member	Precast Beam		Precast Deck Panel	
Description	Support	Mid-Span	M. Steel	GFRP
HSC Bridge				
Positive Gradient				
Gradient	13.19°C	12.50°C	8.36°C	12.91°C
Date	3/23/10	7/13/10	1/31/10	6/27/10
Negative Gradient				
Gradient	-6.90°C	-5.16°C	-2.70°C	-3.91°C
Date	4/9/10	12/10/09	1/31/10	6/27/10
HS-SCC Bridge				
Positive Gradient				
Gradient	12.34°C	11.76°C	5.84°C	9.76°C
Date	3/23/10	5/11/10	5/28/10	7/2/10
Negative Gradient				
Gradient	-6.99°C	-4.66°C	-0.97°C	-2.59°C
Date	1/10/10	12/10/09	1/10/10	9/28/09
Temperature: °F = (1.8 * (°C)) + 32				

The positive thermal gradients for the supports tended to be 1°C (2°F) higher than at the mid-span for both the HSC and HS-SCC girders, and the negative thermal gradients for the supports tended to be 2°C (4°F) larger than at the mid-span for both the HSC and HS-SCC girders. While this variation is minimal, possible considerations for the mid-span having a higher gradient are as follows. The location of the support could experience slightly different temperatures due to shade and the position of the sun. In addition, heat gain and loss is impacted by the addition of the abutment mass. At this location, heat will enter and leave from the top and cause a higher thermal gradient than sections where heat can enter and dissipate more freely at the top and the bottom, such as

at the mid-span. The same effect is true in the winter and can provide a higher negative gradient in the winter.

The GFRP reinforced deck panels had a larger positive and negative thermal gradient than those reinforced with mild steel. This can be contributed due to the position of the deck panels and location of sun, shade, and wind. However, it is possible that the steel could provide a more uniform distribution of heat within the concrete deck panels because of its higher thermal conductivity when compared to GFRP.

Thermal gradients for the HSC and HS-SCC spandrel beams are illustrated in Figures 8.24 and 8.25. In addition, the thermal gradients for the HSC and HS-SCC precast deck panels are displayed in Figures 8.26 and 8.27. The thermal gradients shown are given at the dates considered to have the highest positive and negative thermal gradients for the spandrel beams and precast deck panels.

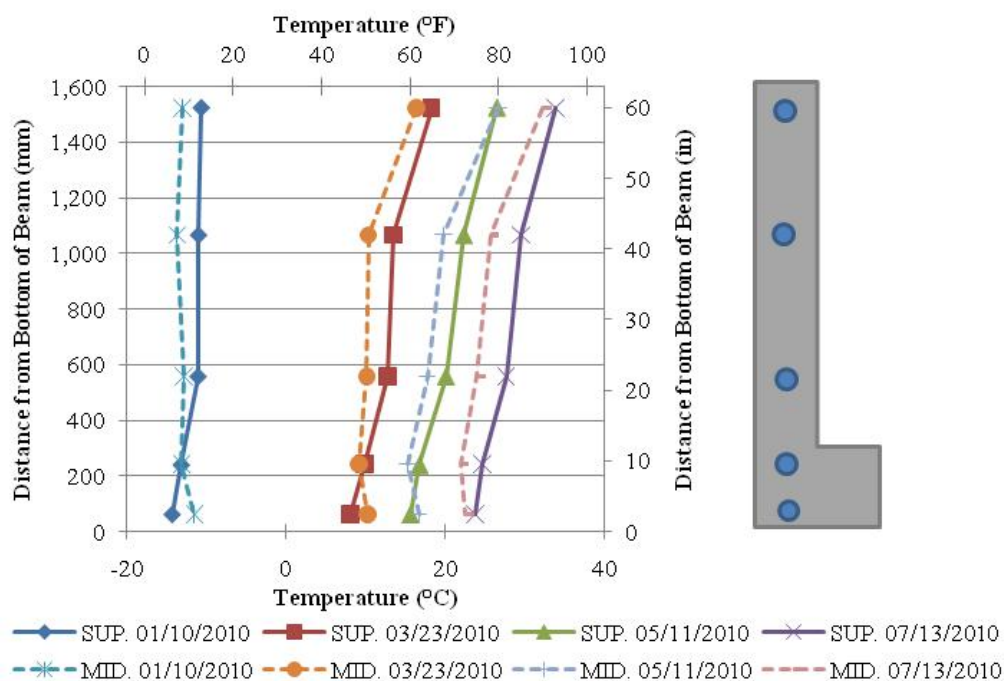


Figure 8.24. Thermal Gradients in HSC Spandrel Beams.

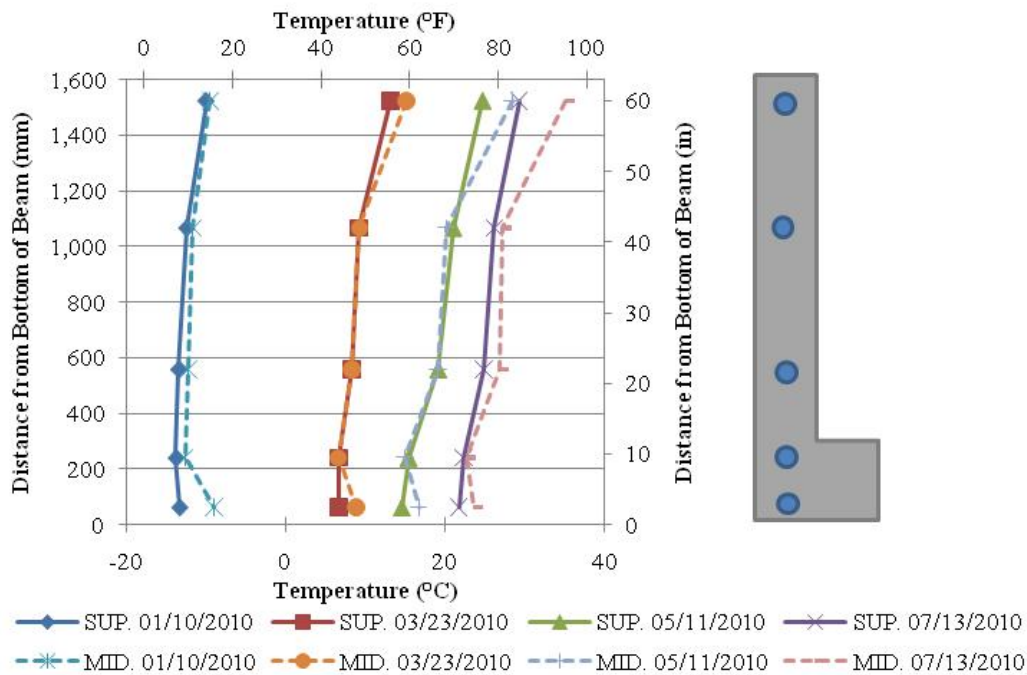


Figure 8.25. Thermal Gradients in HS-SCC Spandrel Beams.

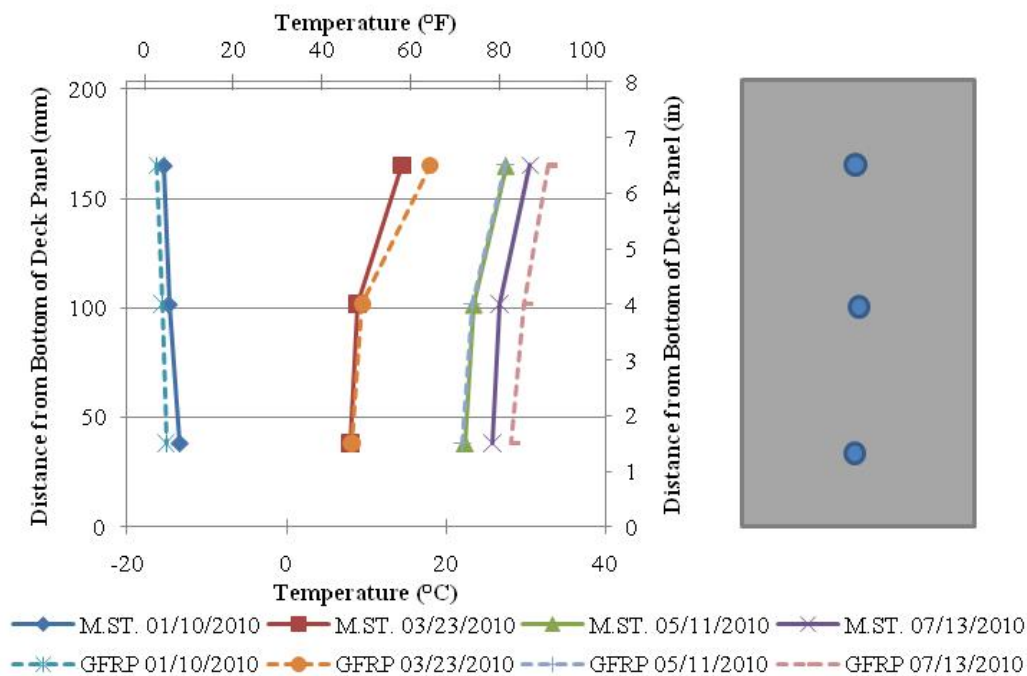


Figure 8.26. Thermal Gradients in HSC Precast Deck Panels.

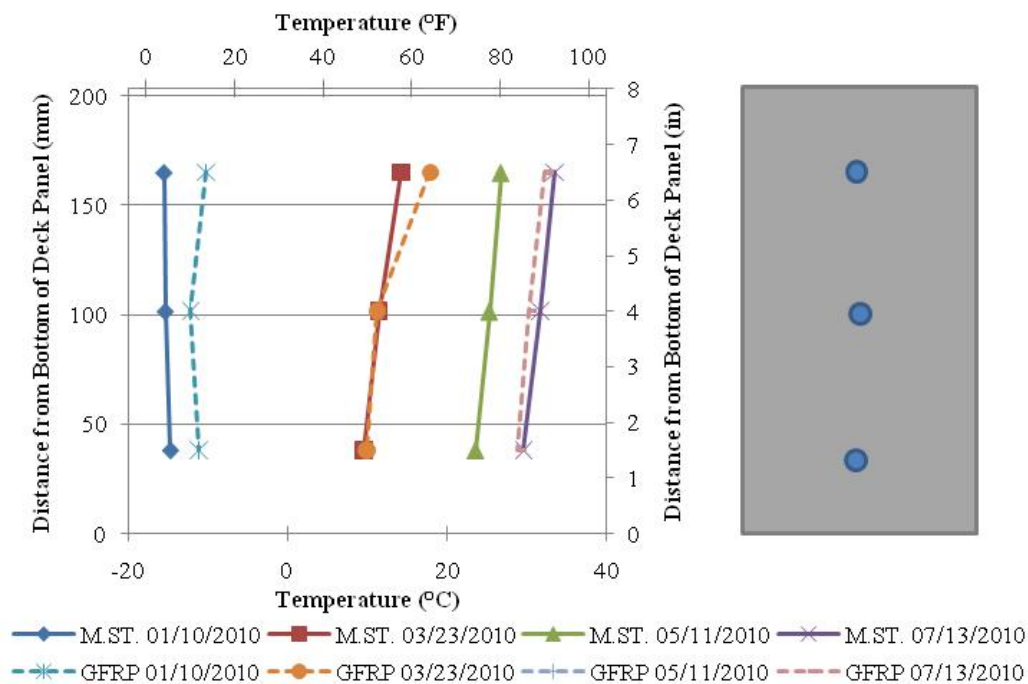


Figure 8.27. Thermal Gradients in HS-SCC Precast Deck Panels.

8.4.3. Discussion. To determine the applicability of HSC and HS-SCC to current design standards, the results for the maximum positive thermal gradients and negative thermal gradients were compared with the AASHTO LRFD Specification (2007). Figures 8.28 and 8.29 illustrate the theoretical positive gradient compared to the support and mid-span of the HSC and HS-SCC spandrel beams. Figures 8.30 and 8.31 illustrate the theoretical negative gradient compared to the support and mid-span of the HSC and HS-SCC spandrel beams.

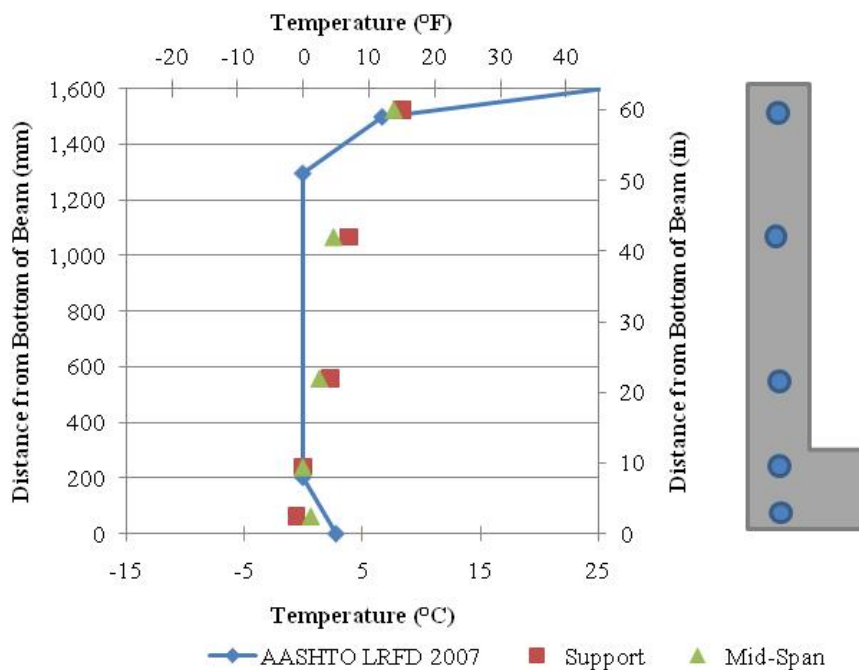


Figure 8.28. Design Positive Gradients vs. HSC Maximum Positive Gradients.

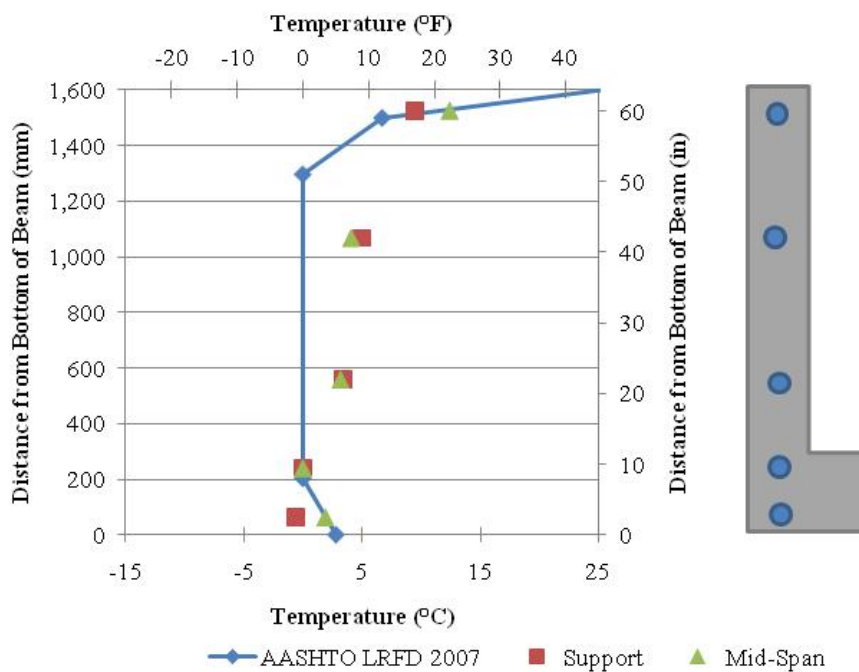


Figure 8.29. Design Positive Gradients vs. HS-SCC Maximum Positive Gradients.

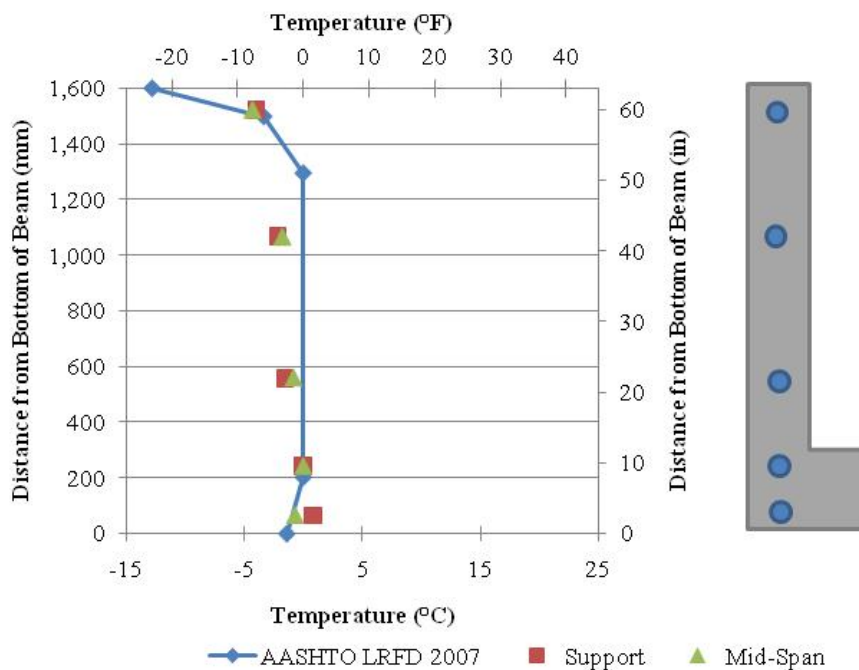


Figure 8.30. Design Negative Gradients vs. HSC Maximum Negative Gradients.

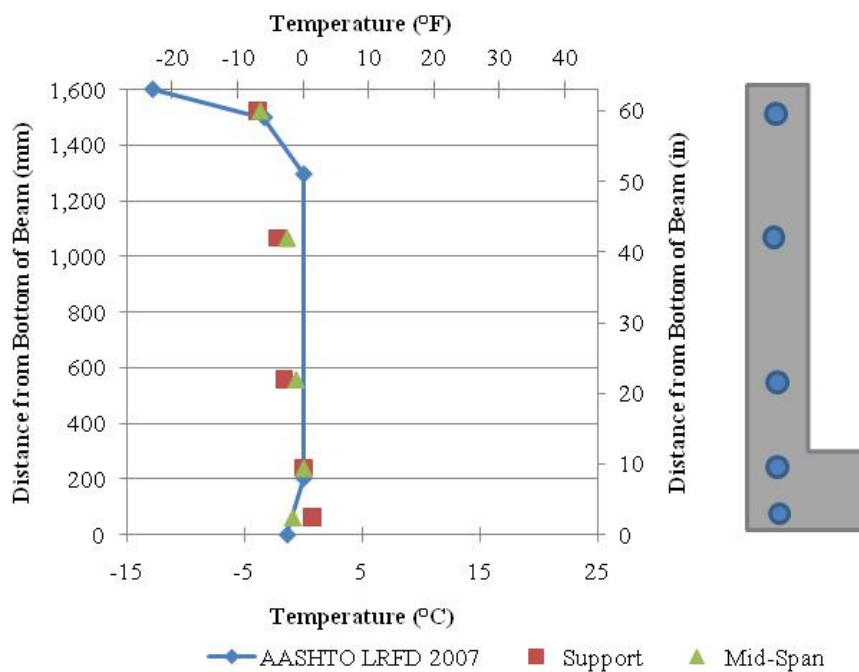


Figure 8.31. Design Negative Gradients vs. HS-SCC Maximum Negative Gradients.

The HSC and HS-SC have similar temperature profiles. When compared to the AASHTO LRFD (2007) model, the top and bottom flanges are relatively close to the model. However, the interior sections of the beam are underestimated by the model. In the HSC spandrel beam at 1,070 mm (42-in.) from the bottom, there is a difference of 3.2°C (5.8°F) between the actual and theoretical results. In the HS-SCC spandrel beam at 1,070 mm (42-in.) from the bottom, there is a difference of 4.5°C (8.2°F) between the actual results and AASHTO LRFD prediction around 5°C (9°F). Furthermore, the HS-SCC appears to have a larger thermal gradient when compared to the AASHTO LRFD model and HSC results. Both HSC and HS-SCC negative thermal gradients are much closer to the AASHTO LRFD model than the positive thermal gradients, and only differentiate at most 1.9°C (3.5°F) from the actual and theoretical results.

8.5. SUMMARY AND CONCLUSIONS

During the test analysis it was determined that the maximum temperature rise of HSC was higher than that of the HS-SCC mixture. The HSC mixture had a maximum temperature rise of 36°C (65°F) for the HSC spandrel beams occurred at the mid-span of the member with an equivalent maximum temperature rise of 8.1°C per 100 kg/m³ (8.6°F per 100 lb/yd³) of cement or 7.5°C per 100 kg/m³ (8.0°F per 100 lb/yd³) of cementitious material. The HS-SCC spandrel beams had a maximum temperature rise of 32°C (58°F) at the mid-span with an equivalent maximum temperature rise of 8.2°C per 100 kg/m³ (8.7°C per 100 lb/yd³) of cement or 6.9°C per 100 kg/m³ (7.4°F per 100 lb/yd³) of cementitious material for the HS-SCC spandrel beams. Both materials have equivalent maximum temperature values lower than 10 to 14°C per 100 kg/m³ (11 to 15°F per 100 lb/yd³) specified by ACI Committee 363 (2010).

Bridge values recorded continuously for a year show that maximum temperatures tended to be 1°C (2°F) higher than the HS-SCC bridges. In addition, precast deck panels reinforced with mild steel had maximum temperatures 0.1°C (0.2°F) higher than the deck panels reinforced with GFRP.

The positive and negative thermal gradients monitored throughout the year tended to be slightly higher for the HSC bridges than for the HS-SCC bridges. In addition, the support locations tended to have a higher thermal gradient than at the mid-span of the

member. Furthermore, deck panels reinforced with GFRP were more inclined to have higher thermal gradients than deck panels reinforced with mild steel.

The positive thermal gradients computed utilizing the AASHTO LRFD (2007) model provided theoretical values that were close to the values of the top and bottom fiber of bridge beams. However, intermediate points appeared to be underestimated by the model. The negative thermal gradients computed with the AASHTO LRFD model were much closer to the actual thermal gradients than the positive gradient model.

9. CONCRETE STRAIN MEASUREMENTS

9.1. INTRODUCTION

Knowing the stresses within a concrete structure is vital for a sound design. It is difficult to measure stress directly. However, strain values can be determined throughout a structure by using strain gauges, such as the VWSGs utilized in this project. By multiplying the strains by the modulus of elasticity of the concrete, concrete stresses can be determined.

Key stages to monitor stresses are prior to release of prestressing strands, immediately after release of prestressing strands, storage, transport, erection, and service. At release, an elastic strain will occur as the prestressing force is applied to the concrete beam. During storage, changes in stress and strain within the concrete member occur with time dependent losses and changes in loading. Changes in stress and strain can also be monitored during transportation of the spandrel beams due to vibrations that occur during transport. During beam erection, deck panels placed on the beam cause a change in the stress and strain distribution within the member due to the addition of the deck panel dead load.

9.2. INTERPRETATION OF GAUGE READINGS

Raw strain readings provided by the VWSGs do not take into account the effects of temperature on the gauge. Roctest Inc. provided an equation and thermal coefficient for the VWSG to determine the actual strain experienced by the concrete. The equation provided by Roctest Inc. for the real strain, ε_r , utilizing the total strain, ε , linear expansion factor for the EM-5 gauge wire, α_c , concrete expansion factor, $\eta\beta$, temperature reading, T_1 , and initial temperature reading (T_0) is displayed in equation 48. For this project, the coefficient of thermal expansion for the VWSG was $11.5 \mu\varepsilon/^\circ\text{C}$ ($6.4 \mu\varepsilon/^\circ\text{F}$). The concrete expansion factor was determined by averaging a linear regression of strain versus temperature at various times throughout the year. The concrete expansion factor values, $\eta\beta$, are listed in Table 9.1.

$$\varepsilon_r = \varepsilon + (\alpha_c - \eta\beta)(T_1 - T_0) \quad (48)$$

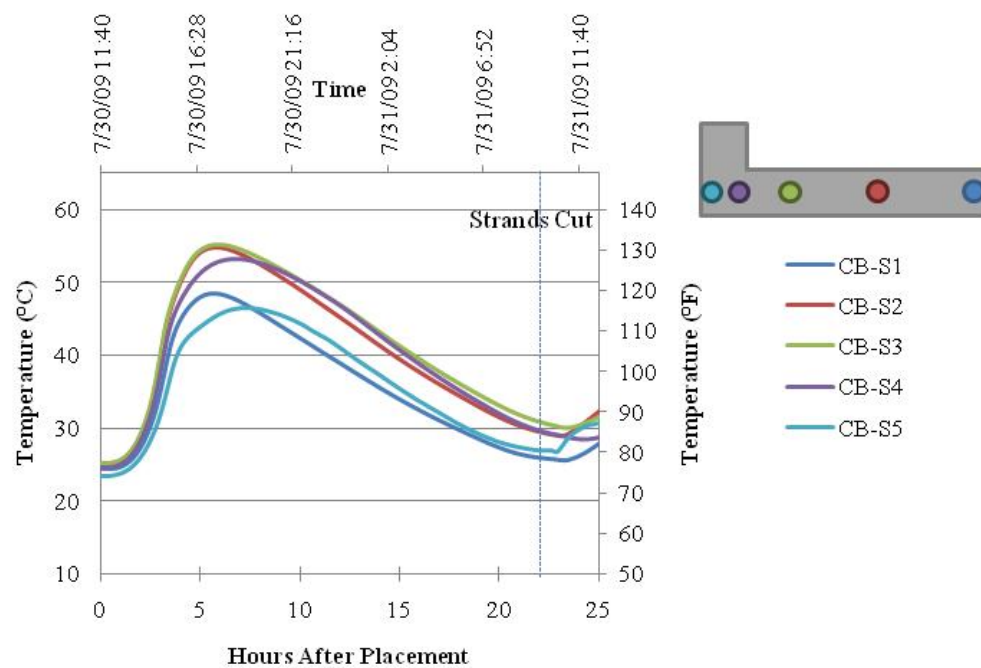
Table 9.1. Concrete Expansion Factors.

Placement Date	HSC	HS-SCC
7/30/2009	12.3	10.1
8/21/2009	11.7	9.1

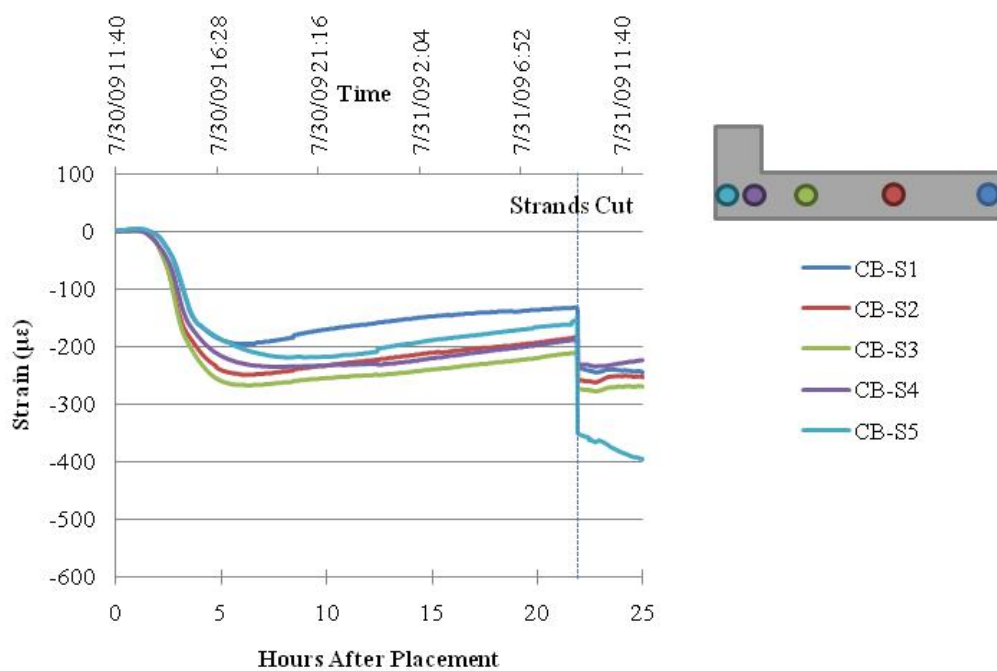
9.3. CONCRETE STRAINS BEFORE RELEASE

9.3.1. Background. Concrete strains prior to release occur as the concrete undergoes concrete hydration. During this period of time, the concrete experiences expansion and contraction within the member. A small contraction occurs with autogenous shrinkage. However, a more significant contraction occurs with drying shrinkage. In addition to shrinkage, expansion and contraction of the concrete due to changes in internal temperature from heat gain and loss from concrete hydration and ambient temperature conditions are expected (Myers and Yang, 2005).

9.3.2. Measurements and Discussion. Vibrating wire strain gauges placed throughout the cross section of the spandrel beam recorded strain and temperature readings every minute during the placement of the concrete. The strains were measured from a base reading from the sensors immediately prior to placement. Figures 9.1 through 9.4 illustrate the strain and temperature measured for both the HSC and HS-SCC spandrel beams at the support and mid-span of the member. In the following figures, compressive strains are negative and tensile strains are positive.

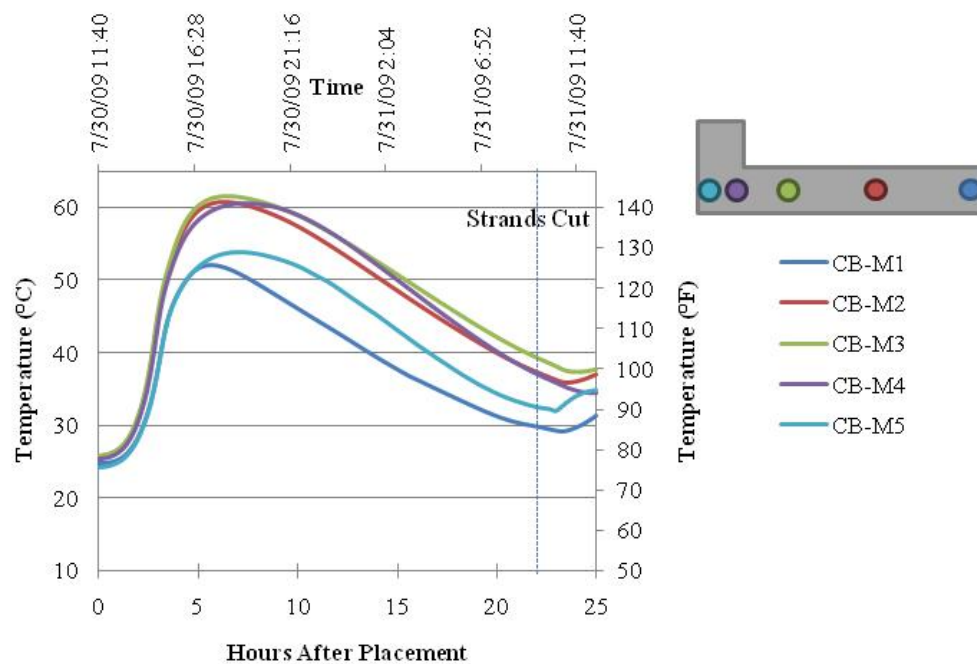


a.) Temperature

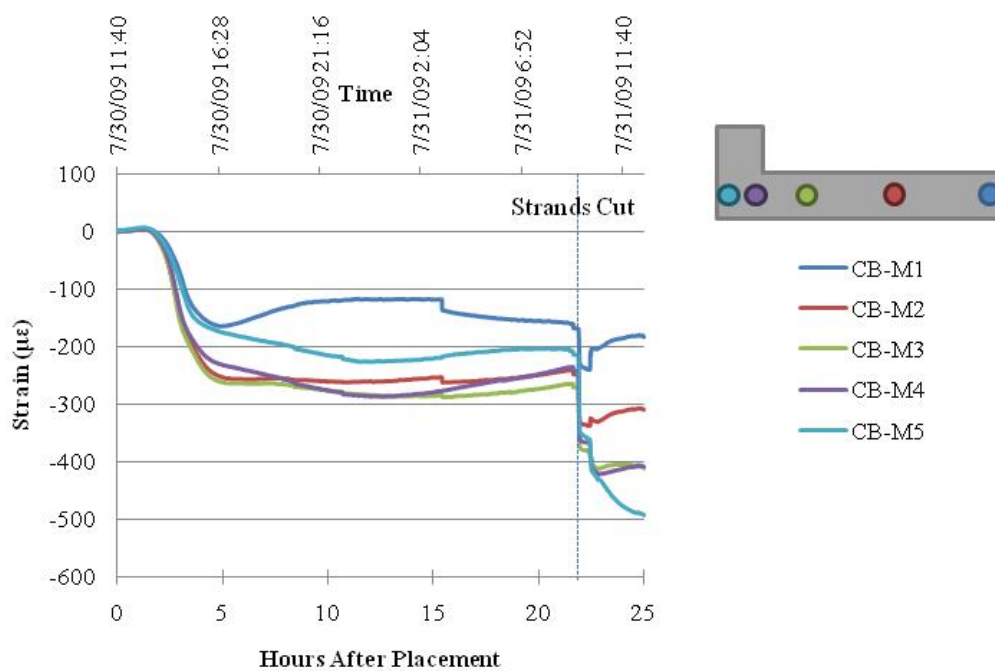


b.) Strain

Figure 9.1. Strains & Temperatures at Support of HSC Beam during Fabrication.

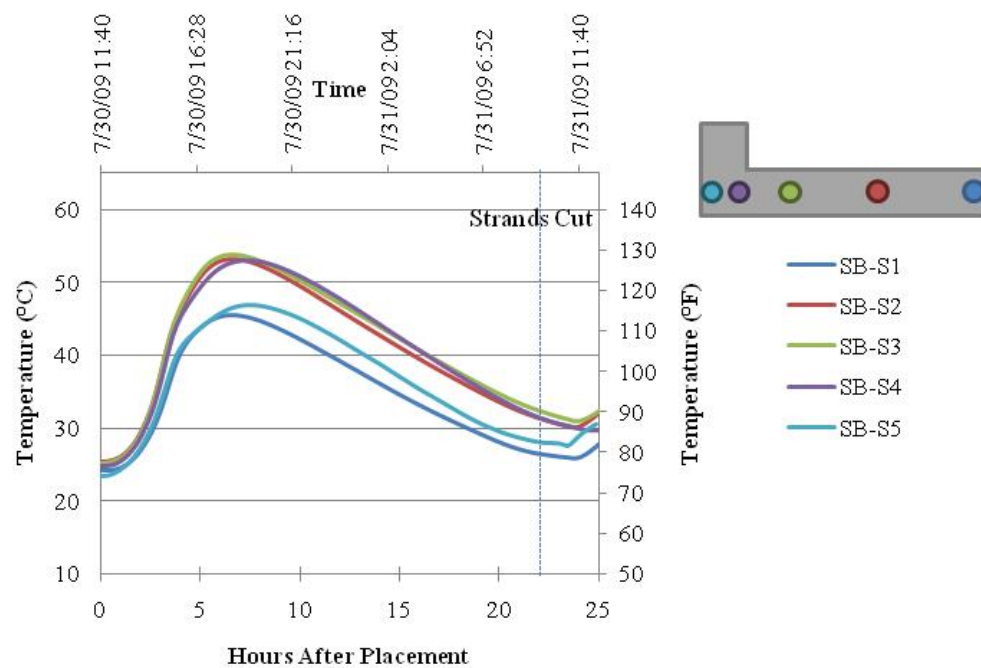


a.) Temperature

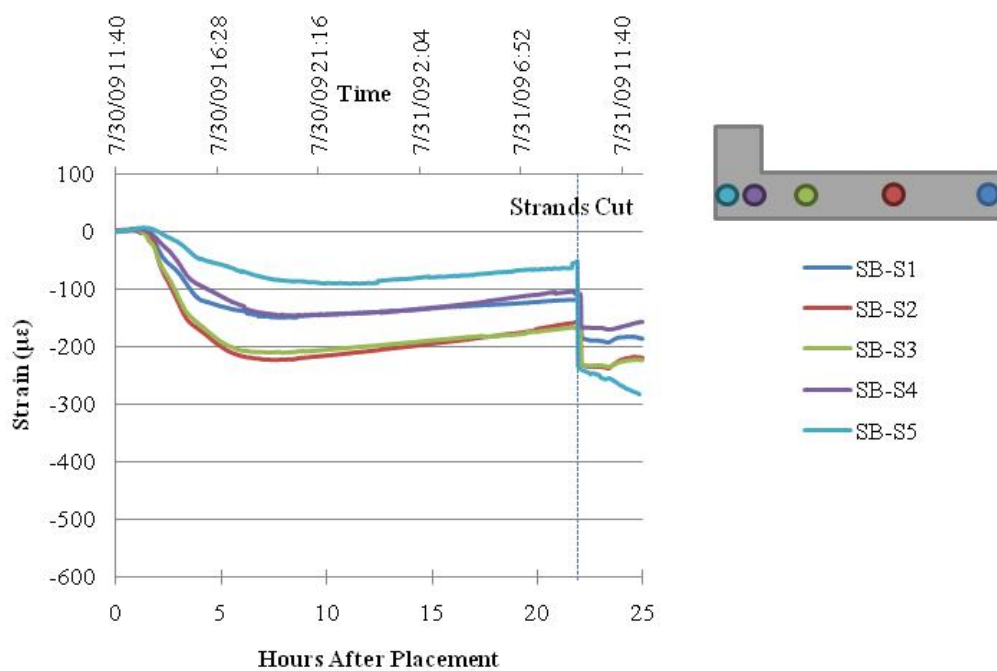


b.) Strain

Figure 9.2. Strains & Temperatures at Mid-Span of HSC Beam during Fabrication.

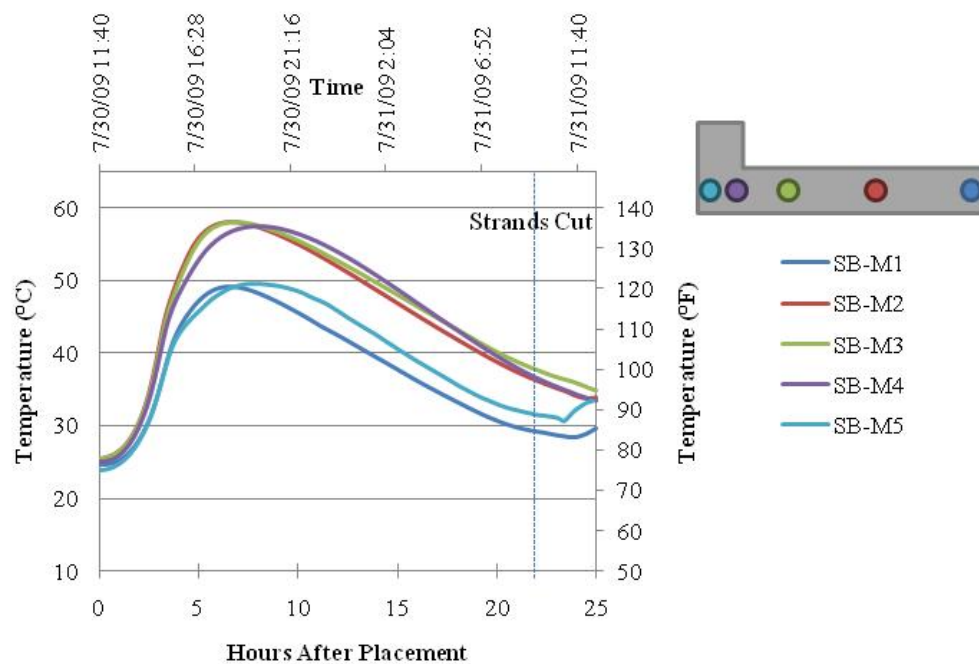


a.) Temperature

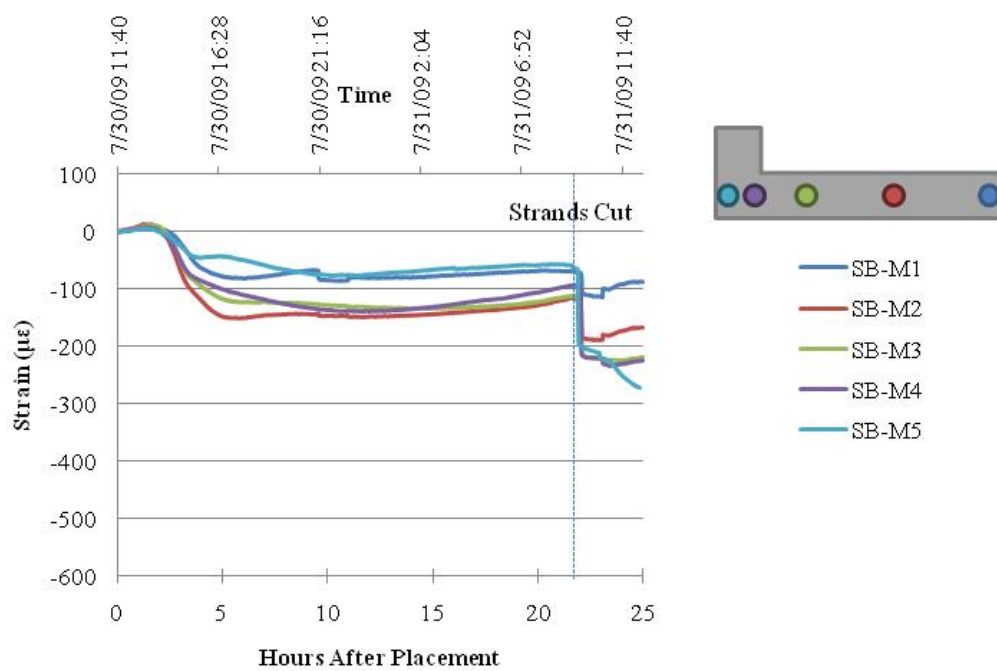


b.) Strain

Figure 9.3. Strains & Temperatures at Support of HS-SCC Beam during Fabrication.



a.) Temperature



b.) Strain

Figure 9.4. Strains & Temperatures at Mid-Span of HS-SCC Beam during Fabrication.

Before the strands were detensioned, both the HSC and HS-SCC spandrel beams underwent a period of contraction during the first hours of placement. However, as the temperatures continued to increase due to concrete hydration, some expansion occurred. Between both the HSC and HS-SCC specimens, the HS-SCC specimen experienced the smallest amount of contraction during concrete hydration. In both the HSC and HS-SCC beams, the VWSGs did not show signs of cracking during concrete hydration. Cracking within the concrete would cause a sudden increase in the tensile strain within the concrete beam.

9.4. CONCRETE STRAINS AFTER RELEASE OF PRESTRESS

9.4.1. Background. Checking fiber stresses at the release of prestress beams is one of key stages to check in design. At this moment, concrete strength is relatively low and can potentially be overstressed when the member is released. At this stage of design, only the axial load from the prestressing force, flexural load caused from eccentricity of the prestressing force, and any self-weight are applied to the member. Limits are provided by codes, such as ACI 318 (2008), that are often used in the design of prestressed concrete members.

9.4.2. Measurements and Discussion. Each beam was fitted with vibrating wire strain gauges throughout the cross section of the support and mid-span. Strain readings were recorded before and after release of the prestress tendons. The strain values were compared to the theoretical strain values determined by dividing the calculated stress values by the mixture's measured modulus of elasticity. This method is displayed in equation 49. In equation 49, the strain, $\varepsilon(y)$, is determined by knowing the prestressing force, P , the cross sectional area of the spandrel beam, A , the moment of inertia of the section, I , the eccentricity, e , the distance from the bottom of the spandrel beam to the centroid, y_b , the distance from the bottom to the location in question, y , the moment applied due to self-weight or an external load, M , and the modulus of elasticity of the member at release, E_{ci} . Since the beam was lying on its side, no moment was considered in the equation. In addition, the prestressing force was assumed to be ninety percent of the original load at release as recommended for low-relaxation tendons (Nawy, 2006) (Brewer & Myers, 2010). This assumption was made because load cells could not

be utilized to determine the actual prestress loss at release as mentioned previously. A comparison between the theoretical values and strain readings are displayed in Figures 9.5 and 9.6 for the mid-span of the HSC and HS-SCC beams. In this comparison, a regression line was fit to the strain data points at the mid-span of the spandrel beams. Both the HSC and HS-SCC beams had r-squared values from 0.95 to 0.99. The values are relatively close to 1.0 indicating that the plane section of the beam remained plane.

$$\varepsilon(y) = \frac{1}{E_{ci}} \left(-\frac{P}{A} - \frac{Pe(y_{bot}-y)}{I} + \frac{M(y_{bot}-y)}{I} \right) \quad (49)$$

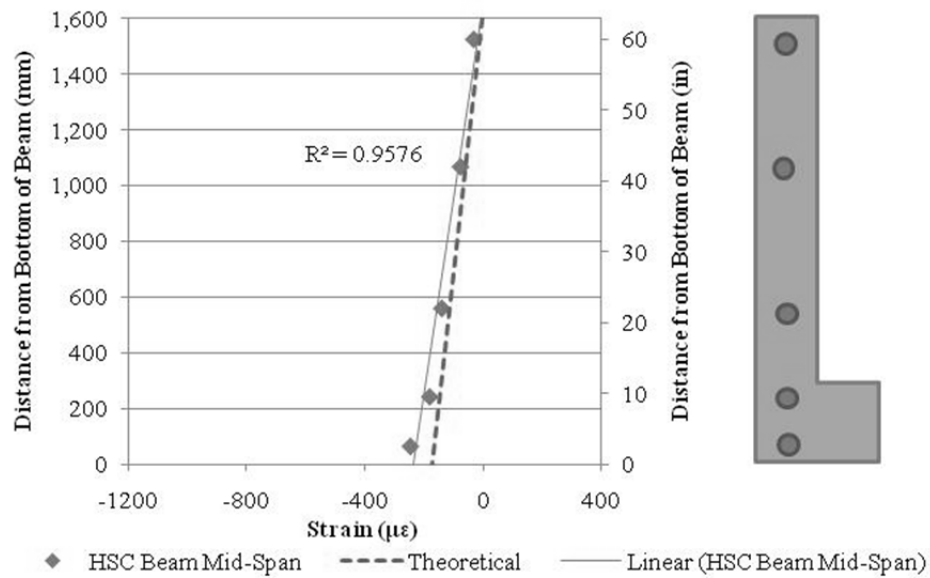


Figure 9.5. Strain Comparison at Mid-Span of HSC Spandrel Beam at Release.

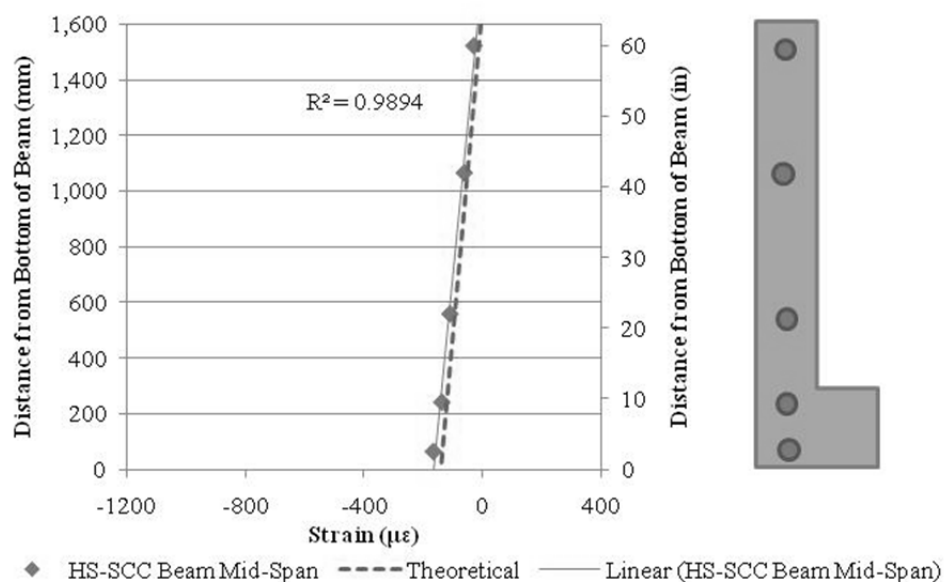
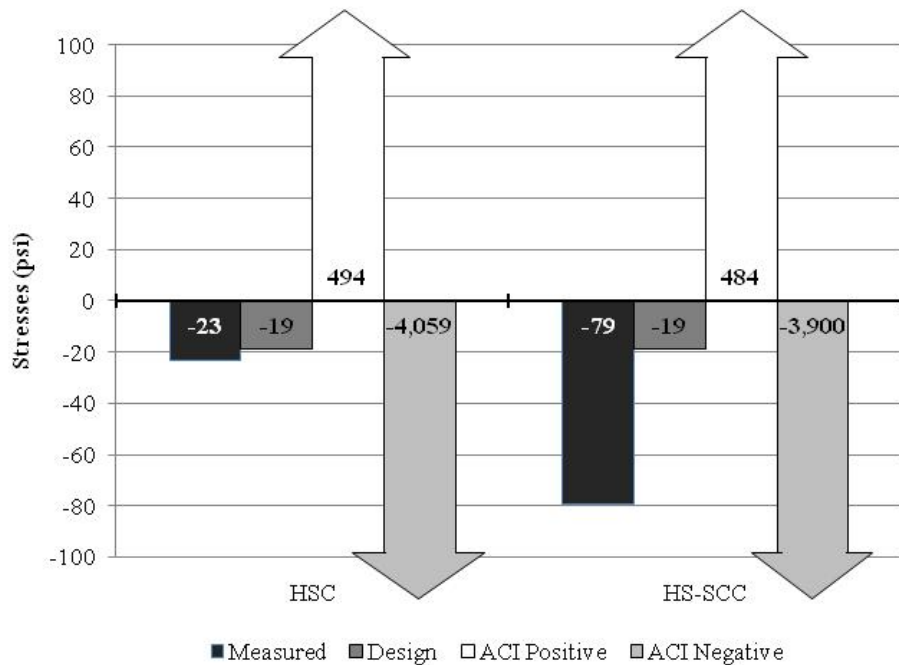


Figure 9.6. Strain Comparison at Mid-Span of HS-SCC Spandrel Beam at Release.

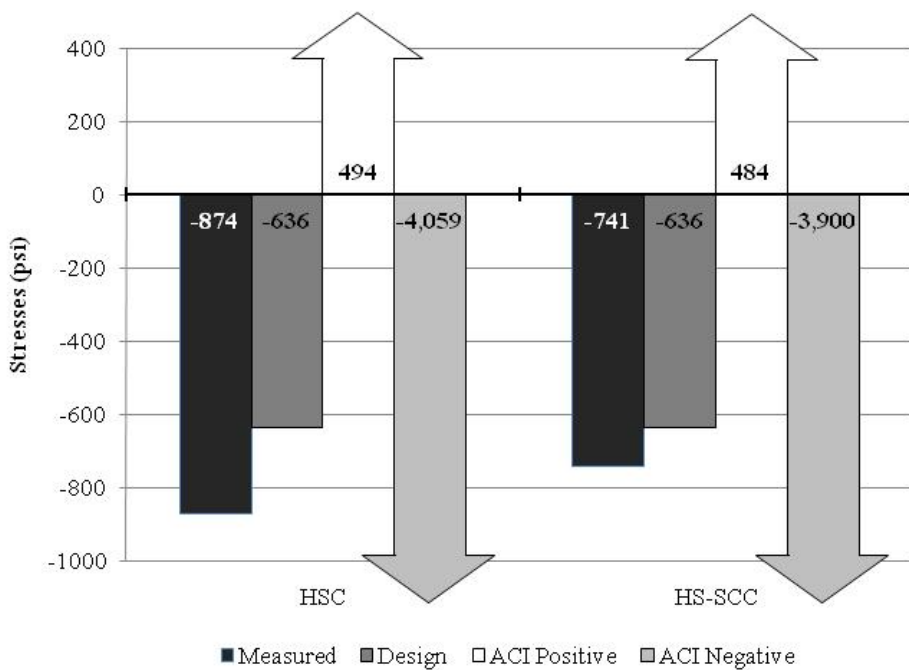
The determined strain data at the mid-span were very close to the predicted values. The HSC bottom fiber compressive strain values tended to be about 27% higher than predicted, and the HS-SCC bottom fiber compressive strain values tended to be about 14% higher than predicted. The support locations were not as accurate due to the necessity to use design equations for the development and transfer length specified by ACI 318 (2008) due to lack of data required to accurately determine the development and transfer length.

Measured stresses determined from linear regression are compared with design and allowable stresses specified in ACI code in Figure 9.7 and 9.8 for the top and bottom of the mid-span of the HSC and HS-SCC spandrel beams. In both Figures 9.7 and 9.8, it is apparent that the measured values were higher than the design values for HSC and HS-SCC. The HS-SCC values were slightly closer to the design values than HSC by about 13% at mid-span bottom. However, at the mid-span top, the HSC stress values were much closer to the design values than the HS-SCC stress values by approximately 56%. The magnitude of stress was well within the boundaries specified by ACI.



Conversion: 1,000 psi = 6.895 MPa

Figure 9.7. Comparison of Stresses at Release for Top Fiber Mid-Span.



Conversion: 1,000 psi = 6.895 MPa

Figure 9.8. Comparison of Stresses at Release for Bottom Fiber Mid-Span.

9.5. CONCRETE STRAINS IN BEAMS DURING STORAGE

9.5.1. Background. Before the bridge girders were transported to the bridge erection site, they were stored in the precasting yard and were subjected to the prestressing force, self-weight, and time-dependent losses. The time dependent losses included creep, shrinkage and relaxation losses.

ACI Committee 435-Deflection of concrete Building Structures (ACI 435R, 1995) provides a time dependent equation to approximate the strain within a concrete member over a period of time. Equation 50, predicts strain, ε , versus time, t , at a distance y from the bottom of the beam.

$$\varepsilon(y, t) = - \left(\frac{1+S_t}{E_{ci}} \right) \left(\frac{P_o}{A} \right) - \left(\frac{1+S_t}{E_{ci}} \right) \left(\frac{P_o e (y_b - y)}{I} \right) + \left(\frac{1+C_{ct}}{E_{ci}} \right) \left(\frac{M(y_b - y)}{I} \right) + \varepsilon_{sh} \quad (50)$$

$$S_t = \frac{P_o - P_e}{P_o} + \left(1 - \frac{P_o - P_e}{2P_o} \right) C_{ct} \quad (51)$$

In the equations above, y is the distance from the bottom of the beam; y_b is the distance from the bottom of the beam to the centroid; P_o is the initial prestressing force at release; P_e is the effective prestressing force at the required time, t ; E_{ci} is the modulus of elasticity of the concrete at release; I is the moment of inertia of the beam cross section; e is the eccentricity; C_{ct} , is the creep coefficient at time, t ; ε_{sh} is the shrinkage strain; S_t is a modification factor that takes into account creep effects. S_t is computed in equation 51.

9.5.2. Measurements and Discussion. The strain gauges within the spandrel beams continued to monitor strain until the bridge spandrels were fabricated. At this time period, both the spandrel beams were supported at multiple sections causing minimal self-weight moment to be applied. Therefore, when determining the theoretical strain, no moment was added to equation 50 for self-weight. The HSC strain profiles versus theoretical profiles are illustrated in Figures 9.9 and 9.10 at the ages of 7 and 14 days. In addition, the 7 and 14 day age strain profiles are presented for HS-SCC in Figures 9.11 and 9.12. The Excel spreadsheet used to compute the HSC and HS-SCC strain profiles using equations 50 and 51 is shown in Appendix D. In addition, any prestress loss was estimated using the PCI Design Handbook (2004).

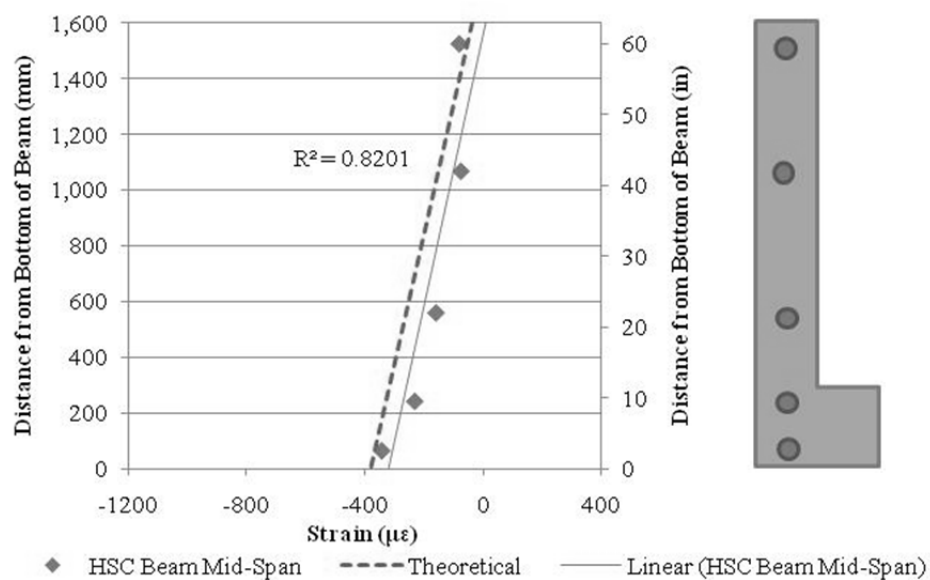


Figure 9.9. Strain at Mid-Span of HSC Spandrel Beam at 7 Days.

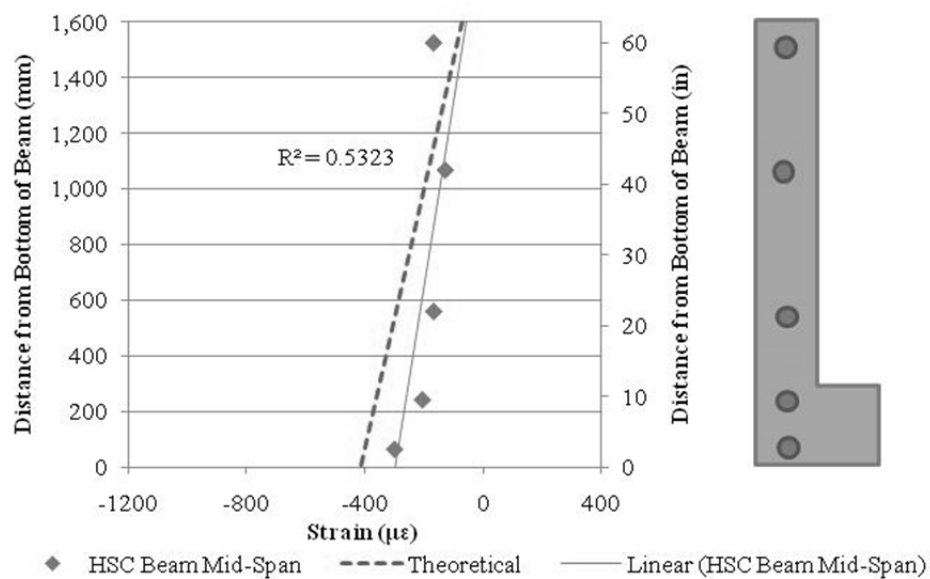


Figure 9.10. Strain at Mid-Span of HSC Spandrel Beam at 14 Days.

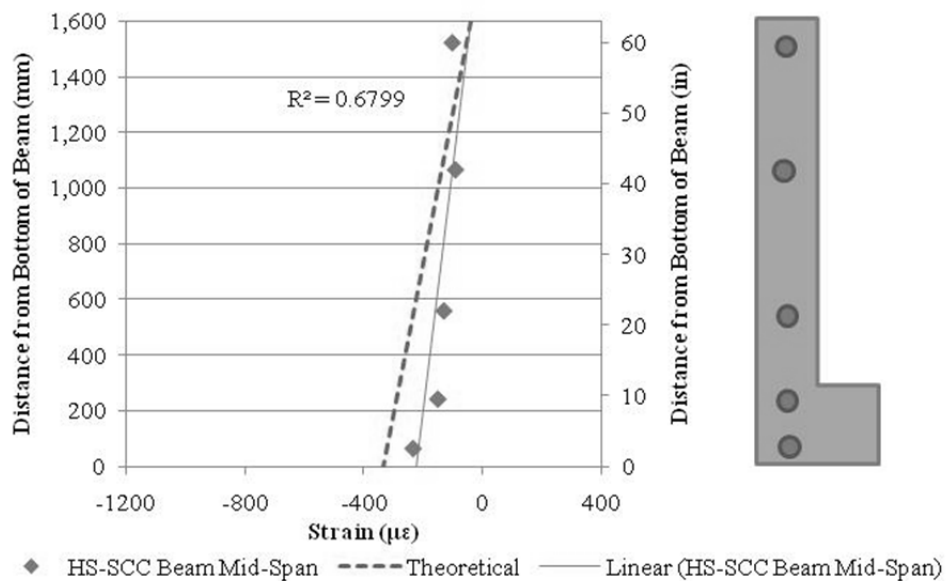


Figure 9.11. Strain of HS-SCC Spandrel Beam at 7 Days.

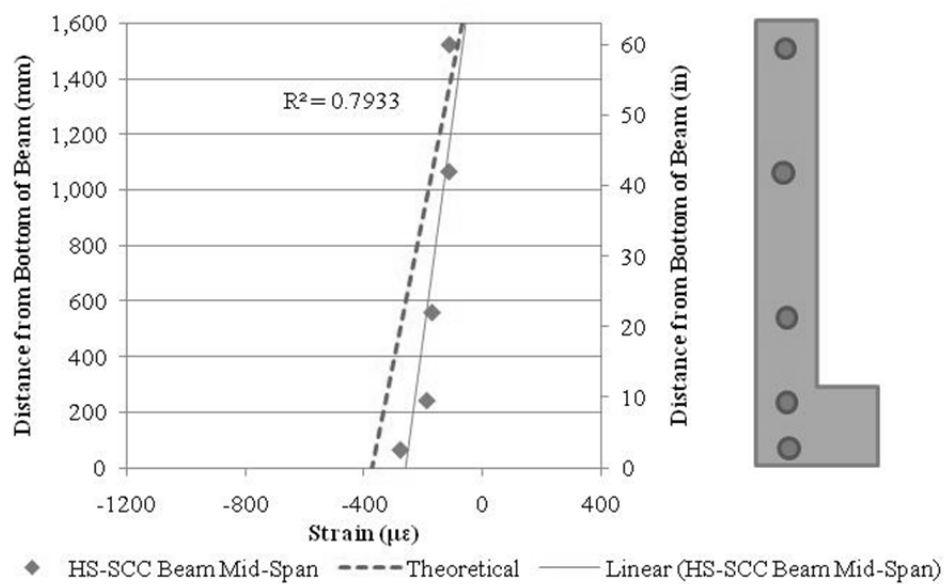


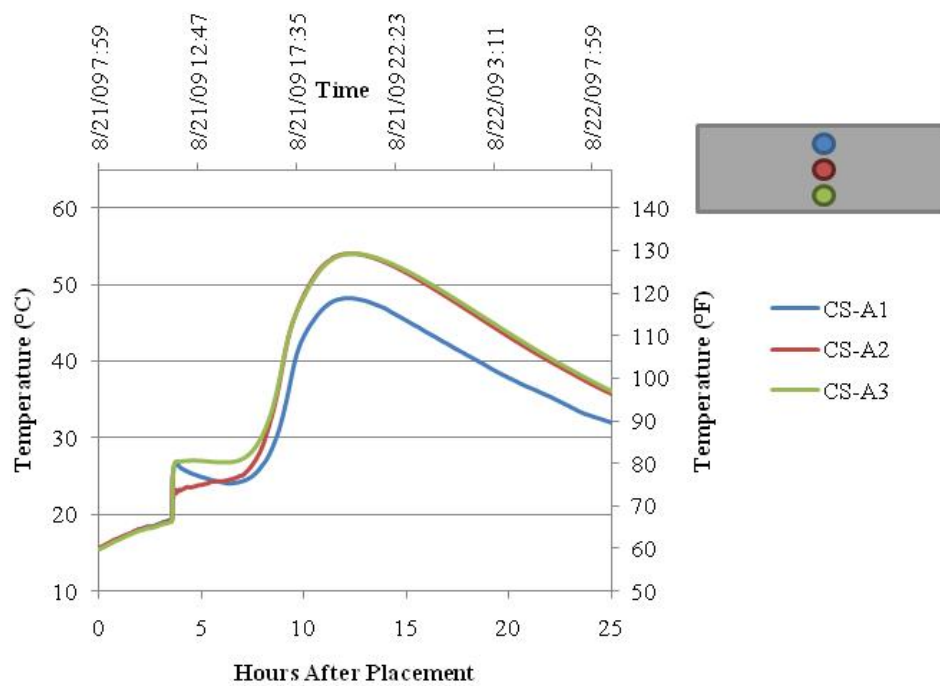
Figure 9.12. Strain of HS-SCC Spandrel Beam at 14 Days.

During the first two weeks, predicted and measured values corresponded fairly well for HSC and HS-SCC. The percentage difference for the HSC strains at release ranged from 15 to 29% and the HS-SCC strains ranged from 15 to 33%. However, as the HSC and HS-SCC beams age, the percentage difference between predicted and measured values became larger. Over time, the time dependent “local” prestress losses varied among the tendons resulting in a non-linear distribution. One may recall that the tendons had varied pre-tensioned levels along the depth of the member. Some tendons, therefore, had time-dependent relaxation, while others did not. This is evident in the R-squared value. Over time, the R-squared value begins to drop and the strain distribution begins to experience a curved non-linear shape. Since the section was designed without a lateral eccentricity by creating symmetry based on strand stress as opposed to geometric symmetry, non-uniform prestress losses affected the strain profiles over time. Furthermore, deck panel loading was not applied directly through the centroid of the spandrel beams. The out of plane moment induced by the deck panel load can further affect the beam strain profile.

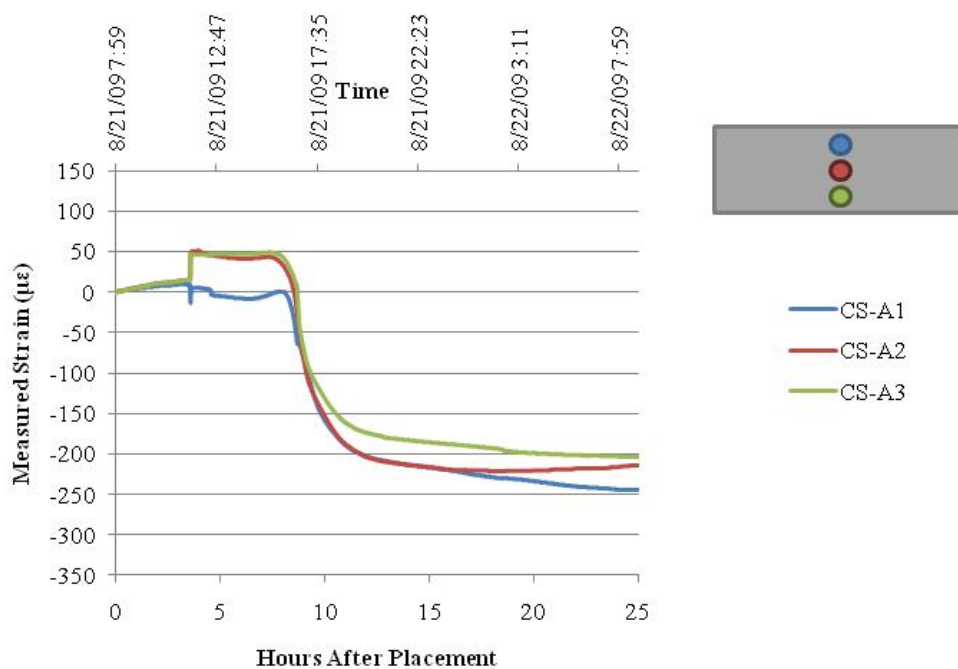
9.6. CONCRETE STRAINS IN DECK PANELS DURING FABRICATION

9.6.1. Background. Similar to the prestressed spandrel beams, the precast deck panels undergo similar concrete hydration strains during fabrication. Strains during fabrication include a small contraction from autogenous shrinkage, a more significant contraction during drying shrinkage, and expansion and contraction due to thermal effects. The amount and type of reinforcing can also influence the level of initial strain in the concrete due to restraint provided by the tensile reinforcing and associated boundary conditions. The amount of strain within the concrete reinforced with GFRP would be expected to have less restraint and affect the thermal expansion and contraction of the concrete due to the lower stiffness of GFRP when compared to mild steel.

9.6.2. Measurements and Discussion. Vibrating wire strain gauges were placed within the mid-span of the precast deck panels close to the top fiber, bottom fiber, and middle of the deck panel and monitored changes in temperature and strain. Figures 9.13 through 9.16 display the temperature and strain readings for HSC and HS-SCC precast deck panels reinforced with mild steel and GFRP.

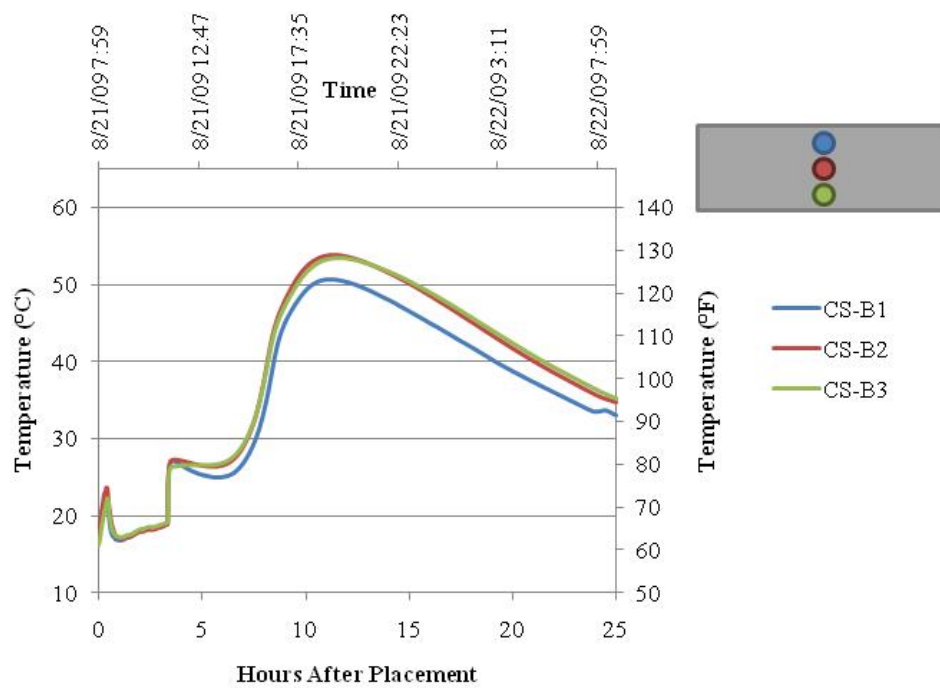


a.) Temperature

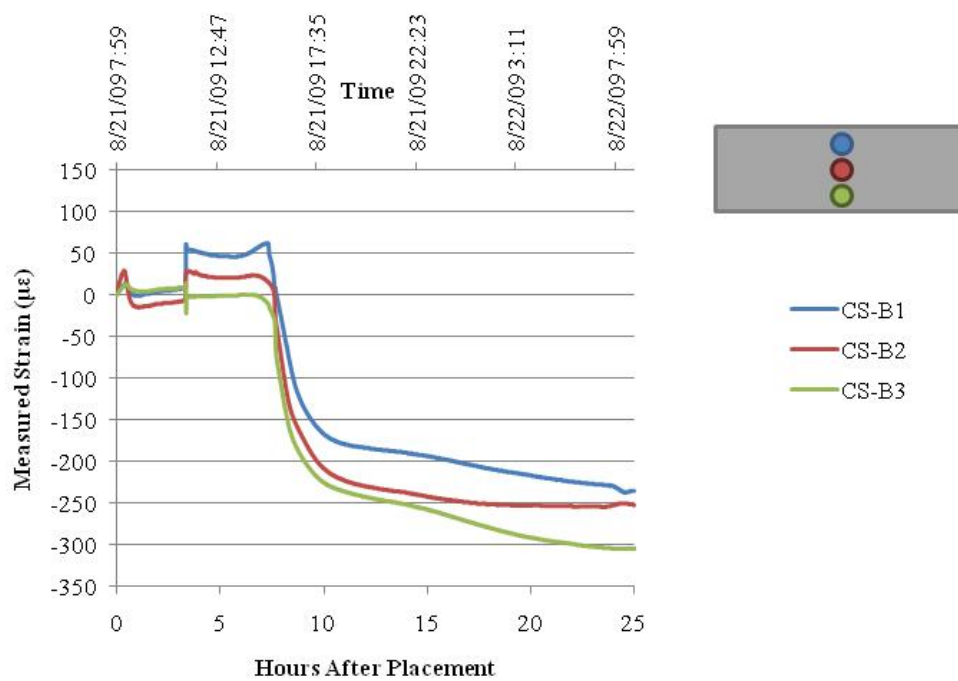


b.) Strain

Figure 9.13. Strain in HSC Deck Panel Reinforced with Mild Steel.



a.) Temperature



b.) Strain

Figure 9.14. Strain in HSC Deck Panel Reinforced with GFRP.

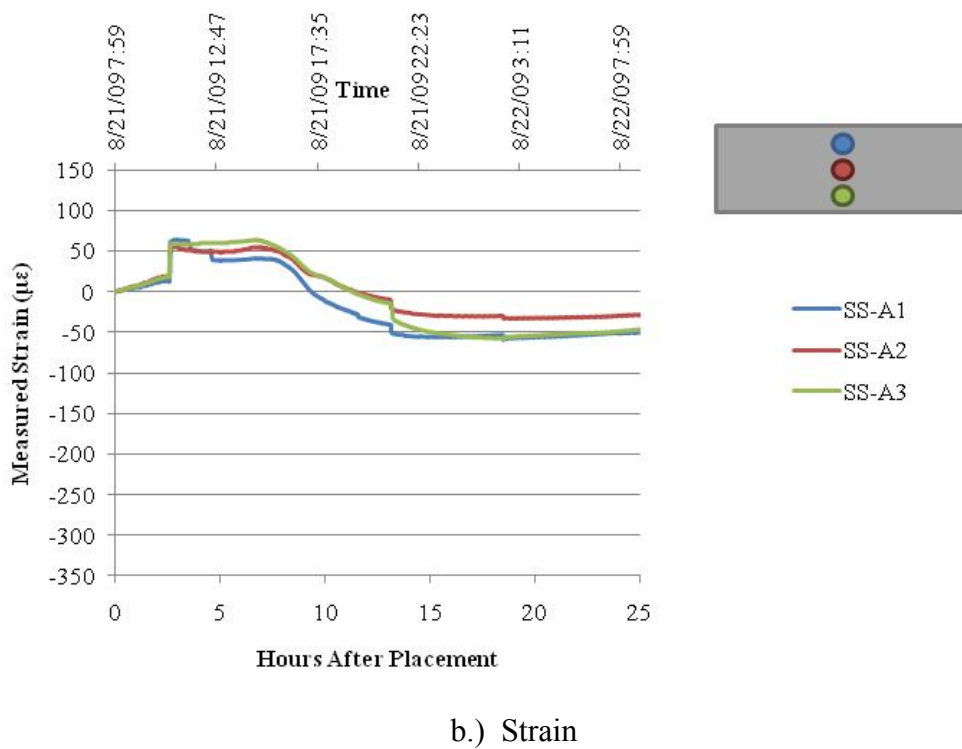
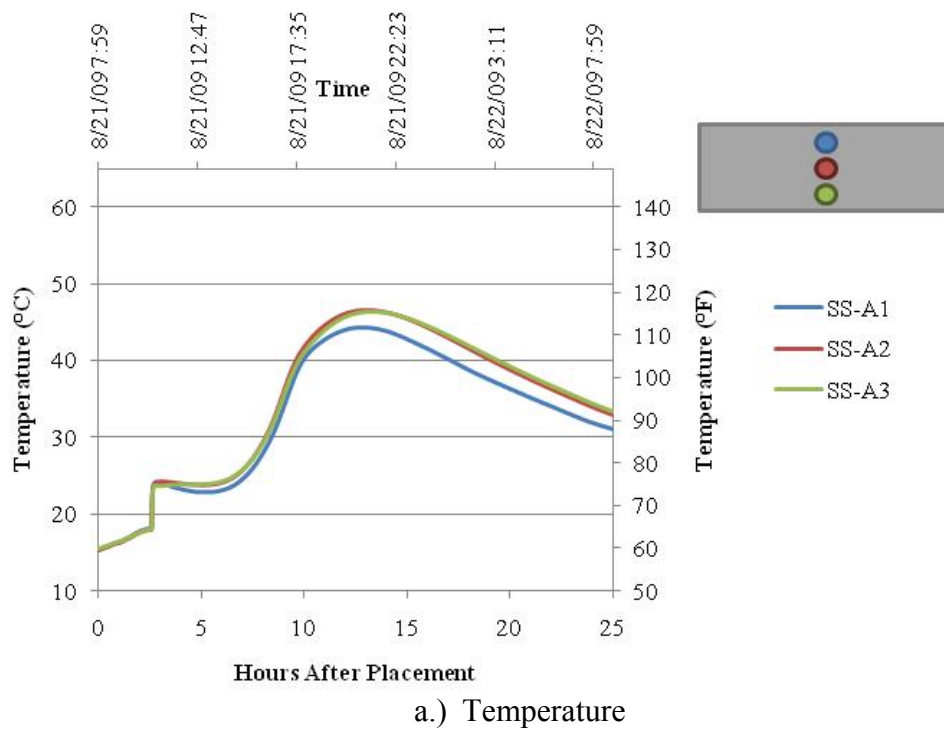
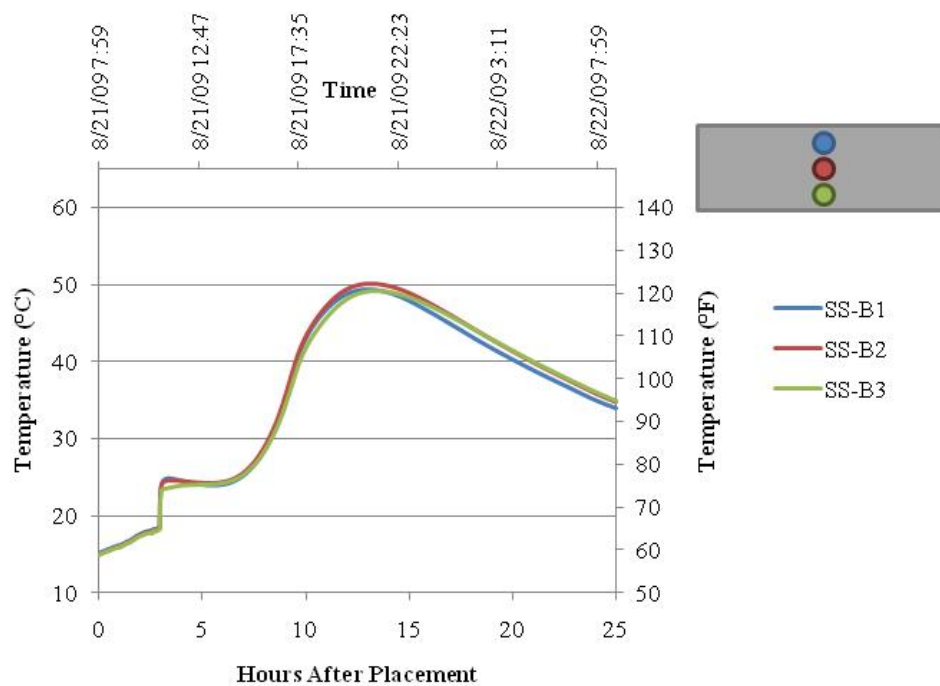
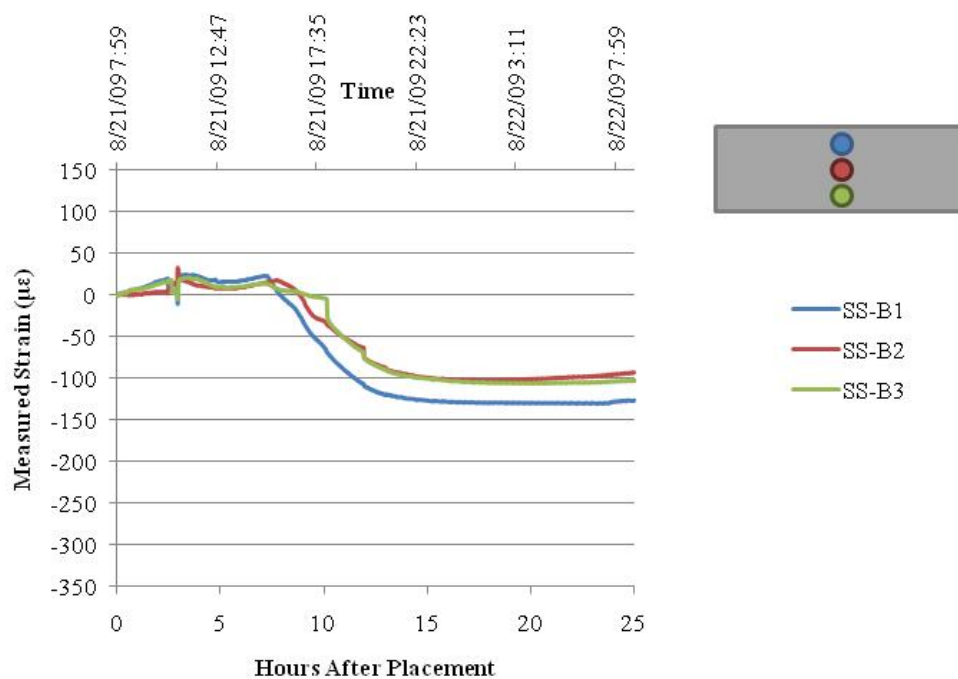


Figure 9.15. Strain in HS-SCC Deck Panel Reinforced with Mild Steel.



a.) Temperature



b.) Strain

Figure 9.16. Strain in HS-SCC Deck Panel Reinforced with GFRP.

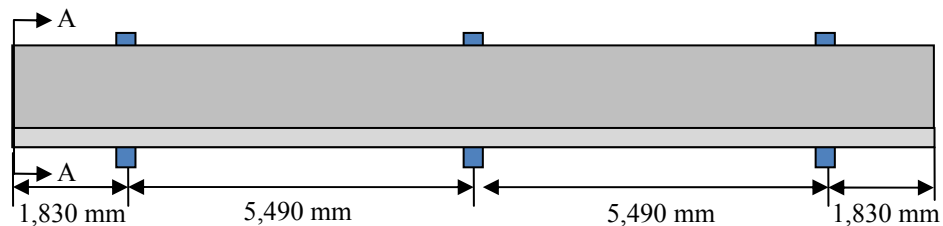
For all mixtures and reinforcing types, the concrete underwent a brief period of expansion in the first three hours. As the deck panels begin to dissipate heat, they begin to cool and undergo a contraction. The contraction due to heat dissipation and shrinkage occurred throughout the remainder of fabrication. The deck panels remained inside the precasting facility and within their forms for three days minimizing any additional strains due to thermal changes.

The initial strains within the HSC were greater than that of HS-SCC by about 170 $\mu\epsilon$. Possible reasons for the additional strain could be due to differences in size of each member, amount of reinforcing, and properties of the constituent material. However, the shrinkage test results shown in Section 7 determined that HSC did have a higher shrinkage value than the HS-SCC.

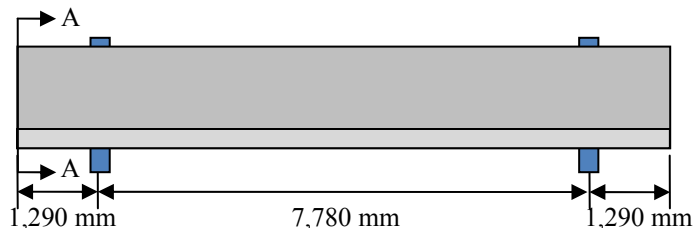
The strains were about 50 $\mu\epsilon$ greater for deck panels reinforced with GFRP than with mild steel. As mentioned earlier, the decrease in stiffness of the GFRP bars could influence the amount of strain with the deck panel cross section.

9.7. CONCRETE STRAINS DUE TO TRANSPORTATION AND ERECTION

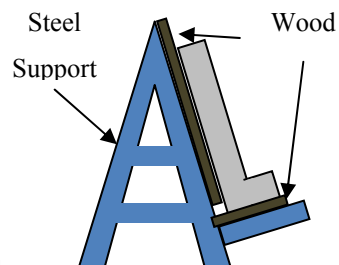
9.7.1. Background. During transportation and erection of beams, changes in strain are expected. During the actual transportation of the members, additional forces caused by acceleration and deceleration of the truck, wind forces, and vibrations due to uneven road pavement will cause changes in strain. When the beams are fabricated on the jobsite, the self-weight of the beam and weight of the deck panel will induce an additional moment on the beams. The support conditions during transport, the lifting points, and the set condition and their relative locations are illustrated in Figures 9.17 and 9.18 during erection.



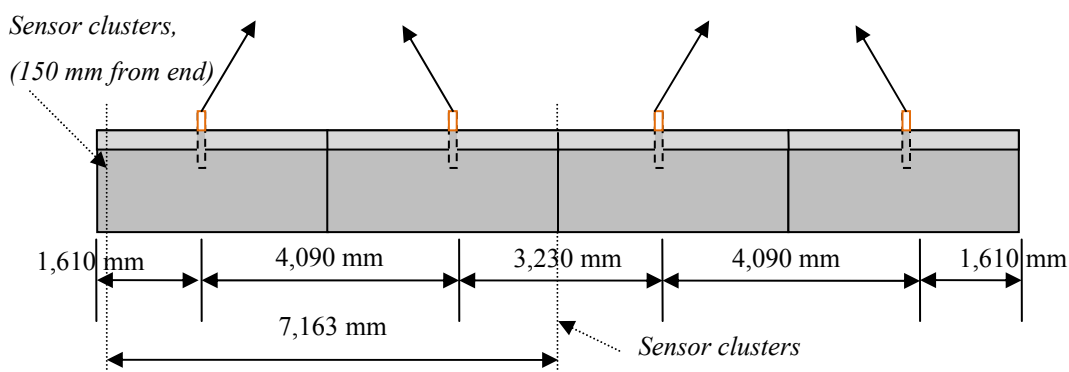
a.) HSC Spandrel Beam on Semi-Truck Trailer



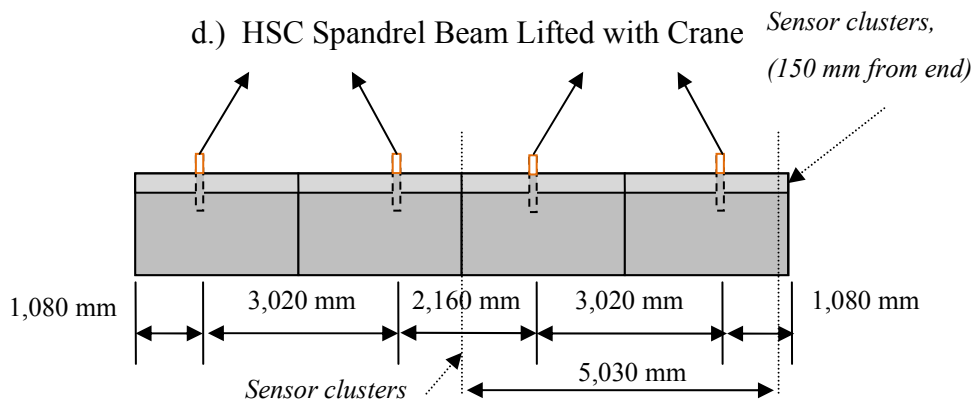
b.) HS-SCC Spandrel Beam on Semi-Truck Trailer



c.) Section A-A



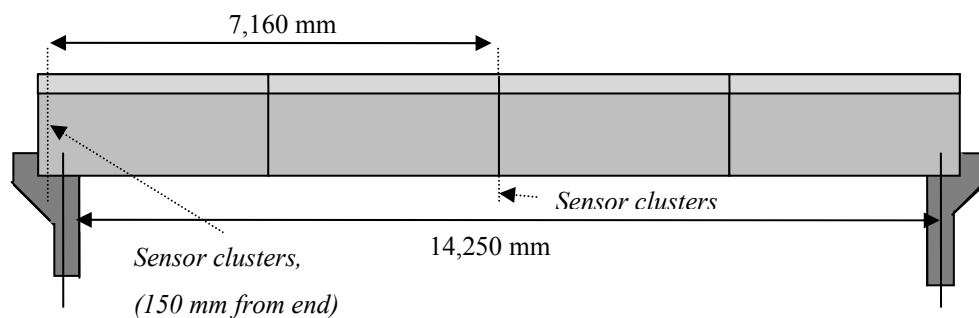
d.) HSC Spandrel Beam Lifted with Crane



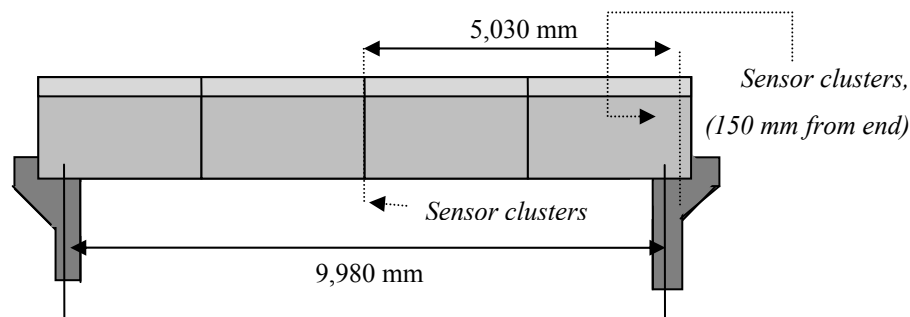
e.) HS-SCC Spandrel Beam Lifted with Crane

Units: mm (1 mm = 0.03937-in.)

Figure 9.17. Bridge Spandrel Beam Transport.



a.) HSC Spandrel Beams



b.) HS-SCC Spandrel Beams

Units: mm (1 mm = 0.03937-in.)

Figure 9.18. Bridge Spandrel Beams Set at Bridge Site.

9.7.2. Measurements and Discussion. VWSGs installed in the spandrel beams during fabrication continued to monitor temperature and strains within the beams during transportation and erection. Figure 9.19 and 9.20 illustrate changes in strain during transportation of the girders from Marshall, MO to Rolla, MO.

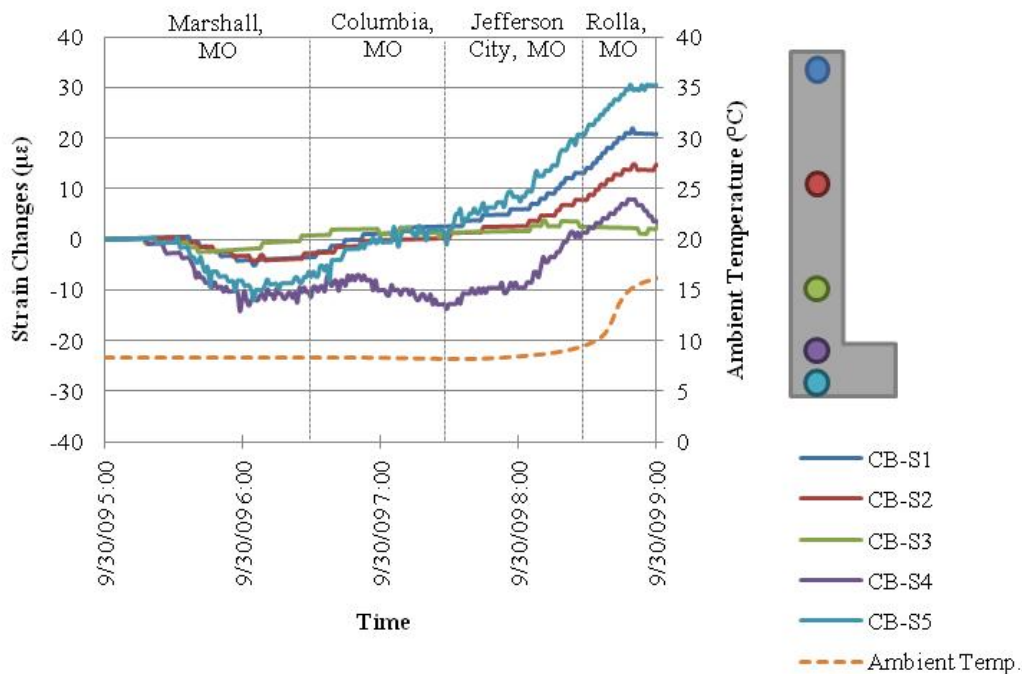


Figure 9.19. Support Strain Changes during Transportation of HSC Spandrel Beam.

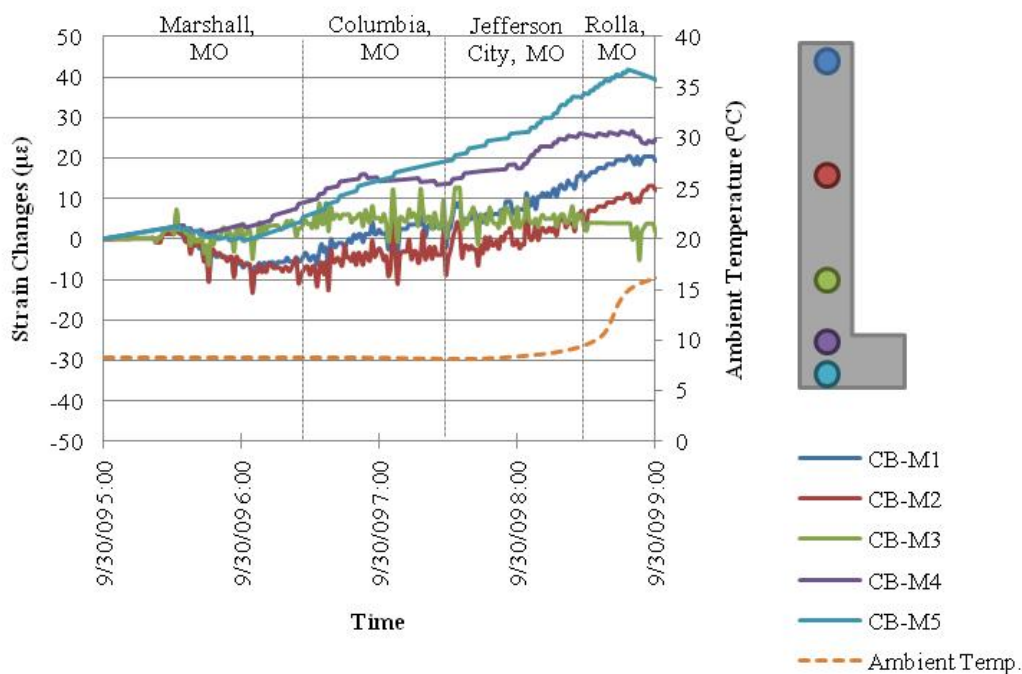


Figure 9.20. Mid-Span Strain Changes during Transportation of HSC Spandrel Beam.

Overall, the changes during transportation were relatively small for the HSC and HS-SCC. The HSC beam underwent a maximum strain change of $30 \mu\epsilon$ at the support and $40 \mu\epsilon$ at mid-span. The HS-SCC beam underwent a maximum strain change of $30 \mu\epsilon$ at the support and $50 \mu\epsilon$ at the mid-span.

After the beams were delivered to the jobsite, they were lifted with a crane, set at the proper location of the abutment, and set with precast deck panels. Each of these situations, as presented previously in Figures 9.17 and 9.18, caused changes within the strain profile of both the HSC and HS-SCC beams. The changes in strain for each change in load for the mid-span of both the HSC and HS-SCC beams are illustrated in Figures 9.21 and 9.22. When the beam was lifted with a crane, a tensile stress was applied to the top and a compressive stress was applied to the bottom causing a reduction in compressive strain at the top and an increase in compressive strain at the bottom. After the bridge beam and deck panels were set, the top fiber compressive stress was increased and the bottom compressive stress fiber was decreased. This is evident in the increase in compressive strain at the top fiber and a decrease in compressive strain at the bottom fiber in the following figures.

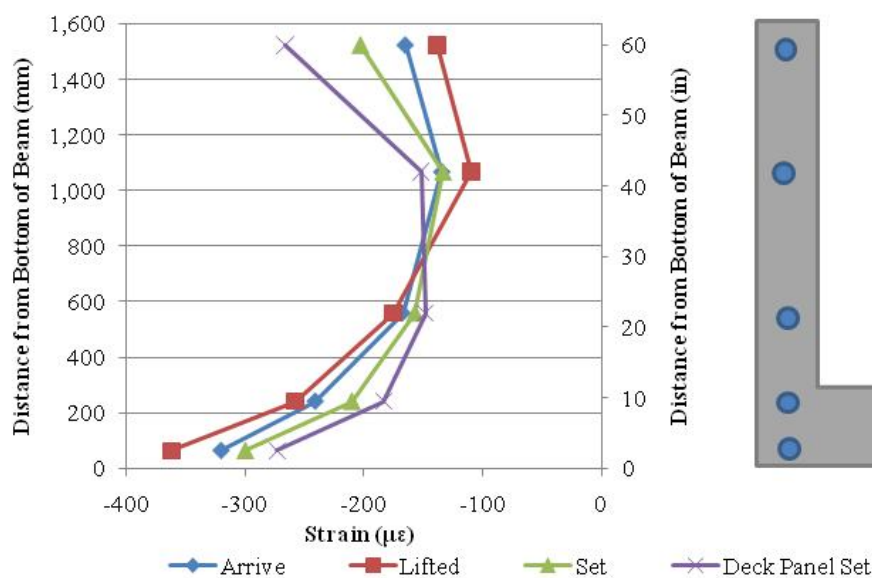


Figure 9.21. HSC Mid-Span Spandrel Beam Strain Profile during Erection.

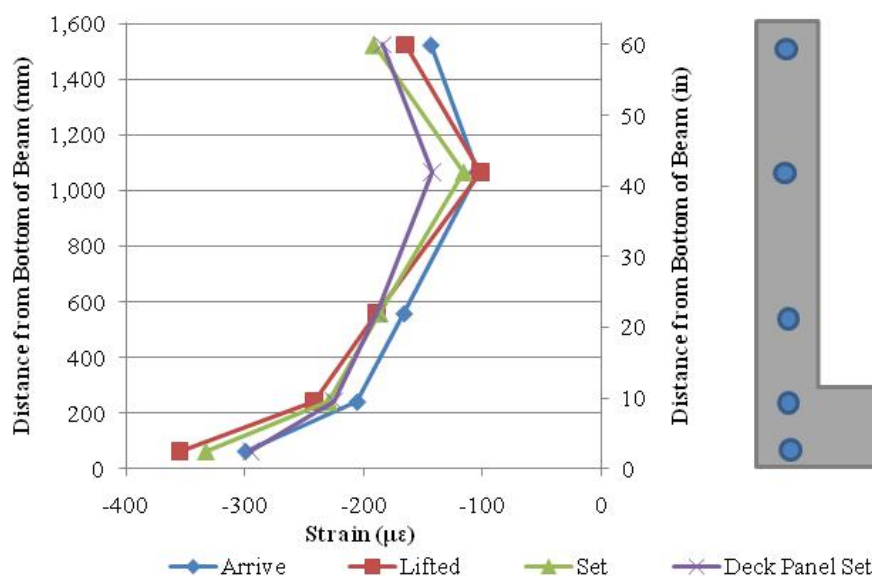


Figure 9.22. HS-SCC Mid-Span Spandrel Beam Strain Profile during Erection.

The measured strains were compared to predicted strains for the mid-span of both the HSC and HS-SCC beams immediately after the loads were applied. The comparison graphs are featured in Figures 9.23 and 9.24. In Figures 9.23 and 9.24, it is apparent that the predicted models do not accurately predict the strain profile in the member due to the non-linear time dependent losses occur along the depth of the member. In addition, a linear regression was attempted on the data. However, due to the complex shape of the strain distribution, one was unable to be determined. On average, the model predicted 60% higher compressive strains for the HSC beam and 50% higher compressive strains for the HS-SCC than measured by the sensors. It is recommended that a more complex model is determined to predict the stresses and strains within the beam.

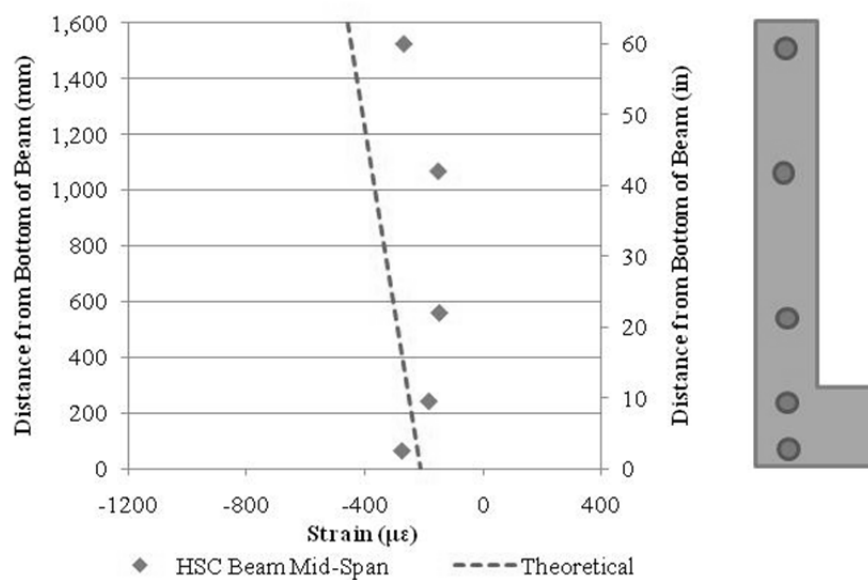


Figure 9.23. Strain Profile after Deck Placement for HSC Beam.

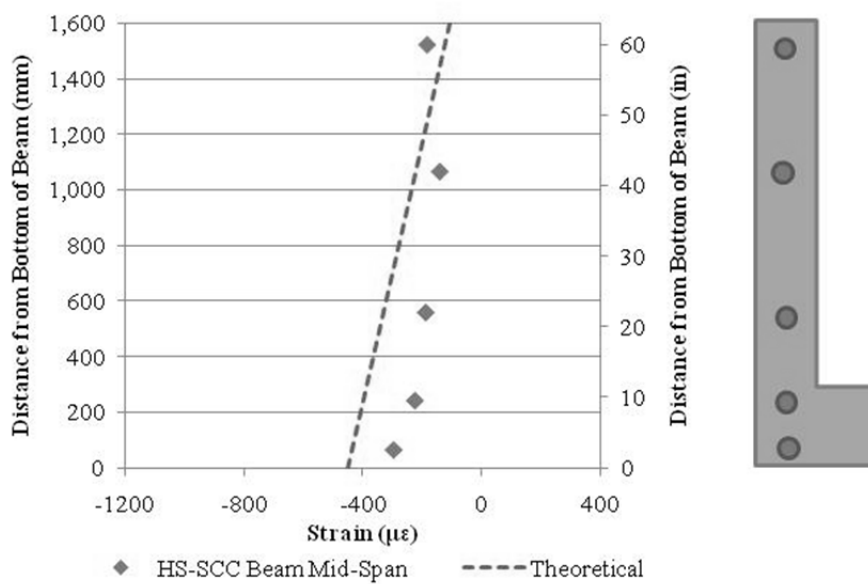


Figure 9.24. Strain Profile after Deck Placement of HS-SCC Beam.

9.8. SUMMARY AND CONCLUSIONS

The concrete stresses that occur during concrete hydration, release, transportation, and service are of great importance in design of concrete bridges. However, due to the difficulty of directly measuring stresses, strain data is collected and compared to theoretical values. Any differences in the strain between HSC and HS-SCC are important to determine to more accurately design structures that wish to utilize HS-SCC.

During concrete hydration of the HSC and HS-SCC spandrel beams and precast deck panels had similar temperature and strain profiles. However, the strains during concrete hydration were slightly higher for HSC than HS-SCC spandrel beams and deck panels.

Upon the release of the prestressing tendons in the spandrel beams, the theoretical values corresponded fairly well with theoretical values. For this project, the HSC bottom fiber compressive strains at release tended to be about 27% higher than predicted, and the bottom fiber HS-SCC compressive strains at release tended to be about 14% higher than predicted. Both of the beams were well within the recommended compressive and tensile release stresses specified by ACI 318 (2008).

The concrete strains of the beams during storage corresponded fairly well with theoretical values for both the HSC and HS-SCC beams. However, as the specimens began to age, the strain profile began to become more complex and non-linear and increased the percentage difference between predicted and measured values. This is true when comparing predicted to measured strain values at erection. During erection, it was found that the HSC had an average percentage difference of 60% and the HS-SCC 50% between actual and theoretical strain data. A more sophisticated model to predict the later-age actual strains within the spandrel beams is recommended.

10. PRESTRESS LOSS MEASUREMENTS

10.1. INTRODUCTION

10.1.1. General. Accurately predicting prestress losses is important in the design of prestressed concrete beams. If prestress losses are not taken into account, beams may become overstressed due to inaccurate knowledge of fiber stresses and serviceability states may be exceeded.

There are several types of losses that contribute to the total prestress loss in a concrete beam. Prestress losses include elastic shortening of the concrete, relaxation of the tendons, creep of the concrete, and shrinkage of the concrete. Equation 52 is used to determine the total prestress loss within a concrete beam (PCI, 2004).

$$\Delta f_{TOTAL} = \Delta f_{ES} + \Delta f_{RE} + \Delta f_{CR} + \Delta f_{SH} \quad (52)$$

In pretensioned concrete, elastic shortening (ES) occurs at release of the tendons when both the prestressing strands and the concrete contracts and decreases the prestressing force. Equation 53 is utilized to determine the change in stress from elastic shortening. In equation 53, f_{cgs} is the stress of the concrete at the centroid of the prestressing strands, E_{ps} is the modulus of elasticity of the prestressing strand and E_{ci} is the modulus of elasticity of the concrete at release. The stress of the concrete at release, is estimated by equation 54 and requires the estimated force at release, P_o , the cross sectional area, A , the moment of inertia, I , the eccentricity of the strand, e , and any moment applied to the beam, M . If the section is uncracked, such as the case in many prestressed applications, the gross moment of inertia and area can be used for calculations.

$$\Delta f_{ES} = \frac{E_p}{E_{ci}} f_{cgs} \quad (53)$$

$$f_{cgs} = -\frac{P_o}{A} - \frac{P_o e^2}{I} + \frac{M e}{I} \quad (54)$$

Relaxation (RE) of the prestressing tendons occurs when the prestressing strands are stressed at an, f'_{pi} , beyond 55% of the yield stress of the strand, f_{py} . The yield stress of the stand, f_{py} , is typically assumed to be 90% of f_{pu} for low-relaxation tendons, 85% of f_{pu} for stress-relieved tendons, and 80% of f_{pu} for prestressing bars (Nawy, 2006). Equation 55 provides the equation for steel relaxation, Δf_{RE} , for time, t , for low-relaxation steel.

$$\Delta f_{RE} = f'_{pi} \frac{\log_{10} t}{45} \left(\frac{f_{pi}'}{f_{py}} - 0.55 \right) \quad (55)$$

Prestress losses due to creep and shrinkage cause additional losses within the member overtime. Creep (CR) losses occur when a sustained load is applied to the concrete beam and result in the shortening of the member over a period of time. The shortening will decrease the amount of prestressing force applied from the tendons to the concrete. In addition, concrete shrinkage (SH) will cause further shortening of the member over time and will promote a reduction of the prestressing force (Nawy, 2006).

10.1.2. Measurement of Prestress Losses Using Internal VWSGs. The VWSGs within each beam were used to indirectly monitor prestress losses within the spandrel beams. In order to determine the prestress losses, the strain at the centroid of the prestressing steel, ϵ_{cgs} , was determined by interpolating the temperature corrected strain data from the sensors and multiplied by the modulus of elasticity of the prestressing strands, E_{ps} . This is demonstrated in equation 56.

$$\Delta f_{P,Meas} = E_{ps} \epsilon_{cgs} \quad (56)$$

The losses determined in equation 57, include losses due to elastic shortening, creep, and shrinkage. However, the losses that occur due to the relaxation of the strand are not included because relaxation losses do not cause a change in strain within the concrete at the location of the prestressing strands. Therefore, equation 57 should be utilized to correct the prestress loss for losses due to strand relaxation.

$$\Delta f_{P,Meas} = E_{ps} \epsilon_{cgs} + \Delta f_R \quad (57)$$

10.2. ELASTIC SHORTENING AT RELEASE

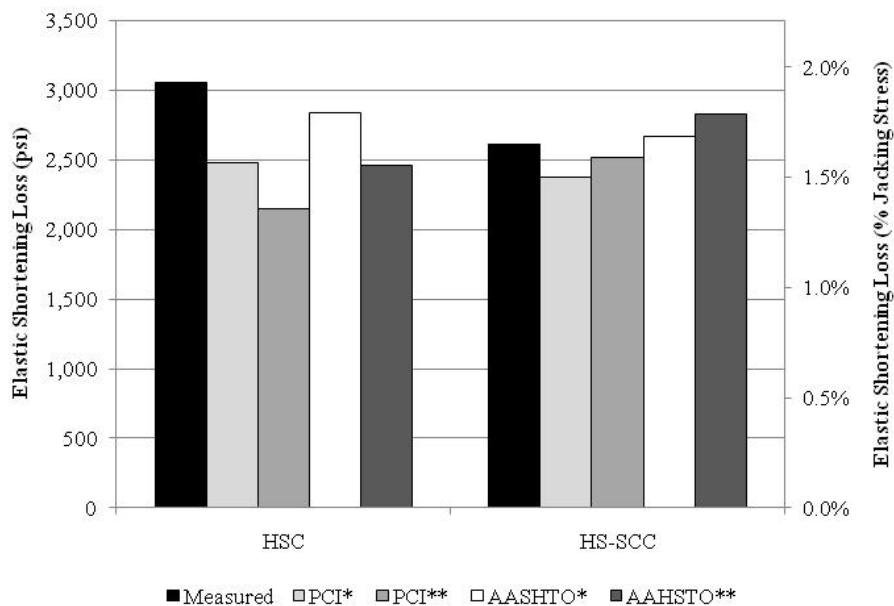
10.2.1. Background. The elastic shortening occurs when both the concrete and strands undergo an instantaneous contraction when the prestress strand is released. The elastic shortening is a function of the modulus of elasticity of the strand, the modulus of elasticity of the concrete at release, and the stress applied to the concrete beam (Myers and Yang, 2005).

10.2.2. Measurements and Discussion. The VWSGs within each of the HSC and HS-SCC beams was used to determine the strain at the center gravity of the prestressing steel. The elastic shortening was determined using equation 56 from the measured strain reading. In addition, the stresses determined were compared to the nominal jacking stress of 1,090 MPa (158.3 ksi). The measured values were compared to predicted values specified in AASHTO LRFD (2007) and the PCI Design Handbook (2004) with actual modulus of elasticity and approximate modulus of elasticity of the concrete determined with equation 5. The results are displayed in Table 10.1. Figure 10.1 displays a comparison of measured losses to predicted for elastic shortening losses and normalized stress losses for beam length.

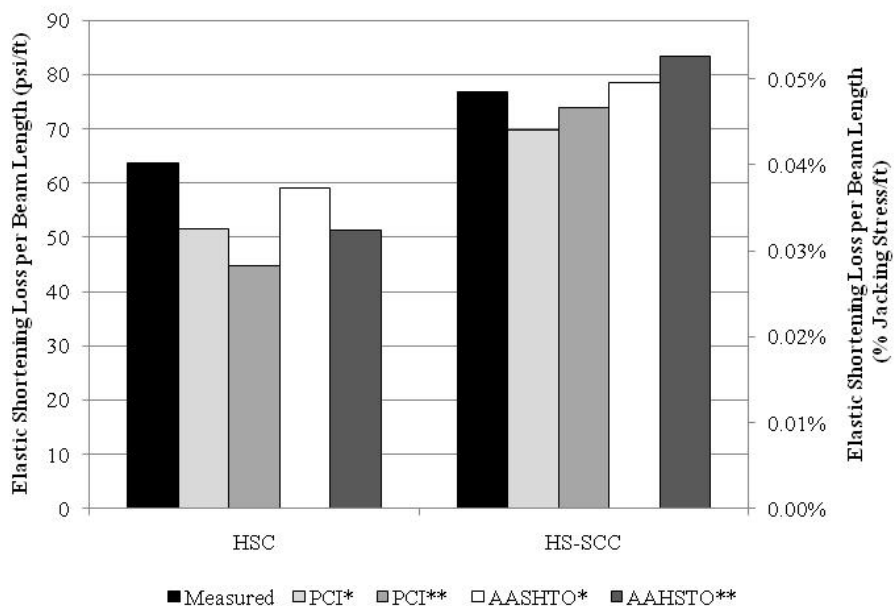
Table 10.1. Measured vs. Predicted Elastic Shortening Losses.

Result Method	HSC				HS-SCC			
	Strain ($\mu\epsilon$)	Stress (psi)	Percent Jacking	M/P Ratio	Strain ($\mu\epsilon$)	Stress (psi)	Percent Jacking	M/P Ratio
MEASURED	105.3	3,054	1.93%	1.00	90.1	2,615	1.65%	1.00
PCI*	85.5	2,478	1.57%	1.23	81.9	2,375	1.50%	1.10
PCI**	74.1	2,149	1.36%	1.42	86.8	2,516	1.59%	1.04
AASHTO*	97.8	2,835	1.79%	1.08	92.1	2,672	1.69%	0.98
AASHTO**	84.8	2,458	1.55%	1.24	97.6	2,830	1.79%	0.92

* Methods using measured MOE, **Methods using approximate MOE,
M – Measured, P – Predicted, 1,000 psi = 6.895 MPa



a.) Elastic Shortening



b.) Elastic Shortening Normalized for Beam Length

* Methods using measured MOE, ** Methods using Approximate MOE

Conversion: 1,000 psi = 6.895 MPa

Figure 10.1. Measured & Predicted Elastic Shortening Losses.

It can be inferred that the measured values of elastic shortening were greater than those predicted by both the PCI and AASHTO methods. The AASHTO equations were more accurate when the actual modulus of elasticity of the material was used in the equation. However, the PCI method was more accurate when the theoretical modulus of elasticity was used in the equation for HS-SCC; the PCI method was more accurate for HSC when the measured modulus of elasticity was employed in the model. Of all of the methods, the AASHTO LRFD equation which implementing the actual modulus of elasticity of the materials produced the most optimal results for both HSC and HS-SCC. This AASHTO LRFD method utilized the same equation as equation 55. When the normalized elastic shortening losses are compared between HSC and HS-SCC, it is apparent that the normalized losses are greater for HSC by approximately 21%. The difference can be attributed to variations in the aggregate and cement within the HSC and HS-SCC paste matrix which affect the modulus of elasticity of the mix at release that in turn affects elastic shortening.

10.3. TOTAL LOSSES

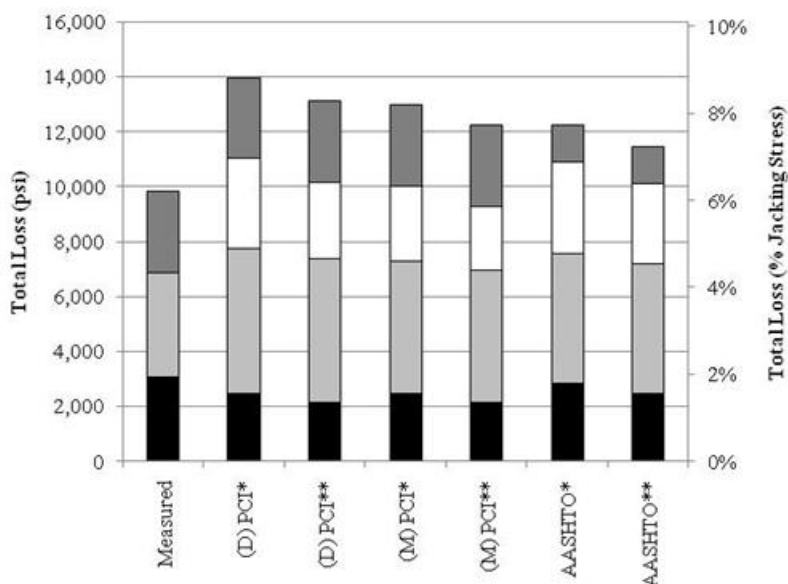
10.3.1. Background. Total losses are often considered for serviceability cases in concrete bridge design. AASHTO LRFD Bridge Design Specification (2007) and PCI Design Handbook (2004) provide estimates that are often used to determine total prestress losses. Each of the design methods involves determining the components of total prestress loss separately. Each method has an equation that estimates elastic shortening, strain relaxation, creep, and shrinkage losses. The methods are provided in Appendix E and Appendix F.

10.3.2. Measurements and Discussion. Strain data received from the VWSGs were interpolated for strain at the center of gravity at the prestressing strand. The measured total prestress loss within the concrete was determined by using equations 56 and 57 specified earlier. However, to determine the amount of creep and shrinkage losses, the elastic shortening losses and strand relaxation were subtracted from the total loss. The measured total loss and analytical models presented by PCI and AASHTO are presented in Table 10.2 for HSC and HS-SCC. PCI values were also determined to see the differences in design and measured creep and shrinkage coefficients.

Table 10.2. Measured & Predicted Total Prestress Losses for Spandrel Beams.

HSC at 365 Days	Losses				Total Loss		Comparison	
	ES (psi)	SH (psi)	CR (psi)	RE (psi)	Stress ($\mu\epsilon$)	% of Jacking	M/P Ratio	Diff. (+,-)
MEAS.	3,054	3,833		2,948	9,840	6.21%	1.00	NA
(D) PCI*	2,478	5,245	3,325	2,917	13,965	8.82%	0.70	+
(D) PCI**	2,149	5,245	2,782	2,939	13,115	8.28%	0.75	+
(M) PCI*	2,478	4,826	2,735	2,942	12,981	8.20%	0.76	+
(M) PCI**	2,149	4,826	2,288	2,962	12,225	7.72%	0.80	+
AASHTO*	2,835	4,704	3,352	1,338	12,229	7.72%	0.80	+
AASHTO**	2,458	4,729	2,921	1,350	11,459	7.74%	0.86	+
HS-SCC at 365 Days	Losses				Total Loss		Comparison	
	ES (psi)	SH (psi)	CR (psi)	RE (psi)	Stress ($\mu\epsilon$)	% of Jacking	M/P Ratio	Diff. (+,-)
MEAS.	2,615	2,128		2,948	7,691	4.86%	1.00	NA
(D) PCI*	2,375	5,257	4,031	2,901	14,564	9.20%	0.53	+
(D) PCI**	2,516	5,257	3,907	2,900	14,580	9.21%	0.53	+
(M) PCI*	2,375	4,836	4,095	2,910	14,217	8.98%	0.54	+
(M) PCI*	2,516	4,836	3,970	2,910	14,232	8.99%	0.54	+
AASHTO	2,672	4,921	3,116	1,346	12,054	7.61%	0.64	+
AASHTO*	2,516	5,257	3,907	2,900	14,580	9.21%	0.53	+
(D) PCI Method in which design parameters for creep and shrinkage were used. (M) PCI Method in which measured parameters for creep and shrinkage were used. ** Methods using measured MOE * Methods using approximate MOE M – Measured Values P – Predicted Values 1,000 psi = 6.895 MPa								

Each of the predicted total prestress loss values overestimated the measured total strain. Only the AASHTO LRFD refined method produced somewhat satisfactory results. The total prestress loss equations had a smaller range difference of 16.5 to 42.0% between the theoretical and measured values for HSC than the range difference of 56.7% to 89.6% for HS-SCC. The equations that applied the actual modulus of elasticity of the concrete were slightly closer to measured results for the HS-SCC mixtures than HSC mixtures. This could be due to the slightly lower modulus of elasticity value for HSC determined during testing that may not provide the true stiffness of the mixture. A visual representation to further show the differences in the measured total prestress loss and predicted prestress losses is illustrated in Figure 10.3 and 10.4. In Figure 10.3 and 10.4, the creep and shrinkage values are lumped together for the measured prestress loss values.



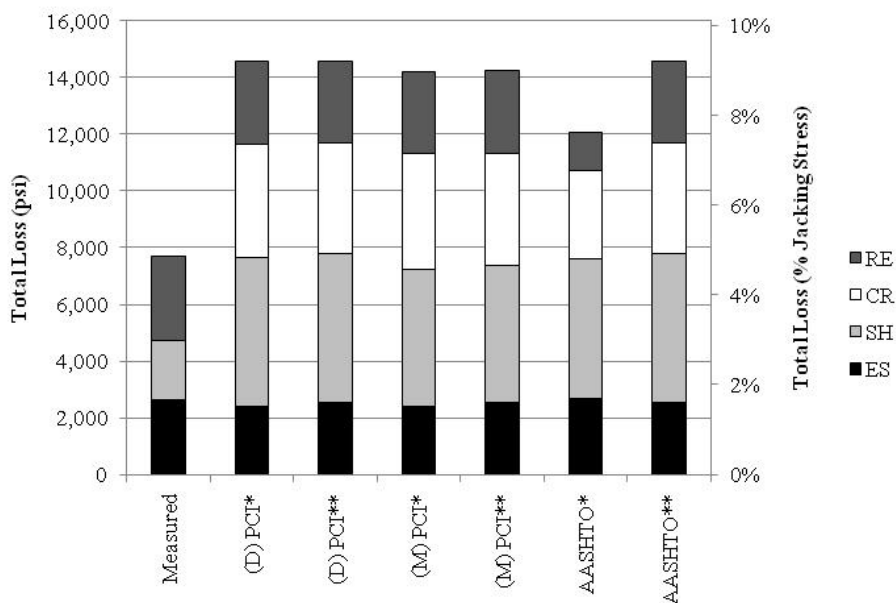
(D) PCI Method in which design parameters for creep and shrinkage were used

(M) PCI Method in which measured parameters for creep and shrinkage were used

* Methods using measured MOE, ** Methods using approximate MOE

Conversion: 1,000 psi = 6.895 MPa

Figure 10.2. Measured & Predicted Total Prestress Losses for HSC Spandrel Beam.



(D) PCI Method in which design parameters for creep and shrinkage were used

(M) PCI Method in which measured parameters for creep and shrinkage were used

* Methods using measured MOE, ** Methods using approximate MOE

Conversion: 1,000 psi = 6.895 MPa

Figure 10.3. Measured & Predicted Total Prestress Losses for HS-SCC Spandrel Beam.

The creep (CR) and shrinkage (SH) values estimated for the total prestress loss are greater than what actually was measured and contributes to the high variance between total measured and total predicted loss. The models do tend to predict HSC losses more accurately than HS-SCC losses, however. The difference is attributed to the models not being calibrated for HS-SCC. However, there is a possibility that the interpolation of the measured data to determine the strain at the center of gravity of the prestressing strand may not be accurate. The accuracy of the linear strain interpolation reduces overtime as the actual strain profile becomes non-linear from the non-linear time dependent losses that occur.

Table 10.3 presents the total measured prestress loss for both the HSC and HS-SCC. By looking at the overall total, the HS-SCC beam had less total prestress loss. However, the data is not normalized to take into account the differences in lengths between bridges. The normalized values indicate that the total loss over a unit length is greater for HS-SCC than HSC by about 10%.

Table 10.3. Total Prestress Losses for HSC & HS-SCC Spandrel Beams.

Material	Length	Total Loss	Total Loss/Length
HSC	14.6 m (48 ft)	67.81 MPa (9,835 psi)	4.635 MPa/m (204.9 psi/ft)
HS-SCC	10.4 m (34 ft)	53.03 MPa (7,691 psi)	5.117 MPa/m (226.2 psi/ft)

10.4. SUMMARY AND CONCLUSIONS

The initial elastic shortening losses for both the HSC and HS-SCC were close to empirical values. However, the AASHTO LRFD (2007) equation for elastic shortening was determined to be the most accurate for both the HSC and HS-SCC beams. In addition, further accuracy was obtained by using the materials true measured modulus of elasticity.

The total losses determined by AASHTO LRFD (2007) and PCI Design Handbook (2004) were not as accurate as those determined by elastic shortening. The later-age creep and shrinkage loss values were greatly overestimated by both design equations. However, a portion of the difference can be contributed to the non-linear later-age strain graphs that were used to determine the measured prestress loss. The predicted total prestress loss to measured total prestress loss percentage difference ranged from 16.5% when using the AASHTO LRFD Refined Method (2007) with an estimated modulus of elasticity to 42.0% with the PCI Design Handbook method (2004) with design parameters. The HS-SCC predicted total prestress loss to measured total prestress loss ranged from 56.7% with the AASHTO LRFD Refined Method with measured

modulus of elasticity to 89.6% when using any of the methods with design parameters. The more the design equations were tailored to individual material properties of the mixture, the better the estimate of total prestress loss for HS-SCC.

When the prestress loss to length of strand is compared between HSC and HS-SCC, HS-SCC has a higher loss per length of approximately 21% for elastic shortening loss and 10% for total loss. This additional prestress total loss can be attributed to the greater effect creep has on the material than on HSC, as determined in Section 7.6.

11. LIVE LOAD TESTING PROGRAM

11.1. INTRODUCTION

Changes in deflection and strain during a bridge's life cycle can occur due to time dependent strength losses of the bridge's materials. Prestress loss and various durability concerns such as cracking can lead to potential serviceability problems. A live load test can be used to determine bench mark values at early-ages and compare them to later-age values to determine any changes that may have occurred throughout a bridge's life cycle.

A static live load test was utilized to compare the deflection in HSC and HS-SCC prestressed precast spandrel beams and precast deck panels. In addition, changes in deflection and compared between deck panels reinforced with mild steel to those reinforced with GFRP for both HSC and HS-SCC bridges. Furthermore, the measured values were compared to theoretical values determined from basic structural analysis for both simply supported and fixed cases.

11.2. LOAD TEST PROGRAM

On August 3, 2010, a static live load test was conducted on both the HSC and HS-SCC bridges to obtain a better understanding of the differences in deflection and strain between the two concrete bridges. The deflection measurements were determined utilizing laser based precise surveying. Temperature data were monitored with the internal VWSGs with built-in thermistors within the spandrel beams and precast deck panels. In addition, basic structural analysis techniques were utilized to predict the simply supported and fixed behavior of both bridges assuming an uncracked cross section and compare them to the measured values.

11.2.1. Load Cases. A Toyota Model 7FGU25 forklift truck weighing 39.3 kN (8,840 lbs) was used to load the HSC and HS-SCC bridges for the static load test. The weight distributed by the front and axle loads was provided by the fork lift manufacturer. Figure 11.1 illustrates the axle weights and locations on the fork lift.

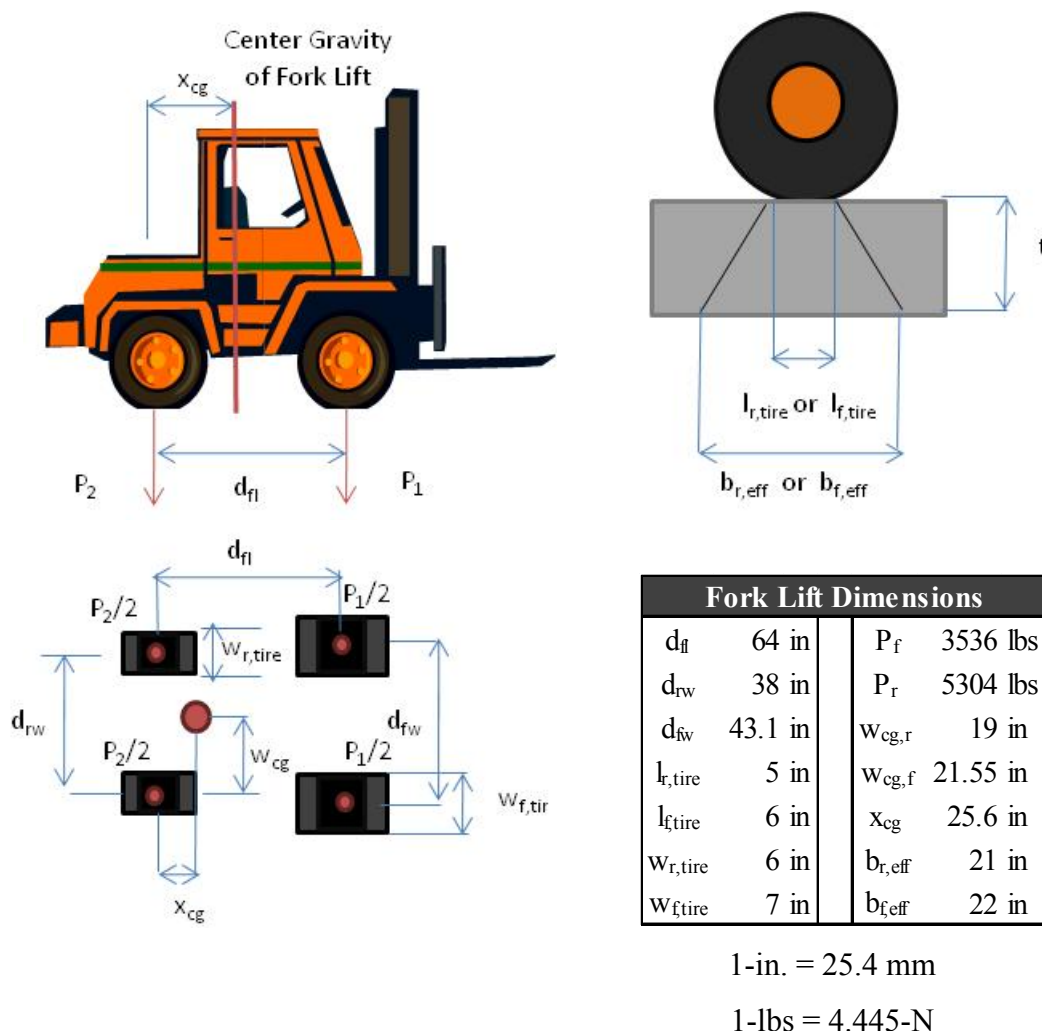


Figure 11.1. Fork Lift Dimensions for Live Load Test.

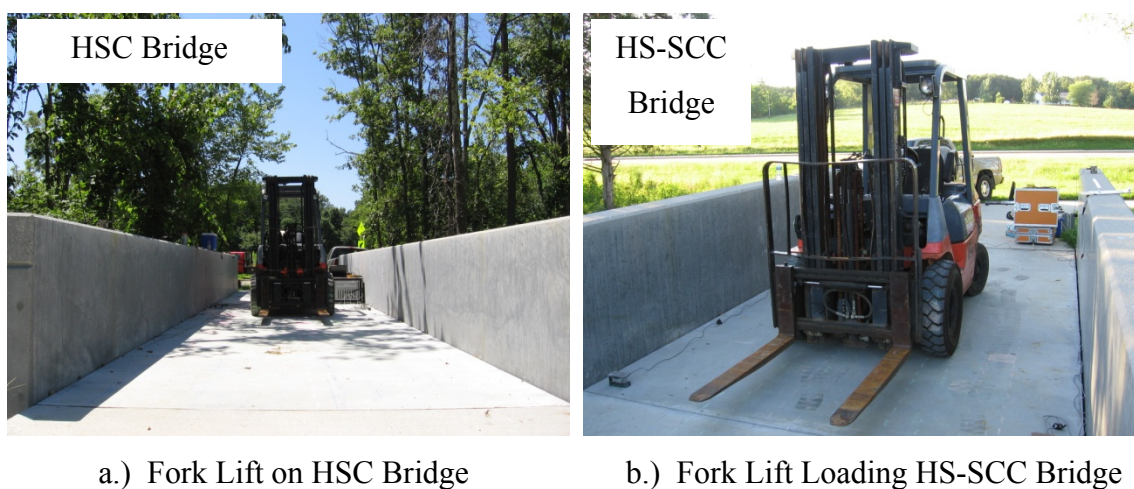
For each bridge, six load cases were utilized in the live load test. Table 11.1 list the locations of the center of gravity for each load case and the start and stop time for each load application. For load cases “A”, “B”, “D”, and “F”, the front of the fork lift faced away from Lion’s Club Drive. For load cases “C” and “F”, the fork lift faced toward Lion’s Club Drive. The mirrored fork lift facing was implemented to create similar loading in both the mild steel and GFRP reinforced deck panels. Figure 11.2 displays the chalk line used to designate front tire load location. In addition, pictures of the fork lift loading both the HSC and HS-SCC bridges are displayed in Figure 11.3.

Table 11.1. Load Case Locations & Times.

HSC Bridge								
HS-SCC Bridge								
Load Case	HSC Bridge				HS-SCC Bridge			
	Center of Gravity		Time		Center of Gravity		Time	
	X (in.)	Y (in.)	Start	Stop	X (in.)	Y (in.)	Start	Stop
A	153.6	53	11:05	11:30	296.4	53	18:13	18:33
B	297.6	53	13:25	13:51	213.6	53	18:33	18:54
C	422.4	53	13:51	14:40	111.6	53	20:04	20:13
D	153.6	70	11:30	11:55	296.4	70	18:54	19:10
E	297.6	70	11:55	13:25	213.6	70	19:39	19:48
F	422.4	70	14:40	15:40	111.6	70	19:53	20:03
Conversion: 1-in. = 25.4 mm								



Figure 11.2. Example Fork Lift Load Path Markings.



a.) Fork Lift on HSC Bridge

b.) Fork Lift Loading HS-SCC Bridge

Figure 11.3. Toyota 7FGU25 Fork Lift on HSC & HS-SCC Bridges.

11.2.2. Bridge Deflections. A laser based precise surveying system utilizing a Leica TCA 2003 Total Station with optical surveying prisms monitored the bridge deflections for the static live load test. The system required the use of two reference prisms and a series of target prisms placed at particular points of interest to monitor the bridge deflection. The reference prisms and bridge mounted target prisms are displayed in Figure 11.4.

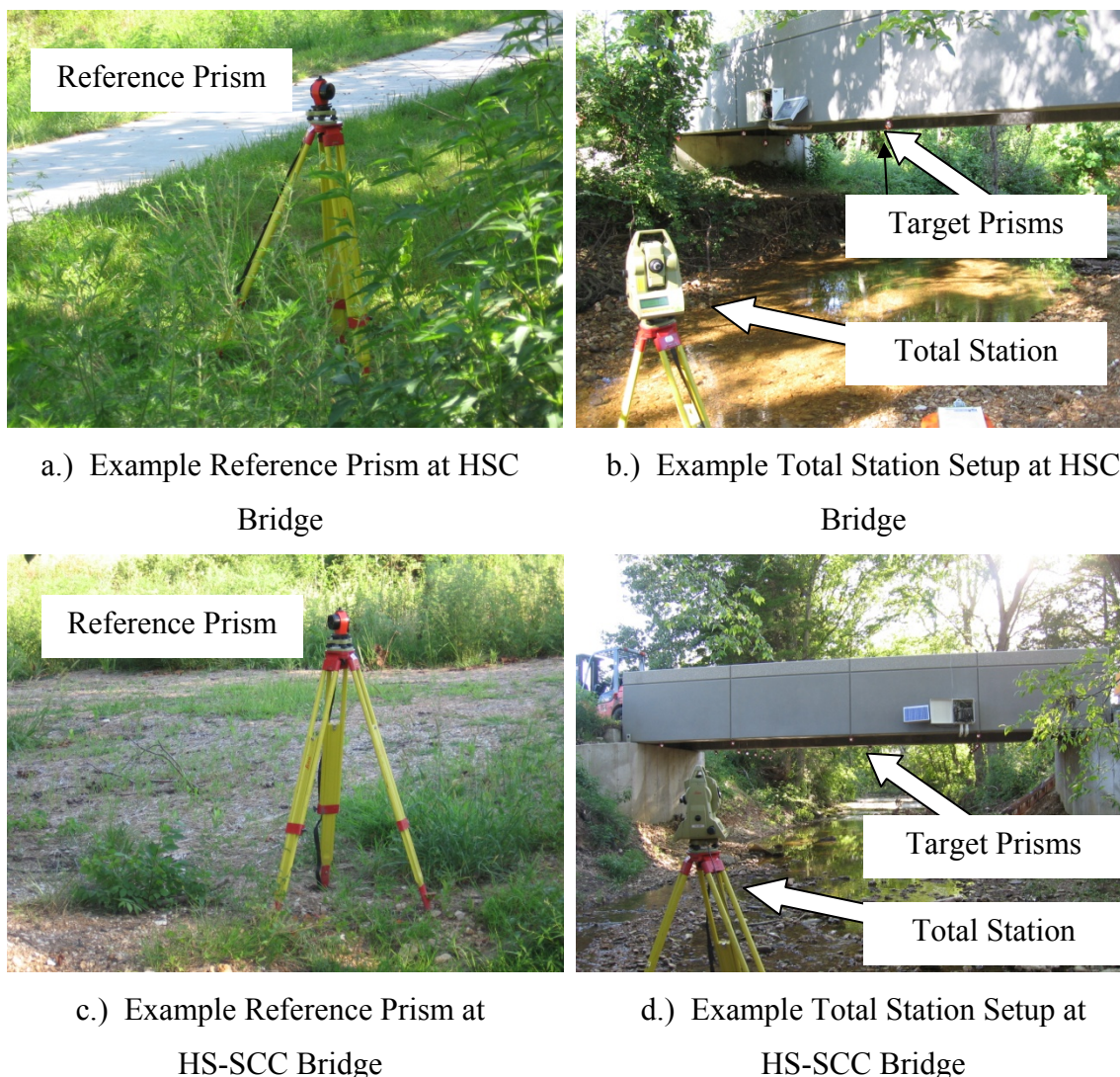


Figure 11.4. Total Station Test Setup.

Before the load test was run, 6 mm (0.25-in.) thick light gauge steel plates that were 70 mm (3-in.) square were epoxied to the underside of the bridges at predetermined locations with five-minute quick set epoxy. The plates were attached to be used for later-age load testing. The magnetized target prisms were fixed each of the steel plates. Deck panel locations required an additional 460 mm (18-in.) long threaded rod to be added to the prisms to extend the prism location to allow them to be in the line of sight. Table 11.2 lists the locations of each of the steel plates on both the HSC and HS-SCC bridges.

Figures 11.5 and 11.6 illustrate the locations of the target prisms on both the HSC and HS-SCC bridges. Installed pictures of the target prisms are shown in Figure 11.7.

Table 11.2. Target Prism Locations.

HSC Bridge						HS-SCC Bridge					
Prism	X (in.)	Y (in.)	Prism	X (in.)	Y (in.)	Prism	X (in.)	Y (in.)	Prism	X (in.)	Y (in.)
1	36	6.2	11	288	133.8	1	36	6.2	11	204	133.8
2	36	133.8	12	432	6.2	2	36	133.8	12	306	6.2
3	144	6.2	13	432	22.5	3	102	6.2	13	306	22.5
4	144	22.5	14	432	44.0	4	102	22.5	14	306	44.0
5	144	44.0	15	432	70.0	5	102	44.0	15	306	70.0
6	144	70.0	16	432	96.0	6	102	70.0	16	306	96.0
7	144	96.0	17	432	117.5	7	102	96.0	17	306	117.5
8	144	117.5	18	432	133.8	8	102	117.5	18	306	133.8
9	144	133.8	19	540	6.2	9	102	133.8	19	372	6.2
10	288	6.2	20	540	133.8	10	204	6.2	20	372	133.8

Conversion: 1-in. = 25.4 mm

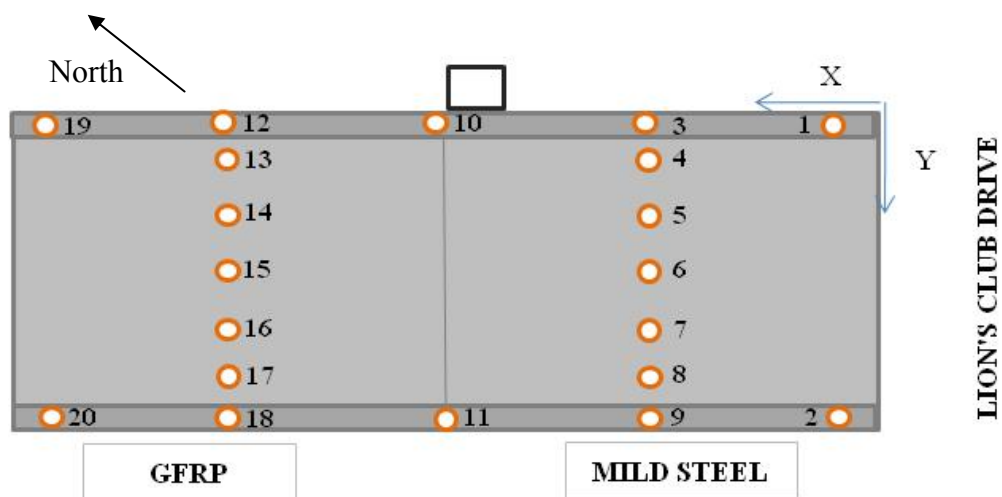


Figure 11.5. Target Prisms on HSC Bridge.

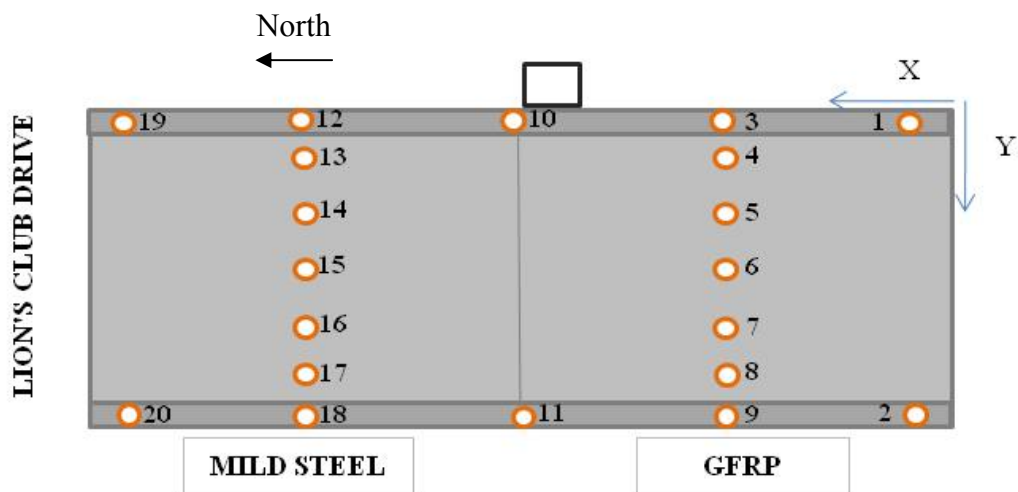
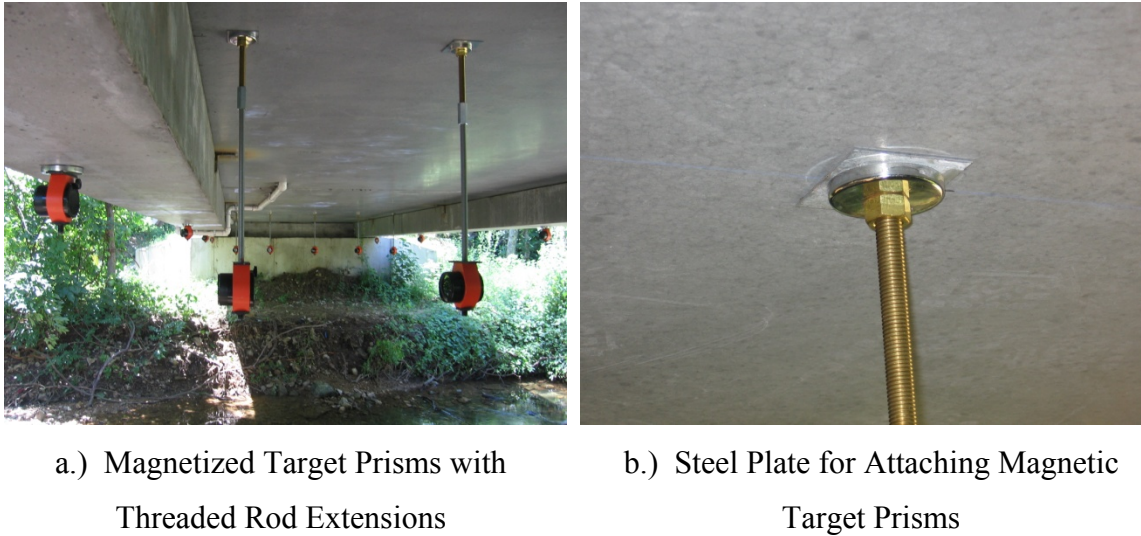


Figure 11.6. Target Prisms on HS-SCC Bridge.



a.) Magnetized Target Prisms with
Threaded Rod Extensions

b.) Steel Plate for Attaching Magnetic
Target Prisms

Figure 11.7. Target Prisms.

After the target prisms were installed, the total station was mounted on top of a tripod that had been well set in the ground at an ideal location that is fairly level with an adequate view of all the prisms. After the total station had been set, the reference prisms were placed at locations on the right and left side of the bridge. The reference prisms are utilized to determine if there was any movement in the total station between readings.

Once the total station, reference prisms, and target prisms were mounted and leveled, the reference prisms and target prisms were recorded in the total station by locating, naming, and recording each prism in the total station's system. Three recordings were made for each prism to ensure proper accuracy. After the precise survey system had been properly setup, the load test was started. The first test involved a baseline dead load reading. After the dead load readings were taken, the loading configurations displayed in Table 10.1 were utilized. After running through the loading configurations, a second dead load test was implemented. The dead load tests were run to determine any camber caused by temperature effects. By utilizing the dead load deflection readings and correlating them with the temperature readings from the internal thermistors in the VWGs, the amount of deflection caused from temperature was

interpolated for each load test. The interpolated data were removed to determine the deflection caused solely from the live load.

It should be noted that as the file size within the total station became larger, the speed of the test to decrease significantly. At the beginning of testing on the HSC Bridge, the test time for the first load case took twenty minutes. However, by the end of testing, the test time for the final load case took approximately 90 minutes. In order to finish testing in a single day, the amount of recordings per prism was reduced from three to one. Since the variance in shots on the HSC bridge was very small, 0.02 mm (0.0006-in), lowering the amount of readings per point was deemed acceptable.

11.3. LIVE LOAD TEST RESULTS

The deflection measurements determined from the live load testing program were compared to theoretical values determined for both fixed and simply supported design equations. In order to compare the measured values to theoretical values, the raw data had to be converted into changes in deflection with temperature effects removed. It should be noted, however, that the load test deflections were extremely small and any correction due to thermal effects, which produced most of the deflection throughout the day, likely affected the confidence level in the corrected values.

11.3.1. Downloading the Deflection Data. A computer was required to download the deflection data from the Leica total station. Once connected to the computer and powered on, Leica Survey Office, software provided by the manufacturer, was used to download the deflection data. Download manager was utilized within the program to access the files in the total station. After the files for the project were copied to the computer hard drive, Microsoft Excel was used to open the survey file. The first column was selected and a text to columns operation was ran from the data menu. By using a fixed width operation, a break was placed before any plus, minus sign, or space. Columns that contained irrelevant information were deleted. Irrelevant information included any columns that contained numbers with excess decimal points or contained a series of repeat numbers. After deleting all irrelevant data, only column one and four were required to determine the change in deflection during loading. Column four had to be divided by 10,000 to convert the elevation in feet.

11.3.2. Converting Raw Deflection Data. Once the raw data received from the Leica total station was converted into elevation, the average of the three readings for each point was subtracted from the average elevation of the baseline readings to determine camber or deflection of the bridge. If any of the three readings per prism varied from the others by 0.13 mm (0.005-in.), they were discarded from consideration in the average. In addition, the difference in the deflection of the morning to afternoon dead loads was correlated with the temperature data from the VWSGs to determine any deflection due to thermal effects during load testing allowing it to be removed. Equation 58 displays the method by which the strains due to the live load are calculated. In equation 58, δ_i is the measured deflection during static live load testing, δ_{D1} is the deflection during the first dead load test, δ_{D2} is the deflection during the second dead load test, T_{D1} is the internal temperature prior to the live load test, T_{D2} is the internal temperature after live load testing, and T_i is the internal temperature at the load case.

Figures 11.8 and 11.9 illustrate the changes in temperature throughout testing for both the HSC and HS-SCC beams. Figure 11.10 and 11.11 provide an interpolation of the deflection of both the HSC and HS-SCC beams at the various load times. Appendix G presents the same method utilized to interpolate the temperature deflections for the remaining beams and precast deck panels.

$$\delta_{LOAD} = (\delta_i - \delta_{D1}) - \left[\frac{(\delta_{D1} - \delta_{D2})}{(T_{D1} - T_{D2})} (T_i - T_{D1}) \right] \quad (58)$$

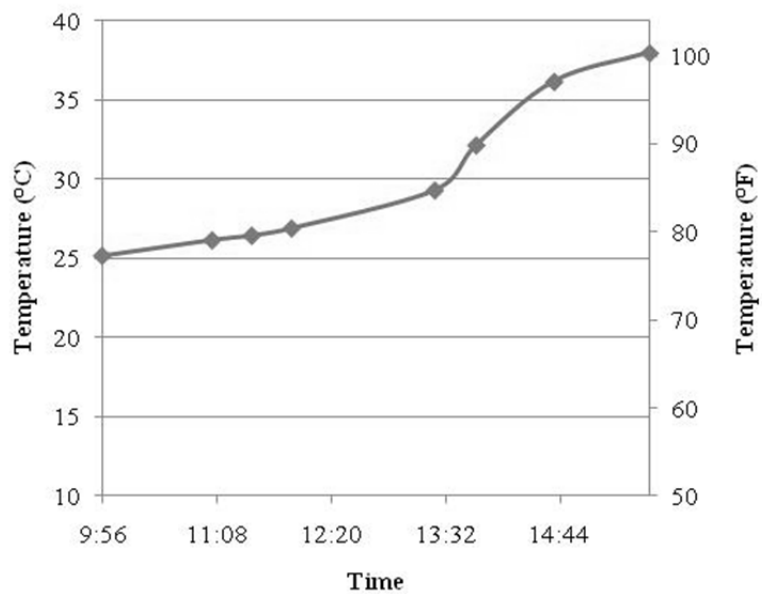


Figure 11.8. HSC Beam Temperature during Load Testing.

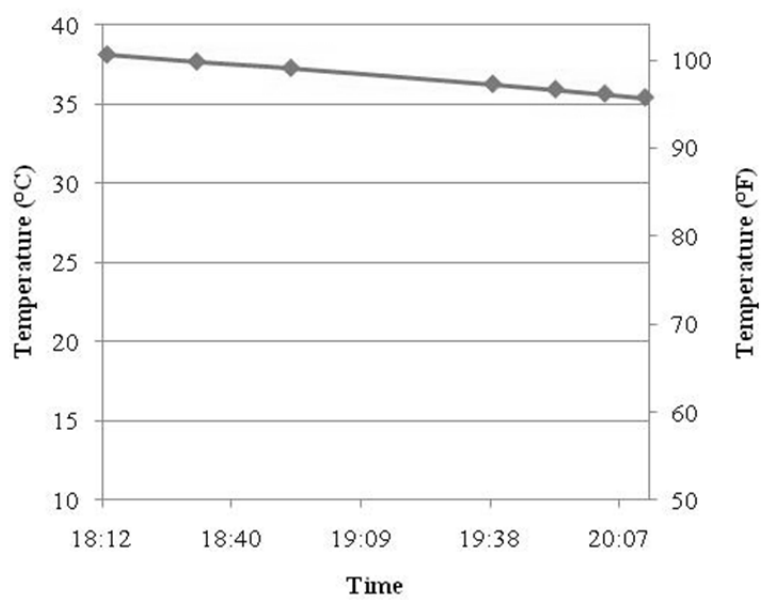
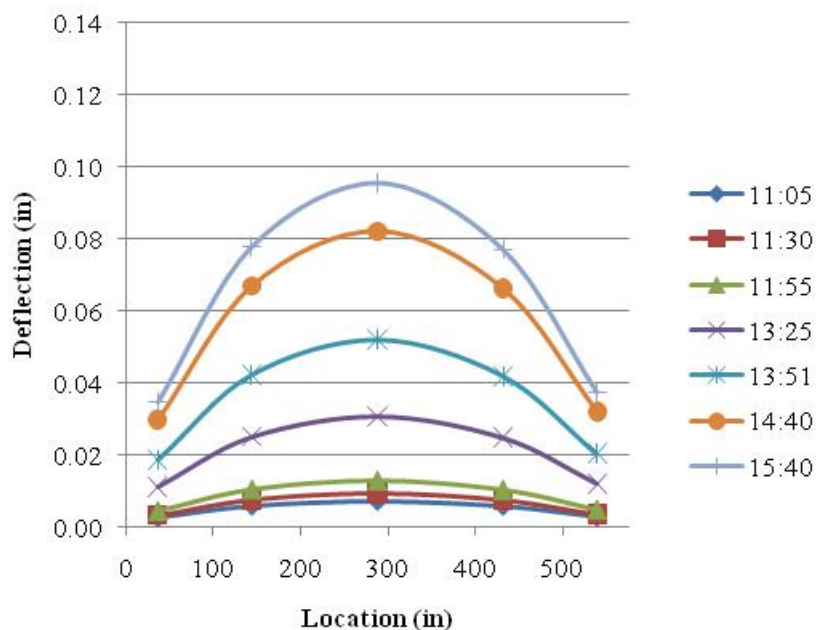
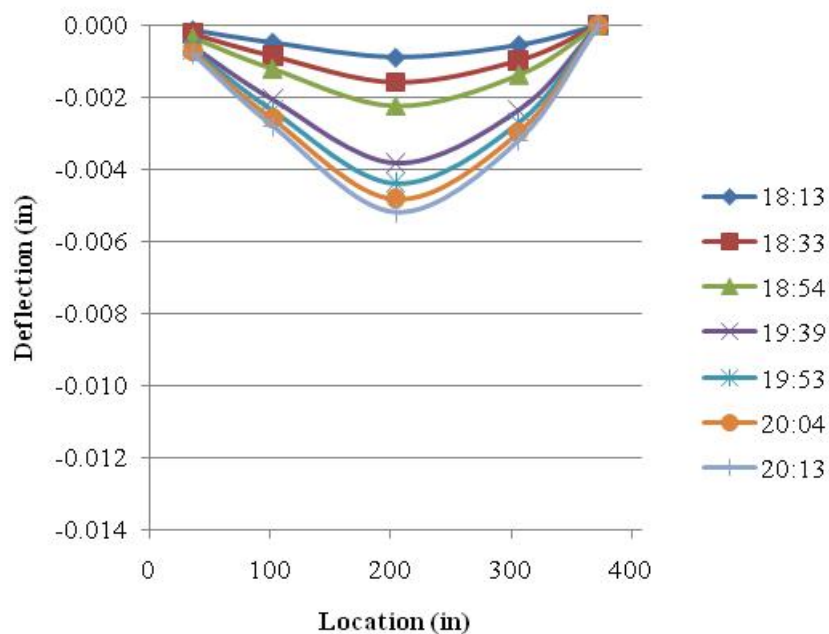


Figure 11.9. HS-SCC Beam Temperature during Load Testing.



Conversion: 1-in. = 25.4 mm

Figure 11.10. HSC Beam Adjustments due to Temperature to Baseline Reading.



Conversion: 1-in. = 25.4 mm

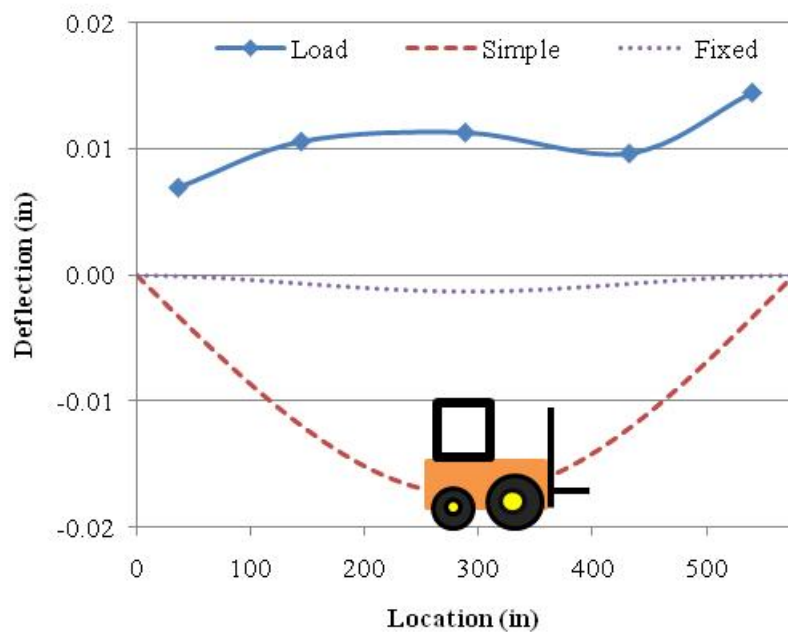
Figure 11.11. HS-SCC Beam Adjustments due to Temperature to Baseline Reading.

11.3.3. Theoretical Deflection Data. The calculated deflections for the HSC and HS-SCC bridge spandrel beams and deck panels were determined using basic deflection equations for both simply supported and fixed cases for two concentrated loads at any point and adding them together using the law of superposition. Both the fixed and simply supported deflections were calculated to compare to the true results. It was assumed that the bridges would be somewhere in between due to the welded connections between the beam and abutments and deck panels and beams.

In the deck panel locations, deflection values had to be interpolated to determine the lateral deck panel deflection at locations where the point of interest was not located under the load. Equation 59 was utilized to determine the deflection at the point of interest. In equation 59, $\delta_{p,A}$ is the deflection in the deck panel at a location “A”, $\delta_{p,i}$ is the deflection in the deck panel at the location of the load, $\delta_{b,i}$ is the deflection in the beam at the load, and $\delta_{b,i,A}$ is the deflection in the beam at “A” induced by the load. If multiple loads are present, the law of superposition allows for the individual deflection calculations to be added together.

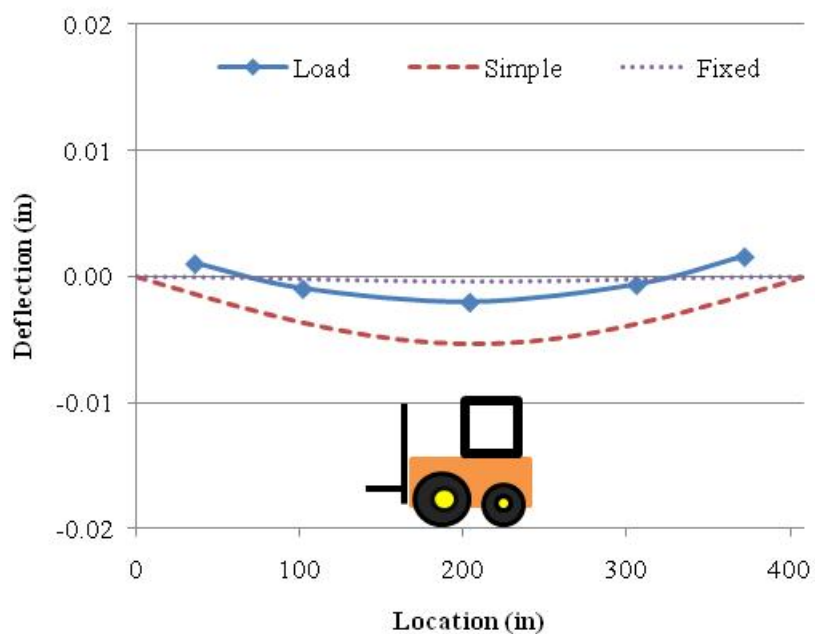
$$\delta_{p,A} = \sum_i^n \left(\delta_{p,i} \frac{\delta_{b,i}}{\delta_{b,i,A}} \right) \quad (59)$$

11.3.4. Deflection Results. A comparison of the deflection results to theoretical deflection results are illustrated in Figures 11.12 and 11.13 for the beam experiencing load case B, Figures 11.14 and 11.15 for the mild steel reinforced deck panel under load case D, and Figures 11.16 and 11.17 for the GFRP reinforced deck panels under load case F. Each of the illustrated load cases provide the maximum deflection for the beam or deck panel. All of the deflection results are presented in Appendix H for the HSC bridge and Appendix I for the HS-SCC bridge.



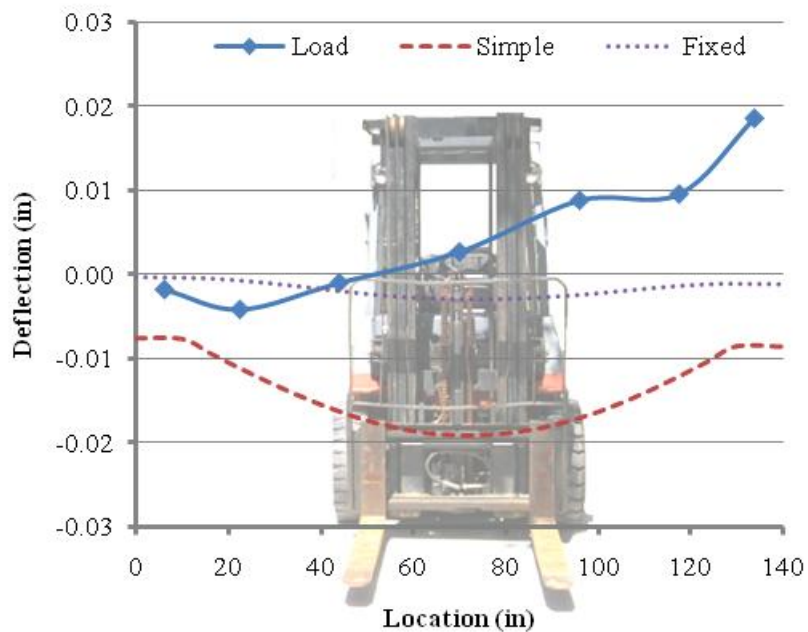
Conversion: 1-in. = 25.4 mm

Figure 11.12. HSC Spandrel Beam Deflection – Load Case B.



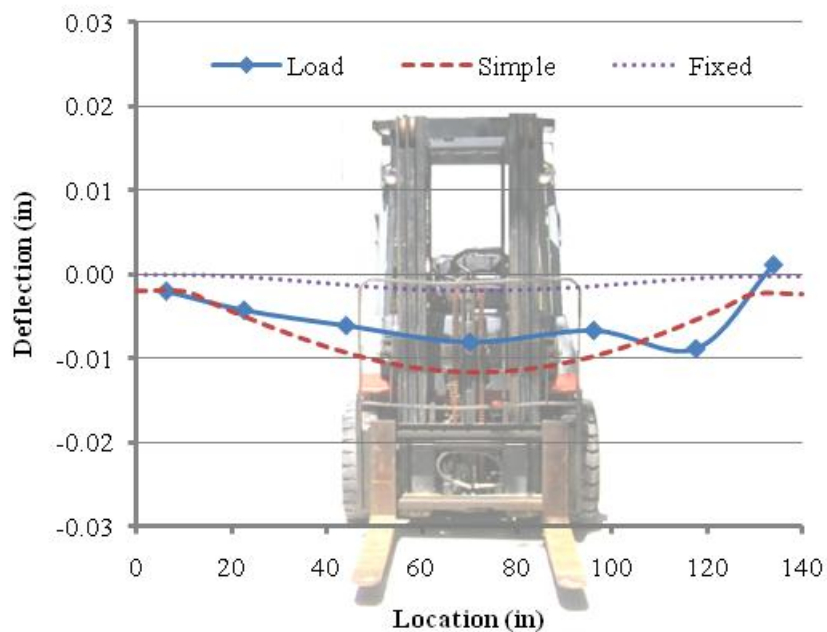
Conversion: 1-in. = 25.4 mm

Figure 11.13. HS-SCC Spandrel Beam Deflection – Load Case B.



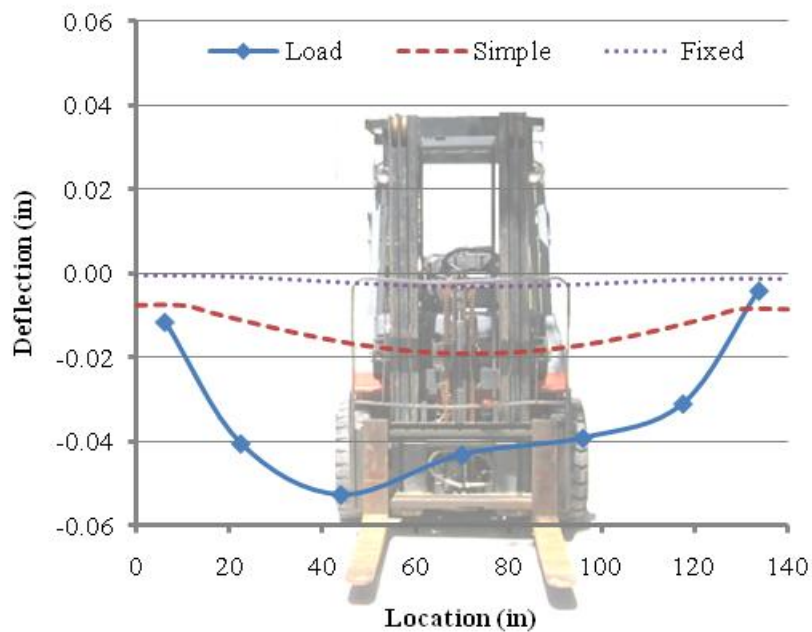
Conversion: 1-in. = 25.4 mm

Figure 11.14. HSC Mild Steel Reinforced Deck Panel Deflection – Load Case D.



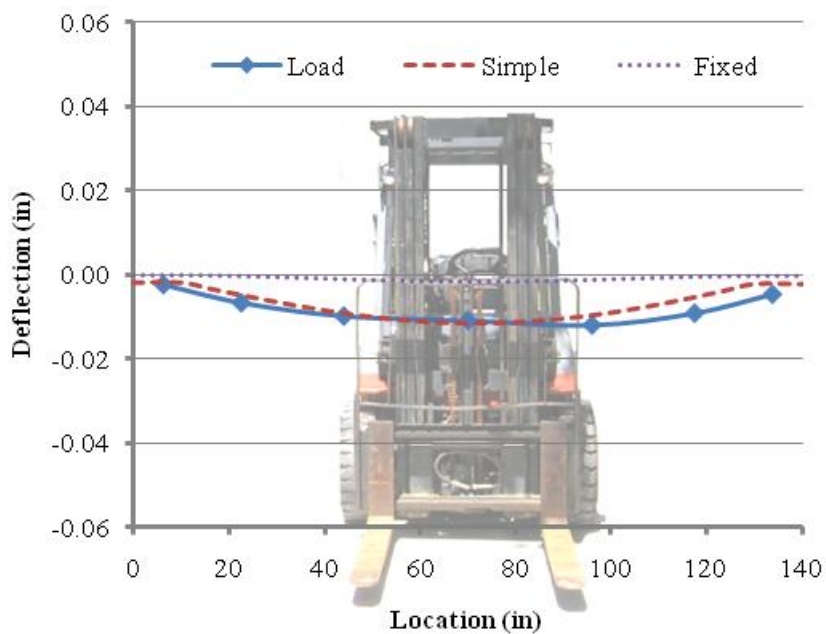
Conversion: 1-in. = 25.4 mm

Figure 11.15. HS-SCC Mild Steel Reinforced Deck Panel Deflection – Load Case D.



Conversion: 1-in. = 25.4 mm

Figure 11.16. HSC GFRP Reinforced Deck Panel Deflection – Load Case F.



Conversion: 1-in. = 25.4 mm

Figure 11.17. HS-SCC GFRP Reinforced Deck Panel Deflection – Load Case F.

From Figures 11.12 to 11.17 presented above, both the HSC and HS-SCC deflections appeared to behave more simply supported than fixed. This is expected due to the welded angle connection utilized to attach the beams to the abutments and the deck panels to the beams.

In addition, in Figures 11.12 to 11.17, it is evident that the HS-SCC beams and deck panels follow the theoretical deflection results much more closely than that of the HSC members. Many factors could influence the accuracy of the test. A few factors that determine the accuracy of testing with a total station include proper modeling of temperature effects, proximity of the total station to the prisms, and amount of deflection. As mentioned previously, when the HSC bridge was tested, three shots were made on each prism point to maintain accuracy. As the file size became larger, the testing process became longer. When the HS-SCC bridge was tested, the amount of shots for each prism was lowered to one. This greatly accelerated the testing process. At lower testing speeds, changes in deflection due to thermal effects, although taken into account, became more prevalent during testing. Since the HS-SCC bridge was tested at a much faster rate and during a time of the day with a lower temperature gradient, a higher accuracy should be expected.

In addition to thermal effects lowering the accuracy of the process, the distance of the total station to the prisms can decrease if the total station is too close. In order to see all of the reference and target points around dense foliage and ground, the HSC test was set up slightly closer to the bridge than the HS-SCC test. Pictures displaying the perspective from the total station to the HSC and HS-SCC bridges are displayed in Figure 11.18.

The load applied to the bridge induced small deflections. With this small amount of deflections, aberrations due to the previous mentioned effects become more pronounced during testing. A higher load or a more accurate testing method would be recommended to produce more consistent test results.

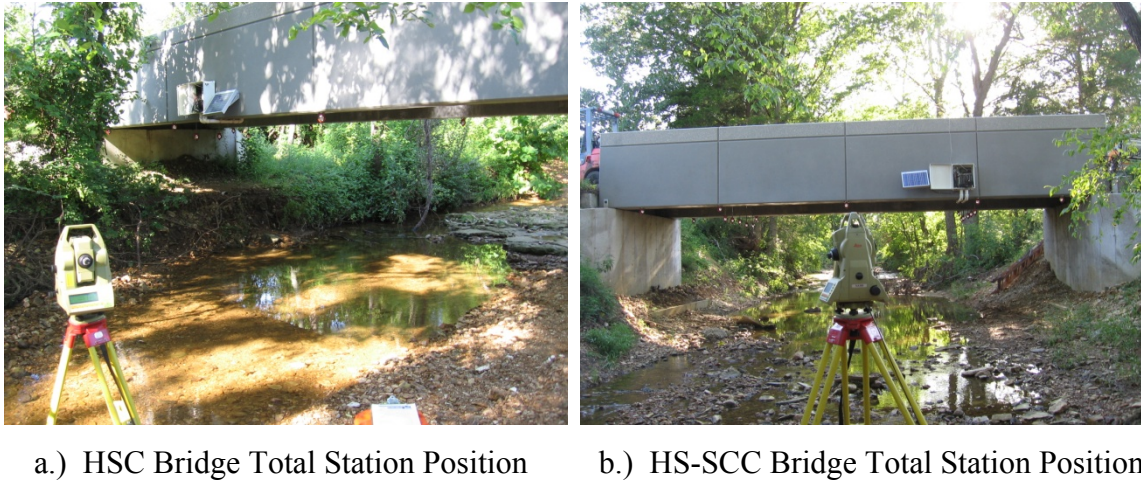
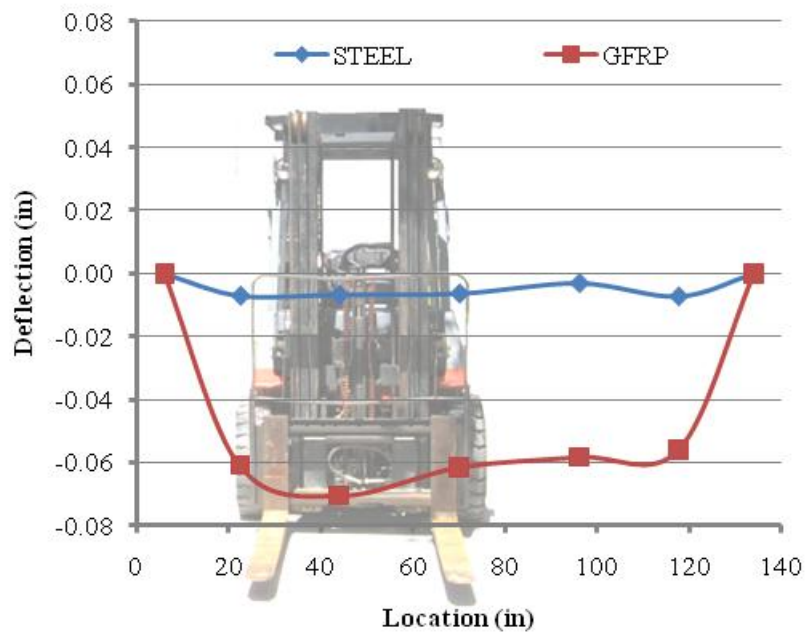


Figure 11.18. Comparison of Total Station Setups.

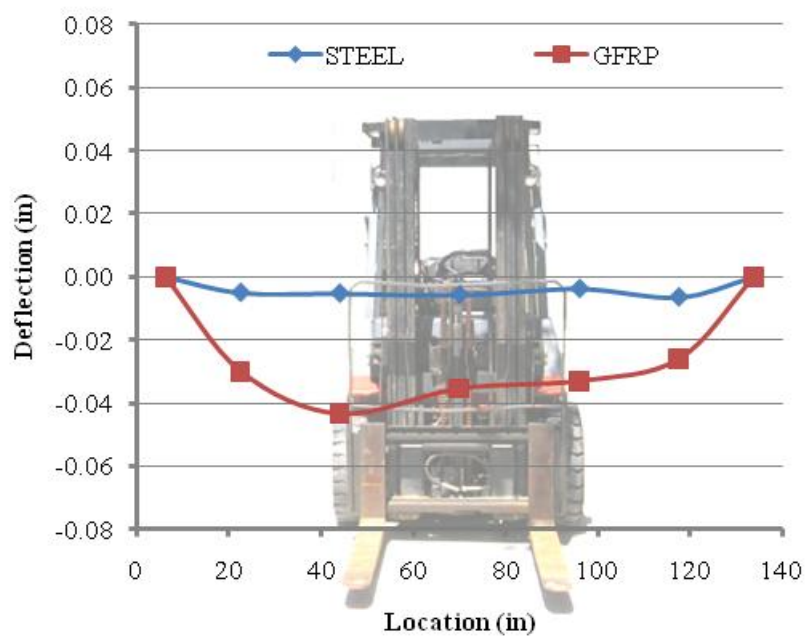
A comparison of the deflection between deck panels reinforced with mild steel and those reinforced with GFRP are shown in Figures 11.19 and 11.20 for the HSC bridge. In addition, Figures 11.21 and 11.22 illustrate a comparison of deflection of deck panels reinforced with GFRP and mild steel for the HS-SCC Bridge. The deflection of the deck panels were normalized by removing the deflection due to the beams.

In the HSC bridge, the maximum deflection was approximately 8 times higher with deck panels reinforced with GFRP than with mild steel. However, in the HS-SCC bridge, the maximum deflection was comparable between reinforcements. Due to the lower modulus of elasticity of the GFRP, higher deflections were expected in the deck panel with such reinforcement. However, any additional deflection perceived in the HSC testing could be due more to thermal effects and other aberrations that occurred during load testing that are much more sensitive during low deflection loading.



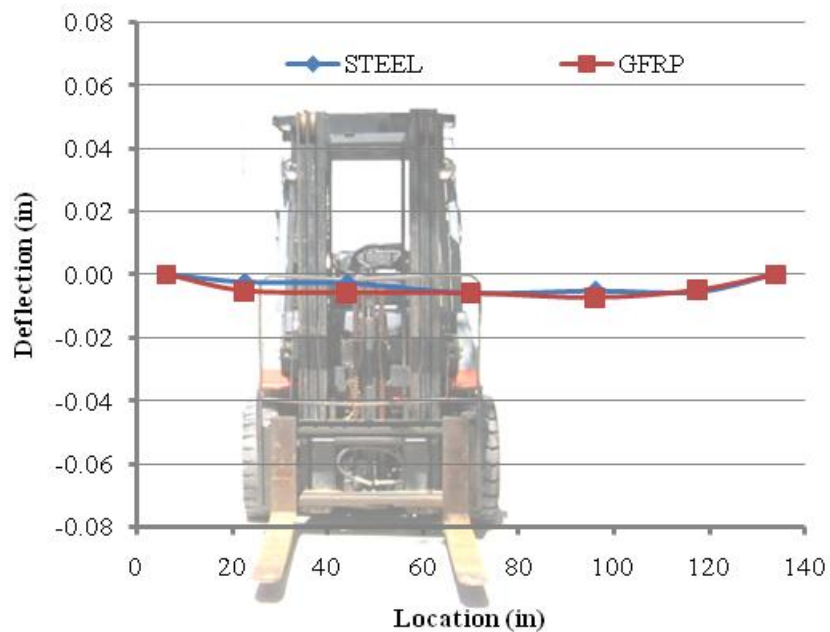
Conversion: 1-in. = 25.4 mm

Figure 11.19. HSC Deck Panel with Steel vs. GFRP Deflection – Load Case A & C.



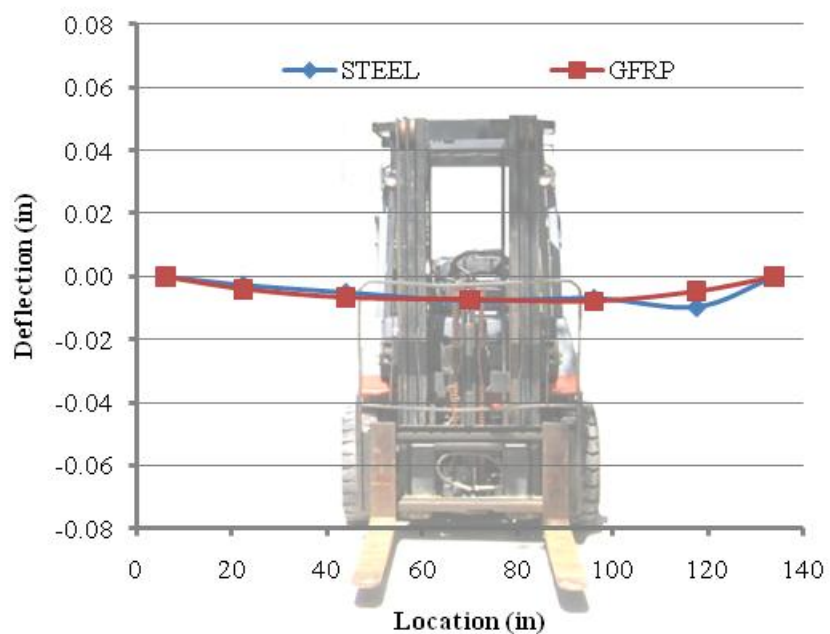
Conversion: 1-in. = 25.4 mm

Figure 11.20. HSC Deck Panel with Steel vs. GFRP Deflection – Load Case D & F.



Conversion: 1-in. = 25.4 mm

Figure 11.21. HS-SCC Deck Panel with Steel vs. GFRP Deflection – Load Case A & C.



Conversion: 1-in. = 25.4 mm

Figure 11.22. HS-SCC Deck Panel with Steel vs. GFRP Deflection – Load Case D & F.

To provide a proper comparison between the deflections of HSC to that of HS-SCC, the deflections needed to be normalized due to length. The results from load case F were used to compare the results of the mid-span deflection of HSC to HS-SCC. Load case F was chosen because the test was immediately followed by the dead load test utilized to remove thermal effects. Since thermal effects were interpolated with temperature data from the sensors, the test results received closest to the dead load test should be most accurate. The computed deflection and comparison with theoretical is displayed in Table 11.3.

Table 11.3. HSC & HS-SCC Comparison of Calculated to Measured Deflections.

Material	Calculated Deflection		Measured Deflection
	Simple	Fixed	
HSC	0.0095 (L/69,100)	0.0003 (L/1,678,400)	0.0083 (L/69,200)
HS-SCC	0.0030 (L/137,900)	0.0001 (L/3,080,800)	0.0026 (L/157,500)
Conversion: 1-in. = 25.4 mm			

From the results, it appears that the HS-SCC had slightly less deflection than that of the HSC. However, any difference in deflection between HSC and HS-SCC could be attributed to the effects mentioned previously such as thermal effects and the proximity of the total station to the target and reference prisms.

11.4. SUMMARY AND CONCLUSIONS

The load test utilizing a fork lift and precision surveying system was completed on an HSC and HS-SCC pedestrian bridge. Both the HSC and HS-SCC bridges displayed deflection results that appeared to be similar to the predicted simply supported deflection values. The deflection of HSC deck panels reinforced GFRP was found to be higher than that reinforced with mild steel. However, the deflection of HS-SCC deck

panels reinforced with GFRP compared to the deflection of panels reinforced with mild steel were similar. Even though the stiffness of the deck panels reinforced with GFRP is slightly less than those with mild steel and could increase the deflection of the deck panels, discrepancies in deflection measurements hinder the validity of the observations.

Due to the small load applied by the fork lift, the high variability of temperatures during the day, short span length, and high girder stiffness, a more precise deflection monitoring system is recommended for an accurate determination of deflections during load testing. In a previous project completed by Holdener on load testing bridges strengthened with FRP, it was reported that the Leica TCA 2003 Total Station was accurate to 0.13 mm (0.005-in.) at a distance of 61 m (200 ft) (Holdener, 2008). Myers and Yang reported that the use of LVDTs provide a much more accurate system of 0.03 mm (0.001-in.) (Myers and Yang, 2005). An LVDT system is recommended for future research on determining the bridge's deflection. In addition, a larger load is recommended to increase the accuracy of the bridge deflection testing. If a larger load is applied to the bridge, more accurate strain readings could be received from the VWSGs to monitor changes in the strain profile due to the load.

12. SUMMARY, CONCLUSIONS, AND RECOMMENDATIONS

12.1. SUMMARY AND CONCLUSIONS OF FINDINGS

The following is a list of the important findings that were determined during the Research program:

1. Two precast, prestressed pedestrian single span bridges were successfully constructed in Rolla, MO, of HSC and HS-SCC. Both of the concrete mixtures had a target 28 day compressive strength of 68.9 MPa (10,000 psi) and a release strength of 24.1 MPa (3,500 psi) which were obtained at the precasting plant. In addition, two different reinforced types were added within the bridges composed of either mild steel or GFRP.
2. For the mixture proportion utilized, the compressive strength of HSC was found to be higher than HS-SCC. The addition of the softer limestone, slightly higher w/cm ratio, and air entrainment may be attributed to the slightly lower compressive strength in the HS-SCC mixture
3. HSC empirical models for modulus of elasticity, modulus of rupture, and splitting tensile strength relating to compressive strength were found to over predict the stiffness and strengths of both the mixtures. Lower compressive, flexural, and splitting tensile strength results can be expected for HS-SCC due to the smaller percentage of coarse aggregates and slightly higher w/cm. However, the stiffness, split tension, and modulus of rupture of HSC was particularly lower than expected. The lower stiffness, tension, and flexural strength could be attributed to the aggregate type and its compatibility within the concrete matrix. Due to higher stiffness values of the aggregate, stress concentrations could have occurred within the mixture causing lower measured values than predicted by the empirical models. The following empirical equations tended to provide the best fit for the concretes investigated in this study.

For modulus of elasticity of HSC (ACI 363R-10, Equation 6-5):

$$E_c = 4.86 * 10^6 k_1 k_2 \left(w_c / 150 \right)^2 \left(f'_c / 8700 \right)^{1/3} \quad (\text{psi}) \quad (4)$$

For modulus of elasticity of HS-SCC (ACI 363-10):

$$E_c = 40,000 \sqrt{f'_c} + 10^6 \quad (\text{psi}) \quad (5)$$

For modulus of rupture of HSC and HS-SCC (ACI 318-08):

$$f_r = 7.5 \sqrt{f'_c} \quad (\text{psi}) \quad (6)$$

For split tension of HSC and HS-SCC (ACI 318-05):

$$f_{ct} = 6.7 \sqrt{f'_c} \quad (\text{psi}) \quad (10)$$

4. Creep values were found to be about 23% higher for HS-SCC than HSC due to the type and amount of coarse aggregate within the representative mixtures. The higher stiffness of the granite within HSC can provide greater resistance to creep than the limestone in the HS-SCC. Since HSC contained higher percentages of coarse aggregate, less creep was expected. The AASTHO LRFD (2007) was found to predict creep the best for both HSC and HS-SCC of all the methods analyzed.
5. Shrinkage values were found to be about 10% higher for HSC than HS-SCC. Since the w/cm ratios were fairly close, type of aggregate within the mixture could have played a more substantial role. AASHTO LRFD (2007) underestimated shrinkage of HSC by 53% and HS-SCC by 35% at 180 days. ACI 209 (1997) overestimated the shrinkage of the HSC by 15% and HS-SCC by 25% at 180 days. The NCHRP Report 628 modified AASHTO LRFD (Khayat and Mitchell, 2009) model suggestion for SCC over predicted the amount of shrinkage of HS-SCC by 25% at 180 days.

6. The maximum temperature rise of HSC was 36°C (65°F) and HS-SCC was 32°C (58°F) during concrete hydration. The equivalent maximum temperature rise for both HSC and HS-SCC were below those specified by ACI 363 (2010).
7. Differences in bridge temperatures between HSC and HS-SCC and deck panels reinforced with mild steel and GFRP were not statistically significant.
8. Positive thermal gradients proposed by AASHTO LRFD (2007) were similar to the values of the top and bottom bridge fibers. The intermediate points appeared to be underestimated by the code model. The negative thermal gradients proposed by the AASHTO LRFD (2007) were much closer to theoretical results for both bridge beams.
9. Bottom fiber concrete strain behavior at release of prestressing was 27% higher than predicted for HSC and 14% higher than predicted for HS-SCC.
10. Concrete strain behavior became increasingly complex due to time-dependent “local” prestress losses that varied among the tendons resulting in a non-linear strain distribution. Furthermore, any dead and live loads applied to the beam were found to be applied at a slight eccentricity through the centroid of the member. Due to these factors, simple mathematical equations for calculating strain tended to become less accurate as the strain profile become more non-linear. For example, during erection, the HSC had an average percentage difference of 60% and HS-SCC 50% between measured and theoretical strain.
11. The total loss of HSC was 68.8 MPa (9,840 psi), approximately 6.21% of the nominal jacking stress of 1,091 MPa (158.3 ksi). The total loss of HS-SCC was 53.0 MPa (7,691 psi), approximately 4.86% of the nominal jacking stress of 1,091 MPa (158.3 ksi).
12. The AASHTO LRFD (2007) overestimated the prestress loss of HSC by 23% and HS-SCC by 57% when the modulus of elasticity measured for the material was used in the prediction model. However, when the empirically predicted modulus of elasticity of HSC is used, the AASHTO equation only overestimates the prestress loss by 16%. The PCI Design Handbook (2004) were not as accurate and overestimated total prestress loss by 24 to 42% for HSC and 85 to 90% for HS-SCC depending whether design or measured parameters were used within the

equation. Any difference in predicted and measured prestress loss can be attributed to non-linear later-age strain graphs that were used to determine the measured prestress loss.

13. When the prestress loss to length of strand is compared between HSC and HS-SCC, HS-SCC has a higher loss per length of approximately 21% for elastic shortening loss and 10% for total loss. This additional prestress total loss can be attributed to the greater effect creep has on the material than on HSC.
14. The measured deflection values for the HSC and HS-SCC bridges were similar to the simply supported deflection values for both the spandrel beams and deck panels.
15. The differences of deck panels reinforced with GFRP and reinforced with mild steel were inconsistent between the HSC and HS-SCC bridges.

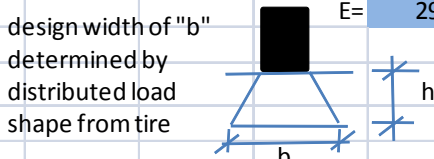
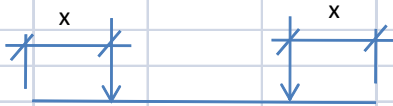
12.2. RECOMMENDATIONS FOR FUTURE RESEARCH

The following are recommended for future research:

1. Temperature and strains should be continued to be monitored in the HSC and HS-SCC pedestrian bridges in Rolla, MO. Long-term changes in strain, temperature, and prestress loss may continue to change as the bridges age.
2. Additional live load tests utilizing LVDTs with a higher load, such as a weighted forklift or multiple forklifts, is required to adequately determine differences in deflection and strains in the HSC and HS-SCC bridges and deck panels reinforced with GFRP and mild steel.
3. Later-age material testing should be completed on the two-year specimens to determine changes in material properties over the next year.
4. An advanced FEM is recommended to better predict the strains and stresses to correlate with the non-linear strain diagrams measured in the bridge. In addition, FEM should be completed on the load test data to more accurately predict the behavior of the beams due to eccentric loading.
5. Continued research should be completed on the differences between creep and shrinkage of HSC and HS-SCC.

6. An investigation for new guidance on temperature gradients for main beam/girder elements that do not fully rest below the deck should be completed.

APPENDIX A.
STEEL AND GFRP DECK PANEL REINFORCEMENT DESIGN

 University of Science & Technology	 Center for Transportation Infrastructure and Safety	PROJECT:	Slab Reinforcement Design for Rolla Bridge Project		
		BY:	Dr. John J. Myers, Kurt Bloch, & Wei Zheng	PAGE:	1
				DATE:	6/11/2009
Necessary Properties:					
Concrete Properties:		GFRP Properties for No. 6 Bar:			
$f'_c =$	10 ksi	$C_E =$	0.7		
$\beta_1 =$	0.65	$f_{fu}^* =$	90 ksi		
$\epsilon_{cu} =$	0.003	$f_{fu} =$	63 ksi		
$E_c =$	180.2498 ksi	$E_f =$	5920 ksi		
Section Properties:		Steel Reinforcement Properties:			
$b =$	24 in	$f_y =$	60 ksi		
$h =$	8 in	$E =$	29000 ksi		
$d =$	7 in	 design width of "b" determined by distributed load shape from tire			
$l_n =$	111 in				
Loading:					
Uniform Loading:		Point Load:			
$LL =$	100 psf	$LL =$	5 k		
$DL =$	100 psf				
$w_u =$	$1.4DL + 1.7LL$				
$w_u =$	620.00 lb/ft/design width	$x =$	2		
$M_u =$	$\frac{1}{8} w_u l_n^2$	$M_u =$	$P_u x + \frac{1}{8} w_u l_n^2$		
$M_u =$	6.63 k-ft/design width	$M_u =$	19.99 k-ft/design width		
$V_u =$	$1.15 w_u \frac{l_n}{2}$	$V_u =$	$1.15 P_u + 1.15 w_u \frac{l_n}{2}$		
$V_u =$	3.30 k/design width	$V_u =$	11.26 k/design width		
Controlling Moment:					
$M_u =$	19.99 k-ft/design width				
Controlling Shear:					
$V_u =$	11.26 k/design width				
<i>ACI 440.1R -2003</i>					

 University of Science & Technology	 Center for Transportation Infrastructure and Safety	PROJECT:	Slab Reinforcement Design for Rolla Bridge Project									
		BY:	Dr. John J. Myers, Kurt Bloch, & Wei Zheng	PAGE:	2							
				DATE:	6/11/2009							
GFRP Flexural Design:												
GFRP Required:												
$A_{f,min} = \frac{5.4\sqrt{f'_c}}{f_{fu}} b_w d \geq \frac{360}{f_{fu}} b_w d$												
$A_{f,min} = 0.72 \text{ in}^2/\text{ft}$												
Try 3 No. 6 bars every foot												
<table border="1"> <thead> <tr> <th>Bar Size</th> <th>Bar Area in²</th> <th>Spacing in</th> <th>A_f in²</th> </tr> </thead> <tbody> <tr> <td>6</td> <td>0.442</td> <td>6</td> <td>0.884</td> </tr> </tbody> </table>					Bar Size	Bar Area in ²	Spacing in	A _f in ²	6	0.442	6	0.884
Bar Size	Bar Area in ²	Spacing in	A _f in ²									
6	0.442	6	0.884									
$A_f = 0.884 \text{ in}^2/\text{ft}$												
$\rho_f = 0.010524$												
$f_f = \sqrt{\frac{(E_f \epsilon_{cu})^2}{4} + \frac{0.85\beta_1 f'_c}{\rho_f} E_f \epsilon_{cu}} - 0.5 E_f \epsilon_{cu}$												
$M_n = \rho_f f_f \left(1 - 0.59 \frac{\rho_f f_f}{f'_c}\right) b d^2$												
$\rho_{fb} = 0.85 \frac{f'_c}{f_{fu}} \beta_1 \frac{E_f \epsilon_{cu}}{E_f \epsilon_{cu} + f_{fu}}$												
$\phi = \begin{cases} 0.50 & \text{for } \rho_f \leq \rho_{fb} \\ \frac{\rho_f}{2\rho_{fb}} & \text{for } \rho_{fb} < \rho_f < 1.4\rho_{fb} \\ 0.70 & \text{for } \rho_f \geq 1.4\rho_{fb} \end{cases}$												
$f_f = 88.08832 \text{ ksi}$												
$M_n = 85.87951 \text{ k-ft/design width}$												
$\rho_{fb} = 0.019286$												
$\phi = 0.5$												
$\phi M_n = 42.93976 \text{ k-ft/design width}$												
$M_u = 19.99 \text{ k-ft/design width}$												
$\phi M_n \geq M_u? \quad \text{YES}$												
GFRP Shear Check:												
Shear Capacity:												
$V_{c,f} = \frac{\rho_f E_f}{90\beta_1 f'_c} 2\sqrt{f'_c} b d$												
$\phi = 0.85$												
$V_{c,f} = 3.578311 \text{ k/design width}$												
$\phi V_{c,f} = 3.041564 \text{ k/design width}$												
$V_u = 11.26 \text{ k/design width}$												
$\phi V_{c,f} \geq V_u? \quad \text{NO}$												
<i>ACI 440.1R -2003</i>												

 University of Science & Technology	 A National University Transportation Center at Missouri S&T	PROJECT:	Slab Reinforcement Design for Rolla Bridge Project		
		BY:	Dr. John J. Myers, Kurt Bloch, & Wei Zheng	PAGE:	3
				DATE:	6/11/2009
GFRP Shear Check:					
<i>Apply steel at the minimum spacing of 18" to flexural reinforcement to increase shear capacity</i>					
$A_s = \frac{E_f A_f}{E_s}$					
$A_s = 0.270687 \text{ in}^2$					
Try No. 5 Bar					
$A_{s, \text{used}} = 0.31 \text{ in}^2$					
Shear capacity can be increased to:					
$V_c = 2\sqrt{f'_c} bd$					
$V_c = 33.6 \text{ k/design width}$					
$\phi V_c = 28.56 \text{ k/design width}$					
$V_u = 11.26 \text{ k/design width}$					
$\phi V_{c,f} \geq V_u? \quad \text{YES}$					
Temperature and Shrinkage Reinforcement for GFRP:					
<i>Temperature and Shrinkage Reinforcement Properties:</i>					
Assume No. 6 Bar					
$f'_{fu} =$	90 ksi	Bar Size	Bar Area in ²	Spacing in	As in ²
$f_{fu} =$	63 ksi				
$E_f =$	5920 ksi				
$\rho_{f,ts} = 0.0018 \frac{60000 E_s}{f_{fu} E_f} \geq 0.0014$					
$\rho_{f,ts} = 0.008398$					
$\rho_{\text{used}} = 0.010048$					
<i>ACI 440.1R -2003</i>					

 University of Science & Technology	 Center for Transportation Infrastructure and Safety	PROJECT:	Slab Reinforcement Design for Rolla Bridge Project		
		BY:	Dr. John J. Myers, Kurt Bloch, & Wei Zheng	PAGE:	4
				DATE:	6/11/2009
Steel Flexural Design:					
<i>Steel Required:</i>					
$\rho_{max} = 0.85\beta_1 \frac{f'_c}{f_y} \left(\frac{3}{7}\right)$		$\rho_{min} = \frac{3f'_c}{f_y} \geq \frac{200}{f_y}$		$\rho = \frac{A_s}{bd}$	
$\rho_{max} =$	0.039464	Bar Size	Bar Area	Spacing	As
$\rho_{min} =$	0.005		in ²	in	in ²
$A_s =$	0.413333	5	0.31	9	0.413333
$\rho =$	0.004921				
$M_n = \rho f_y \left(1 - 0.59 \frac{\rho f_y}{f'_c}\right) b d^2$					
				a =	0.243867 in
$M_n =$	28.42934 k-ft/design width			c =	0.375179 in
$\Phi =$	0.9			$\epsilon_s =$	0.052973
$\Phi M_n =$	25.58641 k-ft/design width			$M_u =$	19.99 k-ft/deisng width
$\Phi M_n \geq M_u?$	YES				
Shear Check with Steel					
<i>Shear Capacity:</i>					
$V_c = 2\sqrt{f'_c} b d$				$\phi =$	0.85
$V_c =$	33.6 k/design width				
$\phi V_c =$	28.56 k/design width			$V_u =$	11.26 k/design width
$\phi V_c \geq V_u?$	YES				
Temperature and Shrinkage Reinforcement for Steel:					
$\rho =$	0.0018	Bar Size	Bar Area	Spacing	As
$\rho_{used} =$	0.002381		in ²	in	in ²
		4	0.2	12	0.2

APPENDIX B.
PROGRAM FOR DAS CR1000

'CR1000 Series Datalogger

'To create a different opening program template, type in new

'instructions and select Template | Save as Default Template

'date:

'program author:

'Declare Public Variables

'Example:

Public PTemp_C, BattV

Public Data1, Data2

Public Mux1(8,6), Mux2(8,6)

Public Digits(16), Linear(16), Temp(16)

Units BattV=Volts

Units PTemp_C=Deg C

'Declare Other Variables

Const Time=30 'Time interval value I set scan and store to the same values

Const TM_Unit=3 'Time Measure 1="mSec", 2="Sec", 3="Min", 4="Hr", 5="Day"

Const Chan1=1 'AVW200 channel 1

Const Chan2=2 'AVW200 Channel 2

Const MuxChan=1 'Starting Mux Channel

Const Reps=8 'Number of Reps

Const BFreq=450 'Begin Frequency

Const EFreq=1100 'End Frequency

Const Xvolt=1 '1 for 5Vp-p or 2 for 12p-p volt Excite

Const CA = 0.00145051 'Coefficients for Steinhart-Hart equation used to convert
resistance to degree for 3K therm.

Const CB = 0.0002369

Const CC = 0.0000001019

```

Dim MLC      'Mux1 variable conversion loop counter
Dim M2LC     'Mux2 variable conversion loop counter 'each variable could of been
reused
Dim Therm    'Temporary temperature reading      'but for clarity I used extra
variables
Dim Therm2   'Un-necessary variable, but for easier learning
Dim Freq     'Temporary Frequency reading to digits
Dim Freq2    'Un-necessary variable, but for easier learning

```

```

DataTable(VWTable1,True,-1)
  DataInterval(0,Time,TM_Unit,10)
  Sample(16,Digits(),FP2)
  Sample(16,Linear(),FP2)
  Sample(16,Temp(),FP2)
  'Sample(48,Mux1(),IEEE4) 'diagnostic readings only, can be dropped when we go to
long term field testing
  'Sample(48,Mux2(),IEEE4) 'diagnostic readings only, can be dropped when we go to
long term field testing
  Minimum(1,BattV,FP2,False,False)
EndTable

```

```
'Main Program
```

```
BeginProg
```

```
SerialOpen(Com1,38400,0,0,10000)
```

```
Scan (Time,TM_Unit,1,0) '(2 * 16 Measurement) = 32 Seconds
```

```
PanelTemp (PTemp_C,250)
```

```
Battery (BattV)
```

```
'Enter other measurement instructions
```

```
AVW200(Data1(),Com1,200,200,Mux1(1,1),Chan1,MuxChan,Reps,Bfreq,Efreq,Xvolt,_
60Hz,1,0)
```

```
AVW200(Data2(),Com1,200,200,Mux2(1,1),Chan2,MuxChan,Reps,Bfreq,Efreq,Xvolt,_
60Hz,1,0)
```

```
PanelTemp(PTemp_C,_60Hz)
```

```
For MLC = 1 To 8 'Mux1 readings read in during MLC loop
```

```
  Freq= Mux1(MLC,1)
```

```
  Digits(MLC)=(Freq^2)/1000 'convert freq. to digits
```

```
  Linear(MLC)= 4.0624*(Freq^2)/1000 'convert freq. to Linear Readings
```

```
  Therm = Mux1(MLC,6)
```

```
  Temp(MLC)=(1 / (CA + CB * LN(Therm) + CC * (LN(Therm)) ^ 3) - 273.15)' *
```

```
1.8 + 32
```

```
Next MLC
```

```
For M2LC = 1 To 8 'Mux2 readings read in during M2LC loop
```

```
  Freq2= Mux2(M2LC,1)
```

```
  Digits(M2LC+8)=(Freq2^2)/1000 'convert freq. to digits
```

```
  Linear(M2LC+8)= 4.0624*(Freq2^2)/1000 'convert freq. to Linear Readings
```

```
  Therm2 = Mux2(M2LC,6)
```

```
  Temp(M2LC+8)=(1 / (CA + CB * LN(Therm2) + CC * (LN(Therm2)) ^ 3) -
```

```
273.15)' * 1.8 + 32
```

```
Next M2LC
```

```
CallTable(VWTable1)
```

```
NextScan
```

```
EndProg
```

APPENDIX C.
GFRP TEST RESULTS

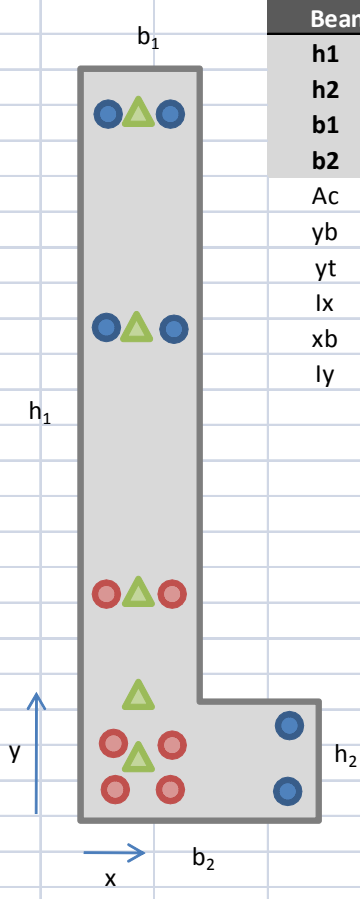
Tensile Testing of GFRP Rebar								
Aslan FRP Hughes Brothers Seward, NE			Information:					
			Rebar Size: RB6	Tested By: R. Colberg				
TEST MACHINE Baldwin Model 120 CS S/N : 1005 Electromechanical 120,000 lbs Capacity Tension/Compression Certification Number 148082709080420 By Instron 27-August-09 Operating System-MTEST Windows Grip V Style			Stock Order: 7028	Test Date: 8/19/2009				
			Work Order: 1	Reinforcement: ECR-Glass				
			Date Produced: 8/13/2009	Filament Diameter: 23 Micron				
			Lot Color Code: Blue D7078	Sizing: Silane				
			Matrix: VE	Yield: 113				
			Formulation: RBVEIP2567-25 FA	No of Ends: 96				
			Test Temp: 77.0°F	Sample Length (in): 48				
			Test R/H: 52%	Free Length (in): 34.125				
			Load Rate: 0.5"/min	Potting Material: Swaged				
Sample No.	Load lbs	Area in ²	Area mm ²	Tensile Strength psi	Tensile Strength MPa	U. Strain in/in	Mod. of Elasticity psi	Mod. of Elasticity Gpa
1	53887.8	0.442	285.0	121973.3	841.0	0.0176	6944342	47.9
2	53334.5	0.442	285.0	120720.9	832.4	0.0170	7105354	49.0
3	53366.8	0.442	285.0	120794.0	832.9	0.0177	6815321	47.0
4	52878.7	0.442	285.0	119689.2	825.3	0.0176	6795649	46.9
5	51797.2	0.442	285.0	117241.3	808.4	0.0169	6918009	47.7
6	52528.6	0.442	285.0	118896.8	813.6	0.0170	6979888	48.1
7	52130.6	0.442	285.0	117995.9	813.6	0.0169	6993964	48.2
8	52310.7	0.442	285.0	118403.6	816.4	0.0175	6755407	46.6
Averages						0.0173	6913492	47.7
Tensile Strength		PSI	MPa	Strain		Extensometer Epsilon Model 3543		
Average		119464.4	823.7	0.0173		Distance from Anchors (in): 14.063		
Sigma		1509.9	10.4	0.0003		LBS of Load at Removal: 19881		
3 Sigma		4529.7	31.2	0.0010		Percent of Load at Removal: 50%		
σ-3 Sigma		114934.7	792.5	0.0163		Span (in): 6		
Sample	Mode of Failure	Additional Lab Test Data						
1	Delam Center	% Glass of Matrix		74.55 / 25.45	ASTM D2584 by wt.			
2	Split Center	Barcol Hardness		61.4	ASTM D2583			
3	Delam Center	Wicking		Not Continuous	ASTM D5117			
4	Delam Center	Transverse Shear (psi)		23559.1	ACI 440 B.4			
5	Delam Center	Apparent Shear (psi)		7883.4	ASTM D4475			
6	Delam Center	Water Absorption		0.1137%	ASTM D570 P7.7			
7	Delam Center	Average 24 Hour						
8	Delam Center	Surface: Undulated Externally Wrapped						
Spacing of Wrap .75 - 1.0"								
Silica Sand applied to Surface During Process								
Samples cut using Diamond Blade Cutoff Saw								
Anchorage are cut to length and whell abrated								
Schedule 40 Pipe								
Rebar Size	Required Tensile Strength (psi / MPa)	Load Cell Min (lbs/ N)	Nominal Diameter (in / mm)	Standard CSA Ao (in / mm)				
6	90000	39762	0.7500	0.4418				
10	620.5	176870	19.05	285.0				
Metric Values								
Per ASTM D7205-06								

APPENDIX D.
EXAMPLE STRESS AND STRAIN CALCULATIONS



Rolla Pedestrian Theoretical
Stress Profiles
Kurt E. Bloch

Page
 No
 1



Beam Section Properties		Prestressing Steel	
h1	63.00 in	fpu	270 ksi
h2	12.00 in	F1	16.3 k
b1	10.00 in	F2	32.3 k
b2	18.00 in	Eps	29000 ksi
Ac	726.00 in ²	Aps	0.153 in ²
y _b	28.13 in	Ags	1.836 in ²
y _t	34.87 in	g _x	6.23 in
I _x	263694.1 in ⁴	g _y	18.28 in
x _b	6.19 in	e _x	-0.04 in
I _y	12509.77 in ⁴	e _y	9.85 in

Location		Initial	
y (in)	x (in)	Force (k)	Stress (ksi)
60	2.5	16.3	106.54
60	7.5	16.3	106.54
42	2.5	16.3	106.54
42	7.5	16.3	106.54
22	2.5	32.3	211.11
22	7.5	32.3	211.11
10	16	16.3	106.54
4	2.5	32.3	211.11
4	7.5	32.3	211.11
2	2.5	32.3	211.11
2	7.5	32.3	211.11
2	16	16.3	106.54

Material Properties Concrete	
Material	HSC
f'ci	6765.28 psi
f'c	12230.90 psi
Eci	3720.00 ksi
Ec	4538.33 ksi
γc	145.00 pcf
L	48 ft

Prestress Loss Information	
V/S	4.412815 in
t1	1 day
t2	7 days
RH	70 %
Ksh	0.92
Cu	1.645
Pj	291.6 k

Loading Information	
Wself	731.0417 plf
Wdeck	447.0833 plf

Mid-Span Moment	
Mbeam	2526.48 k-in
Mdeck	1545.12 k-in

		Rolla Pedestrian Theoretical							Page
		Stress Profiles							No
		Kurt E. Bloch							2
HSC	Prestress Loss								
		MOE (Strand) / MOE (Concrete)							
		when jacking							7.795699
		long-term							6.390016
Elastic Shortening (ES)									
Location	Pi=0.9xPj kips	w plf	M (self) k-in	e in	P/A psi	P*e^2/l psi	M*e/l psi	Stress psi	ES psi
Mid-Span	262.44	731.0417	2526.48	9.85	361.4876	96.58083	94.38351	-363.685	2835.178
Support	262.44	731.0417	0	9.85	361.4876	96.58083	0	-458.068	3570.964
Creep (CR)									
Location	Pi=0.9xPj kips	w plf	M (self & panel) k-in	e in	P/A psi	P*e^2/l psi	M*e/l psi	Stress psi	CR psi
Mid-Span	262.44	1178.125	4071.6	9.85	361.4876	96.58083	152.1057	-305.963	782.272
Support	262.44	1178.125	0	9.85	361.4876	96.58083	0	-458.068	1171.169
Shrinkage (SH)									
Location		Ksh	V/S in	RH %				Stress psi	SH psi
Mid-Span		0.92	4.412815	70				4825.528	4825.528
Support		0.92	4.412815	70				4825.528	4825.528
Relaxation 1 (RE1)									
Location	fpi psi	fpy psi	t2 hours	t1 hours				Stress psi	RE1 psi
Mid-Span	106.5359	243	168	24				0	0
Support	106.5359	243	168	24				0	0
Relaxation 2 (RE2)									
Location	fpi psi	fpy psi	t2 hours	t1 hours				Stress psi	RE2 psi
Mid-Span	211.1111	243	168	24				2113.261	2113.261
Support	211.1111	243	168	24				2113.261	2113.261

		Rolla Pedestrian Theoretical		Page		
		Stress Profiles		No		
		Kurt E. Bloch		3		
Prestress Loss				Loading Info.		
Location	Support	Mid-Span	Self-Wt?	NO		
ES	3570.96 psi	2835.18 psi	Panel?	NO		
CR	1171.17 psi	782.27 psi	Age	7		
SH	4825.53 psi	4825.53 psi	Ld,1 (in)	100.75		
RE1	0.00 psi	0.00 psi	Ld,2 (in)	66.59		
RE2	2113.26 psi	2113.26 psi	Date	8/6/09		
Total1	9567.66 psi	8442.98 psi				
Total2	11680.92 psi	10556.24 psi				
Percent1	8.98 %	7.93 %				
Percent2	5.53 %	5.00 %				
Ploss	19506.20 lbs	17441.28 lbs				
Pload	242.93 k	245.00 k				
Development Length			Support Development Force & Stress			
	F1	F2	Location		Initial	
γ_p	0.28	0.28	y (in)	x (in)	Force (k)	Stress (ksi)
β_1	0.65	0.65	60	2.5	0.883584	5.78
Aps	0.918 in2	0.918 in2	60	7.5	0.883584	5.78
b	10.00 in	10.00 in	42	2.5	0.883584	5.78
dp	61.00 in	61.00 in	42	7.5	0.883584	5.78
ρ_p	0.001505	0.001505	22	2.5	2.749261	17.97
fpu	270 ksi	270 ksi	22	7.5	2.749261	17.97
f'c	12230.90 psi	12230.90 psi	10	16	0.883584	5.78
fps	266.1361 ksi	266.1361 ksi	4	2.5	2.749261	17.97
fse	96.96829 ksi	199.4302 ksi	4	7.5	2.749261	17.97
db	0.5 in	0.5 in	2	2.5	2.749261	17.97
ld	100.75 in	66.59 in	2	7.5	2.749261	17.97
			2	16	0.883584	5.78
			Total		21.79707	142.46
			gx		5.89181	
			gy		15.81922	
			ex		0.30	
			ey		12.31	



**Rolla Pedestrian Theoretical
Stress Profiles**
Kurt E. Bloch

Page
No
4

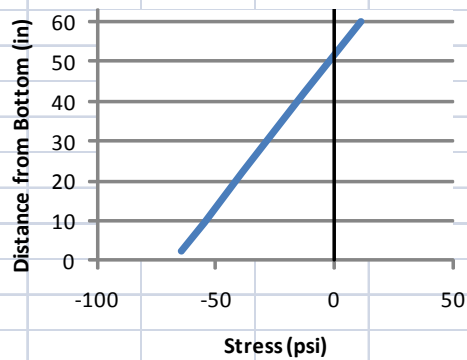
Theoretical Stesses in VWSG's @ Support

Distance from End		6 in		Reduction Due to Transfer?			YES
Location		Pload	P/A	$P \cdot e_y \cdot y / I_x$	$P \cdot e_x \cdot x / I_y$	$M \cdot y / I_x$	Stress
x	y	k	psi	psi	psi	psi	psi
5	60	21.79707	30.02351	-41.67646	0.6185	0	11.03445
5	42	21.79707	30.02351	-18.13923	0.6185	0	-12.5028
5	22	21.79707	30.02351	8.013249	0.6185	0	-38.6553
5	9.5	21.79707	30.02351	24.358548	0.6185	0	-55.0006
5	2.5	21.79707	30.02351	33.511915	0.6185	0	-64.1539

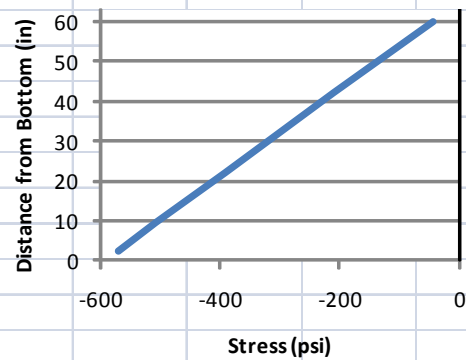
Theoretical Stesses in VWSG's @ Mid-Span

Distance from End		288 in		Reduction Due to Transfer?			NO
Location		Pload	P/A	$P \cdot e_y \cdot y / I_x$	$P \cdot e_x \cdot x / I_y$	$M \cdot y / I_x$	Stress
x	y	k	psi	psi	psi	psi	psi
5	60	244.9987	337.4638	-291.7105	-0.92493	0	-44.8284
5	42	244.9987	337.4638	-126.9638	-0.95577	0	-209.544
5	22	244.9987	337.4638	56.087986	-0.95577	0	-392.596
5	9.5	244.9987	337.4638	170.49538	-0.95577	0	-507.003
5	2.5	244.9987	337.4638	234.56351	-0.95577	0	-571.072

Support Sensors



Mid-Span Sensors





**Rolla Pedestrian Theoretical
Stress Profiles**
Kurt E. Bloch

Page
No
5

Cct	ΔP k	Po k	St	ϵ_{sh} $\mu\epsilon$	Include $\epsilon_{sh}?$
1.17	19.5062	262.44	1.0521928	-25.7293	YES

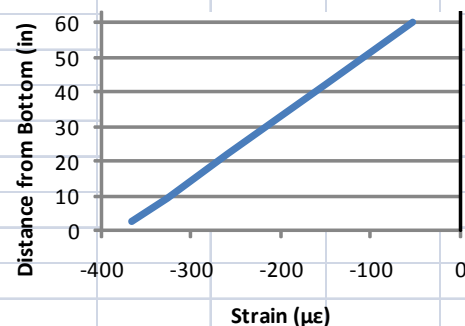
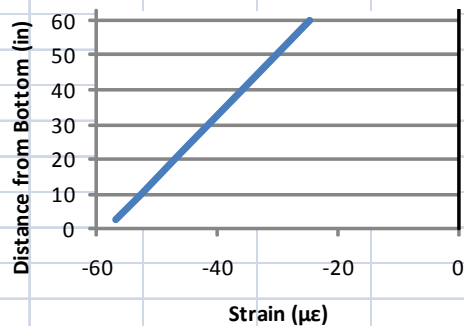
Theoretical Stresses in VWSG's @ Support							
Distance from End		6 in			Reduction Due to Transfer?	YES	
Location		Axial	y-ec	x-ec	Moment	ϵ_{sh}	Total
x	y	$\mu\epsilon$	$\mu\epsilon$	$\mu\epsilon$	$\mu\epsilon$	$\mu\epsilon$	$\mu\epsilon$
5	60	16.56291	-17.8895	0.3412045	0	-25.7293	-24.7438
5	42	16.56291	-7.78623	0.3412045	0	-25.7293	-34.8471
5	22	16.56291	3.439672	0.3412045	0	-25.7293	-46.073
5	9.5	16.56291	10.45586	0.3412045	0	-25.7293	-53.0892
5	2.5	16.56291	14.38493	0.3412045	0	-25.7293	-57.0183
5	63	16.56291	-19.5734	0.3412045	0	-25.7293	-23.0599
5	0	16.56291	15.78817	0.3412045	0	-25.7293	-58.4215

Cct	ΔP k	Po k	St	ϵ_{sh} $\mu\epsilon$	Include $\epsilon_{sh}?$
1.17	17.44128	262.44	1.0646638	-25.7293	YES

Theoretical Stresses in VWSG's @ Mid-Span							
Distance from End		288 in			Reduction Due to Transfer?	NO	
Location		Axial	y-ec	x-ec	Moment	ϵ_{sh}	Total
x	y	$\mu\epsilon$	$\mu\epsilon$	$\mu\epsilon$	$\mu\epsilon$	$\mu\epsilon$	$\mu\epsilon$
5	60	200.6318	-173.43	-0.549897	0	-25.7293	-52.381
5	42	200.6318	-75.4836	-0.549897	0	-25.7293	-150.328
5	22	200.6318	33.3459	-0.549897	0	-25.7293	-259.157
5	9.5	200.6318	101.3643	-0.549897	0	-25.7293	-327.176
5	2.5	200.6318	139.4547	-0.549897	0	-25.7293	-365.266
5	63	200.6318	-189.755	-0.549897	0	-25.7293	-36.0566
5	0	200.6318	153.0584	-0.549897	0	-25.7293	-378.87

Support Sensors

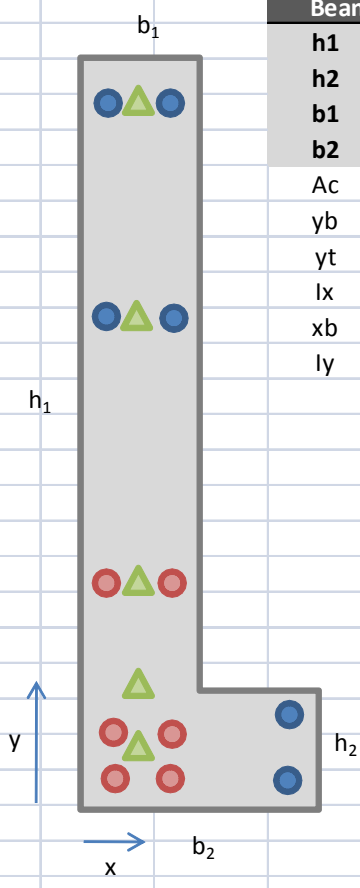
Mid-Span Sensors





Rolla Pedestrian Theoretical
Stress Profiles
Kurt E. Bloch

Page
 No
 1



Beam Section Properties		Prestressing Steel	
h1	63.00 in	fpu	270 ksi
h2	12.00 in	F1	16.3 k
b1	10.00 in	F2	32.3 k
b2	18.00 in	Eps	29000 ksi
Ac	726.00 in ²	Aps	0.153 in ²
y _b	28.13 in	A _{gs}	1.836 in ²
y _t	34.87 in	g _x	6.23 in
I _x	263694.1 in ⁴	g _y	18.28 in
x _b	6.19 in	e _x	-0.04 in
I _y	12509.77 in ⁴	e _y	9.85 in

Location		Initial	
y (in)	x (in)	Force (k)	Stress (ksi)
60	2.5	16.3	106.54
60	7.5	16.3	106.54
42	2.5	16.3	106.54
42	7.5	16.3	106.54
22	2.5	32.3	211.11
22	7.5	32.3	211.11
10	16	16.3	106.54
4	2.5	32.3	211.11
4	7.5	32.3	211.11
2	2.5	32.3	211.11
2	7.5	32.3	211.11
2	16	16.3	106.54

Material Properties Concrete	
Material	HS-SCC
f'ci	6499.49 psi
f'c	10131.40 psi
Eci	4475.00 ksi
Ec	4871.67 ksi
γc	140.00 pcf
L	34 ft

Prestress Loss Information	
V/S	4.385148 in
t1	1 day
t2	7 days
RH	70 %
Ksh	0.92
Cu	2.032
Pj	291.6 k

Loading Information	
Wself	705.8333 plf
Wdeck	431.6667 plf

Mid-Span Moment	
Mbeam	1223.915 k-in
Mdeck	748.51 k-in

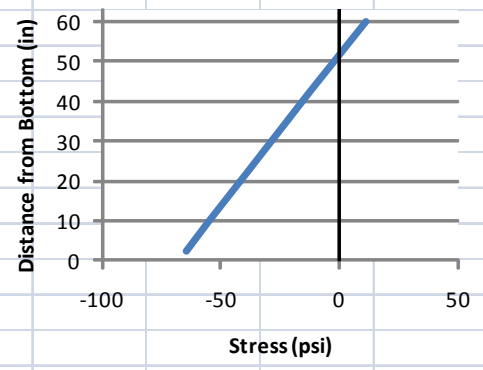
		Rolla Pedestrian Theoretical							Page
		Stress Profiles							No
		Kurt E. Bloch							2
HS-SCC	Prestress Loss								
		MOE (Strand) / MOE (Concrete)							
		when jacking							6.480447
		long-term							5.952784
Elastic Shortening (ES)									
Location	Pi=0.9xPj kips	w plf	M (self) k-in	e in	P/A psi	P*e^2/l psi	M*e/l psi	Stress psi	ES psi
Mid-Span	262.44	705.8333	1223.915	9.85	361.4876	96.58083	45.72266	-412.346	2672.185
Support	262.44	705.8333	0	9.85	361.4876	96.58083	0	-458.068	2968.488
Creep (CR)									
Location	Pi=0.9xPj kips	w plf	M (self & panel) k-in	e in	P/A psi	P*e^2/l psi	M*e/l psi	Stress psi	CR psi
Mid-Span	262.44	1137.5	1972.425	9.85	361.4876	96.58083	73.68528	-384.383	1130.914
Support	262.44	1137.5	0	9.85	361.4876	96.58083	0	-458.068	1347.707
Shrinkage (SH)									
Location		Ksh	V/S in	RH %				Stress psi	SH psi
Mid-Span		0.92	4.385148	70				4836.423	4836.423
Support		0.92	4.385148	70				4836.423	4836.423
Relaxation 1 (RE1)									
Location	fpi psi	fpy psi	t2 hours	t1 hours				Stress psi	RE1 psi
Mid-Span	106.5359	243	168	24				0	0
Support	106.5359	243	168	24				0	0
Relaxation 2 (RE2)									
Location	fpi psi	fpy psi	t2 hours	t1 hours				Stress psi	RE2 psi
Mid-Span	211.1111	243	168	24				2113.261	2113.261
Support	211.1111	243	168	24				2113.261	2113.261

		Rolla Pedestrian Theoretical		Page		
		Stress Profiles		No		
		Kurt E. Bloch		3		
Prestress Loss				Loading Info.		
Location	Support	Mid-Span	Self-Wt?	NO		
ES	2968.49 psi	2672.18 psi	Panel?	NO		
CR	1347.71 psi	1130.91 psi	Age	7		
SH	4836.42 psi	4836.42 psi	Ld,1 (in)	100.21		
RE1	0.00 psi	0.00 psi	Ld,2 (in)	66.05		
RE2	2113.26 psi	2113.26 psi	Date	8/6/09		
Total1	9152.62 psi	8639.52 psi				
Total2	11265.88 psi	10752.78 psi				
Percent1	8.59 %	8.11 %				
Percent2	5.34 %	5.09 %				
Ploss	18744.18 lbs	17802.13 lbs				
Pload	243.70 k	244.64 k				
Development Length			Support Development Force & Stress			
	F1	F2	Location		Initial	
γ_p	0.28	0.28	y (in)	x (in)	Force (k)	Stress (ksi)
β_1	0.65	0.65	60	2.5	0.892136	5.83
Aps	0.918 in2	0.918 in2	60	7.5	0.892136	5.83
b	10.00 in	10.00 in	42	2.5	0.892136	5.83
dp	61.00 in	61.00 in	42	7.5	0.892136	5.83
ρ_p	0.001505	0.001505	22	2.5	2.777451	18.15
fpu	270 ksi	270 ksi	22	7.5	2.777451	18.15
f'c	10131.40 psi	10131.40 psi	10	16	0.892136	5.83
fps	265.3354 ksi	265.3354 ksi	4	2.5	2.777451	18.15
fse	97.38333 ksi	199.8452 ksi	4	7.5	2.777451	18.15
db	0.5 in	0.5 in	2	2.5	2.777451	18.15
ld	100.21 in	66.05 in	2	7.5	2.777451	18.15
			2	16	0.892136	5.83
			Total		22.01752	143.91
			gx		5.891426	
			gy		15.81643	
			ex		0.30	
			ey		12.31	

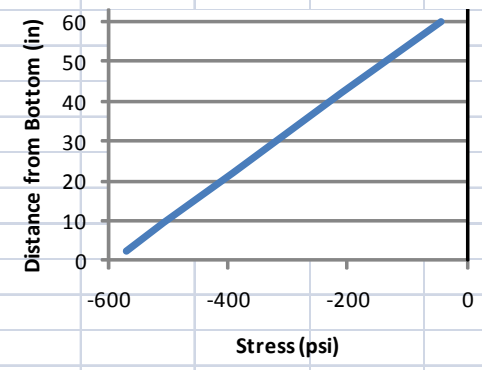
Theoretical Stesses in VWSG's @ Support							
Distance from End		6 in		Reduction Due to Transfer?			YES
Location		Pload	P/A	P*ey*y/lx	P*ex*x/ly	M*y/lx	Stress
x	y	k	psi	psi	psi	psi	psi
5	60	22.01752	30.32717	-42.09054	0.625559	0	11.13782
5	42	22.01752	30.32717	-18.31945	0.625559	0	-12.6333
5	22	22.01752	30.32717	8.092866	0.625559	0	-39.0456
5	9.5	22.01752	30.32717	24.600566	0.625559	0	-55.5533
5	2.5	22.01752	30.32717	33.844879	0.625559	0	-64.7976

Theoretical Stesses in VWSG's @ Mid-Span							
Distance from End		204 in		Reduction Due to Transfer?			NO
Location		Pload	P/A	P*ey*y/lx	P*ex*x/ly	M*y/lx	Stress
x	y	k	psi	psi	psi	psi	psi
5	60	244.6379	336.9668	-291.2808	-0.92357	0	-44.7624
5	42	244.6379	336.9668	-126.7768	-0.95436	0	-209.236
5	22	244.6379	336.9668	56.005375	-0.95436	0	-392.018
5	9.5	244.6379	336.9668	170.24426	-0.95436	0	-506.257
5	2.5	244.6379	336.9668	234.21803	-0.95436	0	-570.23

Support Sensors



Mid-Span Sensors





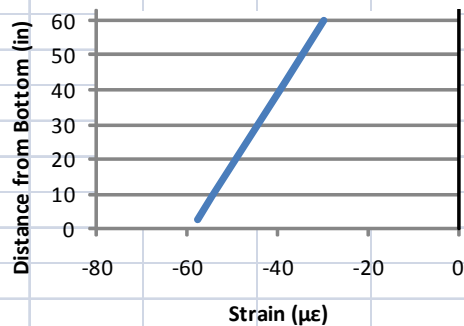
**Rolla Pedestrian Theoretical
Stress Profiles**
Kurt E. Bloch

Page
No
5

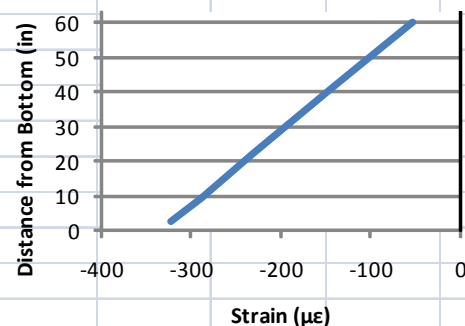
Cct	ΔP k	Po k	St	ϵ_{sh} $\mu\epsilon$	Include $\epsilon_{sh}?$	
1.24	18.74418	262.44	1.1242952	-30.7331	YES	
Theoretical Stresses in VWSG's @ Support						
Distance from End	6 in		Reduction Due to Transfer?			YES
Location	Axial	y-ec	x-ec	Moment	ϵ_{sh}	Total
x y	$\mu\epsilon$	$\mu\epsilon$	$\mu\epsilon$	$\mu\epsilon$	$\mu\epsilon$	$\mu\epsilon$
5 60	14.39639	-15.553	0.2969549	0	-30.7331	-29.8734
5 42	14.39639	-6.76928	0.2969549	0	-30.7331	-38.6572
5 22	14.39639	2.990423	0.2969549	0	-30.7331	-48.4169
5 9.5	14.39639	9.09024	0.2969549	0	-30.7331	-54.5167
5 2.5	14.39639	12.50614	0.2969549	0	-30.7331	-57.9326
5 63	14.39639	-17.017	0.2969549	0	-30.7331	-28.4095
5 0	14.39639	13.7261	0.2969549	0	-30.7331	-59.1526

Cct	ΔP k	Po k	St	ϵ_{sh} $\mu\epsilon$	Include $\epsilon_{sh}?$	
1.24	17.80213	262.44	1.1301103	-30.7331	YES	
Stresses in VWSG's @ Mid-Span						
Distance from End	204 in		Reduction Due to Transfer?			NO
Location	Axial	y-ec	x-ec	Moment	ϵ_{sh}	Total
x y	$\mu\epsilon$	$\mu\epsilon$	$\mu\epsilon$	$\mu\epsilon$	$\mu\epsilon$	$\mu\epsilon$
5 60	172.0689	-148.74	-0.471611	0	-30.7331	-53.5906
5 42	172.0689	-64.7374	-0.471611	0	-30.7331	-137.593
5 22	172.0689	28.59862	-0.471611	0	-30.7331	-230.929
5 9.5	172.0689	86.93364	-0.471611	0	-30.7331	-289.264
5 2.5	172.0689	119.6013	-0.471611	0	-30.7331	-321.932
5 63	172.0689	-162.74	-0.471611	0	-30.7331	-39.5902
5 0	172.0689	131.2683	-0.471611	0	-30.7331	-333.599

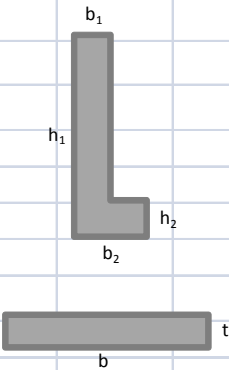
Support Sensors



Mid-Span Sensors



APPENDIX E.
PRESTRESS LOSS SAMPLE CALCULATIONS—AASHTO LRFD 2007 (REFINED)

		PRESTRESS LOSS CALCULATIONS:		Page	
		AASHTO LRFD 2007--REFINED		No	
		Kurt E. Bloch		1	
		Spandrel Beam			
Material	HSC	L	48 ft		
Age	365 days	h_1	63 in		
Properties		h_2	12 in		
f'_c	12919 psi	b_1	10 in		
E_c	4782 ksi	b_2	18 in		
γ	145 pcf	A_c	726 in ²		
		y_b	28.1281 in		
		y_t	34.8719 in		
		$I_{g,beam}$	263694.1 in ⁴		
		Precast Panel			
		t	8 in	b	111 in
		A_c	888 in ²		
		y	4 in		
		I	4736 in ⁴		
Prestressing Steel		Prestress Loss Information			
f_{pu}	270 ksi	V	418176 in ³		
F_1	16.3 kips	S	94764 in ²		
F_2	32.3 kips	V/S	4.412815 in		
E_{ps}	29000 ksi	t_i	1 day		
A_{ps}	0.153 in ²	t_{deck}	63 days		
$f_{jacking1}$	106.5359 ksi	RH	70 %		
$f_{jacking2}$	211.1111 ksi	K_{sh}	0.92		
NO_1	6	C_u	1.645		
NO_2	6				
A_s	1.836 in ²				
P	291.6 kips				
g	18.27709 in				
e	9.851007 in				

	PRESTRESS LOSS CALCULATIONS:	Page
	AASHTO LRFD 2007--REFINED	No
	Kurt E. Bloch	2
Prestress Loss Equations		
Total Loss		
$\Delta f_{pt} = \Delta f_{pes} + \Delta f_{plt}$		
Elastic Shortening		
$\Delta f_{pes} = \frac{E_p}{E_{ct}} f_{cgp}$		
$f_{cgp} = \frac{P}{A_g} + \frac{Pe^2}{I_g} - \frac{M_{self}e}{I_g}$		
$M_{self} = 2526480 \text{ lb-in}$		
$f_{cgp} = 363.6849 \text{ psi}$		
$\Delta f_{pes} = 2835.178 \text{ psi}$		
Losses due to due to shrinkage, creep, and relaxation		
$\Delta f_{plt} = (\Delta f_{psr} + \Delta f_{pcr} + \Delta f_{pr1})_{id} + (\Delta f_{psd} + \Delta f_{pcd} + \Delta f_{pr2} + \Delta f_{pss})_{df}$		
Shrinkage of Girder Concrete to Deck Placement		
$\Delta f_{psr} = \epsilon_{bid} E_p K_{id}$		
$\epsilon_{bid} = k_s k_{hs} k_f k_{td} 0.48 \times 10^{-3}$		
$k_s = \left[\frac{\frac{t}{26e^{0.36(V/S)} + t}}{45 + t} \right] \left[\frac{1064 - 94(V/S)}{923} \right]$		
$k_{hs} = 2.00 - 0.014H$		
$k_{td} = \frac{t}{61 - 4f'_{ci} + t}$		
$k_{id} = \frac{1}{1 + \frac{E_p A_{ps}}{E_{ci} A_g} \left(1 + \frac{A_g e_{pg}^2}{I_g} \right) [1 + 0.7\psi_b(t_f, t_c)]}$		
$\psi_b(t_f, t_c) = 1.9k_s k_{hs} k_f k_{td} t_i^{-0.118}$		
$k_f = \frac{5}{1 + f'_{ci}}$		
$k_s = 1.45 - 0.13(V/S) \geq 1.0$		
$k_{hs} = 1.56 - 0.008H$		

		PRESTRESS LOSS CALCULATIONS:		Page
		AASHTO LRFD 2007--REFINED		No
		Kurt E. Bloch		3
Shrinkage of Girder Concrete to Deck Placement (Cont.)				
$k_{hc} =$	1.00	$k_{id} =$	0.96	
$k_s =$	1.00	$k_{hs} =$	1.02	
$k_f =$	0.64	$k_s =$	0.40	
$k_{td} =$	0.91	$k_{td} =$	0.65	
$\Psi_b(t_f, t_i) =$	1.12	$\epsilon_{bid} =$	81.77 $\mu\epsilon$	
		$\Delta f_{psr} =$	2270.25 psi	
Creep of Girder Concrete to Deck Placement				
$\Delta f_{pcr} = \frac{E_p}{E_{ci}} f_{cgp} \Psi_b(t_d, t_i) k_{id}$				
$f_{cgp} =$	363.68 psi	$k_{td} =$	0.65	
$k_{hc} =$	1.00	$\Psi_b(t_d, t_i) =$	0.80	
$k_s =$	1.00	$k_{id} =$	0.96	
$k_f =$	0.64			
		$\Delta f_{pcr} =$	2169.809 psi	
Relaxation of Prestressing Strands				
211.11 ksi stressed strands will experience relaxation				
$\Delta f_{pr1} = \left[\frac{f_{pt} \log(t)}{k_1' \log(t_i)} \left(\frac{f_{pt}}{f_{py}} - 0.55 \right) \right] \left[1 - \frac{3(\Delta f_{psr} + \Delta f_{pcr})}{f_{pt}} \right] k_{id}$				
$k_1' =$	45 (low relaxation steel)			
$f_{pt} =$	190 ksi			
$k_{id} =$	0.96			
		$\Delta f_{pr1} =$	1338.17 psi	

		PRESTRESS LOSS CALCULATIONS:		Page
		AASHTO LRFD 2007--REFINED		No
		Kurt E. Bloch		4
Shrinkage of Girder Concrete After Deck Placement				
$\Delta f_{psd} = \varepsilon_{bdf} E_p k_{df}$		if $e_{pc} = e_{pg}, k_{df} = k_{id}$		
$\varepsilon_{bdf} = \varepsilon_{tot} - \varepsilon_{bid}$				
$\varepsilon_{tot} =$	168.95	$k_{df} =$	0.96	
$\varepsilon_{bid} =$	81.77			
$\varepsilon_{bdf} =$	87.17			
		$\Delta f_{psd} =$	2433.43 psi	
Creep of Girder Concrete After Deck Placement				
$\Delta f_{pcd} = \frac{E_p}{E_{ci}} f_{cgp} [\psi_b(t_f, t_i) - \psi_b(t_d, t_i)] k_{df} + \frac{E_p}{E_c} \Delta f_{cd} \psi_b(t_f, t_d) k_{df}$				
$\Delta f_{cd} = \frac{M_{slab} e}{I_g}$				
$k_{df} =$	0.96	$M_{slab} =$	128760 lb-ft	
$\psi(t_f, t_i) =$	1.12	$\Delta f_{cd} =$	57.72 psi	
$\psi(t_d, t_i) =$	0.80			
$\psi(t_f, t_d) =$	0.69			
		$\Delta f_{pcd} =$	1182.21 psi	
Relaxation of Prestressing Strands After Deck Placement				
$\Delta f_{pr2} = \Delta f_{pr1}$				
		$\Delta f_{pr2} =$	1338.17 psi	
Shrinkage of Deck Concrete After Deck Placement				
Due to non-composite bridge, no prestress gain is expected				



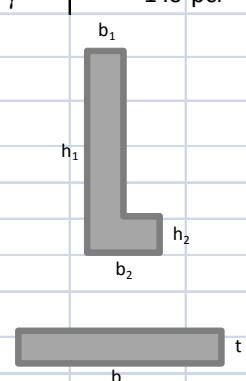
PRESTRESS LOSS CALCULATIONS:
AASHTO LRFD 2007--REFINED
Kurt E. Bloch

Page
 No
 5

Prestress Loss Summary Table

	f_{jack1}		f_{jack2}	
Δf_{pes}	2835.18	psi	Δf_{pes}	2835.18 psi
$\Delta f_{psd,id}$	2270.25	psi	$\Delta f_{psd,id}$	2270.25 psi
$\Delta f_{pcr,id}$	2169.81	psi	$\Delta f_{pcr,id}$	2169.81 psi
$\Delta f_{pr1,id}$	0.00	psi	$\Delta f_{pr1,id}$	1338.17 psi
$\Delta f_{psd,df}$	2433.43	psi	$\Delta f_{psd,df}$	2433.43 psi
$\Delta f_{pcr,df}$	1182.21	psi	$\Delta f_{pcr,df}$	1182.21 psi
$\Delta f_{pr2,df}$	0.00	psi	$\Delta f_{pr2,df}$	1338.17 psi
Total Loss	10890.88	psi	Total Loss	13567.22 psi
ES	2835.18	psi		2835.18 psi
SH	4703.68	psi		4703.68 psi
CR	3352.02	psi		3352.02 psi
RE	0.00	psi		2676.34 psi
Total	10890.88	psi		13567.22 psi
Percent	10.22	%		6.43 %

HSC	365	days
P_{load}=	269.15	kips
P_{loss}=	7.70	%

		PRESTRESS LOSS CALCULATIONS: AASHTO LRFD 2007--REFINED <i>Kurt E. Bloch</i>		Page	
				No	
				1	
		Spandrel Beam			
Material	HS-SCC	L	34 ft		
Age	365 days	h_1	63 in		
Properties		h_2	12 in		
f'_c	11399 psi	b_1	10 in		
E_c	4995 ksi	b_2	18 in		
γ	140 pcf	A_c	726 in ²		
		y_b	28.1281 in		
		y_t	34.8719 in		
		$I_{g,beam}$	263694.1 in ⁴		
		Precast Panel			
		t	8 in		
b	111 in				
A_c	888 in ²				
y	4 in				
I	4736 in ⁴				
Prestressing Steel		Prestress Loss Information			
f_{pu}	270 ksi	V	296208 in ³		
F_1	16.3 kips	S	67548 in ²		
F_2	32.3 kips	V/S	4.385148 in		
E_{ps}	29000 ksi	t_i	1 day		
A_{ps}	0.153 in ²	t_{deck}	63 days		
$f_{jacking1}$	106.5359 ksi	RH	70 %		
$f_{jacking2}$	211.1111 ksi	K_{sh}	0.92		
NO_1	6	C_u	2.032		
NO_2	6				
A_s	1.836 in ²				
P	291.6 kips				
g	18.27709 in				
e	9.851007 in				

	PRESTRESS LOSS CALCULATIONS:	Page
	AASHTO LRFD 2007--REFINED	No
	Kurt E. Bloch	2
Prestress Loss Equations		
Total Loss		
$\Delta f_{pt} = \Delta f_{pes} + \Delta f_{plt}$		
Elastic Shortening		
$\Delta f_{pes} = \frac{E_p}{E_{ct}} f_{cgp}$		
$f_{cgp} = \frac{P}{A_g} + \frac{Pe^2}{I_g} - \frac{M_{self}e}{I_g}$		
$M_{self} = 1223915 \text{ lb-in}$		
$f_{cgp} = 412.3458 \text{ psi}$		
$\Delta f_{pes} = 2672.185 \text{ psi}$		
Losses due to due to shrinkage, creep, and relaxation		
$\Delta f_{plt} = (\Delta f_{psr} + \Delta f_{pcr} + \Delta f_{pr1})_{id} + (\Delta f_{psd} + \Delta f_{pcd} + \Delta f_{pr2} + \Delta f_{pss})_{df}$		
Shrinkage of Girder Concrete to Deck Placement		
$\Delta f_{psr} = \epsilon_{bid} E_p K_{id}$		
$\epsilon_{bid} = k_s k_{hs} k_f k_{td} 0.48 * 10^{-3}$		
$k_s = \left[\frac{\frac{t}{26e^{0.36(V/S)} + t}}{45 + t} \right] \left[\frac{1064 - 94(V/S)}{923} \right]$		
$k_{hs} = 2.00 - 0.014H$		
$k_{td} = \frac{t}{61 - 4f'_{ci} + t}$		
$k_{id} = \frac{1}{1 + \frac{E_p A_{ps}}{E_{ci} A_g} \left(1 + \frac{A_g e_{pg}^2}{I_g} \right) [1 + 0.7\psi_b(t_f, t_c)]}$		
$\psi_b(t_f, t_c) = 1.9k_s k_{hs} k_f k_{td} t_i^{-0.118}$		
$k_f = \frac{5}{1 + f'_{ci}}$		
$k_s = 1.45 - 0.13(V/S) \geq 1.0$		
$k_{hs} = 1.56 - 0.008H$		

		PRESTRESS LOSS CALCULATIONS:		Page
		AASHTO LRFD 2007--REFINED		No
		Kurt E. Bloch		3
Shrinkage of Girder Concrete to Deck Placement (Cont.)				
$k_{hc} =$	1.00	$k_{id} =$	0.96	
$k_s =$	1.00	$k_{hs} =$	1.02	
$k_f =$	0.67	$k_s =$	0.40	
$k_{td} =$	0.91	$k_{td} =$	0.64	
$\Psi_b(t_f, t_i) =$	1.16	$\epsilon_{bid} =$	84.65 $\mu\epsilon$	
		$\Delta f_{psr} =$	2365.93 psi	
Creep of Girder Concrete to Deck Placement				
$\Delta f_{pcr} = \frac{E_p}{E_{ci}} f_{cgp} \Psi_b(t_d, t_i) k_{id}$				
$f_{cgp} =$	412.35 psi	$k_{td} =$	0.64	
$k_{hc} =$	1.00	$\Psi_b(t_d, t_i) =$	0.81	
$k_s =$	1.00	$k_{id} =$	0.97	
$k_f =$	0.67			
		$\Delta f_{pcr} =$	2107.315 psi	
Relaxation of Prestressing Strands				
211.11 ksi stressed strands will experience relaxation				
$\Delta f_{pr1} = \left[\frac{f_{pt} \log(t)}{k_1' \log(t_i)} \left(\frac{f_{pt}}{f_{py}} - 0.55 \right) \right] \left[1 - \frac{3(\Delta f_{psr} + \Delta f_{pcr})}{f_{pt}} \right] k_{id}$				
$k_1' =$	45 (low relaxation steel)			
$f_{pt} =$	190 ksi			
$k_{id} =$	0.97			
		$\Delta f_{pr1} =$	1345.551 psi	

		PRESTRESS LOSS CALCULATIONS:		Page
		AASHTO LRFD 2007--REFINED		No
		Kurt E. Bloch		4
Shrinkage of Girder Concrete After Deck Placement				
$\Delta f_{psd} = \varepsilon_{bdf} E_p k_{df}$		<i>if $e_{pc} = e_{pg}, k_{df} = k_{id}$</i>		
$\varepsilon_{bdf} = \varepsilon_{tot} - \varepsilon_{bid}$				
$\varepsilon_{tot} =$	175.62	$k_{df} =$	0.97	
$\varepsilon_{bid} =$	84.65			
$\varepsilon_{bdf} =$	90.97			
		$\Delta f_{psd} =$	2554.82 psi	
Creep of Girder Concrete After Deck Placement				
$\Delta f_{pcd} = \frac{E_p}{E_{ci}} f_{cgp} [\psi_b(t_f, t_i) - \psi_b(t_d, t_i)] k_{df} + \frac{E_p}{E_c} \Delta f_{cd} \psi_b(t_f, t_d) k_{df}$				
$\Delta f_{cd} = \frac{M_{slab} e}{I_g}$				
$k_{df} =$	0.97	$M_{slab} =$	62375.83 lb-ft	
$\psi(t_f, t_i) =$	1.16	$\Delta f_{cd} =$	27.96 psi	
$\psi(t_d, t_i) =$	0.81			
$\psi(t_f, t_d) =$	0.71			
		$\Delta f_{pcd} =$	1008.36 psi	
Relaxation of Prestressing Strands After Deck Placement				
$\Delta f_{pr2} = \Delta f_{pr1}$				
		$\Delta f_{pr2} =$	1345.55 psi	
Shrinkage of Deck Concrete After Deck Placement				
Due to non-composite bridge, no prestress gain is expected				



PRESTRESS LOSS CALCULATIONS:
AASHTO LRFD 2007--REFINED
Kurt E. Bloch

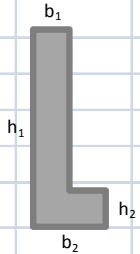
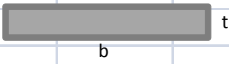
Page
 No
 5

Prestress Loss Summary Table

	f_{jack1}		f_{jack2}	
Δf_{pes}	2672.18	psi	Δf_{pes}	2672.18 psi
$\Delta f_{psd,id}$	2365.93	psi	$\Delta f_{psd,id}$	2365.93 psi
$\Delta f_{pcr,id}$	2107.32	psi	$\Delta f_{pcr,id}$	2107.32 psi
$\Delta f_{pr1,id}$	0.00	psi	$\Delta f_{pr1,id}$	1345.55 psi
$\Delta f_{psd,df}$	2554.82	psi	$\Delta f_{psd,df}$	2554.82 psi
$\Delta f_{pcr,df}$	1008.36	psi	$\Delta f_{pcr,df}$	1008.36 psi
$\Delta f_{pr2,df}$	0.00	psi	$\Delta f_{pr2,df}$	1345.55 psi
Total Loss	10708.61	psi	Total Loss	13399.71 psi
ES	2672.18	psi		2672.18 psi
SH	4920.75	psi		4920.75 psi
CR	3115.67	psi		3115.67 psi
RE	0.00	psi		2691.10 psi
Total	10708.61	psi		13399.71 psi
Percent	10.05	%		6.35 %

HS-SCC	365	days
P_{load}=	269.47	kips
P_{loss}=	7.59	%

APPENDIX F.
PRESTRESS LOSS SAMPLE CALCULATIONS—PCI DESIGN HANDBOOK (2004)

		Prestress Loss Calculations for Precast Pedestrian Bridges in Rolla, MO <i>Kurt E. Bloch</i>		Page
				No
				1
		Spandrel Beam		
Material	HSC	L	48 ft	
Age	365 days	h_1	63 in	
Properties		h_2	12 in	
f'_{ci}	6765 psi	b_1	10 in	
f'_c	12231 psi	b_2	18 in	
E_{ci}	3720 ksi	A_c	726 in ²	
E_c	4538 ksi	y_b	28.128099 in	
γ	145 pcf	y_t	34.871901 in	
		$I_{g,beam}$	263694.09 in ⁴	
		Precast Panel		
		t	8 in	
		b	111 in	
		A_c	888 in ²	
		y	4 in	
		I	4736 in ⁴	
		Prestress Loss Information		
Prestressing Steel		V	418176 in ³	
f_{pu}	270 ksi	S	94764 in ²	
F_1	16.3 kips	V/S	4.412815 in	
F_2	32.3 kips	t_i	1 day	
E_{ps}	29000 ksi	t_{deck}	63 days	
A_{ps}	0.153 in ²	RH	70 %	
$f_{jacking1}$	106.5359 ksi	K_{sh}	1	
$f_{jacking2}$	211.1111 ksi	C_u	2	
NO_1	6	PCI Values?	YES	
NO_2	6	Known E?	YES	
A_s	1.836 in ²			
P	291.6 kips			
g	18.27709 in			
e	9.851007 in			

		Prestress Loss Calculations for Precast Pedestrian Bridges in Rolla, MO		Page
		<i>Kurt E. Bloch</i>		No
				2
Prestress Loss Equations				
Total Loss				
$TL = ES + CR + SH + RE$				
Elastic Shortening				
$ES = \frac{K_{es} E_{ps} f_{cir}}{E_{ci}}$		$f_{cir} = K_{cir} \left(\frac{P_i}{A_g} + \frac{P_i e^2}{I_g} \right) - \frac{M_g e}{I_g}$		
$K_{es} =$	1	$M_g =$	210540 lbs-ft	
$K_{cir} =$	0.9	$f_{cir} =$	317.87808 psi	
$P_i =$	262.44 k			
		$ES =$	2478.0818 psi	
Creep				
$CR = K_{cr} \left(\frac{E_{ps}}{E_c} \right) (f_{cir} - f_{cds})$		$K_{cr} =$ 2		
$f_{cds} = \frac{M_{sd} e}{I_g}$		$M_{sd} =$ 128760 lbs-ft		
		$f_{cds} =$ 57.722145 psi		
		$CR =$	3324.7986 psi	
Shrinkage				
$SH = 8.2 * 10^{-6} K_{sh} E_{ps} \left(1 - 0.06 \frac{V}{S} \right) (100 - RH)$				
$K_{sh} =$	1	$RH =$	70 %	
$V/S =$	4.41 ft			
		$SH =$	5245.1387 psi	

Relaxation	Grade	270	Low Relaxation
-------------------	--------------	------------	-----------------------

$$RE = [K_{re} - J(SH + CR + SH)]C$$

K_{re}= 5000.00
J= 0.04

$$\frac{f_{pi}}{f_{pu}} \geq 0.54, C = \frac{\left(\frac{f_{pi}}{f_{pu}}\right)}{0.21} \left(\frac{\left(\frac{f_{pi}}{f_{pu}}\right)}{0.9} - 0.55 \right)$$

$$\frac{f_{pi}}{f_{pu}} \leq 0.54, C = \frac{P_i}{A_{ps}}$$

106.54 ksi prestresss strands

C= 0.0928418

RE= 423.18 psi

211.11 ksi prestresss strands

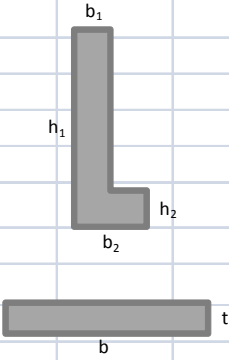
C= 1.1868764

RE= 5409.88 psi

Prestress Loss Summary Table

f _{jack1}			f _{jack2}		
ES	2478.082	psi	ES	2478.0818	psi
CR	3324.799	psi	CR	3324.7986	psi
SH	5245.139	psi	SH	5245.1387	psi
RE	423.18	psi	RE	5409.88	psi
TOTAL	11471.20	psi	TOTAL	16457.90	psi
%f _{jack}	10.76744	%	%f _{jack}	7.7958453	%

HSC	365	days
P _{load} =	265.9611	k
P _{loss} =	9.281645	

		Prestress Loss Calculations for Precast Pedestrian Bridges in Rolla, MO <i>Kurt E. Bloch</i>		Page
				No
				1
		Spandrel Beam		
Material	HS-SCC	L	34 ft	
Age	365 days	h_1	63 in	
Properties		h_2	12 in	
f'_{ci}	6499 psi	b_1	10 in	
f'_c	10131 psi	b_2	18 in	
E_{ci}	4475 ksi	A_c	726 in ²	
E_c	4872 ksi	y_b	28.128099 in	
γ	140 pcf	y_t	34.871901 in	
		$I_{g,beam}$	263694.09 in ⁴	
		Precast Panel		
		t	8 in	
		b	111 in	
		A_c	888 in ²	
		y	4 in	
		I	4736 in ⁴	
		Prestress Loss Information		
		V	296208 in ³	
		S	67548 in ²	
		V/S	4.3851483 in	
		t_i	1 day	
		t_{deck}	63 days	
		RH	70 %	
		K_{sh}	1	
		C_u	2	
Prestressing Steel		PCI Values?	YES	
f_{pu}	270 ksi	Known E?	YES	
F_1	16.3 kips			
F_2	32.3 kips			
E_{ps}	29000 ksi			
A_{ps}	0.153 in ²			
$f_{jacking1}$	106.5359 ksi			
$f_{jacking2}$	211.1111 ksi			
NO_1	6			
NO_2	6			
A_s	1.836 in ²			
P	291.6 kips			
g	18.27709 in			
e	9.851007 in			

	Prestress Loss Calculations for Precast Pedestrian Bridges in Rolla, MO	Page
	<i>Kurt E. Bloch</i>	No
		2
Prestress Loss Equations		
Total Loss		
$TL = ES + CR + SH + RE$		
Elastic Shortening		
$ES = \frac{K_{es} E_{ps} f_{cir}}{E_{ci}}$		$f_{cir} = K_{cir} \left(\frac{P_i}{A_g} + \frac{P_i e^2}{I_g} \right) - \frac{M_g e}{I_g}$
K _{es} = 1	M _g = 101992.92 lbs-ft	
K _{cir} = 0.9	f _{cir} = 366.53892 psi	
P _i = 262.44 k		
	ES= 2375.336 psi	
Creep		
$CR = K_{cr} \left(\frac{E_{ps}}{E_c} \right) (f_{cir} - f_{cds})$		K _{cr} = 2
$f_{cds} = \frac{M_{sd} e}{I_g}$		M _{sd} = 62375.833 lbs-ft
		f _{cds} = 27.96262 psi
	CR= 4030.9461 psi	
Shrinkage		
$SH = 8.2 * 10^{-6} K_{sh} E_{ps} \left(1 - 0.06 \frac{V}{S} \right) (100 - RH)$		
K _{sh} = 1	RH= 70 %	
V/S= 4.39 ft		
	SH= 5256.9811 psi	

Relaxation	Grade	270	Low Relaxation
-------------------	--------------	------------	-----------------------

$$RE = [K_{re} - J(SH + CR + SH)]C$$

$K_{re} = 5000.00$
 $J = 0.04$

$$\frac{f_{pi}}{f_{pu}} \geq 0.54, C = \frac{\left(\frac{f_{pi}}{f_{pu}}\right)}{0.21} \left(\frac{\left(\frac{f_{pi}}{f_{pu}}\right)}{0.9} - 0.55 \right)$$

$$\frac{f_{pi}}{f_{pu}} \leq 0.54, C = \frac{P_i}{A_{ps}}$$

106.54 ksi prestresss strands

C= 0.0928418
 RE= 420.90 psi

211.11 ksi prestresss strands

C= 1.1868764
 RE= 5380.67 psi

Prestress Loss Summary Table

f_{jack1}			f_{jack2}		
ES	2375.336	psi	ES	2375.336	psi
CR	4030.946	psi	CR	4030.9461	psi
SH	5256.981	psi	SH	5256.9811	psi
RE	420.90	psi	RE	5380.67	psi
TOTAL	12084.16	psi	TOTAL	17043.93	psi
% f_{jack}	11.3428	%	% f_{jack}	8.073441	%

HS-SCC	365	days
$P_{load} =$	264.8604	k
$P_{loss} =$	9.70812	

APPENDIX G.
LOAD TEST TEMPERATURE EFFECTS

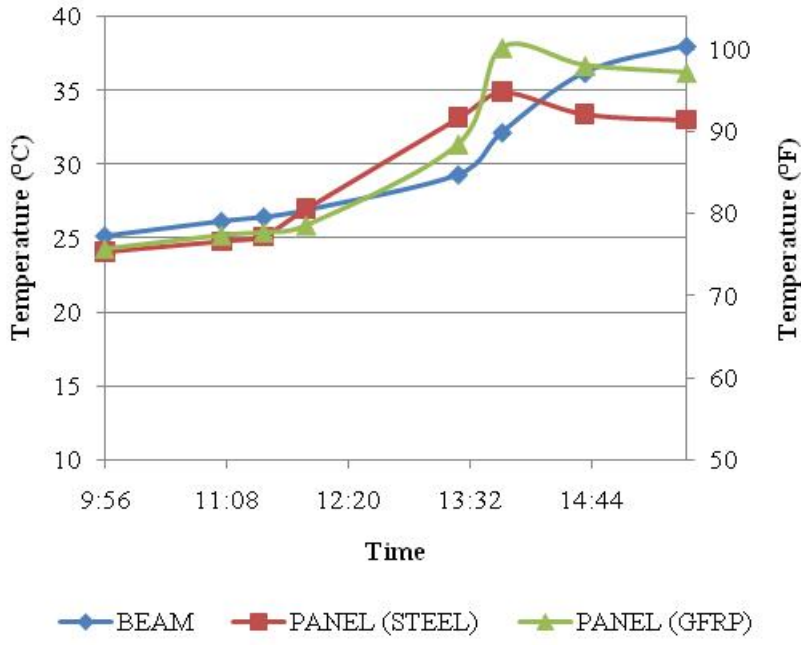
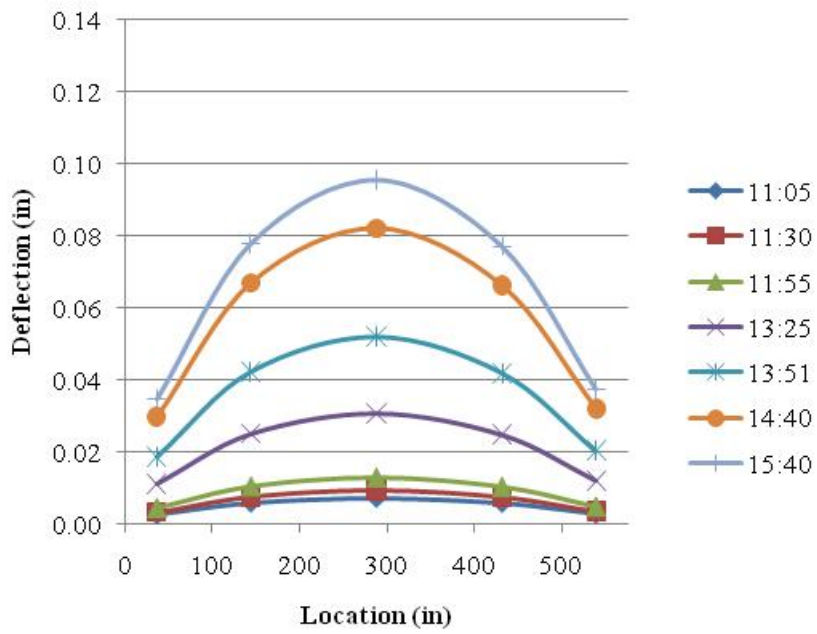
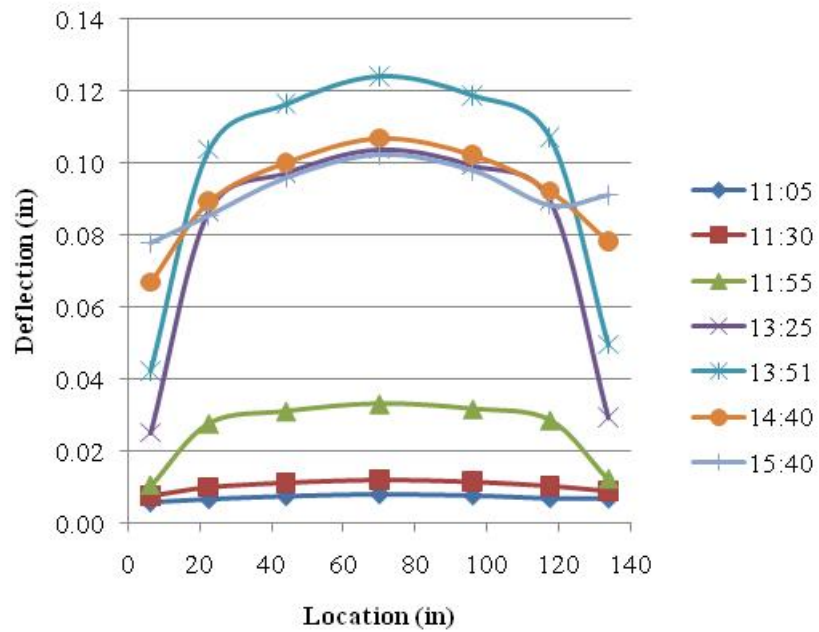


Figure F.1. Internal Temperature vs. Time for HSC Bridge during Load Testing.



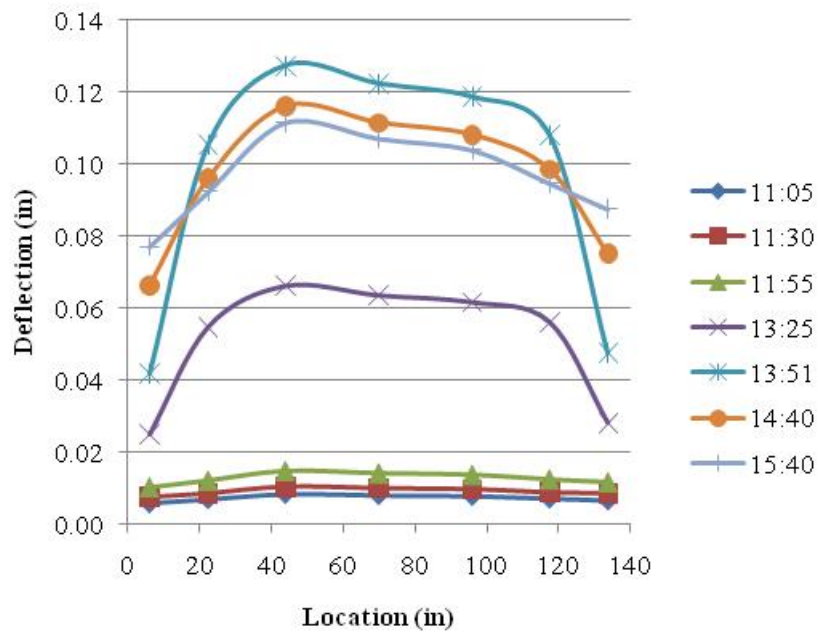
Conversion: 1-in. = 25.4 mm

Figure F.2. Adjustments to HSC Beam for Thermal Effects.



Conversion: 1-in. = 25.4 mm

Figure F.3. Adjustments to HSC Deck Panel with Mild Steel for Thermal Effects.



Conversion: 1-in. = 25.4 mm

Figure F.4. Adjustments to HSC Deck Panel with GFRP for Thermal Effects.

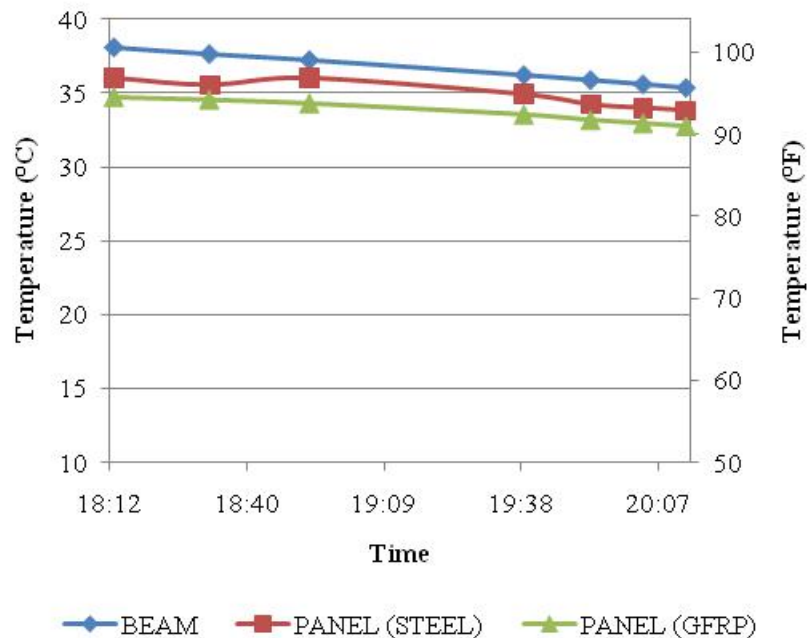
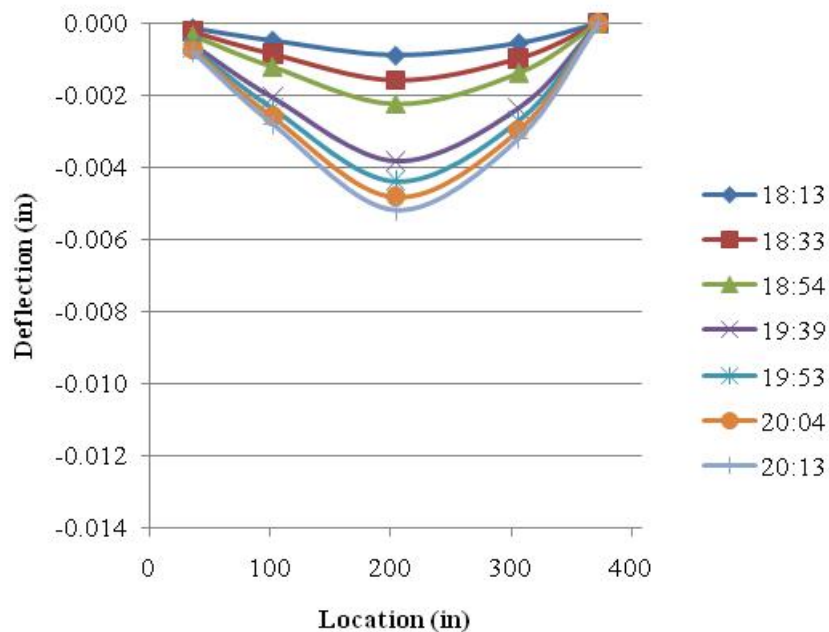
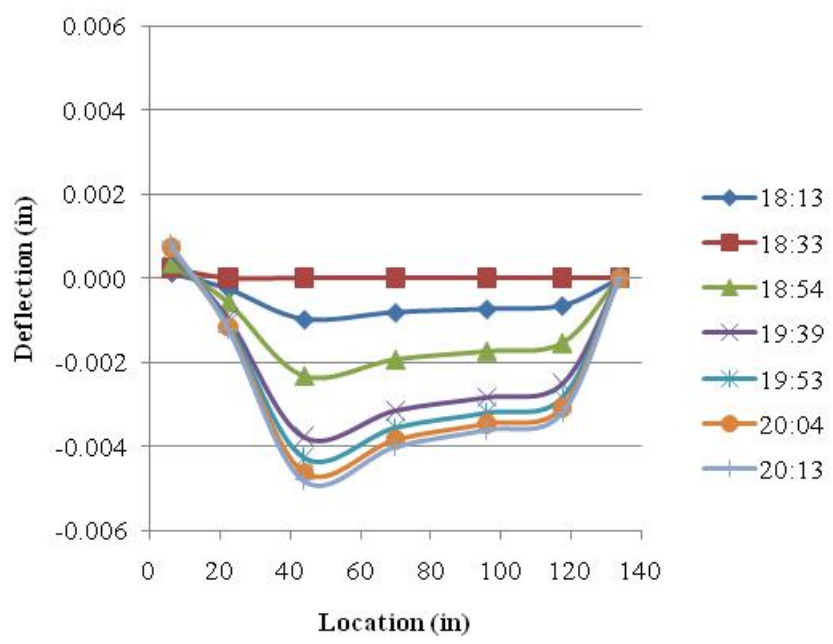


Figure F.5. Internal Temperature vs. Time for HS-SCC Bridge during Load Testing.



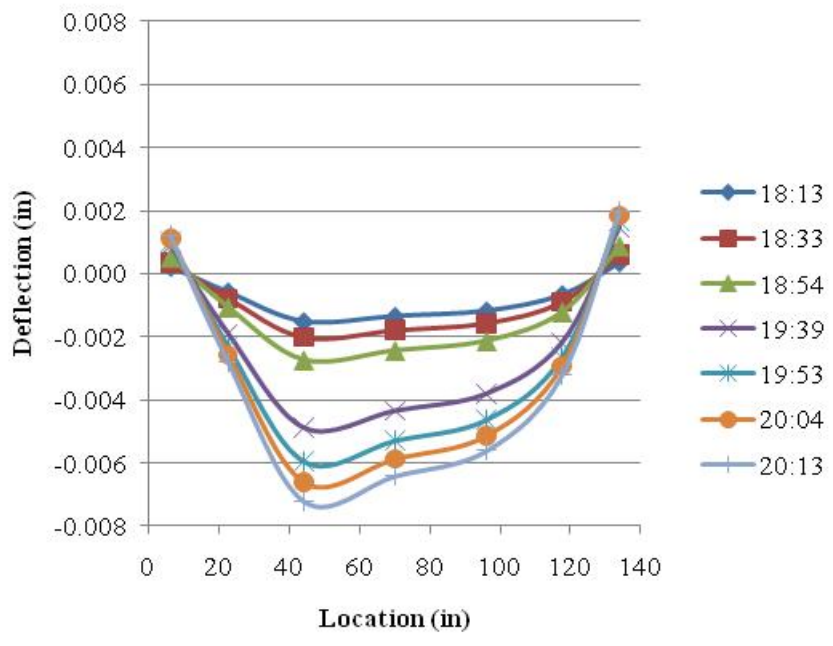
Conversion: 1-in. = 25.4 mm

Figure F.6. Adjustments to HS-SCC Beam for Thermal Effects.



Conversion: 1-in. = 25.4 mm

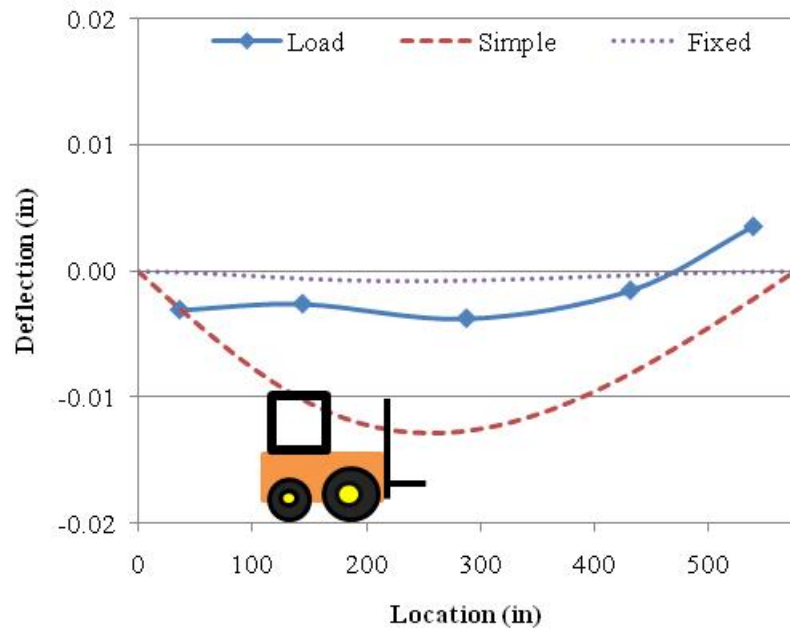
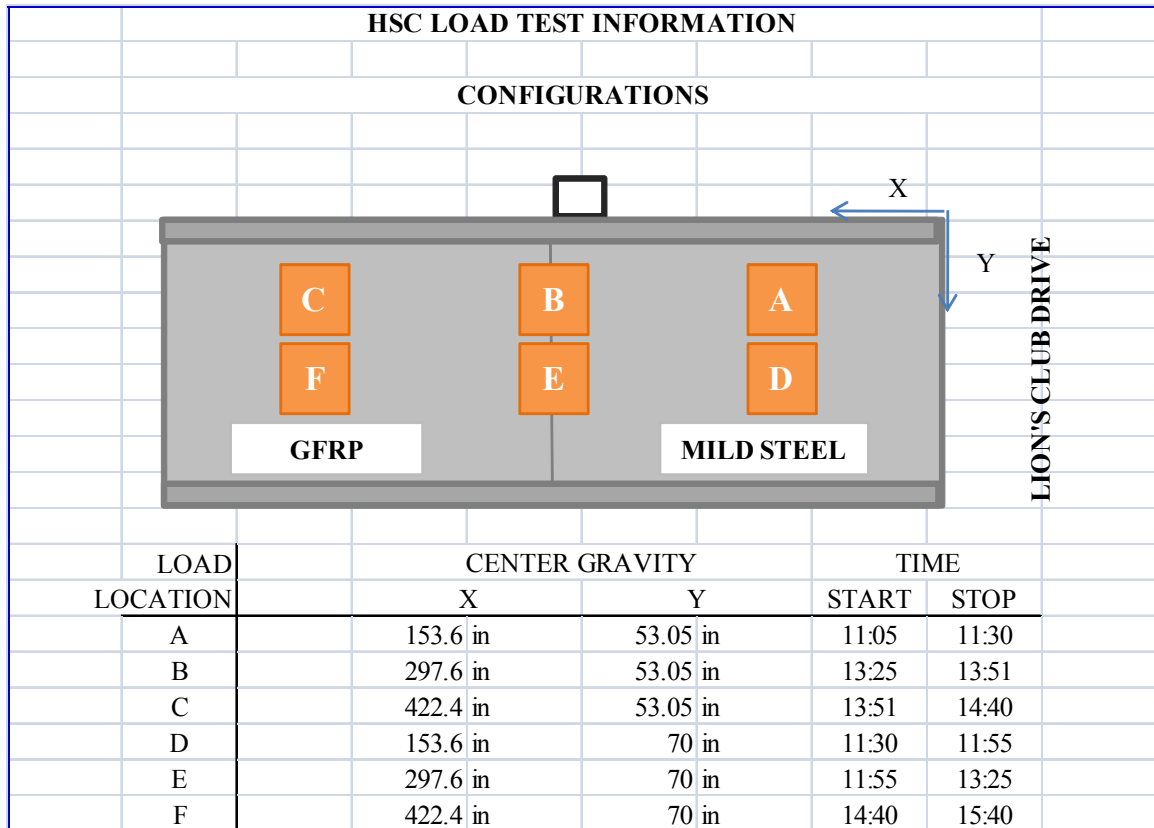
Figure F.7. Adjustments to HS-SCC Deck Panel with Mild Steel for Thermal Effects.



Conversion: 1-in. = 25.4 mm

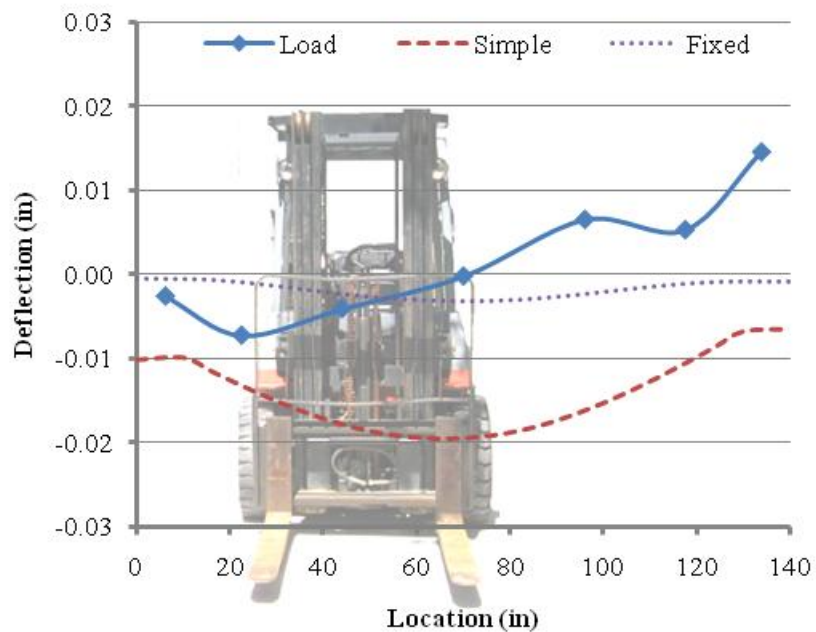
Figure F.8. Adjustments to HS-SCC Deck Panel with GFRP for Thermal Effects.

APPENDIX H.
ROLLA HSC PEDESTRIAN BRIDGE DEFLECTION PROFILES



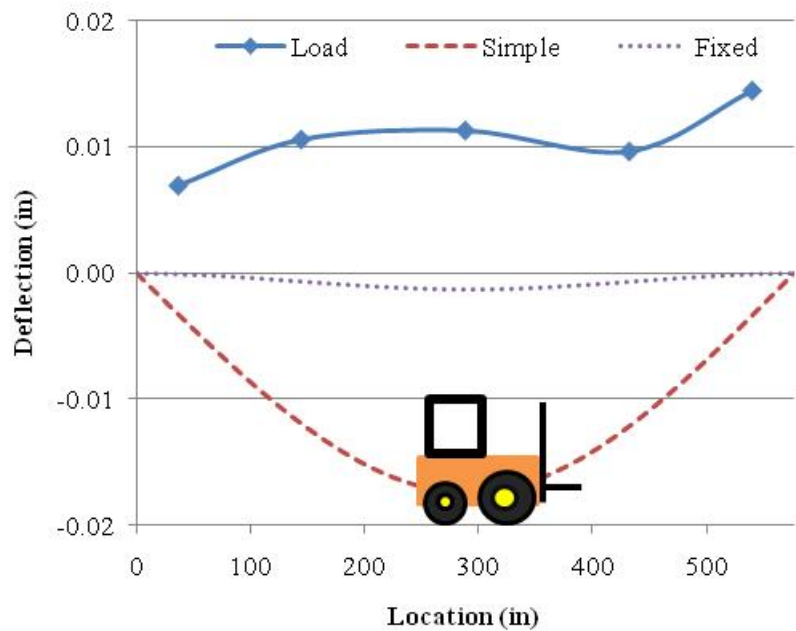
Conversion: 1-in. = 25.4 mm

Figure H.1. HSC Instrumented Beam Deflection Load – Case A.



Conversion: 1-in. = 25.4 mm

Figure H.2. HSC Mild Steel Reinforced Deck Panel Deflection – Load Case A.



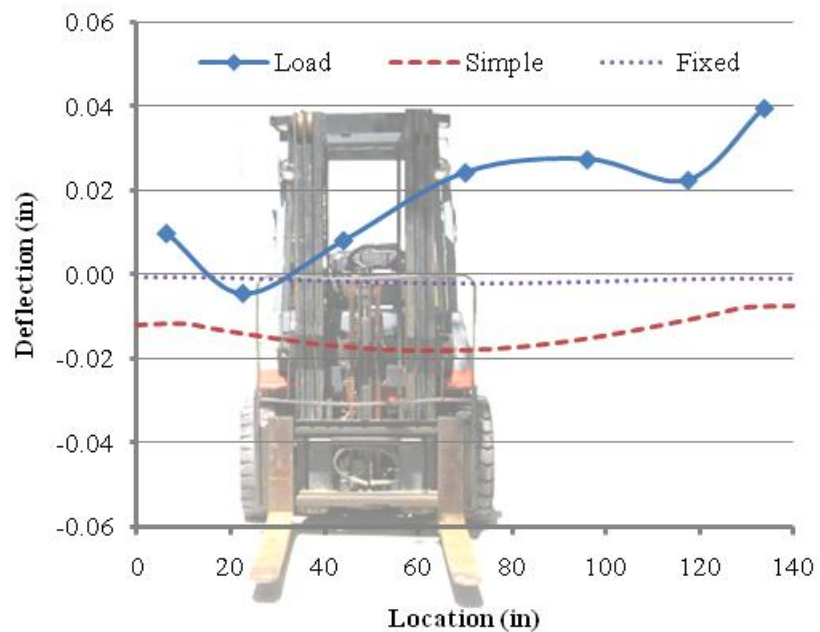
Conversion: 1-in. = 25.4 mm

Figure H.3. HSC Instrumented Beam Deflection – Load Case B.



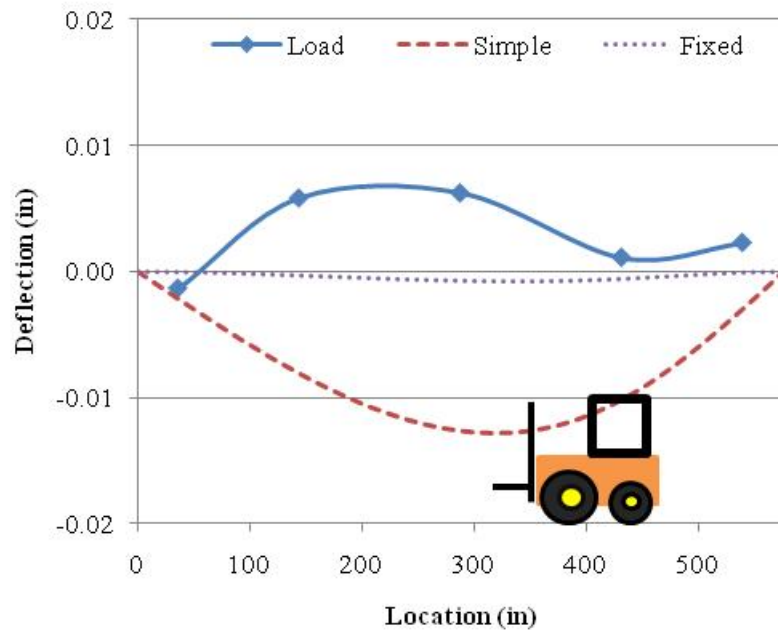
Conversion: 1-in. = 25.4 mm

Figure H.4. HSC Mild Steel Reinforced Deck Panel Deflection – Load Case B.



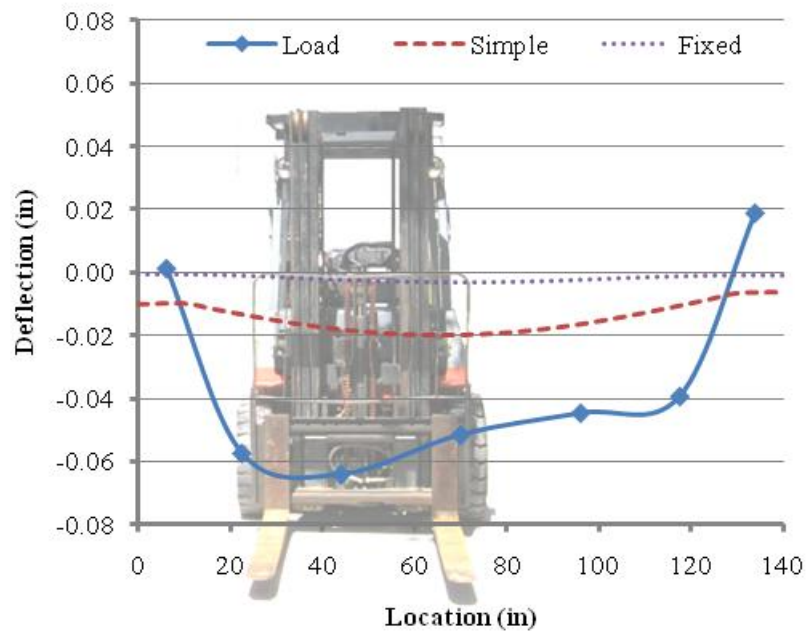
Conversion: 1-in. = 25.4 mm

Figure H.5. HSC GFRP Reinforced Deck Panel Deflection – Load Case B.



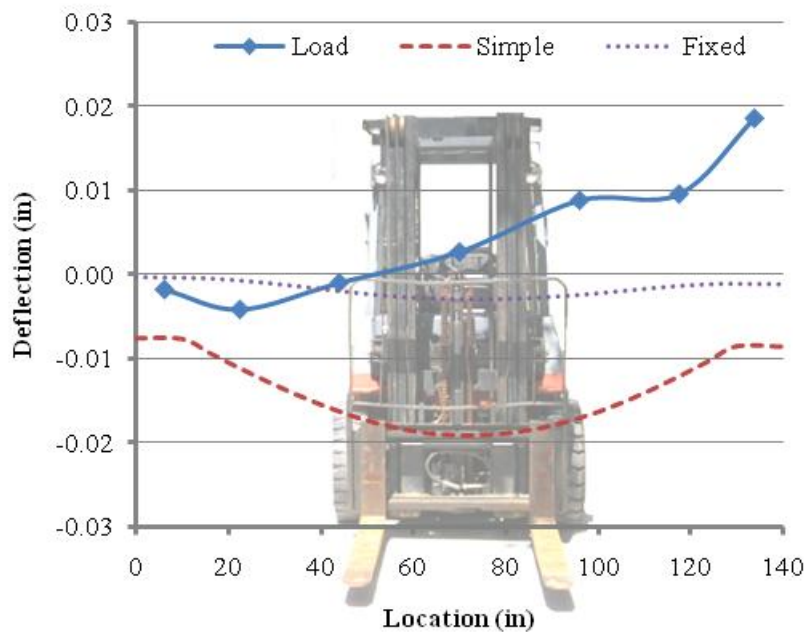
Conversion: 1-in. = 25.4 mm

Figure H.6. HSC Instrumented Beam Deflection – Load Case C.



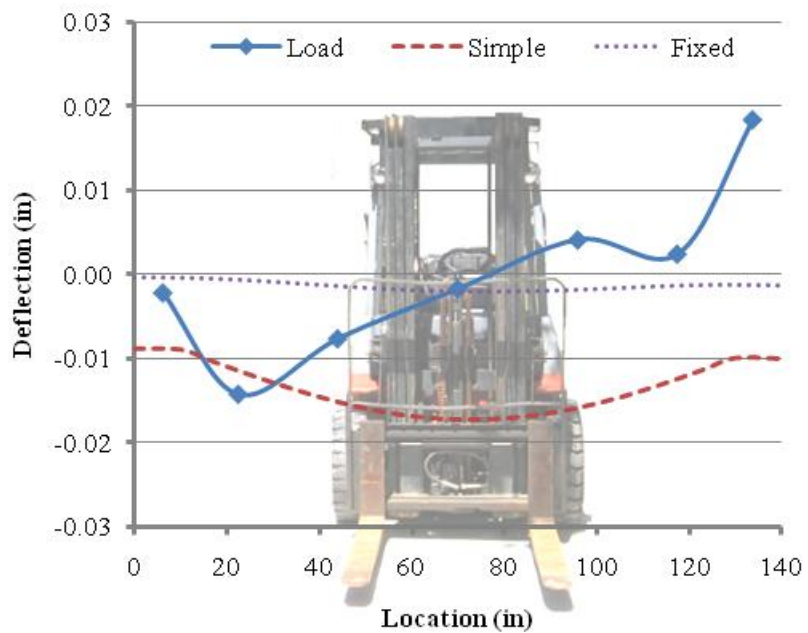
Conversion: 1-in. = 25.4 mm

Figure H.7. HSC GFRP Reinforced Deck Panel Deflection – Load Case C.



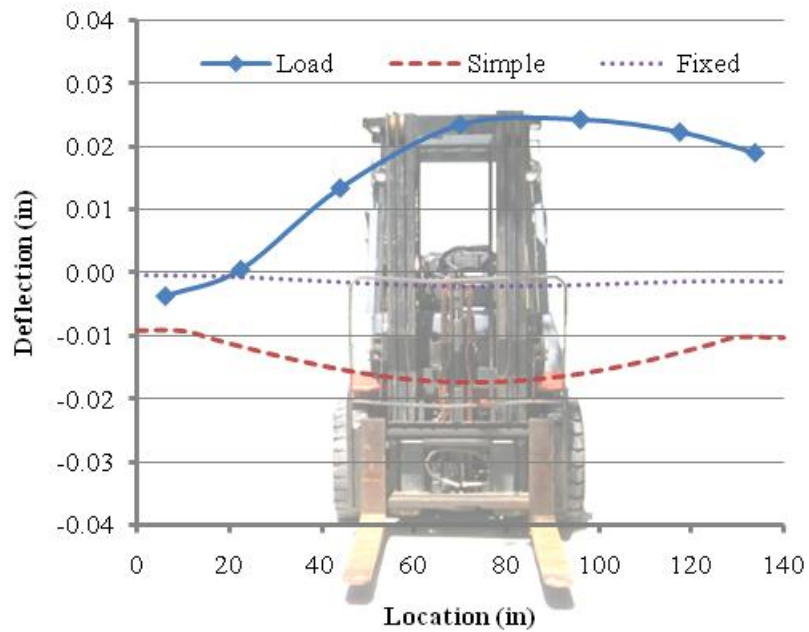
Conversion: 1-in. = 25.4 mm

Figure H.8. HSC Mild Steel Reinforced Deck Panel Deflection – Load Case D.



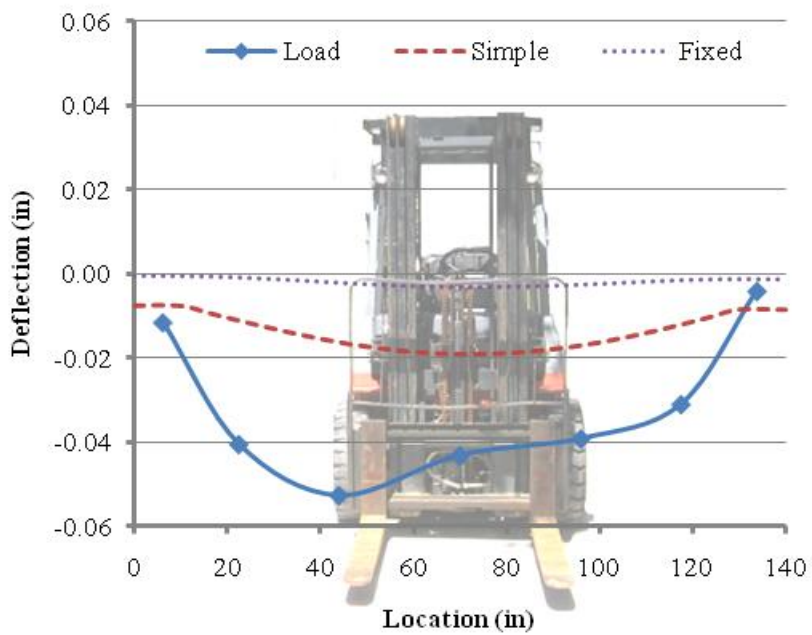
Conversion: 1-in. = 25.4 mm

Figure H.9. HSC Mild Steel Reinforced Deck Panel Deflection – Load Case E.



Conversion: 1-in. = 25.4 mm

Figure H.10. HSC GFRP Reinforced Deck Panel Deflection – Load Case E.

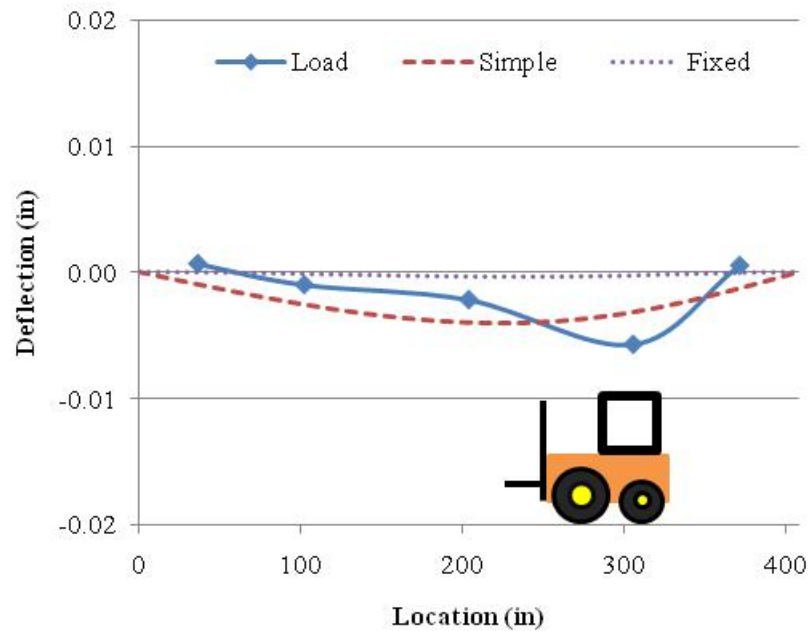
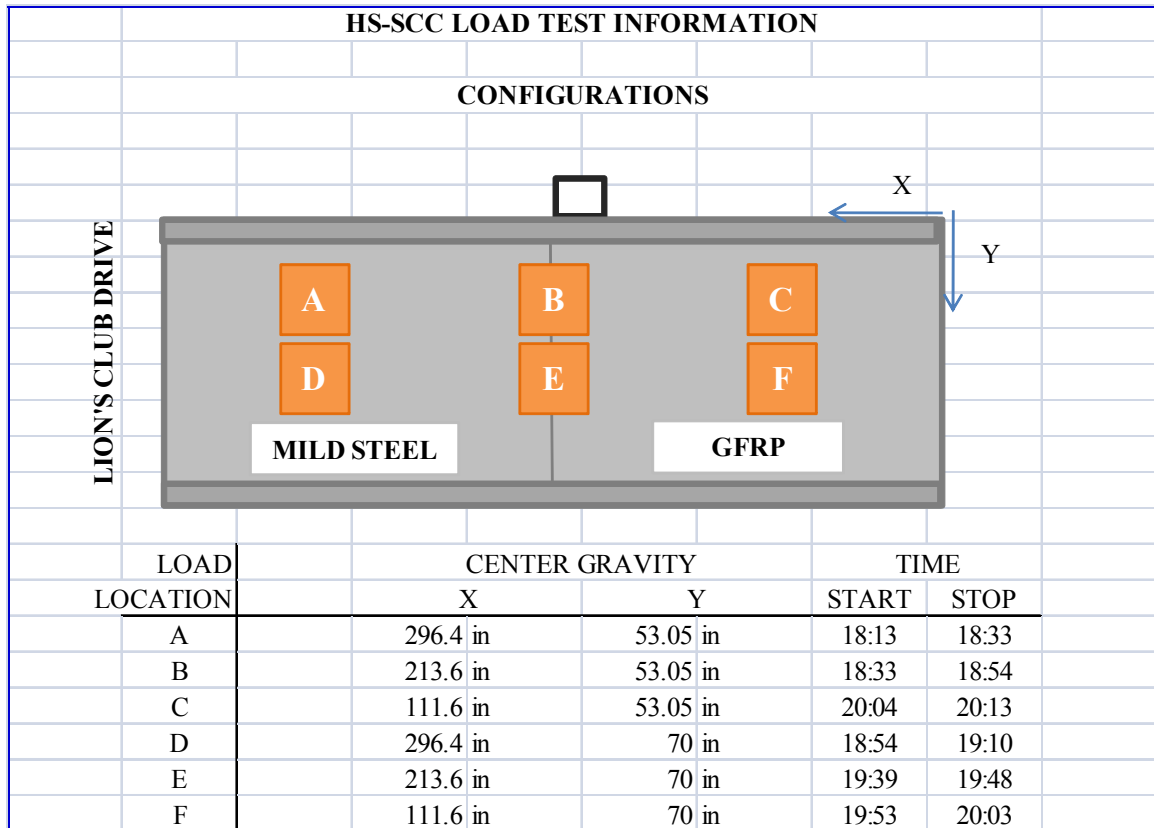


Conversion: 1-in. = 25.4 mm

Figure H.11. HSC GFRP Reinforced Deck Panel Deflection – Load Case F.

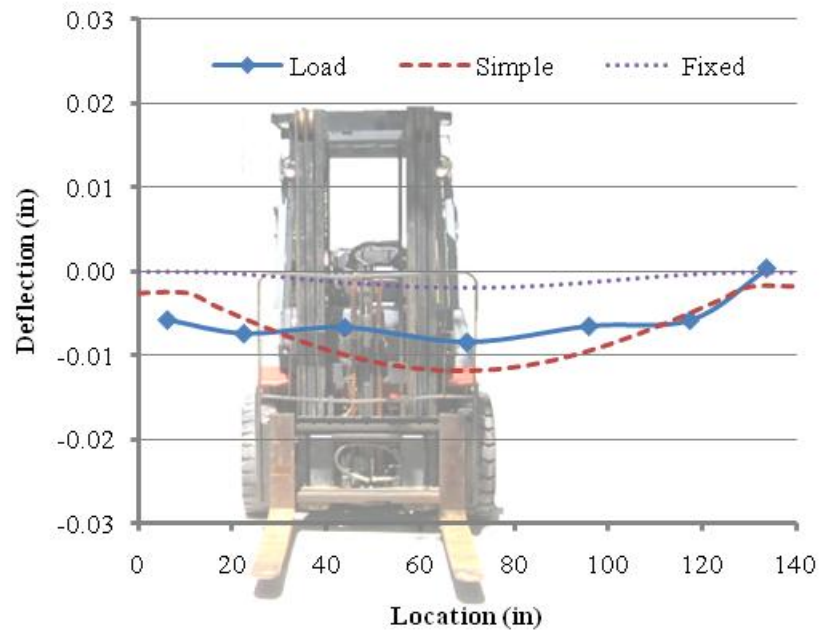
APPENDIX I.

ROLLA HS-SCC PEDESTRIAN BRIDGE DEFLECTION PROFILES



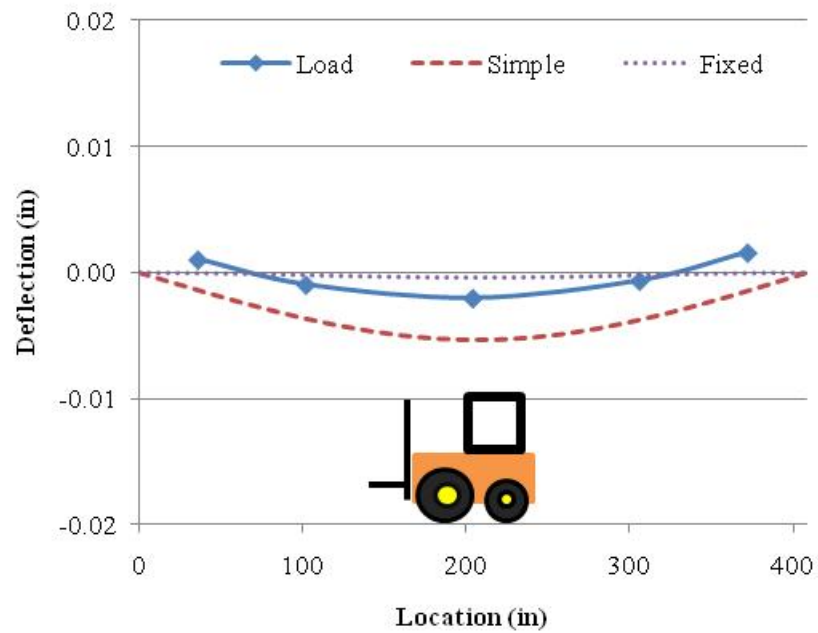
Conversion: 1-in. = 25.4 mm

Figure I.1. HS-SCC Instrumented Beam Deflection – Load Case A.



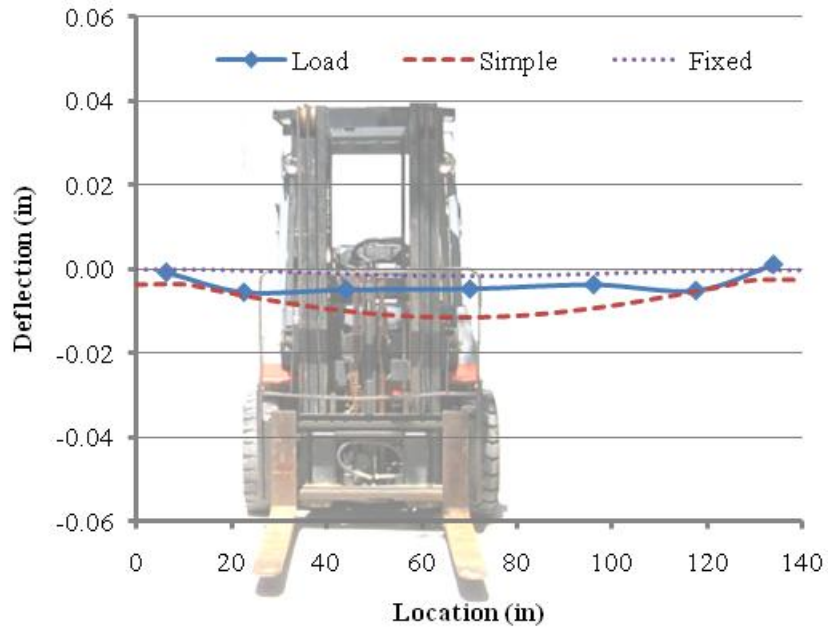
Conversion: 1-in. = 25.4 mm

Figure I.2. HS-SCC Mild Steel Reinforced Deck Panel Deflection – Load Case A.



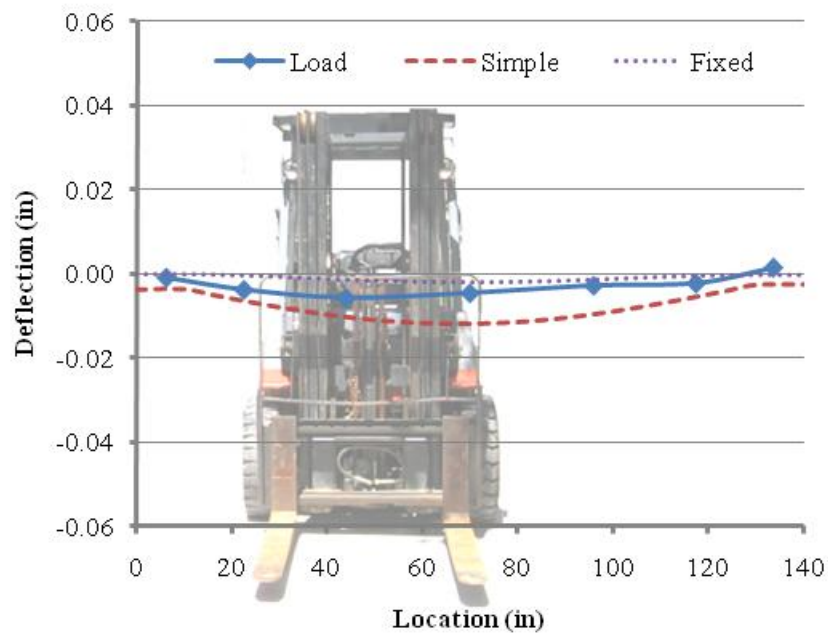
Conversion: 1-in. = 25.4 mm

Figure I.3. HS-SCC Instrumented Beam Deflection – Load Case B.



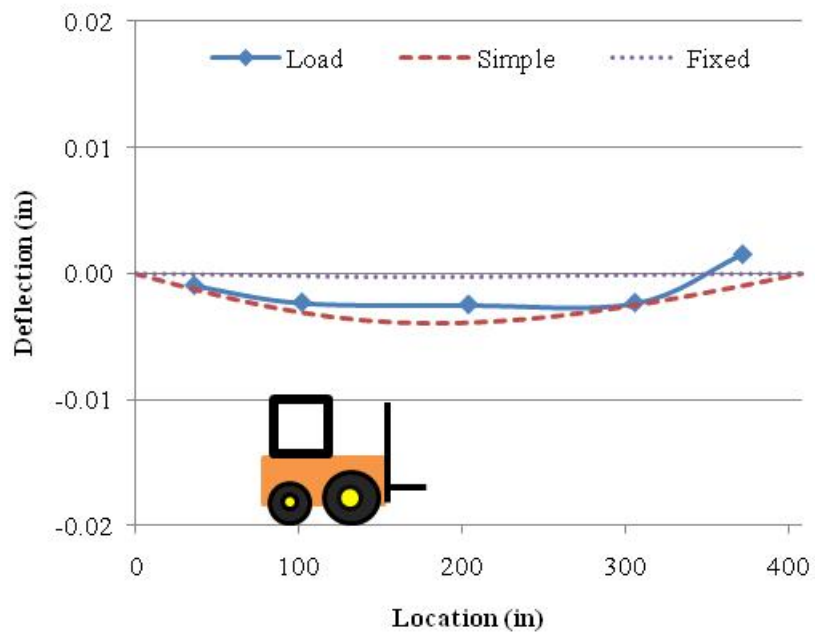
Conversion: 1-in. = 25.4 mm

Figure I.4. HS-SCC Mild Steel Reinforced Deck Panel Deflection – Load Case B.



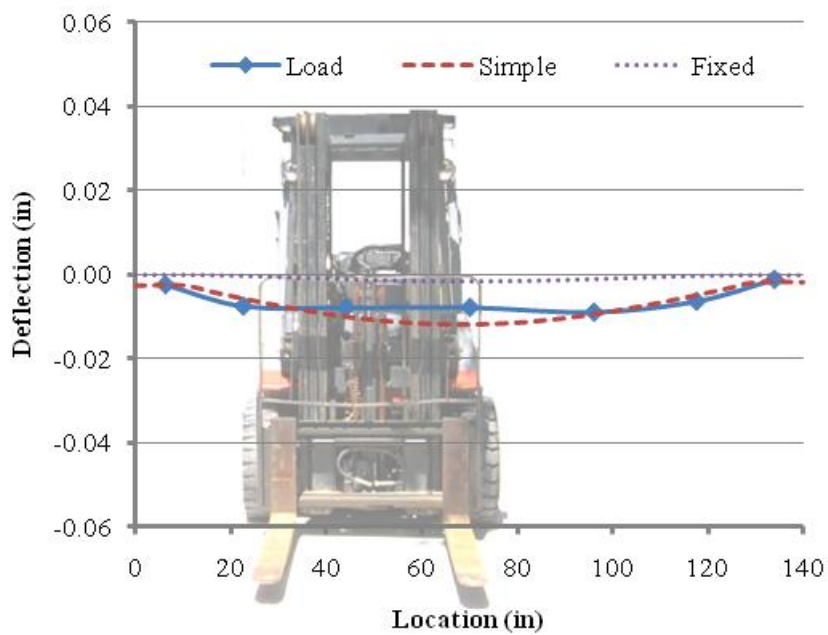
Conversion: 1-in. = 25.4 mm

Figure I.5. HS-SCC GFRP Reinforced Deck Panel Deflection – Load Case B.



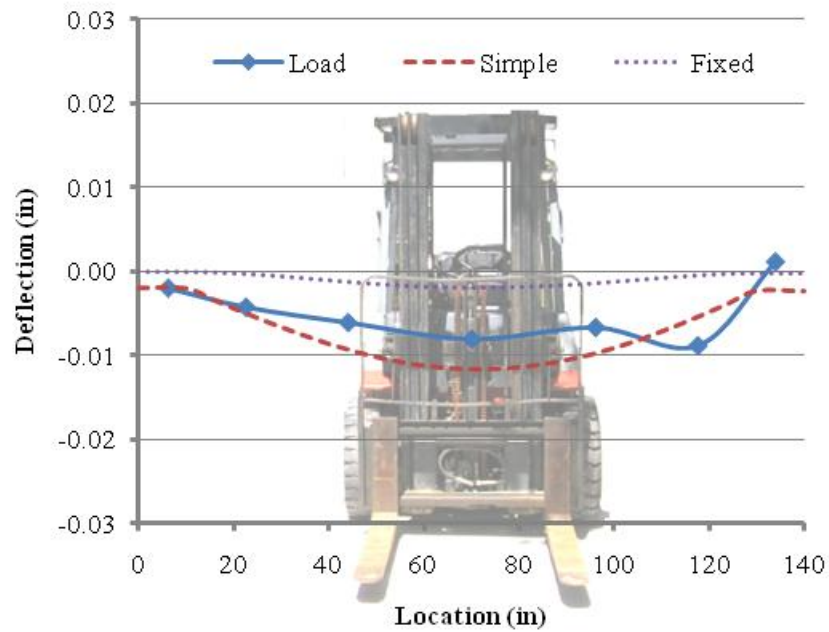
Conversion: 1-in. = 25.4 mm

Figure I.6. HS-SCC Instrumented Beam Deflection – Load Case C.



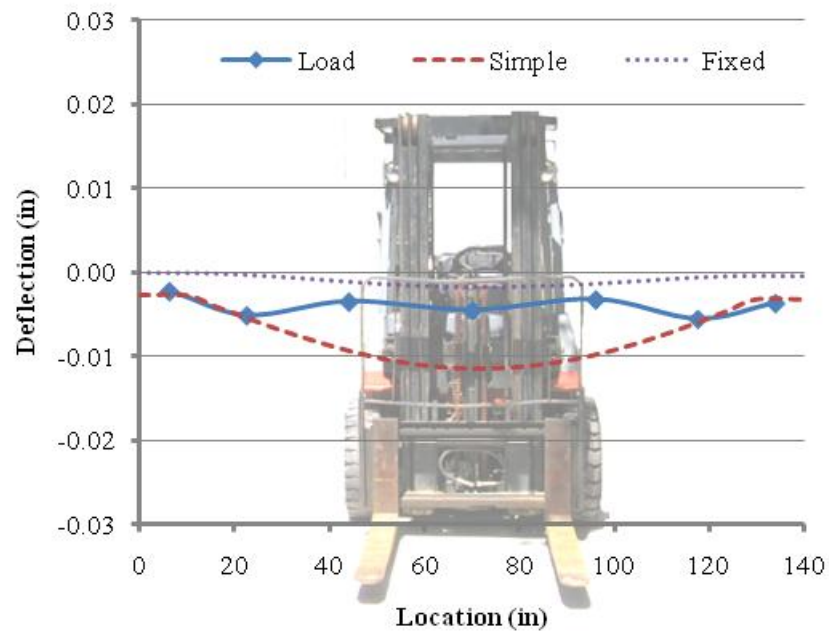
Conversion: 1-in. = 25.4 mm

Figure I.7. HS-SCC GFRP Reinforced Deck Panel Deflection – Load Case C.



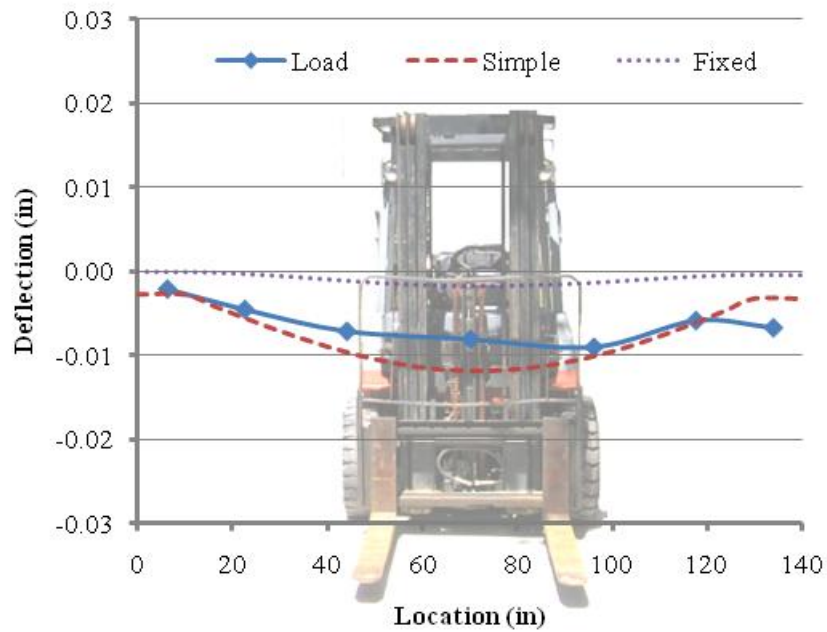
Conversion: 1-in. = 25.4 mm

Figure I.8. HS-SCC Mild Steel Reinforced Deck Panel Deflection – Load Case D.



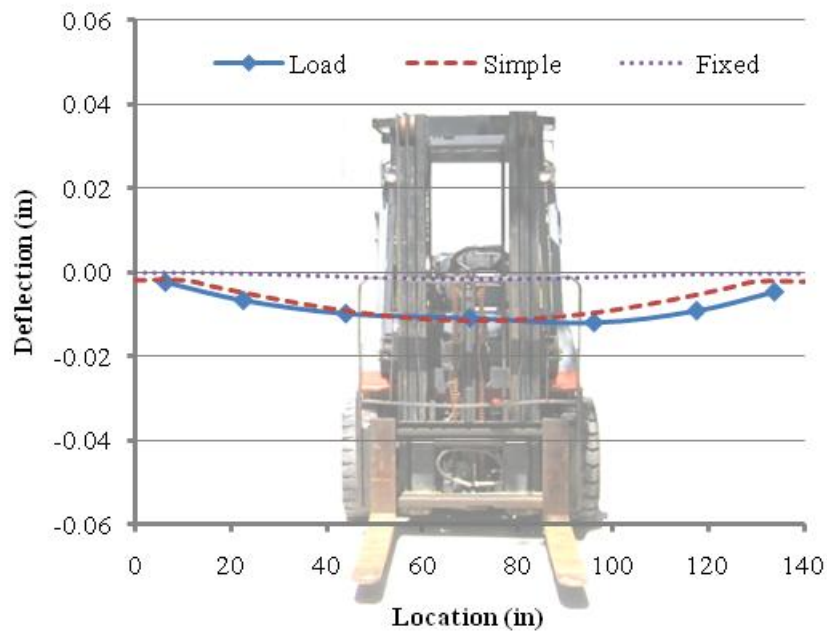
Conversion: 1-in. =25.4 mm

Figure I. 9. HS-SCC Mild Steel Reinforced Deck Panel Deflection – Load Case E.



Conversion: 1-in. = 25.4 mm

Figure I.10. HS-SCC GFRP Reinforced Deck Panel Deflection – Load Case E.

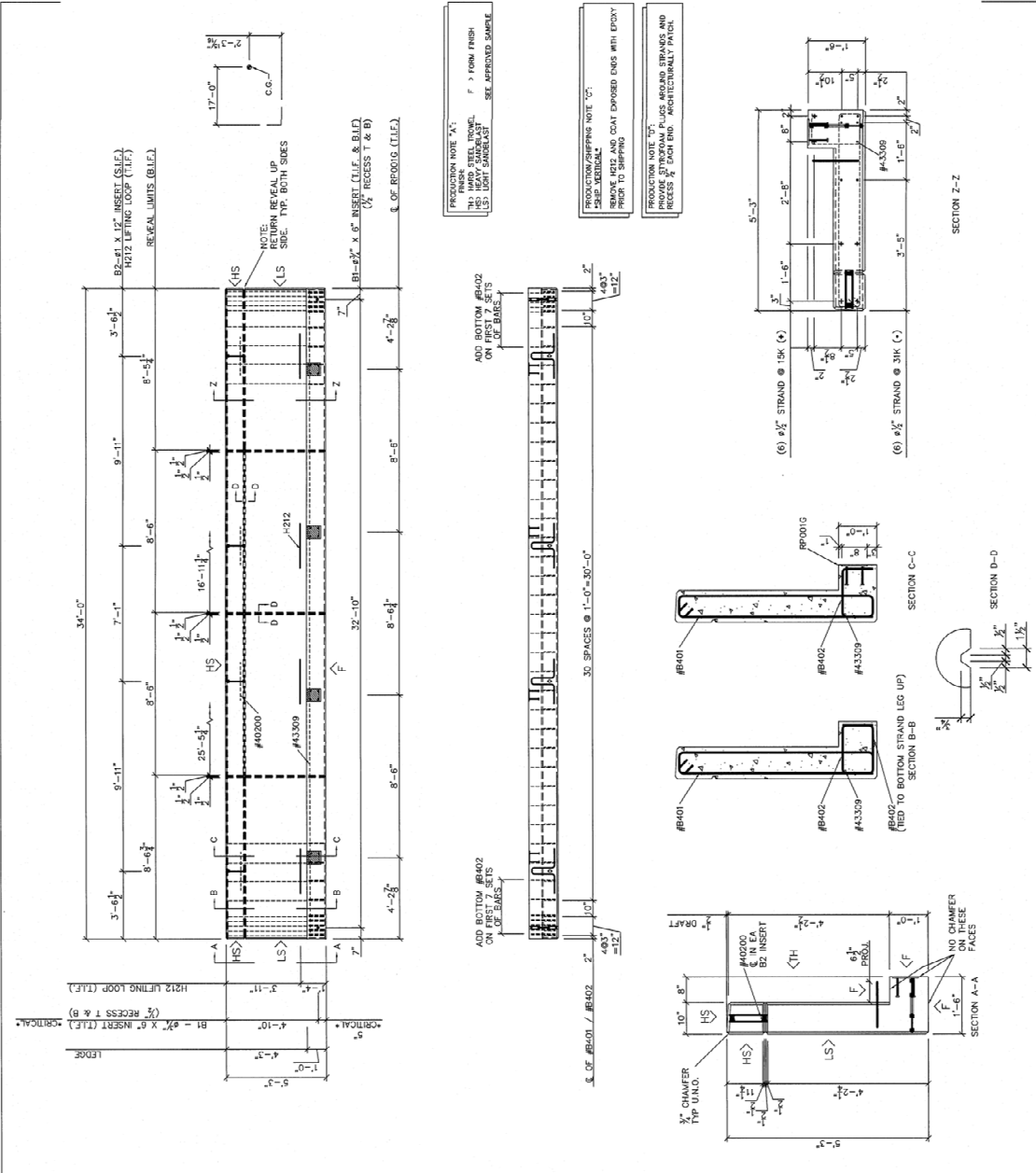


Conversion: 1-in. = 25.4 mm

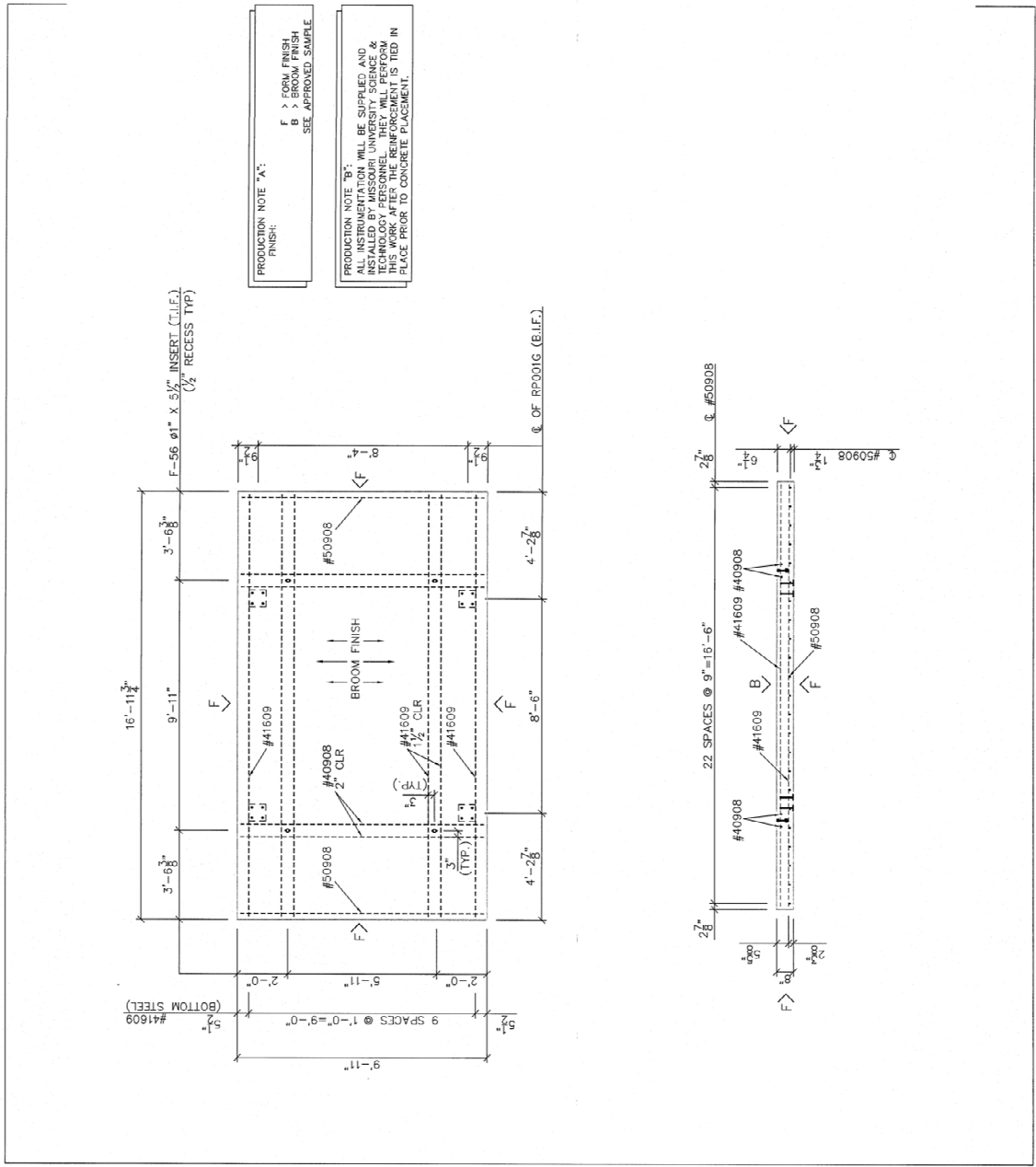
Figure I.11. HS-SCC GFRP Reinforced Deck Panel Deflection – Load Case F.

APPENDIX J.
ROLLA PEDESTRIAN BRIDGE FABRICATION PLANS

REVISIONS		NO.	DATE	REVISION	BY
<p>CONCRETE STRUCTURES CHICAGO, ILL.</p>					
BILL OF MATERIALS		MARK NO.	DESCRIPTION	PER PIECE	
		B07	1" DIA X 12" B-2 INSERT	4	
		H212	1/2" Loop	4	
		RP001G	1/2" X 3/8 X 0'-6"	4	
		(4)	1/2" DIA X 6" H.A.S.	4	
		B08	3/4" DIA# B-1 INSERT (CONNECT W/COIL ROD PRIOR TO CASTING)	4	
		#4220	#4 X 2'-0" STR BAR	4	
		#4339	#4 X 33'-9" STR BAR	1	
		#B401	#4 X 11'-9" BENT BAR	41	
		#B402	#4 X 2'-9" BENT BAR	55	
		<p>CONCRETE FORMULA</p> <p>FACING MIX C.Y. = 0</p> <p>BACK-UP MIX HS-SCC.CX. = 6.31</p> <p>FINISHED AREA S.F. = 726.5</p> <p>PIECE WEIGHT LBS. = 25555</p> <p>MATERIALS DATA</p> <p>CONCRETE TYPE : 150 MP</p> <p>28 DAY STRENGTH : 5000 #</p> <p>STRIPPING STRENGTH : 3500 #</p> <p>REBAR GRADE : GR 60</p> <p>WELDED REBAR : A500C</p> <p>WELDED REBAR : A500C</p> <p>Arch-Panel CODE 060</p>			
		<p>CITY OF IOLA - PEDESTRIAN BRIDGE II</p> <p>DRAWN BY DATE CHECKED BY DATE</p> <p>SPP J.M. 6/26/07</p> <p>MILL DATE PROJECT NUMBER</p> <p>09RBM</p> <p>NUMBER REQUIRED MARK NUMBER</p> <p>1 AP002</p>			



NO.		DATE	REVISION	BY
REVISIONS				
CORONA STRUCTURES (MISSOURI) INC.				
BILL OF MATERIALS				
MARK NO.	DESCRIPTION	PER PIECE		
F-56	1" DIA X 5 1/2" INSERT	4		
RP001G	FB, 8 X 3/8 X 0'-8"	4		
	(4) 1/2 DIA X 6" H.A.S.			
CONCRETE FORMULA				
FACING MIX	CY = 0			
BACK-UP MIX	HS-SOCCY = 4.15			
FINISHED AREA	SF = 168			
PIECE WEIGHT	LES = 16850			
MATERIALS DATA				
CONCRETE TYPE :	150 psi			
28 DAY STRENGTH :	5000 psi			
STRIPPING STRENGTH :	3000 psi			
REBAR GRADE :	GR 60			
WELDED WIRE FABRIC P=25,000 psi				
GRADE	060			
PANEL	060			
CITY OF ROLLA - PEDESTRIAN BRIDGE II				
DRAWN BY	DATE	CHECKED BY	DATE	
SPP	1/25/69	JA	4/25/69	
MILL DATE		PROJECT NUMBER	09FRM	
NUMBER REQUIRED	1	MARK NUMBER	P001	



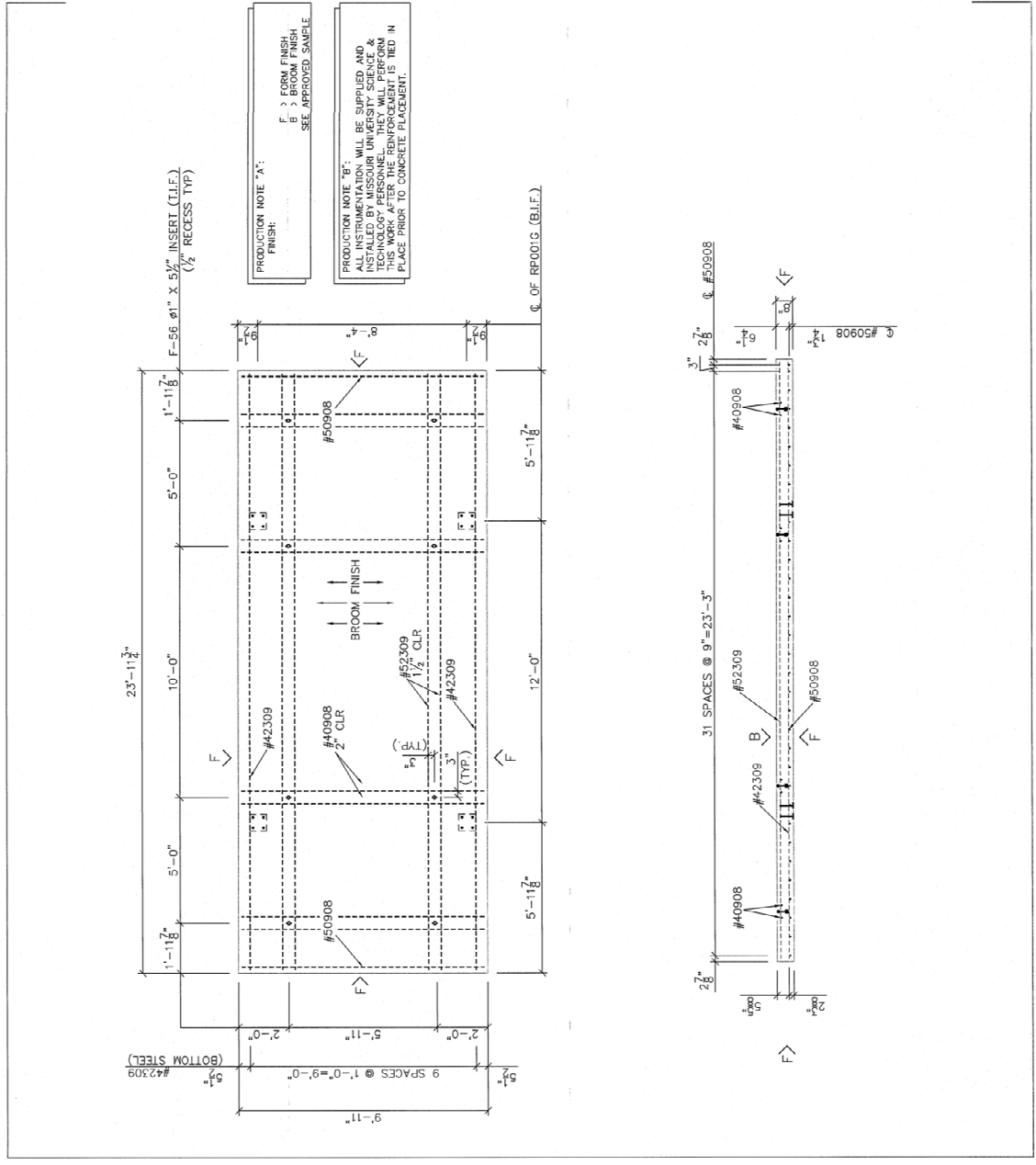
REVISIONS		BY	
NO.	DATE	REVISION	

BILL OF MATERIALS	
MARK NO.	DESCRIPTION PER PIECE
F-56	1" DIA X 5 1/2" INSERT 8
RP001G	FB. 8 X 3/8 X 0'-8" 4
(4)	1/2 DIA X 6" H.A.S.

CONCRETE FORMULA	
FACING MK	C.Y. =
BACK-UP MK	C.Y. = 0
FINISHED AREA	S.F. =
	238
PRICE WEIGHT	URS =
	23800

MATERIALS DATA	
CONCRETE	150 psi
MAX. STRENGTH	5000
STRIPPING STRENGTH	3000 psi
REBAR GRADE	GR 60
WELDED WIRE FABRIC	F _w =65,000 psi
PRODUCT	
Panel	060

PROJECT NAME	
CITY OF ROLLA - PEDESTRIAN BRIDGE I	
DRAWN BY	DATE
SFP	
WILL DATE	PROJECT NUMBER
	OSRBM
NUMBER REQUIRED	MARK NUMBER
1	P003



BIBLIOGRAPHY

- All-Attar, Tareq Salih (2008); "Effect of Coarse Aggregate Characteristics on Drying Shrinkage of Concrete;" Eng & Tech. Vol. 26; No. 2.
- American Association of State Highway and Transportation Officials (1998); "AASHTO LRFD Bridge Design Specifications;" American Association of State Highway and Transportation Officials; Washington, DC.
- American Association of State Highway and Transportation Officials (2002); "AASHTO LRFD Bridge Design Specifications;" American Association of State Highway and Transportation Officials; Washington, DC.
- American Association of State Highway and Transportation Officials (2004); "AASHTO LRFD Bridge Design Specifications;" American Association of State Highway and Transportation Officials; Washington, DC.
- American Association of State Highway and Transportation Officials (2007); "AASHTO LRFD Bridge Design Specifications;" American Association of State Highway and Transportation Officials; Washington, DC.
- American Association of State Highway and Transportation Officials (1998); "Standard Specifications for Highway Bridges;" 16th Edition; American Association of State Highway and Transportation Officials; Washington, DC.
- American Concrete Institute (ACI 209R-92) (1997); "Prediction of Creep, Shrinkage, and Temperature Effects in Concrete Structures;" American Concrete Institute; Detroit, Michigan.
- American Concrete Institute (ACI 211.4R-08) (2008); "Guide for Selecting Proportions for High-Strength Concrete using Portland Cement and Other Cementitious Materials;" American Concrete Institute; Detroit, Michigan.
- American Concrete Institute (ACI 237R-07) (2007); "Self-Consolidating Concrete;" American Concrete Institute; Detroit, Michigan.
- American Concrete Institute (ACI 318-98) (1998); "Building Code Requirements for Structural Concrete;" American Concrete Institute; Detroit, Michigan.
- American Concrete Institute (ACI 318-08) (2008); "Building Code Requirements for Structural Concrete;" American Concrete Institute; Detroit, Michigan.
- American Concrete Institute (ACI 363-92) (1992); "Report on High-Strength Concrete;" American Concrete Institute; Detroit, Michigan.

- American Concrete Institute (ACI 363R-10) (2010); "Report on High-Strength Concrete;" American Concrete Institute; Detroit, Michigan.
- American Concrete Institute (ACI 435R-95) (1995); "Control of Deflection in concrete Structures;" American Concrete Institute; Detroit, Michigan.
- American Concrete Institute (ACI 440.1R-03) (2003); "Guide for the Design and Construction of Concrete Reinforced with FRP Bars;" American Concrete Institute; Detroit, Michigan.
- ASTM C 31/C31 M – 09 (2009); "Standard Practice for Making and Curing Concrete Test Specimens in the Field;" American Society for Testing and Materials; West Conshohocken, Pennsylvania.
- ASTM C 39/C 39 M – 05 (2005); "Standard Test Method for Compressive Strength of Cylindrical Concrete Specimens;" American Society for testing and Materials; West Conshohocken, Pennsylvania.
- ASTM C78 – 08 (2008); "Standard Test Method for Flexural Strength of Concrete (Using Simple Beam with Third-Point Loading);" American Society for Testing and Materials; West Conshohocken, Pennsylvania.
- ASTM C157/C 157M – 08 (2008); "Test method for Length change of hardened Hydraulic-Cement Mortar and Concrete;" American Society for Testing and Materials; West Conshohocken, Pennsylvania.
- ASTM C 469 – 02 (2002); "Standard Test Method for Static Modulus of Elasticity and Poisson's Ratio of Concrete in Compression;" American Society for Testing and Materials; West Conshohocken, Pennsylvania.
- ASTM C 490/C 490M – 08 (2008); "Standard Practice for Use of Apparatus for the Determination of Length Change of Hardened Cement Paste, Mortar, and Concrete;" American Society for Testing and Materials; West Conshohocken, Pennsylvania.
- ASTM C 496/C 496M – 04 (2004); "Standard Test Method for Splitting Tensile Strength of Cylindrical Concrete Specimens;" American Society for Testing and Materials; West Conshohocken, Pennsylvania.
- ASTM C 512 – 02 (2002); "Standard Test Method for Creep of Concrete in Compression;" American Society for Testing and Materials; West Conshohocken, Pennsylvania.
- ASTM C1611/ C 1611M – 05 (2005); "Standard Test Method for Slump flow of Self-Consolidating Concrete;" American Society for Testing and Materials; West Conshohocken, Pennsylvania.

- ASTM D 7205-06 (2005); "Standard Test Method for Tensile Properties of Fiber Reinforced Polymer Matrix Composite Bars;" American Society for Testing and Materials; West Conshohocken, Pennsylvania.
- Burgueno, R.; Bendert, D.A. (2007); "Structural Behavior and Field-Monitoring of SCC Prestressed Box Beams for Demonstration Bridge;" Self-Consolidating Concrete for Precast Prestressed Applications; ACI Fall 2007 Convention; Fajardo, Puerto Rico.
- Brewe, Jared (2009); "Optimization and Behavior of High Performance Concrete in Structural Applications;" *Dissertation*; Missouri University of Science and Technology; Rolla, MO.
- Brewe, Jared E.; Myers, J.J. (2010); "High-Strength Self-Consolidating Concrete Girders Subjected to Elevated Fiber Stresses Part I: Prestress Loss and Camber Behavior;" *Prestress/Precast Concrete Journal*; Chicago, Illinois; Fall 2010; Vol. 55 No.4; pp 59-77.
- Caldarone, Michael A.(2009); *High-Strength Concrete: A Practical Guide*; New York, NY.
- Cousins, T.E. (2005); "Investigation of Long-Term Prestress Losses in Pretensioned High Performance Concrete Girders;" FHWA/VTRC; Virginia Transportation Research Council; Charlottesville, VA.
- Dwairi, Hazim M.; Wagner, Matthew C.; Kowalsky, Mervyn J.; Zia, Paul (2010); "Behavior of Instrumented Prestressed High Performance Concrete Bridge Girders;" *Construction and Building Materials*.
- Dewar, J.D. (1964); "The Indirect Tensile Strength of Concretes of High Compressive Strength," *Technical Report* No. 42.377, Cement and Concrete Association, Wesham Springs, Mar., 12 pp.
- Gross, S.P. (1999); "Field Performance of Prestressed High Performance Concrete Highway Bridges in Texas;" *Dissertation*; University of Texas at Austin.
- Holdener, David J. (2008); "Long Term Monitoring of Bridges Strengthened and Constructed with Fiber-Reinforced Polymer Technologies;" *Thesis*; Missouri University of Science and Technology; Rolla, MO.
- Khayat, Kamal H.; Mitchell, Denis (2009); "Self-Consolidating Concrete for Precast, Prestressed Concrete Bridge Elements;" National Cooperative Highway Research Program Report No. 628; Transportation Research Board; Washington, DC.
- Kocaoz, S.; Samaranayake, V.A.; Nanni, A. (2004); "Tensile Characterization of Glass FRP Bars;" *Composites: Part B*.

- Kukay, Brian; Barr, Paul J.; Halling, Marviwn W. (2007); "A Comparison of Time Dependent Prestress Losses in a Two-Span, Prestressed Concrete Bridge;" 2007 ASCE Structures Congress: New Horizons and Better Practices; Utah State University, Utah.
- MacGregor, James G.; Wight, James K. (2009); *Reinforced Concrete Mechanics and Design* Fourth Edition; Upper Saddle River, New Jersey.
- Young, J.F; Darwin, D.; Mindness, S. (2002); *Concrete*, Second Edition; Prentice Hall; 644 pp, ISBN 0-13-064632-6.
- Myers, J.J. (1998); "Production and Quality Control of High Performance Concrete in Texas Bridge Structures;" *Dissertation*, University of Texas—Austin.
- Myers, J.J.; Carrasquillo, Ramon L. (2000); "Influence of Hydration Temperature on the Durability and Mechanical Property Performance of HPC Prestressed and Precast High-Performance Concrete Beams;" National Research Council; Journal of the Transportation Research Board; 1696, Vol. 1, pp. 131-142.
- Myers, J.J. (1999); "How to Achieve a higher Modulus of Elasticity;" HPC Bridge Views; FHWA Sponsored; NCBC Co-Sponsored Newsletter; Issue No. 5; September/ October.
- Myers, J.J.; Yang, Yumin (2005); "High Performance Concrete for Bridge A6130-Route 412 Pemiscot County, MO;" UTC R39.
- Naito, Clay J.; Parent, Greg; Brunn, Geoffrey (2006); "Performance of Bulb-Tee Girders Made with Self-Consolidating Concrete;" *Prestressed/Precast Concrete Institute Journal*; Chicago, Illinois;
- NCDC; "Quality Controlled Local Climatological Data;" National Climatic Data Center; website: <http://cdo.ncdc.noaa.gov/qclcd/QCLCD?prior=N>.
- Nawy, Edward G. (2006); *Prestressed Concrete: A Fundamental Approach Fifth Edition*; Upper Saddle River; New Jersey.
- Ouchi, Masahiro; Nakamura, Sada-aki; Hallberg, Sven-Erik; Osterberg, Thomas; and Lwin, Myint (2003); "Applications of Self-Compacting Concrete in Japan, Europe and the United States"; ISHPC.
- Phillips, Kimberly A.; Harlan, Matthew; Roberts-Wollman, Carin L.; and Cousins, Thomas E. (2005); "Performance of a Bridge Deck with Glass Fiber Reinforced Polymer Bars as the Top Mat of Reinforcement;" FHWA/VTRC; Virginia Transportation Research Council; Charlottesville, VA.

- Precast/Prestressed Concrete Institute. (1999); "PCI Design Handbook, Fifth Edition," PCI; Chicago, Illinois.
- Precast/Prestressed Concrete Institute. (2004); "PCI Design Handbook, Sixth Edition," PCI, Chicago, Illinois.
- Shahawy, Moshen A. (2003); "Prefabricated Bridge Elements and Systems to Limit Traffic Disruption During Construction," National Cooperative Highway Research Program Report Program Synthesis 324; Washington, DC.
- Trent, Justin D. (2007); "Transfer Length, Development Length, Flexural Strength, and Prestress Loss Evaluation in Pretensioned Self-Consolidating Concrete Members;" *Thesis*; Virginia Polytechnic Institute and State University; Blacksburg, Virginia.
- Tadros, M.K.; Al-Omaishi, N.; Seguirant, S.J.; and Gallt, J.G. (2003); "Prestress Losses in Pretensioned High-Strength Concrete Bridge Girders;" National Cooperative Highway Research Program Report 496; TRB; National Research Council; Washington, DC.